Magnetism in layered Ruthenates
Magnetismus in geschichteten Ruthenaten

Inaugural-Dissertation

zur Erlangung des Doktorgrades
der Mathematisch-Naturwissenschaftlichen Fakultät
der Universität zu Köln

vorgelegt von

Paul C. Steffens

aus Köln

Köln, 2008

Berichterstatter: Prof. Dr. M. Braden
Prof. Dr. A. Rosch

Vorsitzender
der Prüfungskommission: Prof. Dr. L. Bohatý

Tag der letzten mündlichen Prüfung: 23.10.2007

Contents

Contents

1 Introduction

By discussing the magnetism of the layered Ruthenates, this thesis addresses a variety of intriguing phenomena in solid state physics. The restriction on this single class of materials does by no means limit the number of interesting topics to be discussed: they include metamagnetic transitions, quantum critical behavior, magnetic order in general, magnetic fluctuations in highly correlated materials, and unconventional superconductivity.

In the recent years, two members of the family of layered Ruthenates have made these materials widely recognized and attracted significant attention: firstly, this is Sr_2RuO_4 – an unconventional superconductor in which the Cooper pairs are most likely in a triplet state. Secondly, in $Sr_3Ru_2O_7$ the concept of metamagnetic quantum criticality is currently under active debate.

While there are also layered Ruthenates with a higher number of layers, these two cases – the layered perovskite Ruthenates with one or two layers – are the only ones considered here. Starting from these two materials, a variety of other substances are obtained which have very different properties and are of interest on their own right. Substituting Strontium by Calcium, one can continuously vary the chemical composition and arrives finally at Calcium Ruthenate (Ca_2RuO_4 or $Ca_3Ru_2O_7$) which has, driven by structural distortions, entirely different properties. These substances are therefore very well suited to study the interplay between the structural, electronic, orbital and magnetic degrees of freedom. Another interesting variation is achieved by substituting Ruthenium with Titanium, which leads to magnetically ordered states.

This thesis contains the results of experimental work. For the investigation of magnetic properties, neutron scattering is an extremely powerful tool. A number of different neutron scattering techniques has been applied, thereby addressing very diverse aspects of magnetism in the layered Ruthenates and yielding a detailed picture of these materials.

This thesis contains four large chapters, which are organized as follows:

- Chapter 2 does not contain experimental results, but briefly summarizes the foundations of the experimental techniques, some theoretical background including a summary of the relevant formulae, and details of some computational methods used in the discussion of the data. The following chapters refer to this information at many occasions.

- The longest part of the thesis is Chapter 3, which is devoted to the single-layer Ruthenates with mixed Ca/Sr content, $Ca_{2-x}Sr_xRuO_4$. It focuses on the paramagnetic metallic region of the phase diagram, in particular on the Sr-concentrations x=0.2 and 0.62. The most interesting physical phenomenon to be discussed is the metamagnetic transition, which may have similar properties as the metamagnetic transition in $Sr_3Ru_2O_7$. Very strong magnetic fluctuations of different character are related to interesting behavior and are thoroughly studied as function of temperature and magnetic field. The most striking observation is how the nearly antiferromagnetic $Ca_{1.8}Sr_{0.2}RuO_4$ can be turned into a ferromagnet by the magnetic field.

- Continuing with the single-layer Ruthenates, Chapter 4 discusses the magnetic fluctuations in Sr_2RuO_4, which are highly important as they may be responsible for (spin-triplet) pairing in this material. By characterizing a weak but essential part of the fluctuation spectrum that had not been identified so far, it provides a full and consistent description of the magnetic response in Sr_2RuO_4. Briefly, some results are also presented on $Sr_2Ru_{1-x}Ti_xO_4$.

- Finally, Chapter 5 addresses two – rather different – aspects of the magnetism in the bilayer Ruthenates. In $Ca_3Ru_2O_7$, a material which also shows a metamagnetic transition, though quite different from $Ca_{1.8}Sr_{0.2}RuO_4$, a spin density study has been performed. In Ti-doped $Sr_3Ru_2O_7$ it is shown that similar to the single-layer $Sr_2Ru_{1-x}Ti_xO_4$ magnetic order – an incommensurate spin density wave – is induced at Ti-contents of only a few percent, and this magnetic order is characterized in detail. Furthermore, the excitations have been studied.

2 Experimental and theoretical tools

2.1 Inelastic neutron scattering experiments

Most experimental data in this thesis have been collected in inelastic neutron scattering (INS) experiments. Neutron scattering is in general a very powerful tool for the investigation of nuclear and magnetic excitations in condensed matter, because the neutron interacts as well with the nuclei as with the magnetic moments, offers a wide range of energy and momentum transfer and can penetrate deep inside the sample. If suitable (this means often: large enough) samples and sufficient beam-time are available, one can obtain a degree of information on magnetic correlations and magnetic order that is hardly achievable by any other method.

The majority of experiments reported in the following have been performed on triple-axis spectrometers; techniques like time-of-flight spectrometers have not been used for the results presented here. The triple-axis spectrometers that have been used work either with cold or with thermal neutrons, thereby covering the range of energy transfers $\hbar\omega$ between approximately 0.3 meV up to about 10 meV, which has been the interesting range for most problems. (An order of magnitude higher energy transfers are possible with the technique and frequently used for other problems.)

There are several textbooks on neutron scattering, which cover all relevant aspects of the technique and the underlying theory in extensive detail. Classic references are for instance Marshall-Lovesey's book [1, 2], from which most information was taken, or the one of Squires [3]. A newer one with a focus on magnetic scattering is the one of Chatterji [4]. Another recent and very useful one which emphasizes the technical aspects of triple-axis spectrometry, is the book of Shirane [5].

Because this thesis includes no technical development in the field, the reader is referred to these books, and the extensive theory of neutron scattering shall not be reviewed here. In the following sections only some of the most relevant formulas shall be briefly summarized.

The measurements mainly focused on the magnetic scattering in paramagnetic metallic states. The typical magnetic excitations here are fluctuations. They do not have the character of well-defined dispersive branches like for instance magnons, but form a continuum of excitations which contains the information on the spin correlations. As the excitations of the itinerant electrons, they are closely connected to the electronic band structure and Fermi surfaces.

2.1.1 Magnetic neutron scattering

In magnetic neutron scattering, the neutron is scattered by the interaction between the magnetic moment associated with its spin and a magnetic moment in the sample. The inelastic scattering is usually expressed in terms of the imaginary part of the wave-vector and frequency dependent magnetic susceptibility $\chi(Q, \omega)$. The formula for the cross section then reads [1, 4]

$$\frac{d^2\sigma}{d\Omega dE} = N \frac{k_f}{k_i} \frac{r_0^2}{4\pi \mu_B^2} F(Q)^2 e^{-2W(Q)} \frac{1}{1 - e^{-\frac{\hbar\omega}{k_B T}}} \cdot \sum_{\alpha\beta} (\delta_{\alpha\beta} - \hat{Q}_\alpha \hat{Q}_\beta) \cdot \chi''_{\alpha\beta}(Q, \omega) \qquad (2.1)$$

with $r_0 = \frac{\gamma e^2}{m_e c^2} = -5.4$ fm, which gives a measure of the strength of the interaction (same order of magnitude as nuclear scattering lengths). Of special importance are three factors: (i) the magnetic form factor $F(Q)$, which implies that the signal is large only at small momentum transfers Q, (ii) the Bose factor, which takes account of the thermal population of the states and the principle of detailed balance, and (iii) the sum contains the geometrical effect that determines how the different components of the tensor χ contribute. In many cases this term can be simplified to

$$(1 - \hat{Q}_z)\chi''_{zz} + (1 + \hat{Q}_z)\chi''_{xx} \qquad (2.2)$$

Here it becomes evident that it is only the component of χ perpendicular to Q which contributes to the cross section ($\chi_{xx} = \chi_{yy}$). The second important remark is that in this step χ has been split into a longitudinal (χ_{zz}) and transverse (χ_{xx}) part. The choice of z as a quantization and eventual field direction is arbitrary at this point, and in a paramagnetic state without anisotropies or external magnetic field, all components would of course be identical. (Theoretically, the condition for the above simplification is that $\hat{S}^z_{\text{tot}}$ is a constant of motion.)

2.1.2 Using polarized neutrons

Applying (2.2) one can in principle, by measuring at different equivalent Q-vectors, separate the two components χ''_{xx} and χ''_{zz}. In some cases this is quantitatively very inaccurate, because other factors like the experimental geometry, form-factor effects, resolution etc. introduce additional errors. The use of polarized neutrons can provide a great amount of additional information.

In such a case the spin of the neutrons in the incident beam is polarized in a certain direction, and the change of the neutron spin is analyzed after the scattering process, i. e. one measures a *spin-flip* and a *non-spin-flip* intensity. It is possible to choose the polarization of incident and scattered neutrons completely independently in order to measure all components (including the off-diagonal ones) of χ when using a setup named *CRYOPAD*. When one is not interested in these components – and in the

following we restrict on this case – one can use a simpler experimental setup in which the sample stays in the guide field which is produced by Helmholtz coils, meaning that only the component of the final spin along the direction of the incident polarization can be analyzed. If the sample has inversion symmetry, the cross sections depend only on the direction of the polarization $\mathbf{P}$ of the incident neutron, but not if it is 'up' or 'down' along this direction. If one defines a set of orthogonal axes as h_z (=vertical axis), h_x (=parallel to the scattering vector) and h_y ($\perp h_x, h_z$), one has one cross section for spin-flip and non-spin-flip scattering for each of these directions of the incident polarization $\mathbf{P}$:

$$
\begin{aligned}
I^{SF} \quad &\propto \quad \begin{cases} \chi''_{xx}(\mathbf{Q}, \omega) \;+\; \chi''_{zz}(\mathbf{Q}, \omega) \;+\; BG^{SF} & (P \parallel h_x) \\[4pt] \chi''_{zz}(\mathbf{Q}, \omega) \;+\; BG^{SF} & (P \parallel h_y) \\[4pt] \chi''_{xx}(\mathbf{Q}, \omega) \qquad\qquad\;+\; BG^{SF} & (P \parallel h_z) \end{cases} \\[20pt]
I^{NSF} \quad &\propto \quad \begin{cases} BG^{NSF} & (P \parallel h_x) \\[4pt] \chi''_{xx}(\mathbf{Q}, \omega) \;+\; BG^{NSF} & (P \parallel h_y) \\[4pt] \chi''_{zz}(\mathbf{Q}, \omega) \;+\; BG^{NSF} & (P \parallel h_z) \end{cases}
\end{aligned}
\tag{2.3}
$$

These are the six intensities which are measured in such an experiment. In BG^{SF} and BG^{NSF}, a "background", i. e. scattering which is not coherent magnetic, is summarized. It is usually safe to assume that they do not depend on the direction of $\mathbf{P}$, although especially BG^{NSF} can be very large and in general also contains nuclear coherent scattering like phonons. One also has to consider a finite flipping ratio R, i.e. a finite polarization efficiency, and to take into account corrections of the order $\frac{1}{R}$; this should not be neglected for the data collected on IN20 (Chapter 4), for which R is only of the order 10, but this correction can be easily applied. By calculating the differences between the different intensities, the different components of χ are straightforwardly extracted. This offers the unique possibility to measure not only anisotropic susceptibilities, but also to separate the magnetic contribution from other scattering processes.

In general one may say that the gain in information on the scattering process, especially in magnetic scattering, that one obtains from the analysis of the neutron's spin state, is substantial and often very valuable. The severe drawback of the polarized neutron technique is, though, that the loss in intensity is tremendous, too. In practice one therefore has to consider in each case if the use of polarized neutrons is most appropriate for the given problem. In what follows in this thesis, this technique proved to be crucial in Sr_2RuO_4, because there a weak magnetic signal had to be separated from strong nuclear (phonon) scattering. In $Ca_{2-x}Sr_xRuO_4$ an application of polarized neutrons would have been desirable, but is at present hopeless for the reason of counting statistics.

2.1.3 Neutrons and the susceptibility

It has already been mentioned that the cross section is proportional to the imaginary part of the susceptibility $\chi(\mathbf{Q}, \omega)$, which contains the information on the magnetic correlations in the sample and is therefore the quantity one is usually interested in. Unfortunately, two facts complicate the interpretation of the data. Firstly, it is not trivial to convert the measured signal, typically a number of counted neutrons normalized to a monitor count rate, into absolute units for $\chi''(\mathbf{Q}, \omega)$. Secondly, at least strictly speaking, there is not even a proportionality. It is as dangerous as popular to simply take the measured signal in a real INS experiment proportional to $\chi''(\mathbf{Q}, \omega)$, because it may be strongly affected by resolution effects. These two problems will now be shortly addressed.

Resolution effects. When setting a triple-axis spectrometer to a certain energy and momentum transfer $\hbar\omega$ and $\mathbf{Q}$, not only the neutrons from exactly that scattering process will be counted by the detector, but also neutrons from a certain neighborhood around $(\mathbf{Q}, \hbar\omega)$, i. e. the spectrometer has a finite resolution like every physical measuring device. The resolution function of a triple-axis spectrometer can be approximated as an ellipsoid in four-dimensional $\mathbf{Q},\omega$-space [6, 7] and depends on the geometry of the setup, the wavelengths, the collimations etc. and also the sample itself. The problem is that (i) the resolution ellipsoid can be very large (it is often necessary to relax resolution and use focusing to increase the count rate), (ii) that its axes are usually not parallel to the axes in the sample's $\mathbf{Q},\omega$-space and (iii) the resolution function (both the ellipsoid's volume and orientation) may change significantly for different $(\mathbf{Q},\omega)$, i. e. for different scans and even within a single long scan. The second aspect, for instance, can give rise to focusing effects when dispersive modes like phonons or magnons happen to match exactly the resolution ellipsoid; the well-known example and an impressive illustration for this effect is the difference between the focusing and defocusing side in a constant energy scan across a transverse acoustic phonon, which look entirely different although the cross section is the same. These remarks may sound quite pessimistic, but in reality they usually present no serious obstacle as long as they are kept in mind. On the other hand, such effects, when wisely handled, can even be usefully exploited.

A direct correction of measured data for the resolution effect is not possible in practice. The proper way to account for the resolution effect is therefore to really perform the 4D convolution for a given model of the cross section by a suitable software and to compare (fit) it to the data. In this thesis, that has been done using the package RESLIB [8] for MATLAB. This procedure is very general and flexible, but it requires a rather detailed model for the scattering function $S(\mathbf{Q}, \omega)$, and this is why it can not always be applied. In many cases, anyway, one can argue that the features to be observed are broad compared to the experimental resolution (in any direction of $\mathbf{Q},\omega$-space). Then, the effect of the resolution can safely be neglected, a proportionality

between the count rate and $S(\mathbf{Q}, \omega)$ be assumed, and the raw data directly be taken for further treatment or discussion. This applies in particular to magnetic fluctuations in the paramagnetic state, which have usually a large extension in reciprocal space, and therefore to a big part of the data presented later.

The conversion to absolute units. For the reasons discussed above, it would actually not be correct to assign to a measured scan units of susceptibility, because no strict proportionality holds. Nevertheless it can make sense (when the proportionality holds at least approximately), and it is clearly desirable to assign absolute units to a model of $\chi''(\mathbf{Q}, \omega)$ that has been fitted to the data. For somebody who is not experienced with inelastic neutron scattering it may be astonishing that the assignment of reasonable units to the data sometimes presents difficulties, because in the formula for the cross section (2.1) there is no quantity that is not known or could not be determined. There are, though, a number of factors which present problems in practice, including the incident flux, the shape of the sample and how efficiently it is positioned in the beam, absorption effects, the efficiency of the spectrometer components (analyzer, detector etc.) and focusing conditions. The calibration of the intensity with the help of a known signal is therefore usually much more precise. One possibility is to use an acoustic phonon for which the structure factor is known; the advantage is that it can be measured without any change in the experimental setup, the same wavelength and temperature and mostly at similar sample orientation or even at similar values of $\mathbf{Q}$ and ω.

For this purpose, let us recall the cross section for a single phonon branch at the frequency $\omega_{\mathbf{Q}}$ [1]:

$$\frac{d^2\sigma}{d\Omega dE} = N \frac{k_f}{k_i} \frac{1}{2} \cdot \frac{1}{1 - e^{-\frac{\hbar\omega}{k_B T}}} \cdot \frac{1}{\omega_{\mathbf{Q}}} \left| \sum_j \frac{\bar{b}_j}{\sqrt{m_j}} (\vec{\mathbf{Q}} \cdot \vec{\xi}_j) e^{i\vec{\mathbf{Q}} \cdot \vec{\mathbf{d}}_j} e^{-W_j} \right|^2 \cdot \delta(\omega - \omega_{\mathbf{Q}}) \qquad (2.4)$$

where the sum runs over the atoms j; b_j is the coherent scattering length, $\vec{\mathbf{d}}_j$ is the position of the atom and $\vec{\xi}_j$ its polarization vector in this mode. The squared absolute value is the structure factor $|F_{\mathrm{ac}}(\mathbf{Q})|^2$ of the phonon, and for an acoustic phonon the following important limit holds[1] [5] when $\mathbf{Q} = \mathbf{G} + \mathbf{q}$ approaches a reciprocal lattice vector $\mathbf{G}$:

$$\lim_{q \to 0} |F_{\mathrm{ac}}(\mathbf{Q})|^2 = \frac{\mathbf{G}^2}{M} |F_{\mathrm{N}}(\mathbf{G})|^2 \qquad (2.5)$$

where M is the sum of the atomic masses, $M = \sum_j m_j$, and F_{N} is the nuclear structure factor of the Bragg reflection $F_{\mathrm{N}}(\mathbf{G}) = \sum_j \bar{b}_j e^{i\mathbf{G} \cdot \mathbf{d}_j} e^{-W_j}$ which can be easily calculated. The goodness of the approximation to set F_{ac} to this value depends of course

---

[1]Equation (2.5) assumes that $\mathbf{G}$ is parallel to the polarization of the phonon $\vec{\xi}_j$. If this was not fulfilled, one would have to replace $\mathbf{G}$ by its projection.

on how far $\mathbf{Q}$ is away from $\mathbf{G}$. It is not trivial to implement the phonon structure factor for different $\mathbf{Q}$ and requires an elaborate calculation on a special dynamical structure model. For Sr_2RuO_4, fortunately, the lattice dynamics has been studied [9, 10] and a model exists based on which structure factors and frequencies as function of $\mathbf{Q}$ can be calculated by the program "Genax". This has been done for a set of $\mathbf{Q}$'s around (2,0,0), the structure factors then put on a scale of absolute units using equation (2.5) and implemented in a Matlab routine. A graphical representation of this function is displayed in Figure A.1 in the appendix. The known phonon cross section is then used to fit the experimental data taking into account the resolution function of the spectrometer.

In the appendix, a detailed description is given of how this procedure has actually been done. It is in principle simple and straightforward, but requires some care not to get confused by different conventions and units. One needs a function that can describe the magnetic scattering, i. e. a model for $\chi''(\mathbf{Q}, \omega)$. This function is then fit to the experimental data, taking into account the resolution function, Bose factor and form factor. Secondly, by a fit of the scale factor in the phonon function, the relation between experimentally measured counts and real units is determined. One then just has to carefully collect the prefactors and obtains the conversion factor for χ_{model} into physical units as function of $\mathtt{scale}^{Ph}$, $\mathtt{scale}^{Mag}$ and $\lim_{q \to 0} |F_{\mathrm{ac}}(\mathbf{Q})|^2$ in the correct dimension of susceptibility.

Units. A comment should also be made on the units in which $\chi(\mathbf{Q}, \omega)$ is measured, because a variety of different units for susceptibilities is used, most of which even have different physical dimension, and can easily lead to confusion. In the SI system, a susceptibility is in fact a *dimensionless* quantity, according to $M = \chi H$, where M is the magnetization (M and H in units of $\frac{A}{m}$). Because magnetization is magnetic moment per volume and one is often interested in the total magnetic moment of the sample, it is also a common practice to give susceptibility directly in the dimension of a volume (m^3 in SI) and then again normalize it to a certain amount of sample, for instance one mole. The parallel use of the cgs system does not make things simpler, but it is at least easy to make the connection. In cgs, B and H have the same dimension, while in SI $B = \mu_0 H$ (in vacuum), or $B = \mu_0(H + M)$ with $M = \chi H$. The difference is thus basically the μ_0 ($\mu_0 = 4\pi \cdot 10^{-7} \frac{Vs}{Am}$). By expanding the units, one can easily realize that the physical dimension of μ_0 is $\frac{\mathrm{energy \cdot volume}}{(\mathrm{magnetic\ moment})^2}$. When intending to give a susceptibility in a system where $\mu_0 = 1$ like in cgs, its dimension will therefore be the inverse of the one just given. After integration over the sample volume and normalization to the number of magnetic atoms as mentioned above, it is obvious that the susceptibility can be written in units of $\frac{\mu_B^2}{eV}$ per magnetic atom. This is the unit in which $\chi(\mathbf{Q}, \omega)$ is usually given, at least in the context of neutron scattering.

Some useful conversion factors are:

$$1\,\frac{\mu_B^2}{eV}\text{ per f.u. } = 3.233\cdot 10^{-5}\text{ emu}\cdot\text{mol}^{-1} \quad \textbf{(cgs)} \tag{2.6}$$

$$= 6.674\cdot 10^{-4}\text{ Å}^3\text{ per f.u.} \quad \textbf{(SI)} \tag{2.7}$$

When taking the lattice constants of Sr_2RuO_4, a=b=3.87 Å, c=12.74 Å, the volume per formula unit (f.u.) is 95 Å^3 (half the volume of the tetragonal unit cell), so that in SI for Sr_2RuO_4

$$1\,\frac{\mu_B^2}{eV}\text{ per f.u. } = 7.102\cdot 10^{-6} \tag{2.8}$$

Within a few percent this applies to $Ca_{2-x}Sr_xRuO_4$ for all x and temperatures and gives a rough estimate of the actual size of the field produced by the induced moments; one can thus state that unless for very large numerical values of χ, i. e. up to at least $10^4\,\frac{\mu_B^2}{eV}$, it is so small that one can safely neglect effects like demagnetization factors etc.

It is finally mentioned that

$$1\,\frac{\mu_B^2}{eV}\,\hat{=}\,5.79\cdot 10^{-5}\frac{\mu_B}{T} \tag{2.9}$$

This is a simple relation between the applied field $\mu_0 H$ and the induced magnetic moment. In combination with (2.6), it follows

$$1\text{ emu}\cdot\text{mol}^{-1}\,\hat{=}\,1.79\frac{\mu_B}{T} \tag{2.10}$$

2.2 Spin fluctuations in metals

2.2.1 The susceptibility in the metallic state

When studying the magnetic properties of solids, there are generally the two contrary approaches of regarding either localized or itinerant magnetic moments. The former picture is suitable for magnetic moments that are localized in real space, typically on certain magnetic ions, and have a fixed (mostly integer) size. The magnetization of a material is determined by what amount of magnetic moments is polarized in the interplay of entropy (temperature), external field and interaction of the magnetic moments – giving rise to a Curie law for the susceptibility. The picture of itinerant electrons is more suited for metals and regards electrons in the $\vec{k}$-states ("localized in reciprocal space") instead in real space. Because of the Pauli principle, only the electrons close to the Fermi level are relevant for most magnetic properties, and in a polarized state, the magnetic moment per atom can have any fractional value.

These two approaches are conceptually very different. For many materials it is obvious which is the better suited one – that one usually works very well, leaving

the more intermediate cases as the more "interesting" ones, and it is not always trivial to reconcile these two pictures. Sr_2RuO_4 is a good metal and clearly needs a treatment in an itinerant picture. When going more to the Ca-side of the series $Ca_{2-x}Sr_xRuO_4$, correlation and localization effects become gradually more important, and the question for the appropriate way to understand the magnetic properties is less simple. In the metallic region of the phase diagram, the itinerant picture appears as the more adequate one and enables to better follow the evolution for different Sr-contents, and should therefore be used.

A good text about magnetic neutron scattering in an itinerant system is for instance Ref. [11] (an early report on magnetism in Nickel by R. D. Lowde), and the standard Reference for spin fluctuations is Moriya's book [12]. As these concepts are very fundamental in the following, the most relevant aspects and formulae will now briefly be summarized.

In a metal, where the magnetism depends on the itinerant electrons, all magnetic properties are very closely related to the particular band structure of the material. One of the basic results of solid state physics is the so-called Pauli susceptibility of a metal, which basically states that the paramagnetic susceptibility is proportional to the density of states at the Fermi level:

$$\chi_P = \mu_0 \mu_B^2 \rho(E_F) \tag{2.11}$$

This is usually a small and nearly temperature independent quantity.

Very important effects can arise from the interaction between the electrons. In a molecular-field theory, the spins feel, in addition to the external magnetic field, the molecular field produced by the polarization of magnetic moments in the sample, giving rise to a positive feedback mechanism and enhancing the susceptibility over the value χ_P. The "effective" field is thus $H_{\text{eff}} = H + \frac{U}{\mu_0 \mu_B^2} M$ with $M = \chi H$, where χ is the "true", renormalized susceptibility. Solving this self-consistently, as M is also $\chi_P H_{\text{eff}}$, one obtains $\chi = \frac{\partial M}{\partial H} = \chi_P (1 + \frac{U}{\mu_0 \mu_B^2} \chi)$, or

$$\chi = \frac{\chi_P}{1 - \frac{U}{\mu_0 \mu_B^2} \chi_P} \tag{2.12}$$

For large enough U and χ_P this quantity will diverge – this is the well-known Stoner criterion for the appearance of ferromagnetism. The molecular field is due to exchange, that means it is important to remember the well-known fact that its physical origin is not the magnetic dipolar interaction, but the Coulomb interaction of the electrons which would enter in the Hamiltonian as $U \sum n_\uparrow n_\downarrow$.

This short introduction, which can be found in any basic solid state physics textbook, has been recalled here, because these two steps – the calculation of the "bare"

susceptibility depending on the properties of the band structure, and secondly includ-ing the correlation effects – are exactly what has to be done also in the more com-plicated situation of calculating the susceptibility in the very general case of nonzero wave vectors and frequencies.

The generalized susceptibility

To generalize the susceptibility to its full $\vec{q}$- and ω-dependence one has to regard the effect of a magnetic field that varies in space and time – characterized by the wave vector $\vec{q}$ and the frequency ω – which will perturb electrons from $(\vec{k}, E_{\vec{k}})$ into $((\vec{k}+\vec{q}), E_{\vec{k}+\vec{q}})$. One thus has to consider the possible processes corresponding to the excitation of an electron from a state $\vec{k}$ into a state $\vec{k}+\vec{q}$ which cost the energy $\hbar\omega = E_{\vec{k}+\vec{q}} - E_{\vec{k}}$. Here, $E_{\vec{k}}$ is the energy of an electron at $\vec{k}$ and is determined by the band dispersion. To make the treatment even more general, one also takes into account the effect of a finite exchange splitting Δ of the bands, i. e. a ferromagnetic state. The energies $E_{\vec{k}}$ then depend on the spin direction ($\uparrow$ or $\downarrow$) and are $E_{\vec{k}}^{\sigma} = E_{\vec{k}} + \frac{1}{2}\sigma\Delta$ (σ=+,-).
When regarding the effect of the field to first order (linear response) one finds

$$\chi_0^{\sigma_1\sigma_2}(\vec{q},\omega) = \mu_0(g\mu_{\mathsf{B}})^2 \frac{1}{N} \lim_{\epsilon\to0+} \sum_{\vec{k}} \frac{f\left(E_{\vec{k}+\vec{q}} + \frac{1}{2}\sigma_2\Delta\right) - f\left(E_{\vec{k}} + \frac{1}{2}\sigma_1\Delta\right)}{E_{\vec{k}+\vec{q}} - E_{\vec{k}} - \hbar\omega + \frac{1}{2}(\sigma_2-\sigma_1)\Delta + \epsilon i} \tag{2.13}$$

This is the so-called Lindhard function, and gives correctly the real and the imagi-nary part of the susceptibility. In the nominator, $f(E)$ is the Fermi distribution function accounting for the occupation of the initial and final states and thus giving the correct weight in the sum over the Brillouin zone. The denominator is the difference of the ini-tial and final energies and $\hbar\omega$. It seems not possible to understand the whole formula straightforwardly in an intuitive way, and it has indeed quite complicated properties. The correct derivation appears, though not particularly difficult, too long and technical to be reproduced here and would not provide additional insight; it can be found for instance in Refs. [1, 12][2]. Instead, a few comments on its properties and the way of calculating it shall be made.
Of special interest is the imaginary part of χ, because it determines the neutron scattering cross section. By using the identity

$$\mathrm{Im} \lim_{\epsilon\to0+} \frac{1}{x+\epsilon i} = -\pi\delta(x) \tag{2.14}$$

---

[2]A heuristic argument to roughly understand the form of (2.13) without the advanced formalism in these References would be the following. The field $H(r)$ which varies in space like $\cos(qr)$ is treated as a perturbation. The correction term to the electronic states ψ_k in first order perturbation theory has a denominator containing the energy differences in the correct form. The magnetization M(r) is obtained as the sum over all $\vec{k}$ of $|\psi_k^+(r)|^2 - |\psi_k^-(r)|^2$, weighted with $f(E_k)$ and regarding only terms up to first order in H. Then χ is $\partial M/\partial H$ and has the overall form of the sum over $\vec{k}$ with the difference of Fermi functions in the nominator and the energies in the denominator.

one can express it in a much more convenient form:

$$\text{Im } \chi_0^{\sigma_1\sigma_2}(\vec{q},\omega) = \pi\mu_0(g\mu_\text{B})^2 \frac{1}{N} \sum_{\vec{k}} \left(f(E_{\vec{k}}^{\sigma_1}) - f(E_{\vec{k}+\vec{q}}^{\sigma_2})\right) \cdot \delta\left(E_{\vec{k}+\vec{q}}^{\sigma_2} - E_{\vec{k}}^{\sigma_1} - \hbar\omega\right) \quad (2.15)$$

This has a clearer meaning: the sum over the Brillouin zone "counts" the possible excitations of electrons from $(\vec{k};\sigma_1;E_{\vec{k}}^{\sigma_1})$ into $((\vec{k}+\vec{q});\sigma_2;E_{\vec{k}+\vec{q}}^{\sigma_2})$, and the delta function ensures the energy conservation. In other words, such an excitation creates an electron-hole pair, because an electron is promoted to $\vec{k}+\vec{q}$ and a hole is left at $\vec{k}$. It can occur from any occupied into any empty state, so for a given $\vec{q}$, usually excitations with different ω are possible, and in $\vec{q}$-ω space these processes form a continuum with boundaries that are determined by the band dispersion. This continuum is directly represented by χ'', while the real part χ' is usually non-zero everywhere. Expression (2.15) has the symmetry $\text{Im } \chi_0^{\sigma_1\sigma_2}(\vec{q},\omega) = -\text{Im } \chi_0^{\sigma_2\sigma_1}(-\vec{q},-\omega)$. In particular, it is always zero for ω=0.

Concerning the spin states, there are four possibilities for (σ_1,σ_2); two spin-flip and two non-spin flip cases. In a paramagnet (Δ=0) without external field and no anisotropy in spin space, all these are of course equivalent and the situation simplifies a lot. Otherwise, the spin-flip excitations correspond to the transverse, and the non-spin-flip excitations to the longitudinal part of the susceptibility. In the case of non-zero Δ, the continuum of spin-flip excitations looks *very* different from the one of non-spin-flip excitations – it has for instance, at $\vec{k}$=0 and in a certain region around it, a gap (Δ at $\vec{k}$=0).

For $\vec{k}$=0 and ω=0 (and Δ=0), i. e. in a uniform and static magnetic field, equation (2.13) reduces to the Pauli susceptibility which depends on $\rho(E_F)$: for $\vec{q}\rightarrow 0$, the sum becomes $\sum_{\vec{k}} \partial f(E_{\vec{k}})/\partial E_{\vec{k}}$, which basically counts the number of states at the Fermi level.

When there are more than one electronic bands involved like in Sr_2RuO_4 (three bands), one has to take into account processes between different bands. In (2.13), one has to replace the sum by

$$\sum_{\vec{k}} \ldots \rightarrow \sum_{\vec{k},m,n} M_{\vec{k}\sigma_1 m,\,(\vec{k}+\vec{q})\sigma_2 n} \frac{f(E_{\vec{k}+\vec{q},n}^{\sigma_2}) - f(E_{\vec{k},m}^{\sigma_1})}{E_{\vec{k}+\vec{q},n}^{\sigma_2} - E_{\vec{k},m}^{\sigma_1} - \hbar\omega + \epsilon i} \quad (2.16)$$

Here, the M's are the matrix elements for the transitions between the bands m and n. In the very simplest manner, one may approximate these as 1 for $mn \in \{\alpha,\beta\}$ or $mn = \gamma$, and zero otherwise (following Mazin et al. [13]). A better expression for the case $mn \in \{\alpha,\beta\}$, which allows quantitative analysis, is given in Reference [14].

The exchange interaction

Like in the simple case of the Pauli susceptibility, the so determined "bare" susceptibility is in reality enhanced by the exchange interaction. In the very same manner as (2.12), the true susceptibility reads

$$\chi(\vec{q},\omega) = \frac{\chi_0(\vec{q},\omega)}{1 - \frac{I}{\mu_0(g\mu_{\mathrm{B}})^2}\chi_0(\vec{q},\omega)} \tag{2.17}$$

With this, it is obvious that there can be magnetic instabilities – when the denominator becomes zero – at any $\vec{q}$, like antiferromagnetic or incommensurate antiferromagnetic ordered states (static spin density waves). This form of the susceptibility is usually called the RPA-form ("Random Phase Approximation", as in the derivation certain terms are neglected due to their phase relation). The RPA theory usually works well in predicting the ground state. Quantitative corrections then arise from the effect of spin fluctuations on the equilibrium state, which have to be considered in a self-consistent way. A theory considering these, which is quantitatively an improvement of RPA and correctly contains many properties at higher temperatures, would be the Self-Consistent Renormalization (SCR) Theory; for details see Ref. [12]. In general, one would also have to consider that the I used here might in fact have a $\vec{q}$-dependence, $I(\vec{q})$. This is, however, often neglected.

In addition to spontaneous magnetic order that may appear, the exchange enhancement (2.17) has another very important consequence. Its imaginary part is

$$\chi''(\vec{q},\omega) = \frac{\chi_0''(\vec{q},\omega)}{(1 - \tilde{I}\chi_0'(\vec{q},\omega))^2 + (\tilde{I}\chi_0''(\vec{q},\omega))^2} \tag{2.18}$$

with $\tilde{I} = \frac{I}{\mu_0(g\mu_{\mathrm{B}})^2}$. It can have a contribution outside the continuum, i. e. where $\chi_0''(\vec{q},\omega) = 0$, when the first term in the denominator is also zero,

$$1 - \tilde{I}\chi_0'(\vec{q},\omega) = 0. \tag{2.19}$$

This may be regarded as a "dynamical" Stoner criterion. It defines sharp branches of excitations, which in a ferromagnetic state start at $\vec{q}$=0, ω=0 with an initially quadratic slope until at some point they merge into the continuum [1, 12]. These *collective modes* are the magnons, behaving very much like the magnons in for instance a Heisenberg ferromagnet.

In the framework of this theory, the equations (2.13) and (2.17) contain all magnetic properties from the static ones up to the various excitations and thus entirely determine the response in a magnetic neutron scattering experiment.

2.2.2 Calculating the susceptibility

The non-trivial part in the calculation of $\chi(\vec{q}, \omega)$ for a known band structure (i. e. known $E_{\vec{k}}$) is the evaluation of the Lindhard function[3].

Except for very simple cases, it cannot be evaluated analytically, but the sum has to be computed by a numeric integration over the Brillouin zone using a discrete mesh of $\vec{k}$-points. In general, one sees from (2.18) that even for the knowledge of the imaginary part of the interacting susceptibility, one needs to know *both the real and the imaginary part of* χ_0. However, (2.13) cannot be computed straightforwardly for its real and imaginary part. For the imaginary part, the limit $\epsilon \rightarrow 0$ is inconvenient. For the real part, there is a problem with the denominator: it can become zero or extremely small while the nominator stays finite – different signs on both sides of such singularities prevent the sum from diverging, but are hard to handle in a numeric computation. It is thus not sufficient to simply sum up (2.13) for a set of $\vec{k}$-points.

The more convenient fact, on the other hand, is that one may reduce the problem to two dimensions in the case of the Ruthenates; this does not only make the illustration simpler, but also reduces the complexity of the computation drastically. The way of calculation chosen here is thus the following.[4]

After all, the computation of the imaginary part of the Lindhard function appears more easy, because one can make use of (2.15). In the sum, contributions come only from those $\vec{k}$, where both the delta function is not zero (energy conservation) and, secondly, the differences of the Fermi functions is finite. These two conditions are illustrated in Figure 2.1 for a certain $\vec{q}$ and ω in the simple case of an isotropic band in two dimensions at T=0 and with Δ=0. Let the blue circle be the occupied states in reciprocal space ($f(E_{\vec{k}}) = 1$). The energy of the final state must be $E_{\vec{k}} + \hbar\omega$, and if the initial state is on the Fermi surface, the final state will be on the surface with $E = \varepsilon_F + \hbar\omega$ (an "enlarged Fermi surface"). The possible initial states can thus simply be identified as the points where this higher energy surface, shifted by $-\vec{q}$, intersects the original Fermi surface, which would here be only two points. It is of course also possible to excite electrons from below the Fermi surface – the possible initial states lie on the red dashed line defined by $f(E_{\vec{k}+\vec{q}}) = f(E_{\vec{k}}) + \hbar\omega$ (in the general case not necessarily a straight line). The

Figure 2.1: Illustration how to evaluate the sum for $\chi''(\vec{q}, \omega)$ in (2.15). (Explanation in the text.)

---

[3]If they were not known, to obtain realistic $E_{\vec{k}}$ would of course also be a highly (even more) non-trivial problem...

[4]Calculating the generalized susceptibility is of course a frequently encountered problem in solid state physics. However, no suitable ready-to-use software seems to be freely available. Therefore, an own algorithm has been implemented in Matlab and (its time-critical parts) in C.

second condition is easy to see in the Figure: only states where $f(E_{\vec{k}}) \neq f(E_{\vec{k}+\vec{q}})$, i. e. outside the intersection area of the circles, contribute.

Typically, $\hbar\omega$ is of the order of a few meV, which is a very small energy relative to the variations of $E_{\vec{k}}$ (Fermi velocities), so only states very close to the Fermi surface contribute. These are usually *very* few states, except in the case of Fermi surface nesting: when significant parallel sections of the Fermi surface exist, the intersection of original and shifted surface does, for the right $\vec{q}$, no longer consist of only two $\vec{k}$, but a much larger set of $\vec{k}$'s. Secondly, also the thermal energies are relatively small, so the thermal smearing of the Fermi surfaces does not have a very strong effect.

The fact that these criteria are quite strict and reduce the set of contributing $\vec{k}$'s to very few, sets the demand for a fine mesh of $\vec{k}$'s when sampling the Brillouin zone. A simple algorithm for the Brillouin zone integration would then just have to identify the relevant $\vec{k}$ and compute the Fermi function differences (even this only if aiming to include the case T$\neq$0). Despite the rather simple principle, accuracy[5] and efficiency require substantial effort during the design of a good algorithm. However, the more detailed discussion would now become very technical and shall therefore be omitted here. As a final remark about the complexity of the calculation, in the general case, to compute χ'' for all $\vec{q}$, the complexity is n^4 (where n is the number of $\vec{k}$-points per dimension) in two dimensions (n^2 as initial and final states each)[6]. For large n the computation times are substantial, but yet allow the computation of full maps with a quite good level of detail (n$\sim$200 mostly sufficient, n$\sim$400 still possible). Notice this is only because the problem has been reduced to two dimensions; otherwise the solution would become *really* laborious.

With this algorithm the whole ω-spectrum of the imaginary part of χ is calculated for each $\vec{q}$ of interest. Then, the real part is obtained by the Kramers-Kronig relation, avoiding any further problems with the real part, and the calculation of the interacting susceptibility (2.17) from the Lindhard function is straightforward.

With this method, extensive calculations of $\chi(\vec{q}, \omega)$ have been performed for Sr_2RuO_4 in order to examine the effects of the different bands and I's. Some of the results are shown in the context of the discussion of Sr_2RuO_4 (Chapter 4) – including a demonstrative example of how the effect of the exchange enhancement drives the system towards an incommensurate magnetic instability.

Such examples also show that despite the considerable effort related to such calculations, it is sometimes possible to gain a qualitative understanding by much simpler considerations[7]. This is because peaks in χ are often related to nested Fermi sur-

---

[5]For instance, a less trivial problem is how to best account for the finite $\vec{k}$-point-sampling – requiring to work with "almost" energy conserving $\vec{k}$ and then to properly normalize their contribution. Here, linear approximations using the gradients of $E_{\vec{k}}$ needed to be applied.

[6]Fortunately, it takes no longer to obtain the full frequency spectrum, as every pair $\vec{k} \rightarrow (\vec{k} + \vec{q})$ contributes to only one ω.

[7]One should also be aware that the great level of detail that such calculations produce may give the
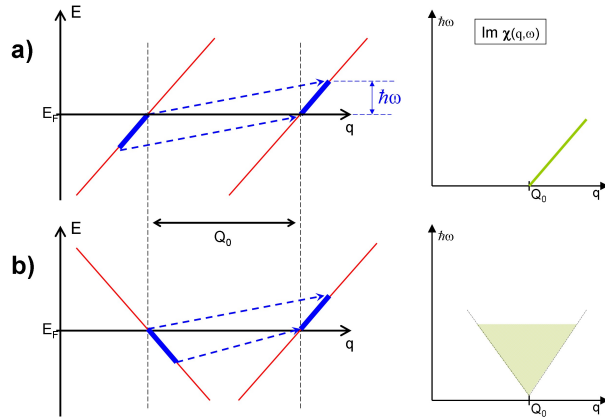
Figure 2.2: Why parallel bands are *not* favorable to create a nesting peak.

The figure shows the possible electronic excitations from one section of a band that crosses the Fermi level to another one, separated by the nesting vector Q_0, for the cases that the two sections have the same (a) or opposite (b) slope (Fermi velocity). The condition that excitations are only possible from occupied states (below E_F) into empty states defines the states that contribute to the sum in the Lindhard function (thick blue line). For a given excitation energy $\hbar\omega$, all possible excitations in (a) are at the same wave vector $Q_0 + c \cdot \hbar\omega$, if c is the slope of the band. The number of possible excitations is proportional to $\hbar\omega$. Therefore, $\chi''(\mathbf{Q},\omega)$ has the form $\chi''(\mathbf{Q},\omega) \propto \omega \cdot \delta(\frac{\hbar\omega}{c} + Q_0 - q)$ and is a line in q-ω-space, as sketched on the right side. In the other case, when the bands have opposite slope (b), the excitations with a given energy cover the q-range between $Q_0 - \frac{\hbar\omega}{c}$ and $Q_0 + \frac{\hbar\omega}{c}$, i. e. cover the region in q-ω-space as shown in the lower right, with constant weight everywhere. The imaginary part of the bare susceptibility χ_0 thus has a sharper feature in case (a), but what is the real part? It can conveniently be obtained vie Kramers-Kronig analysis as the integral of $\frac{\chi''(\omega)}{\omega}d\omega$. In case (a), this reduces to the integral over the delta function and is therefore constant for all $q > Q_0$, so there is *no* peak at the nesting vector Q_0. In case (b), as χ'' is a constant in the shaded region, the integral is taken over $\frac{1}{\omega}$. The lower limit of the integral is the lower limit of the shaded region, $c|Q_0 - q|$, so upon approaching Q_0 it gets very large and gives rise to a peak in χ'. (The logarithmic divergence is only limited by the fact that at small energies below $\hbar\omega \sim kT$ the spectral weight of χ'' is reduced by the thermal population of the initial and final states.)

These considerations, although restricted to only a one-dimensional idealized situation, make it plausible why bands should have opposite rather than parallel slope to give rise to a nesting peak in the susceptibility. One can convince oneself easily that for instance the α/β nesting in Sr_2RuO_4 fulfills this condition. As a final remark it is mentioned that if, contrary to this reasoning, parallel bands produced a magnetic instability, one would have to expect *any* metal to have a ferromagnetic instability because an arbitrary band structure is perfectly nested with itself, i. e. at $Q_0 = 0$.

faces, and the nesting vectors can often easily by identified geometrically from a plot of the Fermi surface. As a remark, it should be mentioned that (as may be a bit counter-intuitive) Fermi velocities of opposite sign are more favorable to produce a nesting peak in χ than parallel ones; this is argued within the framework of the Lindhard function in Figure 2.2. For any quantitative statement, of course, the proper computation of $\chi_0(q, \omega)$ is important, and this is the main value of such computations.

impression of a better knowledge than is actually correct, because smaller features can depend on details of the band structure parameters, which are often not known precisely enough.

Relation to the neutron scattering cross section

With the so determined components of the susceptibility, the relation to the neutron scattering cross sections (2.1), (2.2) is [15]:

$$\chi_{xx}, \chi_{yy} = \frac{1}{4}\left(\frac{\chi_0^{+-}}{1-\tilde{I}\chi_0^{+-}} + \frac{\chi_0^{-+}}{1-\tilde{I}\chi_0^{-+}}\right) \tag{2.20}$$

$$\chi_{zz} = \frac{1}{4}\frac{\chi_0^{++}+\chi_0^{--}+2\tilde{I}\chi_0^{++}\chi_0^{--}}{1-\tilde{I}^2\chi_0^{++}\chi_0^{--}} \tag{2.21}$$

2.2.3 Approximations of $\chi''(\mathbf{Q},\omega)$ near magnetic instabilities

Nearly ferromagnetic metal.

As discussed in the preceding section, the detailed form of the susceptibility at arbitrary q and ω is in the RPA theory given by the details of the band structure (via the Lindhard function). To compute it requires some effort and a careful regard of the special situation. Even more serious is the fundamental problem that often there is no detailed knowledge available about the band structure (the $E_{\vec{k}}$'s), so the absolutely necessary information is missing.

It is possible, though, to analytically treat the problem in an approximative, but very general way for simple models like for instance that of a general single (isotropic, but not necessarily parabolic) band. In such a case, only few parameters are necessary and by the appropriate mathematical treatment and expansions to the lowest relevant orders, general equations can be obtained for the behavior close to the magnetic instability. This is very useful, because for a certain region in q-ω-space these universal approximations allow a description of $\chi''(\mathbf{Q},\omega)$ without knowledge about the details of the band structure etc.

The general expression (see for instance [12, 16]) is

$$\chi^{-1}(q,\omega) = \chi^{-1}(q) \cdot \left(1 - i\frac{\omega}{\Gamma(q)}\right) \tag{2.22}$$

The imaginary part of this is

$$\chi''(q,\omega) = \frac{\omega\Gamma_q\chi_q}{\omega^2 + \Gamma_q^2} \tag{2.23}$$

with the q-dependent characteristic frequency and susceptibility

$$\Gamma_q = \gamma q \chi_q^{-1} \tag{2.24}$$

and

$$\chi_q^{-1} = \chi^{-1} + cq^2 \tag{2.25}$$

Here, χ is the macroscopic susceptibility, i. e. $\chi'(q=0, \omega=0)$. γ and c are parameters that can be derived from the band structure. c determines the q-width of χ_q, as is

obvious when taking the reciprocal of (2.25). For γ, Lonzarich et al. [16] give the expression $\frac{2}{\pi}\chi_p v_F$ which has been derived for an isotropic single band model. With (2.24) and (2.25), one can rewrite (2.23) as

$$\chi''(q,\omega) = \chi \cdot \frac{\frac{\omega}{\varepsilon} \cdot \xi q}{(\frac{\omega}{\varepsilon})^2 + (\xi q)^2 \left(1 + (\xi q)^2\right)^2} \quad \left(= \frac{\chi}{1 + (\xi q)^2} \cdot \frac{\omega \Gamma_q}{\omega^2 + \Gamma_q^2} \right) \tag{2.26}$$

where the new parameters ε and ξ have been used:

$$\xi = \sqrt{c\chi} \;,\quad \varepsilon = \frac{\gamma}{\chi \xi} = \frac{\gamma}{\chi^{\frac{3}{2}} c^{\frac{1}{2}}} \tag{2.27}$$

In this form, the parameters have an intuitively clear meaning: ξ is a correlation length which determines the width of the spectrum in momentum space, and ε determines the energy scale. This form is also very convenient for fitting purposes, although from the physical point of view it has to be kept in mind that these parameters do not vary independently when approaching the magnetic instability ($\chi \to \infty$) from the paramagnetic state (ε and ξ depend on χ, see (2.27)).

When there is no full symmetry in spin space, for instance due to anisotropies in the system, which are in practice often present, or due to a magnetic field, these equations can still be used, but one has to regard the superposition of fluctuations with different polarizations. These may have different amplitude and different characteristic frequencies, and eventually only one component diverges when approaching a transition.

Nearly antiferromagnetic metal.

In the case of a nearly antiferromagnetic metal, i. e. close to a magnetic instability characterized by *any* wave vector $q_0 \neq 0$, the argumentation is analogous, except a small but important difference. In equation 2.24, the q on the right-hand side is replaced by a factor 1, so Γ_q can now be written in the form

$$\Gamma_q = \Gamma_0 \left(1 + \xi^2 (q - q_0)^2\right) \tag{2.28}$$

This means that in contrast to the nearly ferromagnetic case, where (2.24) and (2.25) yield $\Gamma_q = \Gamma_0 \cdot \xi q \cdot (1 + \xi^2 q^2)$ which approaches zero near $q = 0$, the characteristic frequency stays now finite at q_0. Nevertheless, Γ_0 as function of temperature does of course approach zero when the system approaches the magnetic instability.

The approximation corresponding to (2.26) for the imaginary susceptibility near the antiferromagnetic instability is

$$\chi''(q,\omega) = \chi \cdot \frac{\frac{\omega}{\varepsilon}}{(\frac{\omega}{\varepsilon})^2 + \left(1 + \xi^2 (q - q_0)^2\right)^2} \tag{2.29}$$
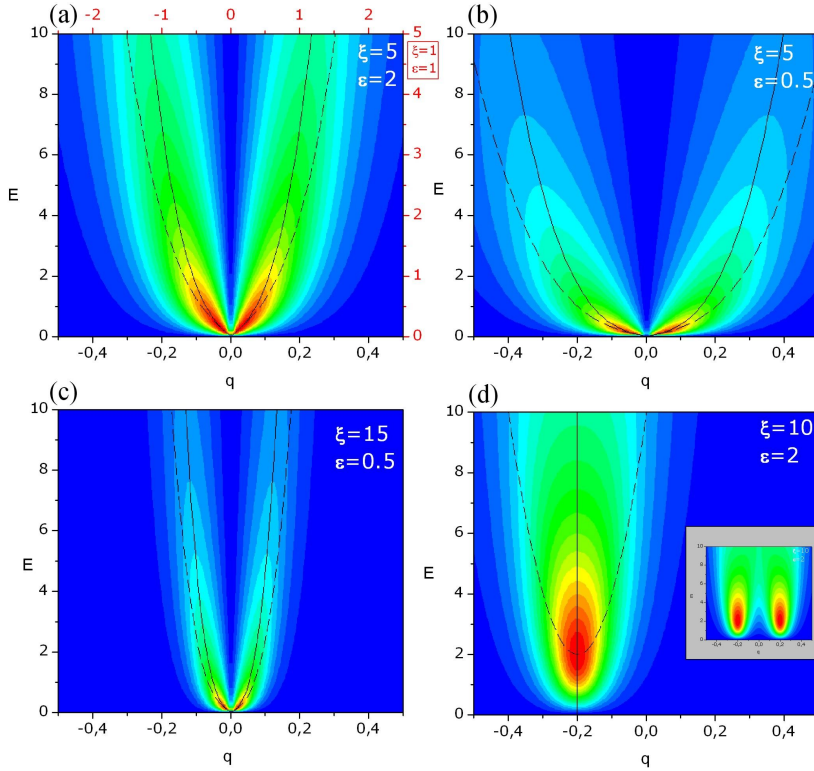
Figure 2.3: Graphical representation of the expressions (2.26) and (2.29) for the magnetic fluctuations in nearly ferromagnetic and antiferromagnetic metals. The first three pictures correspond to the ferromagnetic paramagnon with different parameters for the correlation lengths and characteristic energies. All units are arbitrary, but loosely inspired by meV and rel. lattice units and the $Ca_{2-x}Sr_xRuO_4$ scenario discussed later. Anyway, a change of the parameters means nothing than a change of the Q or E-scale, so apart that, the pictures are identical – the "generic" paramagnon for $\varepsilon, \xi = 1$ corresponds to the red scale in the first figure. The lower right panel corresponds to the incommensurate antiferromagnetic case with $q_0 = 0.2$; the inset is the sum of two such contributions on the positive and negative side. The solid lines show the points where the maxima in fictitious Q-scans would be expected, the dashed lines indicate the maxima of energy scans.

where $\varepsilon = \Gamma_0$ has been used in order to use the same symbols as in (2.26) in the ferromagnetic case.

Figure 2.3 shows the characteristic shape of the spectra calculated using the expressions (2.26) and (2.29). In the case of the ferromagnetic paramagnon the overall appearance is similar to that of a dispersive mode like a true magnon. In contrast to the latter, this is a continuum of excitations, but still relatively sharply peaked in certain

regions. Due to the continuous spread of intensity, a "dispersion" is hard to define because the maxima in cuts along lines at constant energy or constant q, respectively, lie on different lines[8], see the solid and dashed lines in Figure 2.3. In an experiment, in which typically either constant-Q or constant energy scans are performed, this has to be kept in mind in addition to the usual resolution effects.

In the antiferromagnetic case, $\chi''(q)$ for constant ω obviously always has its maximum at q_0, so in constant energy scans no shift of the signal, i. e. no dispersive behavior is expected. Only the width of the peak increases, and for the HWHM one gets

$$\frac{1}{\xi}\sqrt{-1 + \sqrt{2 + \frac{\omega^2}{\varepsilon^2}}} \tag{2.30}$$

i. e. at the characteristic energy $\omega = \varepsilon$ one has $HWHM \simeq \frac{0.86}{\xi}$. A constant energy scan can be well approximated by a Gaussian of the appropriate width:

$$\chi''(q,\omega)|_{\omega=\omega_0} \simeq \chi \cdot \frac{\frac{\omega_0}{\varepsilon}}{(\frac{\omega_0}{\varepsilon})^2 + 1} \cdot \exp\left(\frac{-\xi^2(q-q_0)^2}{\sqrt{2 + \frac{\omega_0^2}{\varepsilon^2}} - 1} \ln(2)\right) \tag{2.31}$$

This is the usual practice in the analysis of experimental data.

It is also clear from the equations 2.26 and 2.29 that for a given q (except $q = 0$ in the case of the ferromagnetic paramagnon), the energy dependence can always be written in the form

$$\chi''(\omega) = \chi'(0)\frac{\omega\Gamma}{\omega^2 + \Gamma^2} \tag{2.32}$$

Note that the prefactor of the fraction is always the real part of χ at $\omega = 0$, which follows from the Kramers-Kronig relation. This spectral form is commonly called a *"single relaxor"*.

Determination of Γ and $\chi'(0)$ from the experiment Based upon the single relaxor spectral representation $\chi''(\omega) = \chi'(0) \cdot \frac{\omega\Gamma}{\omega^2+\Gamma^2}$ for fixed q, the parameters Γ and $\chi'(0)$ can in principle be extracted from the values c_1, c_2 at two different energies ω_1 and ω_2:

$$\Gamma = \sqrt{\omega_1\omega_2\frac{c_1\omega_1 - c_2\omega_2}{c_2\omega_1 - c_1\omega_2}} \tag{2.33}$$

$$\chi'(0) = \frac{\omega_i^2 + \Gamma^2}{\omega_i\Gamma}c_i \tag{2.34}$$

---

[8]The maxima of the constant-energy scans fall on the curve

$$\hbar\omega(q) = \varepsilon \cdot \xi q \cdot \sqrt{1 + 6(\xi q)^2 + 5(\xi q)^4}$$

Though simple and convenient, this relation requires a reasonable choice of the two energies (not too close together) and not too large errors to give stable results. When more data is available, e.g. an energy scan, a conventional fit will of course produce more reliable values. (2.33) and (2.34) can nevertheless be very useful in some cases, for instance for the efficient determination of temperature dependencies of these parameters.

2.2.4 Contribution of spin fluctuations to the specific heat

The spin fluctuations can, like other excitations of the solid, contain a certain amount of energy, so they are expected to contribute to the specific heat. To lowest order, their contribution is linear in T, so they manifest themselves in the electronic specific heat coefficient $\gamma = C/T$. In a "normal" paramagnet far from magnetic instabilities, i. e. without strongly enhanced fluctuations, though, their effect is usually negligible. When magnetic fluctuations become important, for instance close to the Curie temperature in a ferromagnet, their effect on the specific heat can also become very large.

Intuitively it is clear that the spin fluctuation contribution to the specific heat will be the greater, the lower their energy (their characteristic frequency) and the larger their number is (the number of modes with different q, i. e. the coverage of the Brillouin zone). The quantitative treatment is non-trivial, but is now theoretically well studied: a number of publications, especially by Lonzarich, Moriya and their coworkers, has addressed this problem [17–25]. The specific heat arising from the spin fluctuations is calculated as

$$C_{sf} = -T\frac{\partial^2 F_{sf}}{\partial T^2} \tag{2.35}$$

where F_{sf} is the spin fluctuation free energy,

$$F_{sf} = \sum_{\nu,q} \int_0^\infty \mathrm{d}\omega\, f(\omega)\frac{1}{\pi}\frac{\Gamma_\nu(q)}{\omega^2 + \Gamma_\nu(q)^2} \tag{2.36}$$

Here, ν is the polarization of the spin fluctuation (two perpendicular and one parallel to M)[9] and $f(\omega)$ is the free energy of an oscillator of frequency ω:

$$f(\omega) = \frac{\hbar\omega}{2} + k_B T \ln(1 - \mathrm{e}^{-\frac{\hbar\omega}{k_B T}}) \tag{2.37}$$

The actual derivation is then laborious, but as it has been pointed out in Refs. [18, 19] in the low temperature limit a remarkably simple expression holds:

$$\gamma_{sf} = \frac{1}{N}\frac{C_{sf}}{T} = \frac{1}{N}\frac{\pi k_B^2}{\hbar}\sum_q \frac{1}{\Gamma(q)} \tag{2.38}$$

---

[9]In the following, isotropic fluctuations are assumed, and the sum over ν is replaced by a factor 3.

In other words, the contribution of the spin fluctuations to the electronic specific heat coefficient is given by the inverse spin fluctuation frequencies in the Brillouin zone; taking the *average* of $1/\Gamma$ rather than the sum gives the contribution per magnetic atom. This important result corresponds to the intuitively obvious fact that the low energy excitations have a larger contribution to the specific heat, because they can more easily be occupied with nonzero quantum numbers at low temperature.

The prefactor πk_B^2 in convenient units is $2.25 \frac{J \cdot meV}{mol \cdot K^2}$, so one can easily estimate the order of magnitude of the specific heat carried by spin fluctuations. If for instance a fluctuation with $\hbar\Gamma$ in the order of 1 meV covers effectively 10% of the Brillouin zone, γ_{sf} would be $225 \frac{mJ}{mol\,K^2}$ – a relatively large value.

The distinct spectra of $\chi''(\mathbf{Q}, \omega)$ for the nearly ferro- and antiferromagnetic cases have important consequences for the spin fluctuation contribution to the specific heat – it is more drastically enhanced in the ferromagnetic case where $\Gamma(q)$ vanishes close to $q = 0$ (2.24). This can cause fundamentally different behavior: while the theory predicts a $T^3 \ln T$ divergence of the specific heat in a ferromagnet, there should be no significant enhancement in the antiferromagnetic case [25]. This applies to 3-dimensional magnets – that the behavior can generally depend on the dimensionality of the system is also intuitively clear from (2.38) because possible divergences tend to be more easily averaged to a finite value in higher dimensions (recall for instance that $\int \frac{1}{r}$ is infinite in two, but finite in three dimensions).

Despite the simplicity of (2.38) its application in practice can present difficulties: to perform a calculation of γ_{sf}, one needs the full q-dependence of Γ. In a typical neutron scattering experiment, this cannot be achieved by direct measurement (requiring energy scans at a large number of, possibly three-dimensional, q). More or less crude approximations have thus to be used.

One obvious approach would be to apply the parameterizations of $\chi''(\mathbf{Q}, \omega)$ as they have been discussed in Section 2.2.3: then one needs only a small number of experimentally accessible parameters like energy and momentum widths. Replacing the sum by an integration, one may even attempt an analytical evaluation of the sum in (2.38). Using the integral $\frac{1}{\pi Q_c^2} \int_0^{Q_c} \mathrm{d}^2 q \frac{1}{\Gamma_q}$ to perform the average in two dimensions and the expressions for Γ_q in the antiferromagnetic and ferromagnetic cases, this gives

$$\gamma_{sf} = \frac{\pi k_B^2}{\hbar} \cdot \frac{1}{\Gamma_0} \cdot \begin{cases} \frac{\ln(1+\xi^2 Q_c^2)}{\xi^2 Q_c^2} & \text{(AFM)} \\ \frac{2\arctan(\xi Q_c)}{\xi^2 Q_c^2} & \text{(FM)} \end{cases} \tag{2.39}$$

Q_c determines the radius around the magnetic instability in q-space up to which the integration is performed and should be chosen in a way that the Brillouin zone is approximately covered. As a second possibility in the antiferromagnetic case, one might also approximate the average by taking $\Gamma_q = \Gamma_0$ in a radius of the half width of the peak measured at the energy transfer $\hbar\Gamma_0$ and taking $\Gamma_q = 0$ outside this region. With the width according to (2.30), the average over the region $(q - q_0) < Q_c$ (as

above) is then $\frac{0.74}{\xi^2 Q_c^2}$ which corresponds to the expression (2.39) for $\xi Q_c \approx 1$, i. e. for rather short correlation lengths in the range of the atomic distances. For sharper peaks the neglect of fluctuations at q's outside the half width produces smaller results than (2.39).

This consideration gives an impression of the accuracy of such procedures and that the results of such calculations are to be taken rather as an estimate. Even (2.39), though obtained analytically, is certainly not exact because it uses a small-q expansion around the magnetic instability throughout large parts of the Brillouin zone where it may be rather poor or where there may be overlap of contributions from different q_0. Generally, the whole treatment is based on the rather idealized model of a metal with only a single band; the situation in real materials like the Ruthenates can be assumed to be more complicated. As already mentioned, also the input parameters may be difficult to provide, because one may in an experiment observe the superposition of longitudinal and transverse components, or, as it is the case in $Ca_{2-x}Sr_xRuO_4$, a superposition of contributions from different magnetic instabilities. Despite these limitations, the basic arguments do still hold and the procedure may be expected to produce a reasonable estimate of the specific heat value and to provide valuable qualitative understanding on the spin fluctuation contribution to it.

2.3 Spin densities and polarized neutron diffraction

2.3.1 The measurement of flipping ratios

In contrast to the neutron spectroscopy techniques which have been described so far, the diffraction techniques focus on the elastic neutron scattering. One may of course use a triple-axis spectrometer for a diffraction experiment by setting the analyzer to zero energy transfer. Although in some cases this procedure is advantageous, for instance in order to reduce background, a standard diffractometer works without an analysis of the energy (and spin) of the scattered neutron. The elastic scattering contains the information on the time-independent correlations in the sample and is usually used for crystal structure determination. While information on the nuclear structure can be obtained by many techniques like x-ray or neutron diffraction, each either on single-crystalline or powder samples, magnetic neutron diffraction can not only determine the overall magnetic structure but also the distribution of the magnetic moment within one unit cell. This is accomplished with a polarized neutron diffractometer, such as 5C1 at the LLB or D3 at the ILL. These diffractometers work with a polarized neutron beam of a short wavelength from the reactor's hot source, and the polarization can be reversed by a spin flipper mounted on the incident beam. After diffraction from the crystal, the intensity is measured without further analysis of spin or energy. The direction of the neutron polarization is the vertical axis, i. e. parallel to the magnetic field. This is usually also the direction of the magnetic moments in the

sample – if they are fully aligned by the strong magnetic field. In such a case there is only non-spin-flip scattering, cf. (2.3), but when there is at the same time a nuclear and magnetic contribution, the cross section is different for the two polarizations (spin up/down) . This is because

$$I^+ \propto (F_N + F_M)^2$$
$$I^- \propto (F_N - F_M)^2$$

(2.40)

where I^+ and I^- are the measured intensities for spin up and down, F_{M} and F_{N} are the nuclear and magnetic structure factors, and the magnetic moment is perpendicular to the scattering vector. In a measurement with an unpolarized neutron beam, the intensity would be $\frac{1}{2}(I^+ + I^-) \propto F_N^2 + F_M^2$, i. e. the interference term $2F_M F_N$ would cancel out. This makes a determination of small F_{M} very difficult, and the fact that from separately measured I^+ and I^- one can take the ratio $I^+/I^- \approx 1 + 4\frac{F_M}{F_N}$ which is linear in the (usually small) ratio $\frac{F_M}{F_N}$, is the great advantage of the polarized neutron technique. It brings the *tremendous* improvement without which a measurement of large sets of F_{M} would not be possible.

A restriction arises mainly from the use of a large cryomagnet, so that the sample can only be rotated around the vertical (field) axis and one can access only a narrow range of scattering vectors close to the horizontal plane, depending on how much the detector can be lifted or lowered out of the horizontal plane (about -5...+20 degrees on 5C1).

In the experiment the so-called flipping ratio $R = \frac{I^+}{I^-}$ is measured for an as large as possible set of Bragg reflections. In the very general case the expression for the flipping ratio is

$$R = \frac{I^+}{I^-} = \frac{F_N F_N^* + \vec{F}_{M\perp} \cdot \vec{F}_{M\perp}^* + \left((F_N F_{M\perp z}^* + F_N^* F_{M\perp z}) - i(\vec{F}_{M\perp} \times \vec{F}_{M\perp}^*)_z \right)}{F_N F_N^* + \vec{F}_{M\perp} \cdot \vec{F}_{M\perp}^* - \left((F_N F_{M\perp z}^* + F_N^* F_{M\perp z}) - i(\vec{F}_{M\perp} \times \vec{F}_{M\perp}^*)_z \right)} \quad (2.41)$$

Here, $\vec{F}_M$ is the magnetic structure factor (remember that this is in general a vector with three complex components), $\vec{F}_{M\perp}$ is its part perpendicular to the scattering vector $\mathbf{Q}$, and z denotes the vector components along the polarization axis (vertical axis).

This quite complicated formula can be simplified, when, as usual, further assumptions can be made. For instance, in most cases the magnetic field aligns the magnetic moments in the sample parallel to the field. For the refinement, this has the great advantage that the magnetization can be treated as a scalar quantity instead as a vector. Then, if α is the angle between the field and the scattering vector[10] $\mathbf{Q}$, the expression

---

[10]The geometrical factor $\sin^2 \alpha$ arises from the dependence on the orientation of neutron spin, magnetic moment and scattering vector relative to each other; it is, contrary to intuition, correct to take it always squared in the formulae (2.42) and (2.43).

for the flipping ratio is

$$R = \frac{F_N'^2 + F_N''^2 + 2\sin^2\alpha\,(F_N'F_M' + F_N''F_M'') + \sin^2\alpha\,(F_M'^2 + F_M''^2)}{F_N'^2 + F_N''^2 - 2\sin^2\alpha\,(F_N'F_M' + F_N''F_M'') + \sin^2\alpha\,(F_M'^2 + F_M''^2)} \qquad (2.42)$$

Here F' and F'' are the real and imaginary parts of the structure factors. When the structure is centrosymmetric, all the imaginary parts become zero and the expression further simplifies to

$$R = \frac{F_N^2 + 2\sin^2\alpha\,F_N F_M + \sin^2\alpha\,F_M^2}{F_N^2 - 2\sin^2\alpha\,F_N F_M + \sin^2\alpha\,F_M^2}, \qquad (2.43)$$

which, in the case of $\alpha{=}90\,°$, would reduce to (2.40).

2.3.2 Constructing the spin density from flipping ratio data

The magnetic structure factors F_{M} are the Fourier transform of the magnetization distribution $M(\mathbf{r})$. The aim is to reconstruct $M(\mathbf{r})$ from the measured R's. To do this, one obviously needs to know the nuclear crystal structure, i.e. the F_{N}'s. A good structure determination is therefore a prerequisite for any determination of $M(\mathbf{r})$. The second important point to note is that in the centrosymmetric case, the F_{M} can then directly be calculated from the flipping ratios by equation 2.43, while this is impossible in the non-centrosymmetric case. This is basically a consequence of the phase problem in the latter case.

There are different possibilities which can be used to obtain $M(\mathbf{r})$. These are:

1. **Fourier inversion**. Because the F_{M} are the Fourier coefficients of $M(\mathbf{r})$, the most natural way to obtain $M(\mathbf{r})$ is to apply the inverse Fourier transform

$$M(\mathbf{r}) = \frac{1}{V} \sum_{hkl} F_M(h, k, l)\, e^{-2\pi i(hx+ky+lz)} \qquad (2.44)$$

2. **Refinement of a model**. One may construct a model of the spin density around certain atoms and then refine certain parameters to obtain a best fit to the experimental data. This procedure corresponds approximately to the usual refinement of atomic structures where for instance the atomic positions are the refined parameters of a certain structural model. A model for the spin density can consist of a combination of magnetic wave functions (for instance d-orbitals) or, more general, of a multipolar expansion. Here, the coefficients of the spherical harmonics would be the refined parameters.

3. **Maximum entropy**. The unit cell is divided into a grid of points. The spin density at each point is refined independently with the objective to maximize the total entropy of the distribution (explanation below) under the constraint of consistency with the measured data. The resulting distribution is the most probable one.

Each of these methods has its advantages and disadvantages. The Fourier method is very simple and works without any prior assumptions about the distribution, i.e. is "model-free". The most serious drawback is that the lack of completeness in the data set introduces systematical errors in the result. This means that in principle *all* (h,k,l) are necessary for the reconstructions, but all those which have not been measured are artificially assumed as zero – an assumption that can introduce very problematic artifacts in the calculated map. Another problem is that the information from the error bars is entirely ignored; as errors are often significant, this may be very important information. All observations are weighted equally, and large values, though with high uncertainty, may cause erroneous results.

A further general advantage of the two other models is that they can be applied directly on the measured flipping ratios, while for the Fourier inversion one first has to obtain the F_{M}, which is not always possible. In practice, unfortunately, some of the available software nevertheless requires the F_{M} instead of the R's – a restriction without physical justification.

By minimizing the deviation from the measured data, i.e. a χ^2-like term, the model-refinement techniques can properly account for the experimental uncertainty, and meaningful parameters can directly be extracted (with their respective uncertainty). The problem is transferred to setting up a reasonable model. The assumptions normally impose strong restrictions on the magnetization distribution (its place, symmetry constraints, etc.) and make this a highly non-trivial task. Unexpected features may be accidentally overlooked because they are not considered in the model.

Finally, a maximum entropy reconstruction avoids many of these problems. As disadvantages one might at most note the relatively high computational effort (which is nowadays no problem) or the subliminal scepticism of some people against this method. It is (at least compared to the others) indeed relatively new, but since several years well established for instance in crystallography and the reconstruction of electron densities from x-ray data [26].

In spite of similarities and some identical formulae, this entropy is not to be confused with the thermodynamic entropy: it has originally been developed in the 1940's and 50's in the context of information theory by Shannon [27]. Connections to statistical physics do nevertheless exist [28], and since then this concept has become widely used in a variety of quite different fields, like image processing and reconstruction (for instance in medicine or astronomy, treating noisy pictures). First applications on polarized neutron diffraction have been reported by Papoular [29].

Maximum Entropy Method

The idea lies in Bayes' theorem or the question: Given a measurement, what can be inferred about the "real" situation? – an obviously very fundamental question for any experiment. This process of *backward* inference from a "statistical sample" (a measurement) on a model is therefore sometimes called *Bayesian inference*. The

aim is to extract as much information as possible from the measured data – but, equally important, *not more*[11]. Intuitively it is clear that the degree of information that can be obtained depends on the number of observations and their accuracy (their error bar). Concerning the inferred model (the spin density map), a map with pronounced features and large differences between different points contains more information than a flat distribution. As a quantitative measure for the information of a map with values ρ_i at each pixel i, one uses the entropy

$$S = -\sum_i p_i \log p_i \qquad (2.45)$$

A discussion about what such a *measure of information* actually means, about information at all, bias, confidence and credibility would of course be a highly interesting topic (including a potential for philosophic digressions), but is far beyond the scope of this text. Let us therefore conclude here with two general technical remarks. Firstly, it *is* possible, when desired, to include some prior information in the refinement. This can be information available from whatever source that one deliberately wants to make use of[12]. How to use this option is a non-trivial question about which different opinions exist. According to R. Papoular, the prior information must be included to really make the maximum entropy result the *most probable* one, and it is the deviation of the Maximum Entropy solution from the prior density which contains the only *new* information that the Maximum entropy method can provide. In practice, this could typically be the deviation of the spin density from a spherical distribution around the magnetic ions. If the prior information on a pixel is τ_i, (2.45) becomes

$$S = -\sum_i p_i \log \frac{p_i}{\tau_i} \qquad (2.46)$$

The second remark concerns the definition of S which obviously requires all the p_i to be strictly positive, while in a magnetization map negative values may occur. For this reason, one works with *two* strictly positive components and takes their difference to obtain $M(\mathbf{r})$.

Computation of the maximum entropy map

Spin density reconstruction from polarized neutron data is by now a standard method, but not very often applied – in Europe, the ILL and the LLB are running one such diffractometer each. Perhaps this is a reason why at present there is no widely spread

---

[11]For instance, series truncation in a Fourier reconstruction can give pronounced features in a map – this would be much "information", but an entirely wrong information for which in fact no justification is in the data. As another example, when setting up a certain model, one unavoidably introduces artificial information by making assumptions on the appropriate type of model.

[12]This is also sometimes used when the stability of a solution is to be tested.

software available for maximum entropy treatment of the data. The existing programs are mostly specialized on very particular cases and/or require substantial effort to be adopted to the problems that are discussed here. In addition, these programs usually refine on the magnetic structure factors instead on the Flipping ratios – an annoying restriction for which there seems to be no objective reason, except that they have been adopted from the case of x-ray diffraction and electron densities – and are therefore not suited for non-centrosymmetric structures. Therefore, an own refinement algorithm has been implemented in Matlab. It uses an iterative procedure following the concepts of references [30, 31] and has been extended to perform the refinement directly on the measured flipping ratios, thus allowing the refinement of non-centrosymmetric structures.

The aim of the computation is to maximize the entropy (2.45) under the constraint that $\chi^2 = 1$; this expresses the requirement that the solution is consistent with the data, and takes naturally into account the experimental errors. χ^2 is expressed as

$$C = \frac{1}{N} \sum \frac{(R_{\text{cal}} - R_{\text{obs}})^2}{\sigma^2}, \qquad (2.47)$$

where the sum runs over all the N observed reflections hkl. The R_{obs} are the observed flipping ratios and the R_{cal} are calculated at each iteration from the refined spin density ρ_i. The ρ_i are the pixels of the map on a three dimensional mesh which represents the asymmetric part of the crystallographic unit cell.

Finding the constrained maximum of the entropy is achieved with the use of a Lagrange multiplier λ by finding the extremum of $Q = S - \lambda\chi^2$; the condition is thus $\partial Q/\partial \rho_i = 0$. The algorithm works with an iterative approximation [32, 33]

$$\rho_i^{(n+1)} = \rho_i^{(n)} \cdot \exp\left(-\lambda \frac{\partial C(\rho^{(n)})}{\partial \rho_i}\right), \qquad (2.48)$$

starting with a uniform map[13][14].

Some general remarks about the algorithm include:

- It assumes fully aligned magnetic moments, so considers only a single (the vertical) component of $\vec{M}$. Flipping ratios are calculated using (2.42).

---

[13]For λ, one simply starts with a guess. It can then be automatically reduced in the case of divergence (C gets larger instead smaller) or increased in the case of too slow convergence.

[14]There are by now much more sophisticated algorithms (see for instance Refs. [26, 34]) with better properties concerning efficiency, stability and convergence, which are being sold for a variety of commercial applications [35]. Nevertheless, the "older" algorithm implemented here has been used successfully since the beginning of the applications of the Maximum entropy principle, is today the basis of the programs MEED/MEND [32, 33], and proved also successful in the present cases.

- For the repeated evaluation of the Fourier transforms, tables of sin- and cos-values are maintained which include the full information on the space group symmetry. The performance is thus drastically enhanced, however on the cost of excessive memory usage, which may then become the limiting factor in practice.

- Under the assumption of fully aligned magnetic moments in the paramagnetic state, the amplitude of the magnetization is taken to have the same symmetry as the crystallographic space group. High symmetry, or in other words, a small asymmetric unit, facilitates the computation significantly.

- The algorithm can take account of imperfect polarization of the incident beam, separately for both spin directions. A factor p^+ respectively p^- then has to be added to the interference terms in (2.42) in the nominator and denominator. If the flipper of the spectrometer works perfectly, p^+ and p^- are equal and depend on the monochromator or other polarizing device, but for imperfect flipping, significant differences have been observed.

- Twinning can, in a simplistic way, be taken into account by assuming that the intensities for either spin direction are given as the sum of the individual intensities (eventually weighted by a twin fraction) for this spin direction of the reflections which contribute to the measurement. This can easily be accounted for by summing the calculated intensities in the calculation of the flipping ratio and in (2.47) but may also be problematic depending on the situation.[15]

- By storing $\sin^2 \alpha$, as obtained directly from the spectrometer angles, for each reflection instead of using an orientation matrix, different sample orientations can be taken into account without further effort. (One has of course to assume that the distribution $M(r)$ does not depend on the field direction.) The algorithm can also handle multiple groups of data points in a single refinement, which may differ in their p^+/p^- if they were taken under different experimental conditions.

In addition to the important fact that it can handle non-centrosymmetric structures, these last three points are to be considered as convenient details of the algorithm; some of them were useful in the present cases. Some further information and in particular some technical details are given in the appendix.

---

[15]Theoretically the simple summation requires that the reflections are *exactly* at the same spectrometer angles, at least with respect to the resolution. Normally, in the measurement of flipping ratios, it is no problem (except lower statistics) when the reflections are not exactly centred, as the reduction factor of the intensities cancels out in the division. This is no longer the case when summing several intensities, which can then have different weight that leads to erroneous results. For instance, one would have to consider that reflections of orthorhombic twins may either be at the same position, far away from each other or partially overlapping.

3 $Ca_{2-x}Sr_xRuO_4$ and the metamagnetic transition

3.1 Magnetism in $Ca_{2-x}Sr_xRuO_4$

3.1.1 Magnetic properties in the metallic state

Among the single-layer Ruthenates, Sr_2RuO_4 is clearly the one which has attracted the most interest since the year 1994, when the superconductivity was discovered [38]. Although the investigation of related materials, which arise from Sr_2RuO_4 by doping, was initially mainly motivated by the superconductivity, it was soon realized that these materials are of interest on their own right and for very different reasons. As a first evidence of this versatile physical behavior, one may take Ca_2RuO_4 which has, despite its close relationship to Sr_2RuO_4, many properties that one might describe as opposite to Sr_2RuO_4 – it is a Mott-insulator up to 357 K and has antiferromagnetic order below 110 K (for the synthesis and some basic properties of Ca_2RuO_4 see Refs. [39] and [40–42]). The Ca and Sr ions both have the charge 2+, so the substitution is isovalent, and the relevant difference is only the smaller radius of the Calcium ion.
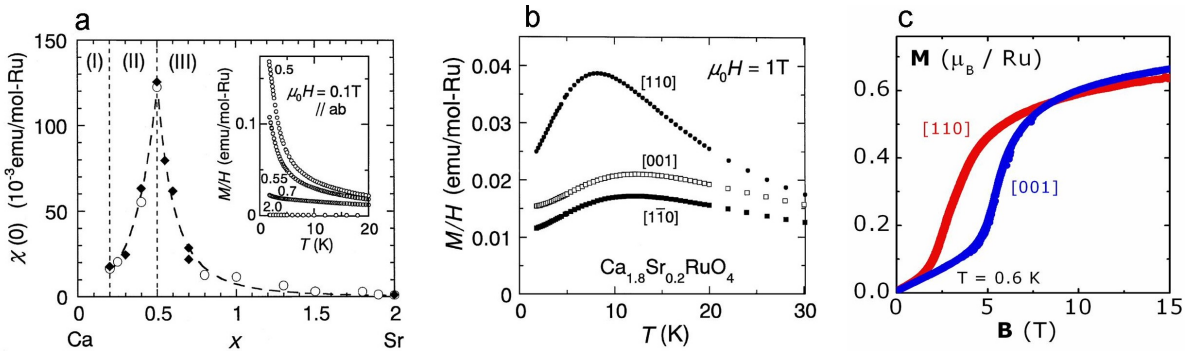

Figure 3.1: Magnetic properties of $Ca_{2-x}Sr_xRuO_4$. (a): Susceptibility at T=2 K as function of the Sr-concentration (inset: temperature dependence). (b): Susceptibility of $Ca_{1.8}Sr_{0.2}RuO_4$ as function of temperature in different directions (in tetragonal notation; in the orthorhombic cell with a≈5.33 Å and b≈5.30 Å one has $\chi_a > \chi_b$). (c) Magnetization as function of magnetic field for $Ca_{1.8}Sr_{0.2}RuO_4$ and the metamagnetic transition. All data by S. Nakatsuji et al. [36, 37].

The change of physical properties must therefore be closely related to the structural changes that are induced by the Ca substitution, and Ca$_2$RuO$_4$ is indeed strongly structurally distorted with rotated, tilted and compressed RuO$_6$ octahedra.
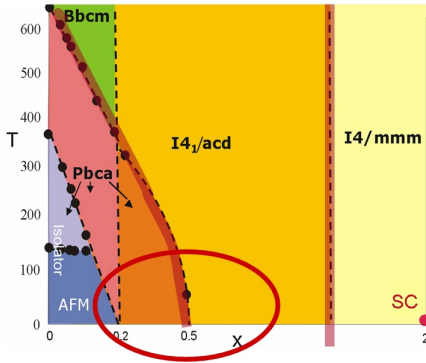

Figure 3.2: Structural phase diagram of Ca$_{2-x}$Sr$_x$RuO$_4$ (explanation see text). The red circle marks the region which is of particular interest in this chapter. The metamagnetic transition is observed between x=0.2 and x=0.5 at low temperature.

The phase diagram of Ca$_{2-x}$Sr$_x$RuO$_4$ can to a large extent be understood in terms of the structural distortions [43]: the RuO$_6$ octahedra as the basic structural unit can be rotated around the c-axis and tilted around an axis in the ab-plane, and the octahedron itself can be distorted by changing some of the bond lengths, predominantly as a compression or elongation along the c-axis. In general, the structural distortions are the stronger, the lower the Sr-content x and the lower the temperature (see the phase diagram in Ref. [43] and Figure 3.2). Sr$_2$RuO$_4$ (x=2) has the K$_2$NiF$_4$-structure without such rotation or tilt. Beyond a discontinuous structural phase boundary at about x=1.5, a rotation of the octahedra is observed. The structure is still tetragonal, but the unit cell doubled within the plane as well as along c (due to a different rotation direction of next-nearest layers), and the space group is I4$_1$/acd. This structure, with increasing rotation angle towards smaller x, covers the whole range of the phase diagram until x=0.2 (at high temperature) respectively x=0.5 (at low temperature). Between x=0.2 and 0.5 at low temperature, the structure has an additional tilt distortion, yielding an orthorhombic unit cell of relatively low symmetry (with two Ca/Sr and four crystallographic O-sites) in space group Pbca (referred to as D-Pbca to distinguish from the other Pbca phases at lower x). The region between x=0.2 and slightly above x=0.5 is the one that is of particular interest in the following, as indicated in Figure 3.2. This region is bounded towards lower x by a first order structural phase transition (the vertical line at x=0.2 in the phase diagram) which separates regions with different rotation distortion from each other – next-nearest layers are rotated in the same sense at x<0.2. This may appear at first sight as rather a detail of the structure, but it is beyond this phase boundary where a metal-insulator transition appears which is coupled to another first-order structural transition. At low temperature, the phase at x≥0.2 is thus very close to the insulating phase, but still well separated from it by this phase boundary. The region x<0.2 of the phase diagram would be very interesting on its own, but shall not be considered in detail here.

The region of interest at x≥0.2 is metallic and paramagnetic, i. e. has no static magnetic order at any temperature, but is yet extremely interesting due to its magnetic properties. A short summary of the most important magnetic properties [36,44] is reproduced in Figure 3.1. Although paramagnetic, the susceptibility at low temperature is extremely dependent on the Sr-content x. When coming from the side of high x, the susceptibility increases dramatically towards x=0.5. Here, the mate-

rial is obviously close to a ferromagnetic instability; from a Curie-Weiss fit, the Weiss temperature is near zero, and a cluster glass, i. e. a freezing of short range ferromagnetically ordered clusters, has been observed near x=0.5 below 1 K [37].

The structural changes as function of the Sr-content are obviously directly related to the magnetic properties. The increase of the susceptibility towards x=0.5 coincides with the growing rotation angle of the RuO_6 octahedra, an effect that can be easily qualitatively understood when considering that the rotation reduces the bandwidth (mainly of the in-plane states) and thereby increases the density of states at the Fermi level [45]. The critical concentration x=0.5, below which the susceptibility is suppressed, coincides with the second order structural transition to the tilted phase. In the tilted phase, the correlations are predominantly antiferromagnetic, while at high temperature above the tilt transition, the system seems to continue its evolution from higher x and to be ferromagnetically correlated, as shown for instance by the Curie-Weiss parameters [44]. It is also remarkable that the effective magnetic moment thus extracted corresponds quite exactly to S=1/2, while in an atomic picture one would expect S=1. In this region of the phase diagram, the electronic specific heat coefficient $\gamma_e = \frac{C_p}{T}$ is extremely large (see Figure 3.3) – at values otherwise observed only in a few heavy fermion compounds. This fact, the unusual susceptibility behavior and deviations of the resistivity from a T^2 law [44] are some indications for the presence of sizeable magnetic fluctuations, the existence of which has already been proved by neutron scattering [46] and nuclear magnetic resonance (NMR) [47].

In the region $0.2 \leq x \leq 0.5$, the susceptibility is anisotropic in the plane, reflecting the lower symmetry of the orthorhombic lattice. It is very remarkable that the significant suppression of the susceptibility is observed only at quite low temperature: the temperature dependence of the susceptibility shows a peak at about 10 K (exact value dependent on the field direction), which does not correspond to magnetic order. When extrapolating the curve from higher temperature, one would arrive at values of the same order like at x>0.5. This unusual suppression of the susceptibility can be "reversed": at a magnetic field of about 2.5 T (in the plane), a metamagnetic transition is observed, seen as a nonlinear increase in magnetization as function of field. Above the transition, the moment is still smaller, but approaching 1 μ_B. This metamagnetic transition, especially the detailed study of magnetic correlations below, at and above the transition, is the main subject of this chapter.

The metamagnetic transition cannot be regarded as an isolated phenomenon but is of course intimately related to the magnetic properties at different fields, temperatures and Sr-concentrations. For instance the susceptibility maximum near 10 K seems to be a rather general feature (also observed in $Sr_3Ru_2O_7$ [49]) closely related to the metamagnetic transition – this is clear intuitively when regarding the phase diagram in Figure 3.4a (discussed below in more detail) by arguing that the system still experiences part of the crossover, though at some distance from the actual transition when going along the T-axis, and is also proved theoretically in theories of the meta-
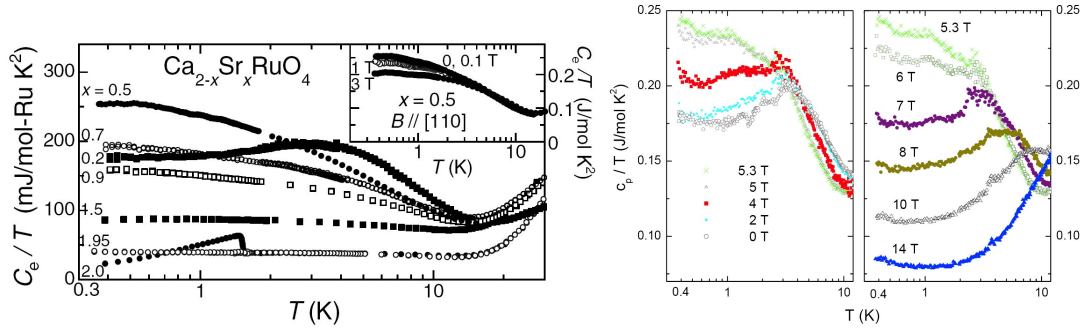
Figure 3.3: Specific heat c_p/T on a logarithmic temperature scale. Left: Specific heat of $Ca_{2-x}Sr_xRuO_4$ for a wide range of Sr-concentrations (by S. Nakatsuji et al. [37]). Right: specific heat of $Ca_{1.8}Sr_{0.2}RuO_4$ at different magnetic fields (measurement and figure by Th. Zabel [48].)

magnetic transition [50, 51]. In some sense, and the observations to be discussed in this chapter support this statement, the metamagnetic transition is just a striking manifestation of the interplay of different types of magnetic correlation in the system.

What exactly microscopically happens at the transition, is by now not entirely known. The magnetic properties in general, and the metamagnetic transition in particular, must be closely related to the electronic configuration, the band structure and the Fermi surface. There is indeed some evidence for a Fermi-surface reconstruction [52], though the exact kind of that change is not specified. What is quite well established on the other hand, is the structural effect that is coupled to the magnetic properties [53, 54]. This structural effect is observed both as function of temperature with and without field (thermal expansion) and as function of magnetic field (magnetostriction). Its signature are length changes along the crystallographic directions; these can be, as shown by neutron powder diffraction experiments, traced back to changes of the bond lengths between the Ru-ion and the ligand oxygen atoms, i. e. compression or elongation of the RuO_6 octahedron. These influence the energies of the different electronic states relative to each other and will therefore redistribute a certain (small) number of electrons between the different orbitals. In an electronic structure with narrow bands and high densities of state, there may then be a strong impact on the magnetic properties. Whatever is the exact mechanism of this effect, it is clear that structure and magnetism are very intimately related to each other. As an impressive example one may mention the magnetostriction and magnetization curves $\Delta c(H)$ and $M(H)$ (see for instance Ref. [53]) which bear so much similarity with each other that they are hardly distinguishable.

In addition to the structural effects, the metamagnetic transition has also been shown to be strongly related to the electronic specific heat (Figure 3.3). The highest value is reached at the critical field of the transition, and the reduction on both

sides, especially the high-field side, is very substantial. The electronic specific heat coefficient can be strongly enhanced by magnetic fluctuations. The maximum as function of field may thus straightforwardly be understood in terms of enhanced fluctuations close to the transition – the situation is however obviously more complicated at intermediate temperature, where $\gamma(T)$ has a double peak structure [55].

The metamagnetic transition has been studied in detail for $Ca_{1.8}Sr_{0.2}RuO_4$, but is of course present also at higher x, with slightly decreasing transition field [56]. It is natural to ask up to which Sr-concentration it can be observed. This question has been addressed in detail for the case of $Ca_{1.5}Sr_{0.5}RuO_4$ [54]. In $Ca_{1.5}Sr_{0.5}RuO_4$ there is no clear metamagnetic transition any more, but the thorough study of the magnetization and the structural effects show that some of the signatures of the metamagnetic transition can still be found in $Ca_{1.5}Sr_{0.5}RuO_4$, though at a magnetic field shifted essentially to zero – that means only the high-field side of the transition remains to be observed. Although this should probably not be called a metamagnetic transition any more, it is helpful to intuitively understand the properties of $Ca_{2-x}Sr_xRuO_4$ at different x, here for instance the high susceptibility at small fields similar to the one at the transition field in $Ca_{1.8}Sr_{0.2}RuO_4$, in a more consistent and unified way.

The role of the different orbitals To a large extent, the rich and complicated behavior of this material and also some problems in its understanding are related to the existence of the three t_{2g}-states that cross the Fermi level and that are partly occupied by the total of four electrons. In Sr_2RuO_4, the three states d_{xy}, d_{xz} and d_{yz} are indeed equally occupied [57], but by the influence of the crystal structure on the band structure and the energies of the states, electrons can be continuously shifted among the orbitals and the occupation numbers can in principle assume any value. There is also no reason why the different states should not contribute to the electronic and magnetic properties in a very different way. This is clearly a very important and interesting question, but the electronic configuration in $Ca_{2-x}Sr_xRuO_4$ in the range of intermediate x is still not definitely clear, and some of the proposals that have been made differ from each other very significantly.

There is no doubt that in Ca_2RuO_4 the electronic structure is considerably different from that in the metallic region and in Sr_2RuO_4. Due to the strong flattening of the RuO_6 octahedra in the insulating phase [41] the energy of the d_{xy} states is lowered. There is wide agreement that its occupation number is considerably increased, although the given values do vary between 1.5 and 2 electrons [58–61], with some kind of orbital order [62–65] and probably a strong temperature dependence, reflecting the temperature dependent structural distortions. The insulating low-temperature (S-Pbca) phase of Ca_2RuO_4 and $Ca_{2-x}Sr_xRuO_4$ with $x \leq 0.2$ is separated from the rest of the phase diagram by a quite drastic structural phase transition and may thus have a very different electronic configuration. In the metallic region at $x \geq 0.2$, the local structural distortion around the Ruthenium atom is small compared to Ca_2RuO_4 and the

RuO$_6$ octahedra continue to be slightly elongated along the vertical direction like in Sr$_2$RuO$_4$. Rotation and tilt of the octahedra nevertheless vary considerably and are of course expected to influence the electronic states. For this region, there are quite different proposals that vary not only quantitatively.

A work that received much attention is the theoretical (LDA(+U),DMFT) study by Anisimov et al. [60]. It claims that electrons are transferred from the xy orbitals into the other ones (the opposite effect as what happens when continuing towards Ca$_2$RuO$_4$) yielding a configuration $(n_{xz,yz}, n_{xy}) = (3, 1)$. Most remarkably, the three electrons in the xz/yz states are then claimed to undergo a Mott transition and to adopt an orbital order. A local moment S=1/2 would then be expected in these states (as it corresponds nicely with the experimental data, and also the metamagnetic transition may be explained [66]) , while the xy electrons remain metallic and the actual metal-insulator transition happens only later when also the third band becomes insulating. Since the Mott transition does not occur simultaneously in the three orbitals, this scenario has been called the "orbital selective Mott transition" (OSMT). Intuitively, there is no obvious reason why this should not happen when several orbital states are involved, and was also found later in thorough theoretical work by other groups, either in general or more specialized on the Ruthenate case [67–71] (however the last with the d$_{xy}$ states being the first to become localized). When closer looking at it, though, this is apparently a very delicate question, and because this is a problem of quite general significance, it has caused an intensive debate. There is now evidence that such orbital selective transitions are generally possible, but in the particular case of Ca$_{2-x}$Sr$_x$RuO$_4$ by now the majority of the experimental (and theoretical) results speak rather against this scenario.

Other theoretical studies on the Ca$_{2-x}$Sr$_x$RuO$_4$ system [45, 61, 72] argue that in Ref. [60] the structural distortions might not have been taken into account properly and come to the conclusion that there is not yet such a significant redistribution of orbital occupation away from equal filling (n_{xy} being slightly increased) and that the magnetic moment stems predominantly from the d$_{xy}$ states. More generally, Liebsch [73] has argued that interorbital Coulomb interactions may enforce a simultaneous Mott transition in the different orbitals, and later [74] proposed a more detailed scenario where the metal-insulator transition occurs at once by filling the d$_{xy}$ states completely simultaneously to a Mott localization in the then half-filled d$_{xz,yz}$ states. An even different argument is that it might be an oversimplification to neglect the e$_g$ states, as the d$_{x^2-y^2}$ orbital seems to be lowered considerably in energy by hybridization effects and to play an important role [72, 75].

In the context of the orbital occupations it should finally be mentioned that the occupation changes discussed here, which nearly approach the order of integer numbers, are certainly much larger than the redistribution of electrons discussed in context with the structural effects at the metamagnetic transition. There is no quantitative estimate of the latter, but they should be regarded to be on a significantly lower scale.

Experimentally, it is not straightforward to probe how the Mott transition occurs,
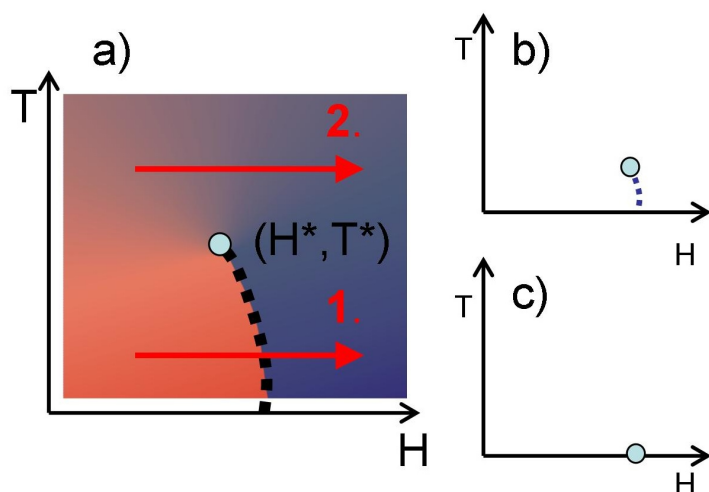
Figure 3.4: Schematic H-T phase diagram with the metamagnetic transition (dashed line) and its critical end point at different positions (H*, T*).

which are the localized and itinerant states and how different states are occupied; this is probably one of the reasons for the long-lasting debate. Nevertheless, there are by now some results from different experimental methods that allow to judge the different proposals. The spin-density results in Ref. [76] and in this thesis indicate that the magnetic moment has predominantly the spatial character of the d_{xy} states. An optical conductivity experiment [77] found evidence that the $d_{xz,yz}$-bands are still itinerant near x=0.5, and the results of ARPES [78] also show the three Fermi surfaces (in contrast to the expectation that the Fermi surfaces of the localized states should disappear) and that there is no huge change in their occupation number. Because the inelastic magnetic neutron scattering is also directly related to the band structure of the material, the results to be discussed in this chapter will also provide a quite precise and strong statement which supports these facts.

3.1.2 The metamagnetic transition

Metamagnetic transitions, crossovers, and quantum criticality

The existence of the metamagnetic transition in $Ca_{1.8}Sr_{0.2}RuO_4$ is deduced from the magnetization curve (Figure 3.1c) and its sudden increase by an amount of about 0.4 μ_B at a field that depends on the direction. In general, the term *metamagnetic transition* is used in the context of a transition that is induced by a magnetic field, and the typical hallmark of a metamagnetic transition is a discontinuous increase of the magnetization at a certain value of the magnetic field. This may apply to situations with very different underlying physics. For instance, it may result from a spin-flip or spin-flop effect in an ordered state, as it is the case in the antiferromagnetic $Ca_3Ru_2O_7$ (see Chapter 5). Another scenario may be that the magnetic field stabilizes a magnetic ground state (for instance S=1) over a non-magnetic (S=0) one, which would

result in the appearance of a finite magnetization at that certain value of the field. These two variants apply rather to a picture of localized magnetic moments, but of course it is also possible to have metamagnetic transitions in itinerant electron systems. A simple example would be a metal with a band structure such that a peak in the density of states exists that becomes suddenly occupied by electrons of one spin direction when it is shifted below the Fermi level by the exchange splitting.

In a more strict sense, a metamagnetic transition is a real phase transition of first-order character, and a generic phase diagram in the H,T-plane is shown in Figure 3.4. Regarding part (a) of the figure, the dashed line would be the metamagnetic transition, and when passing it as function of field like arrow No. 1, one would observe the signatures of a first-order phase transition, in particular, the magnetization would display a truly step-like increase. When going along arrow No. 2, one would not cross the phase transition line, but nevertheless observe a behavior reminiscent of the metamagnetic transition. The magnetization curve would be expected to show a still non-linear, but smooth increase in the region near H^*. This case is actually not a metamagnetic transition, but a crossover phenomenon. The line of first-order phase transitions terminates in a critical end point, at which the transition would have second-order character.
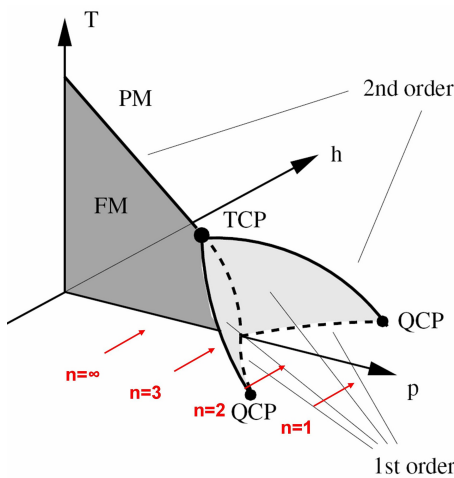

Figure 3.5: Phase diagram for itinerant metamagnets (from Ref. [79]) where p is a control parameter that may be of different nature. The arrows are an attempt to roughly locate the Ruddlesden-Popper series $Sr_{n+1}Ru_nO_{3n+1}$ of the Ruthenates in this phase diagram. (TCP = tricritical point, QCP = quantum critical point)

As the metamagnetic transition is a first-order phase transition, it does normally not give rise to quantum critical behavior. There may, however, exist a further control parameter like pressure, chemical doping etc., which can influence the position of the critical end point (H^*, T^*). One can thus imagine to lower its temperature T^* by tuning this control parameter, as sketched in Figure 3.4b, and at some point, one may eventually completely suppress it to zero (case (c)). In this case – with the second-order phase transition at T=0 – one would indeed expect quantum critical behavior, having a "metamagnetic quantum critical end point" [51].

In theoretical work based on a mean-field theory, a generic phase diagram for itinerant metamagnetism has been established [50, 79], see Figure 3.5. Apart from temperature and magnetic field it includes a control parameter p that may have different physical meaning. The phase diagram contains the ferromagnetic and paramagnetic phases and two "wings" of first-order metamagnetic transitions. The edge of these wings is a line of second-order phase transitions, and where it reaches T=0, the quantum critical (end) points are situated. An attempt to show in a qualitative sense where the Ruthenates would be situated in such a phase diagram (following [80]) is also included in this figure: $SrRuO_3$ is an itinerant ferromagnet [81] and is not considered to

show behavior related to the metamagnetic transition, and Sr_2RuO_4 is well in the paramagnetic regime. The underlying tendency towards ferromagnetism is, though, still present in Sr_2RuO_4, as demonstrated for instance by the ferromagnetic fluctuations discussed in Chapter 4 of this thesis, but so weak that it shows under no conditions any ferromagnetic, neither any metamagnetic behavior. $Sr_4Ru_3O_{10}$ is ferromagnetic at low temperatures, but studies in the recent years revealed a generally very interesting and highly complicated behavior [82–87] including a metamagnetic transition for fields in the a,b-plane. Despite some anomalous, perhaps quantum criticality related behavior [88], this material is obviously not in very close vicinity to the metamagnetic quantum critical end point. About the Ruthenates with n>3, i. e. with more than three layers, not much is known so far, but it is reasonable to expect that their properties will reflect their position between n=3 and n=∞. Finally, $Sr_3Ru_2O_7$ (details see next paragraph) is, like Sr_2RuO_4, paramagnetic at any temperature, but has a metamagnetic transition and can, by magnetic fields along the c-axis, be brought very close to the quantum critical end point of the metamagnetic transition. All these examples would actually occupy a certain range on the p-axis in Figure 3.5 when tuning them by different means: in the case of $Sr_3Ru_2O_7$, this has for instance been shown for pressure and, very importantly, for the direction in which the field is applied (angle to the c-axis) – depending on the angle, there is either a well-defined first-order metamagnetic transition or the quantum critical behavior. In the single-layer compound, one may consider chemical doping as a means to bring the system very close to ferromagnetic order ($Ca_{1.5}Sr_{0.5}RuO_4$) and into the region where the metamagnetic behavior is observed ($Ca_{1.8}Sr_{0.2}RuO_4$; the Ca doping does obviously not act monotonously on the p-axis, nor continuously, due to structural transitions). How close $Ca_{1.8}Sr_{0.2}RuO_4$ is to the quantum critical end point, is to be discussed below.

Metamagnetic transition in the bilayer Ruthenate

The scenario of a metamagnetic quantum critical end point seems to be realized for the metamagnetic transition in $Sr_3Ru_2O_7$. $Sr_3Ru_2O_7$ is the double-layer relative of Sr_2RuO_4 and is also a good metal [49,89] possessing the bilayer perovskite structure with a moderate rotation of the RuO_6-octahedra of 6.8° [90,91]. It is paramagnetic down to lowest temperatures, but apparently close to ferromagnetism (which can be induced by pressure) [49,92]. It has a metamagnetic transition near 5.5 T for fields in the ab-plane and 7.8 T for fields along the c-axis [89]. The difference between these values already indicates that the direction of the magnetic field is important, and, more remarkably, it can be used as a control parameter to influence the temperature of the critical end point and to control the evolution (a)→(b)→(c) in Figure 3.4. For the field parallel to the c-axis, the critical end point is suppressed below 50 mK [93] and quantum critical behavior is observed, as deduced for instance from the non-Fermi-liquid behavior of the electrical resistivity in parts of the H,T-phase diagram [94].

So far, the picture is quite clear. Nevertheless, the physics of $Sr_3Ru_2O_7$ and its

metamagnetic transition is far from being fully understood. When closer studying the properties of $Sr_3Ru_2O_7$, one finds for instance not only one, but several metamagnetic transitions [95] and that a mysterious new phase forms around the quantum critical point [96]. Explanations for it are still controversial and include a symmetry-lowering Pomeranchuk instability of the Fermi surface and, related to it, a so-called electronic nematic fluid [97] (that means in general that the itinerant electron properties have a lower rotational symmetry than implied by the symmetry of the lattice), and on the other hand, the possible formation of magnetic domains [98, 99].

Also, concerning the deeper understanding of magnetic fluctuations at different fields, there is not yet a consistent picture established. Results from neutron scattering experiments are only published for zero magnetic field [100, 101], and a ^{17}O-NMR study finds strong fluctuations consistent with quantum criticality near the transition field, but of rather antiferromagnetic character [102], which is quite surprising at first sight. More information would be clearly desirable – to obtain these data by inelastic neutron scattering is a task comparable to the purpose of the experiments described in this chapter for $Ca_{1.8}Sr_{0.2}RuO_4$, and the experiments by English and Japanese groups have been going on in parallel.

Metamagnetic transition in the single-layer Ruthenate – is it quantum critical?

Compared to $Sr_3Ru_2O_7$, the metamagnetic transition in $Ca_{2-x}Sr_xRuO_4$ has attracted less interest. It is of course the probable existence of the metamagnetic quantum-critical end point and the fact that $Sr_3Ru_2O_7$ has been the first material on which to develop and to experimentally test this concept in detail, which caused this great interest and the subsequent high number of publications. In principle, one may expect the single-layer Ruthenate $Ca_{1.8}Sr_{0.2}RuO_4$ to have many similar properties. One drawback in the case of $Ca_{1.8}Sr_{0.2}RuO_4$ is that it consists of a mixture of Ca and Sr on the same lattice site which inevitably introduces significant chemical disorder in the system. For $Sr_3Ru_2O_7$ it had been shown that sample purity is an extremely important prerequisite for the observations of many of the quantum critical properties.

It is not only this rather practical, though very important aspect of sample homogeneity, but also the fundamental question if $Ca_{1.8}Sr_{0.2}RuO_4$ exhibits quantum critical behavior at all.

The first point to address is if the so-called metamagnetic transition is a transition at all, that means if the observations are due to a first order phase transition or if they are rather a crossover phenomenon (Figure 3.4). At first sight, the broad shape of the magnetization curve speaks against the phase transition scenario. There are, however, two facts to be considered: firstly, the unavoidable inhomogeneities due to the chemical disorder associated with the Ca/Sr-mixture, are expected to broaden any transition as one would actually be observing a distribution of transition fields. Nanoscale electronic inhomogeneities in $Ca_{2-x}Sr_xRuO_4$ due to the doping have been found and quantified in a recent combined STM and ARPES study [103] and seem

to be quite substantial in $Ca_{2-x}Sr_xRuO_4$. Secondly, a phase separation might occur at a first order metamagnetic transition, as suggested recently [99] (based on the idea of so-called Condon domains [104] stabilized by magnetic dipolar interactions). This has been suggested to explain the peculiar behavior of $Sr_3Ru_2O_7$ near its quantum critical point, and seems to play a role also in $Sr_4Ru_3O_{10}$ [86].

Without further information, it is difficult to judge whether these arguments can quantitatively account for the large width of the transition that is still more than one Tesla even at the lowest temperatures.[1] The absence of any measurable hysteresis [54] and the increasing sharpness of the transition (there shown for magnetostriction) down to lowest temperatures rather speak against a broadened first-order transition. Moreover, the transition field is, near x=0.2, not very strongly dependent on the Sr-concentration [56], so inhomogeneities in the Sr-content x alone should not cause a too great broadening of the transition. On the other hand, random local structural distortions that manifest themselves as variations of the tilt and rotation angels might be significant and could probably explain the broadening.

Therefore, no definitive statement about the character of the metamagnetic transition can be made at present. The term metamagnetic *transition* is used throughout this text, in accordance with the literature, but not necessarily to be regarded in its strict sense. The most desirable experiment in order to reveal the character of this metamagnetic transition would probably be a measurement of the ac-susceptibility. This method has proved very useful in the case of $Sr_3Ru_2O_7$ [93].

Certainly, the critical end point is not far away. One may thus either have a critical end point at very low positive temperature, a quantum critical end point, or a virtual critical end point at negative temperature (as if one would continue Figure 3.4 to a case (d)) – more correctly this last case would mean that there is *no* critical end point in the H,T-plane, but in a phase diagram like in Figure 3.5 the quantum critical end point is very near in p-direction.

So is there any indication of quantum critical behavior? With the available data, one may address this question by regarding the structural effects, because it has been shown that metamagnetic quantum criticality has particular signatures in thermal expansion [105, 106]. The analysis of J. Baier [54, 55] proves the expected sign change and symmetric behavior of $\frac{\alpha}{T}$ (α is the thermal expansion coefficient) around the critical field. Also quantitatively the expected relations are fulfilled to some extent, except very close to the critical field. The remaining discrepancies might be well explained by the inhomogeneities mentioned above. In conclusion, one can thus not yet finally say to what extent quantum critical physics determines the behavior of $Ca_{1.8}Sr_{0.2}RuO_4$. Even if present, the disorder would not allow to observe its signatures in a "pure" way. The observations so far indicate that $Ca_{1.8}Sr_{0.2}RuO_4$ is at least quite close to a quantum critical point.

---

[1]The width of the transition may be defined in an empirical way by taking the field derivatives of the magnetization curve or other suitable quantities and regarding the width of the peak.

3.1.3 Overview

The rest of this chapter is organized as follows: a first section summarizes the experimental aspects concerning samples and spectrometers, some technical remarks about the measurement procedure and the data analysis, and is dedicated to the reader interested in the details of the experimental procedures. It follows a discussion of some rather general aspects of magnetic scattering in the single-layer Ruthenates and the results of a spin-density measurement on $Ca_{1.8}Sr_{0.2}RuO_4$. Then, because only two Sr-concentrations have been thoroughly studied by the inelastic techniques, and because different aspects are of special interest in each of them, the discussion will be split into these two cases: first, the sample deep inside the metamagnetic region of the phase diagram (x=0.2), and then a sample that shows no clear metamagnetic transition any more, but is near the susceptibility maximum (x=0.62).

Concerning the former, the metamagnetic transition is the central point of interest. As it turns out that the magnetic field causes profound changes, first the zero-field properties will be discussed in detail, then the field dependence and the transition itself, and finally the properties beyond the transition, i. e. in the high-field phase. The discussion of the sample with the higher Sr-concentration focuses more on the nearby ferromagnetic instability and is somewhat shorter – firstly, this sample had already been studied earlier in some aspects, and secondly, despite the quite different behavior of this material there are important similarities to the sample with x=0.2. After this separate discussion, a concluding section will summarize the results and point out the relations between the different behavior as function of field, temperature and Sr-concentration.

3.2 Experimental aspects

Samples.   The inelastic neutron scattering measurements reported here have been performed on $Ca_{2-x}Sr_xRuO_4$ crystals with two different Sr-concentrations *x*: firstly, on a sample with x=0.62, i. e. in the *$I4_1/acd$*-region of the phase diagram where there is no clear metamagnetic transition observed. This concentration is close to the concentration x=0.5 which has the maximum susceptibility (Figure 3.1a); at x=0.5 itself no large enough crystal has been available. As a second sample, a crystal with x=0.2 was studied. Both crystals were grown using a floating zone method by Satoru Nakatsuji at the University of Kyoto [107]. In inelastic neutron scattering, a large sample amount is very important, and especially in the measurements on these Ruthenates it turned out that the scattered intensity is still much lower than desirable, yet just sufficient.

In both cases the crystals were of approximately cylindrical shape.   The $Ca_{1.38}Sr_{0.62}RuO_4$ crystal (C385-2) had about 34 mm length and 4 mm diameter (mass 1.77 g) and the $Ca_{1.8}Sr_{0.2}RuO_4$ crystal (OT4A) 29 mm length and 4.6 mm diameter

(mass 1.93 g). The latter has been cut into two pieces which have then again been coaligned and fixed on a small aluminium holder. This construction allows the mounting in the cryomagnet (typical diameter 20 mm) and the convenient reorientation by screwing it upon different sample holders. Figure 3.6 shows the complete setup of the two coaligned $Ca_{1.8}Sr_{0.2}RuO_4$-crystals, an aluminium frame, and cadmium shielding.

The sample orientations that have been used are either [100]/[010], i. e. with the *a*,b**-plane in the horizontal scattering plane, or [100]/[001], with the *c** axis in the scattering plane. The tetragonal notation is used here, with approximate low temperature lattice constants a=b=3.76 Å, c=12.55 Å for $Ca_{1.8}Sr_{0.2}RuO_4$. In $Ca_{1.38}Sr_{0.62}RuO_4$, only *c* is notably different; c=12.65 Å due to the absence of the tilt distortion of the structure.

The $Ca_{1.8}Sr_{0.2}RuO_4$ crystal has been characterized on the G4.3 spectrometer at Saclay. A difference in the orthorhombic lattice constants *a* and *b*, which is expected to be about 0.5% at low temperature, could not be detected. In the space group *Pbca*, the tilt of the octahedra causes superstructure reflections $(h,0,l)$ with h uneven and l even, while the corresponding reflections with h and k exchanged are forbidden. Nevertheless the reflections (1,0,2), (1,0,4), (3,0,2) and (3,0,4) have been observed with approximately equal intensity in the two possible inequivalent crystal orientations (*a* and *b* exchanged). This proves that the crystal is twinned with approximately equal amounts of both twins. In view of the very

Figure 3.6: The $Ca_{1.8}Sr_{0.2}RuO_4$ crystal in the mounting used in the magnet on Panda. The sample is mounted in an aluminium frame to which cadmium shielding has been attached.

anisotropic magnetic properties, this is important for the further analysis of the data. It has also been proved that no 327-impurity phase is present in the crystal. Regarding the $(2,1,l)$ reflections, it was found that intensity appears on half-integer l-values, but not on the integer ones. This proves (see for instance the discussion in [108]) that the crystal is in the so-called *D-Pbca* phase and not in the *L-Pbca* phase, which is in close proximity in the phase diagram [43]. In *D-Pbca*, the octahedra of next-nearest layers are rotated in the opposite sense.
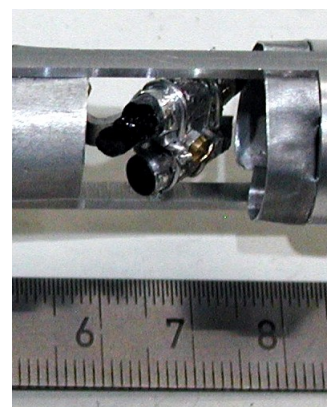
Spectrometers. A considerable number of different spectrometers has been used for the inelastic neutron scattering measurements on $Ca_{2-x}Sr_xRuO_4$. This is partly due to the different capabilities of the spectrometers (thermal/cold energy range, availability of sample environment like magnets etc.) and partly due to the fact that huge amounts of beamtime were necessary to obtain sufficient information despite the low count rates – beamtime that is difficult to obtain in a single neutron facility. The largest part of the data without magnetic field has been obtained on the triple-axis spectrometers of the LLB: 4F1 and 4F2 in the cold neutron range and 1T and 2T in the thermal range – 2T turned out to be better suited for these studies due to a lower and better defined background at low scattering angles and higher intensity. On IN14, a mea-

surement at very low temperature with a dilution cryostat has been performed on $Ca_{1.38}Sr_{0.62}RuO_4$. Magnetic field experiments with vertical cryomagnets and fields up to 10 T have been carried out on Flex (HMI) – the flux of which was by far too low – and IN12 on $Ca_{1.38}Sr_{0.62}RuO_4$, and on IN22 and PANDA in the case of $Ca_{1.8}Sr_{0.2}RuO_4$. All experiments have been performed with unpolarized neutrons – the expected intensity loss due to the polarized neutron setup appeared unacceptable despite the potential advantages.

The total amount of beamtime is about six to seven weeks for each of the two concentrations. Further six weeks had (among other samples) already been spent on $Ca_{1.38}Sr_{0.62}RuO_4$ before the year 2003 by Oliver Friedt, especially on 1T (and at some points – where explicitly mentioned – also these data will be included or referred to for completeness and comparison).

Practical aspects. The interesting energy ranges in the context of magnetic fluctuations in $Ca_{2-x}Sr_xRuO_4$ are rather low – energy transfers higher than 8 meV have not been studied, and most studies even focused on the region ≤ 4 meV. This range is easily covered by cold neutron spectrometers, but the use of thermal spectrometers has been very helpful due to the higher flux which they offer. On the thermal spectrometers, typically k_f=2.662 Å^{-1} was used. The energy resolution is then such that the lowest energy transfer that can be reasonably measured is about 2 meV. On the cold neutron spectrometers, typically k_f=1.5 Å^{-1} (and in few cases smaller k_f) has been used, which allows for measurements down to approximately 0.4 meV without too large increase of background. To suppress higher order wavelengths, Beryllium filters have been used on the cold neutron spectrometers, and PG-filters on the thermal ones. Because it is highly important to suppress higher orders when working near (1,0,0) (note that (2,0,0) is a very strong Bragg peak), one or even two PG-filters have been installed on k_f.

As the magnetic response is not sharp in q-ω-space, no high resolution is necessary. In contrast, any possible increase of intensity is highly desirable, so usually focusing conditions (with open collimations) have been used.

The measurements without magnetic field have been carried out in standard orange cryostates (except one in the dilution cryostat), which permit a lowest temperature of approximately 1.5 K, like the cryomagnets. A technical aspect to be mentioned here is that the helium exchange gas in the sample chamber can cause additional inelastic scattering, mostly at small q and ω, by the recoil of the Helium core (Fig. 3.7). This scattering is also temperature dependent, and is stronger and sharper at low temperature. It turned out to cause a well visible contribution in some of the scans on the cold spectrometers – this could be considered in the data treatment, but it is therefore best to have only very small amounts of Helium around the sample.

Data analysis and presentation. All reciprocal lattice vectors are generally given in relative lattice units and refer to the *tetragonal setting* of the unit cell (3.8·3.8·12.5 Å).

The splitting of the total beamtime in different independent measurements on different spectrometers is a disadvantage insofar as it makes the total data set more difficult to analyze and data taken under different conditions can not directly be compared. To some extent, this has to be considered at the time of the experiment by concentrating on a certain aspect and solving it in a single configuration. On the other hand, it is still desirable to simultaneously treat data from different measurements. In most cases it is possible to compare different configurations by regarding equivalent scans. In addition, an acoustic phonon near (2,0,0) has sometimes been measured and permits a quantitative comparison. After background subtraction and adjustment of a scale factor it turned out that indeed the data of different measurements is mostly identical within error bars. The comparison to phonon scattering is a further useful test when comparing intensities. In such cases it can be helpful to merge and to average different data sets. Strictly speaking, such a procedure is of course not correct as it cannot account for different experimental resolutions and related problems, and it is in fact only possible for identical conditions (orientation, wavelength, etc.). Then it makes indeed sense, for instance for plotting purposes, resolving weak signals, generally getting a better impression of the shape of the signals and reducing the amount of redundant data. The more correct procedure is to keep separate data sets, but to simultaneously fit them, taking account for the respective resolution functions. Using the appropriate Matlab libraries, it has been possible to perform such fits for data sets consisting of a few hundred points, allowing for different resolution functions and scale factors in parts of the data set.

Finally, the different conditions under which the data have been collected also have an advantage: it is easier to identify spurious signals, and it increases, wherever there is agreement between different measurements, the credibility of the results.

Figure 3.7: Scattering (intensity) of helium gas (following [1]). At higher temperature, the distribution rapidly broadens and weakens.

Comment on constant energy scans: rocking vs. straight scans The magnetic correlations are essentially two-dimensional, so the magnetic scattering does, apart form factor and geometrical effects, not depend on the L-component of the momentum transfer. When c^* is in the scattering plane, L can therefore be chosen with some freedom. On the one hand, the modulus of Q should be small in order to benefit from a higher magnetic form factor. On the other hand, the background can be higher at small scattering angles (the largest effect being the approach to the direct beam), and especially long scans require huge variations of the spectrometer angles. Typical scans run across large parts of the Brillouin zone, and a large variation of the scattering angle is undesirable as it could result in a non-constant background. This can
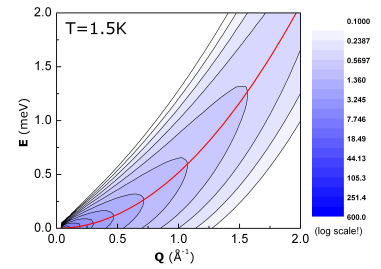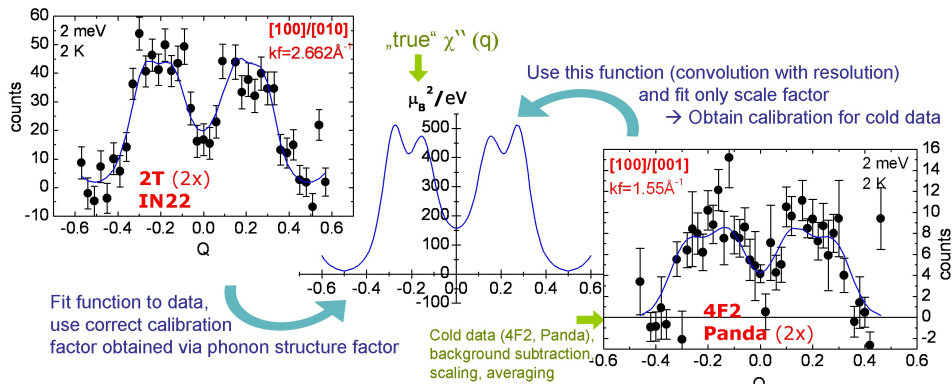
Figure 3.8: Obtaining the correct calibration for the different data sets. First, data is merged and averaged, where possible, i. e. where measured under the same experimental conditions (orientation, wavelength, etc.). For the thermal data set with k$_f$=2.662 the calibration via the acoustic phonon is available, and the parameters of a suitable model function can be fitted to the data in correct units. Data for which no direct calibration is available are fit using this function and thus the correct scale factor for these data is obtained.

be avoided by performing true rocking scans, i. e. only turning the sample rotation angle. This type of scan has the additional advantage that the magnetic form factor remains constant throughout the whole scan (at least if the form factor is isotropic). Following these ideas, a large portion of the scans have been performed as rocking scans and has then been plotted versus the H-component of Q (the steps in H are thus not equidistant). On the other hand, it requires very large sample rotation angles. In a typical scan across (0,0,1.6) the crystal has to be rotated by approximately 60 degrees in each direction. In such long scans, other effects (like sample holder, crystal shape etc.) can again cause background variation and other problems. It finally turned out that under good experimental conditions, in particular good control of the background, there is no significant difference between the rocking scan and scans along straight lines in Q-space.

Calibration to absolute units   The calibration of magnetic scattering follows the procedure with an acoustic phonon on (2,0,0) as described in section A.1. This procedure includes the fit to a scattering function for which a suitable model has to be assumed (see later in this chapter). Where possible, this procedure yields the desired calibration in a very straightforward way. Concerning the present data, there is the additional problem that for the large set of data collected with k$_f$=1.55Å^{-1} in the

100-001 orientation, no suitable phonon can be measured[2]. It is therefore the most convenient way to use the correctly calibrated scattering function and to directly determine the calibration factor for these data from it. For each data set – i. e. basically the thermal data in *a/b* orientation with k_f=2.662 Å^{-1}and the cold data in *a/c* orientation with k_f=1.55 Å^{-1} – the effective resolution function has to be known. Figure 3.8 summarizes the process of the calibration and the relation of the data sets used here to each other.

3.3 Magnetic neutron scattering on $Ca_{2-x}Sr_xRuO_4$

3.3.1 Magnetic origin of the signal and magnetic form factor

Concerning the magnetic form factor of the Ru^{4+} ion, several aspects need to be considered. Firstly, no values are tabulated in the literature, only values for Ru and Ru$^+$ are available [109]. As it is argued in Ref. [76], the data for Ru$^+$ may be considered as a good approximation to describe the magnetic form factor. Secondly, it is clear that the form factor will have some anisotropy – the spin density studies with polarized neutrons have very clearly demonstrated the anisotropic spin density distribution. The extension of this distribution is larger in the plane than perpendicular to it. Because the magnetic form factor is the Fourier transform of the spatial distribution, it is obvious that the form factor decreases more rapidly in the H and K directions of reciprocal space and varies more slowly in the L-direction. Using the tabulated values for $j_{0,2,4}$ and the spherical harmonic functions it is possible to calculate the contribution of different orbital states to the magnetic form factor. Though a rather rough approximation, it is helpful because in this way one can account for the fact that the spin density has mainly d$_{xy}$-character. This gives the form factor a complicated three-dimensional anisotropy, but the only relevant feature is the anisotropy between in-plane (more rapid decrease) and out-of-plane. Other effects are not expected to be important, particularly not in view of the statistics that is usually achieved in the inelastic scattering experiments.

For the $Ca_{1.38}Sr_{0.62}RuO_4$ sample, the Q-dependence of the magnetic signal has been analyzed in detail. To study the dependence on H and K is hardly possible, because no equivalent signals at suitable different Q can be practically measured. In contrast, the fact that the signal is not expected to depend on the L-component, permits to measure the L-dependence continuously over an interesting range. Using a [100]/[001] orientation on 4F and working at 10 K, where there is a relatively strong signal, the magnetic scattering at Q=(0,0,L) has been measured at different values of L. The results of some full rocking scans at different scattering angles (dif-

---

[2]Due to scattering angle restrictions, the only possible Bragg point is (0,0,2) where the phonon is, however, only very weak due to the low structure factor and the small Q^2.
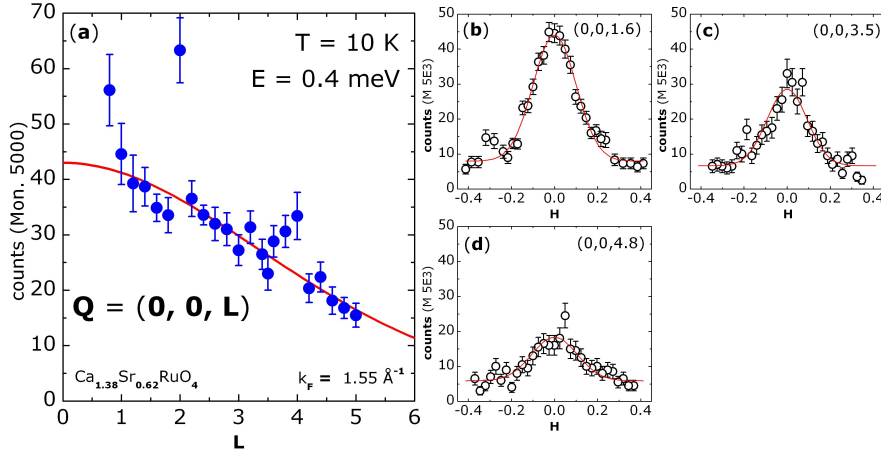
Figure 3.10: Magnetic signal in $Ca_{1.38}Sr_{0.62}RuO_4$ at different momentum transfers $Q = (0, 0, L)$. (b)-(c) show rocking scans at three different L-values. In (a), the amplitude of the signal is plotted as function of L. Here, a smooth background has been subtracted that has been determined from the scans and from background points collected at identical scattering angle. Near (0,0,2) and (0,0,4), the count rate seems to be enhanced probably by the influence of the nearby structural Bragg points. The line corresponds to to the calculated squared magnetic form factor, as discussed in the text. (Monitor 5000 corresponds to approx. 5 minutes counting time.)

ferent L) and of an L-Scan on (0,0,L) are summarized in Figure 3.10. In the rocking scans there is no indication of changes in the shape of the signal as function of L, apart the reduced intensity at higher L. The decrease as function of L seems to be monotonous, except near the Bragg points (0,0,2) and (0,0,4), and can be described by the squared magnetic form factor, if an anisotropic form factor is assumed. The isotropic Ru$^+$ form factor would require a faster decrease – in Figure 3.9 the effect of different orbital contributions to $F(Q)^2$ is estimated. The numbers correspond to the relative weight of the d$_{xy}$ state, i. e. 33% means an equal contribution of xy, yz and xz, while 100% a pure xy character. The line in Figure 3.10a has been calculated using 80% d$_{xy}$ character. This method is of course to be considered rather as an estimate, and the statistics of the inelastic signal does generally not permit a high accuracy. Furthermore, these considerations are limited by possible differences in the radial part between Ru$^+$, for which the values were taken, and Ru^{4+}, and other effects like magnetization on oxygen are not included. Nevertheless it qualitatively demonstrates that the anisotropy caused by the non-spherical distribution plays a role, and thereby confirms the expectations from the spin density results.

The agreement of the Q-dependence with the expected decrease of the magnetic form factor is a very strong argument that the observed signal is indeed magnetic in

origin.[3] Other arguments include the temperature dependence (the decrease towards higher temperature would not be expected for phonons) and the two-dimensionality (L-independence). Also, no optical phonon branches are expected, because the energy transfers are too low.

Practical aspects and other possible signals The measurements in the [100]/[010] orientation have all been performed around Q=(1,0,0), which is a zone centre in two dimensions, i. e. when neglecting the correlations between the layers. Structurally, this Bragg reflection is forbidden, both in *$I4_1$/acd* and the lower *Pbca* symmetry of $Ca_{1.8}Sr_{0.2}RuO_4$. This (and the symmetrically equivalent points) is the only position in reciprocal space where measurements on a magnetic zone centre can be performed, because at the other integer (H,K,L) there are either strong Bragg reflections or |Q| is so large that the magnetic form factor is too low. Although (1,0,0) is structurally not allowed, in $Ca_{1.8}Sr_{0.2}RuO_4$ significant intensity has been found in elastic scans – about 10^{-3} of the intensity on (2,0,0), which is a strong Bragg reflection. Its origin is not entirely clear; apart some $\frac{\lambda}{2}$ contribution, there is probably an effect of structural disorder. A structural disorder effect related to the layer stacking has for instance also been observed in $Ca_{1.38}Sr_{0.62}RuO_4$ where the (0,0,2) reflection has extremely long tails in L-direction.

Figure 3.9: Squared magnetic Form factor as function of the L-component of the momentum transfer for different contributions of the xy states (see text).

The elastic intensity on (1,0,0) has been found to be responsible for a spurious peak in many of the transverse Q-scans across (1,0,0). It is reproducible on different thermal spectrometers and probably due to picking up the elastic signal with a tail of the resolution function; in the scans with the typical step size of ΔQ=0.03, it concerns only one point. No influence is expected from acoustic phonons at (1,0,0). By scaling the intensity of the acoustic phonons at (2,0,0), which has been precisely measured, with the factor $\sim$1000 of the elastic intensity, and eventually a factor 4 due to Q^2, one can estimate any phononic intensity at (1,0,0) to be safely below the limit of detection.

3.3.2 Spin density in $Ca_{1.8}Sr_{0.2}RuO_4$

The magnetic form factor is intimately related to the spatial distribution of the magnetic moment. The above analysis of the inelastic magnetic scattering in $Ca_{1.38}Sr_{0.62}RuO_4$ has already demonstrated that the magnetization is not spatially isotropic on the Ru sites. In general, though, the analysis of the inelastic signal is not well suited to
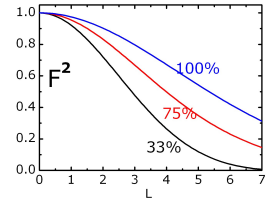
---

[3]In his thesis, O. Friedt [110] has performed an analysis of the L-dependence on the incommensurate position in $Ca_{1.38}Sr_{0.62}RuO_4$ (in a more limited L-range 3-4.25) and has also been able to describe it by the magnetic form factor.

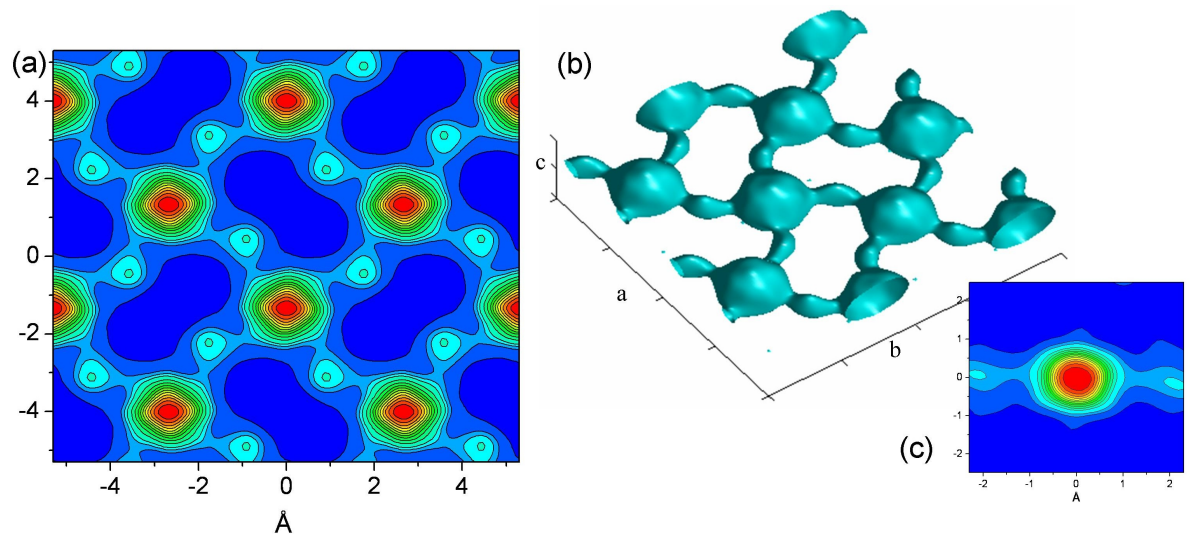Figure 3.11: Spin density in $Ca_{1.8}Sr_{0.2}RuO_4$ at B=7 T. (a) Projection onto the a,b-plane (four unit cells), (b) isosurface showing a 3D-view of the basal RuO_2 layer and (c) a vertical cut through the spin density (slice plane defined by z-axis and the in-plane O(1)-Ru-O(1) bond).

precisely determine magnetic form factors because the intensities are low and the signal depends on many other factors.

Precise studies of the magnetization distribution can be performed using the polarized neutron diffraction technique. For $Ca_{1.5}Sr_{0.5}RuO_4$, a spin density study has been published by A. Gukasov et al. [76]. It showed very clearly that the spin density at B=7 T strongly resembles the d_{xy} orbitals of the Ru-ions and that a significant amount of magnetization is also located on the in-plane oxygen atoms. This is in good qualitative agreement with the considerations in the preceding section.

In view of the various suggestions concerning the electronic configurations of $Ca_{2-x}Sr_xRuO_4$ at different x (see Section 3.1 above) and in particular in view of possible changes at the metamagnetic transition, it appeared interesting to extend these studies to $Ca_{1.8}Sr_{0.2}RuO_4$. For this purpose, a small $Ca_{1.8}Sr_{0.2}RuO_4$ single crystal has been investigated on 5C1 by polarized neutron diffraction. At an applied field of 7 T, i. e. above the metamagnetic transition, a set of flipping ratios on 158 symmetrically independent reflections (in *Pbca*)[4] has been collected in two sample orientations; about a quarter of these have a deviation from 1 that is larger than three times their experimental error.

Below the metamagnetic transition the magnetization has been found too low to enable the measurement of flipping ratios with a reasonable accuracy, so no statement

---

[4]Note that due to the lower space group symmetry than in $Ca_{1.5}Sr_{0.5}RuO_4$ the number of independent reflections is higher, and, correspondingly, the statistics worse.

can be made here about eventual changes at the metamagnetic transition. For the high field phase, though, the spin density could be refined; the results are summarized in Figure 3.11.

Most apparently, the spin density is confined to the Ru-O-planes, and it is mainly located on the Ruthenium sites; this confirms the basic expectations. Like in the case of $Ca_{1.5}Sr_{0.5}RuO_4$, there is a significant amount of magnetization on the in-plane oxygen sites, and the continuous distribution reflects the itinerant character of the electrons.

Besides these similarities, there are also some noteworthy differences to $Ca_{1.5}Sr_{0.5}RuO_4$. These can roughly by summarized by stating that the peculiarities of the $Ca_{1.5}Sr_{0.5}RuO_4$-results are less pronounced: the amount of magnetization on oxygen seems to be slightly lower, and in particular the d_{xy}-shape of the spin density on the Ruthenium sites is much weaker. There is, though, still significant deviation from a spherical distribution, and despite the lower symmetry (basically twofold at the Ru site) there are still features with a fourfold symmetry reminiscent of $Ca_{1.5}Sr_{0.5}RuO_4$. In general, however, the density appears, in all three spatial directions, more spherical than in $Ca_{1.5}Sr_{0.5}RuO_4$.

It is hard to estimate to what extent this is related to the quality of the data set. Compared to the $Ca_{1.5}Sr_{0.5}RuO_4$ data, the situation is more difficult in $Ca_{1.8}Sr_{0.2}RuO_4$ mainly due to the lower symmetry of the lattice. This requires more reflections to be measured in order to produce a refinement with the same level of detail. Furthermore, the crystal seemed to be somewhat less well suited and, to a certain extent, twinning may have complicated the problem. As a consequence, the data quality is expected to be lower – this does not mean wrong measurements, but mainly that the error bars are larger. As it is an intrinsic property of the maximum entropy treatment to account for the statistical significance of the observations and to produce the most probable – i. e. the flattest and least-featured map consistent with the data – this may explain in parts why there are less pronounced features visible in this case.

A problem that can quite safely be excluded is the procedure of the data treatment and refinement. In order to estimate this, the old $Ca_{1.5}Sr_{0.5}RuO_4$ data that were published in Ref. [76] have been reinvestigated using exactly the same procedures of data treatment and the same software. In doing so, the published results and thus the differences to $Ca_{1.8}Sr_{0.2}RuO_4$ were well confirmed. In addition, the centrosymmetry of the lattice made it possible to use other refinement programs than the self-written one, and with the program package `Mend` well consistent results have been obtained.

One may thus conclude that there are indeed some (not very large, but significant) differences in the spin density distribution between $Ca_{1.5}Sr_{0.5}RuO_4$ and $Ca_{1.8}Sr_{0.2}RuO_4$. In $Ca_{1.8}Sr_{0.2}RuO_4$ the contribution of the out-of plane states (d_{xz} and d_{yz}) is larger, thereby giving the spin density distribution a more spherical character. It would be interesting to see whether the studies that have been carried out by a Japanese group on the same problem, have come to a similar result.
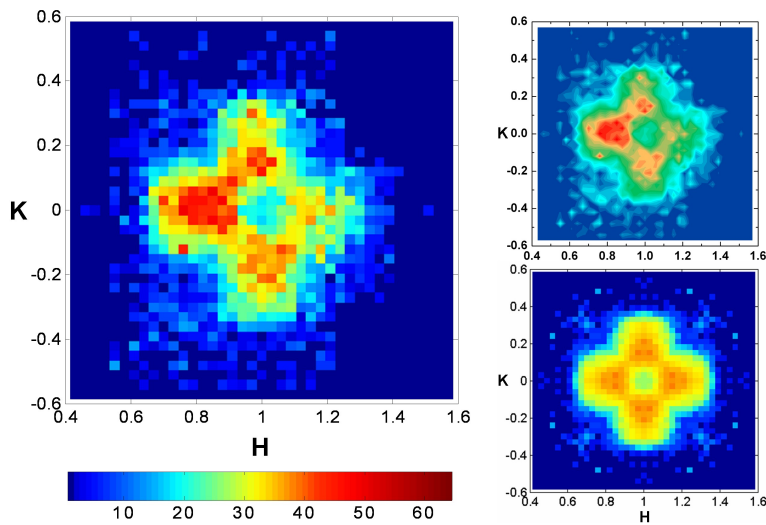
Figure 3.12: Inelastic neutron scattering intensity in $Ca_{1.8}Sr_{0.2}RuO_4$ around (1,0,0). Data are taken without magnetic field at 2 K and 2.5 meV energy transfer (on 2T). The large figure shows the data as it has originally been collected (each pixel corresponding to one point in the measurement). A smooth (scattering-angle dependent) background has been subtracted and isolated points with spurious peaks have been replaced by the average of their neighbors. The upper small figure on the right side shows the same data, but using a different plotting algorithm based on calculated contour lines. The lower small figure shows the dataset after it has been fully symmetrized and corrected for the magnetic form factor.

3.4 Magnetic correlations in $Ca_{1.8}Sr_{0.2}RuO_4$

3.4.1 Below the metamagnetic transition

The macroscopic physical properties, like the anomalous temperature dependence of the susceptibility which is strongly suppressed at low temperature, or the high value of the specific heat coefficient γ, and the results obtained earlier on $Ca_{1.38}Sr_{0.62}RuO_4$ [46] indicate the probable presence of strong antiferromagnetic correlations. In order to characterize the magnetic correlations, a large amount of data has been collected, covering a wide energy range and the whole range of possible momentum transfers.

The best overview is probably obtained by regarding the intensity map in Figure 3.12. In this map, Q_{FM}=(1,0,0) is in the centre. As discussed in the preceding section, this is not a Bragg point in the structure of $Ca_{1.8}Sr_{0.2}RuO_4$, but only in two dimensions, i. e. when regarding a single Ru-O-plane. Therefore, it is also *not* a ferromagnetic
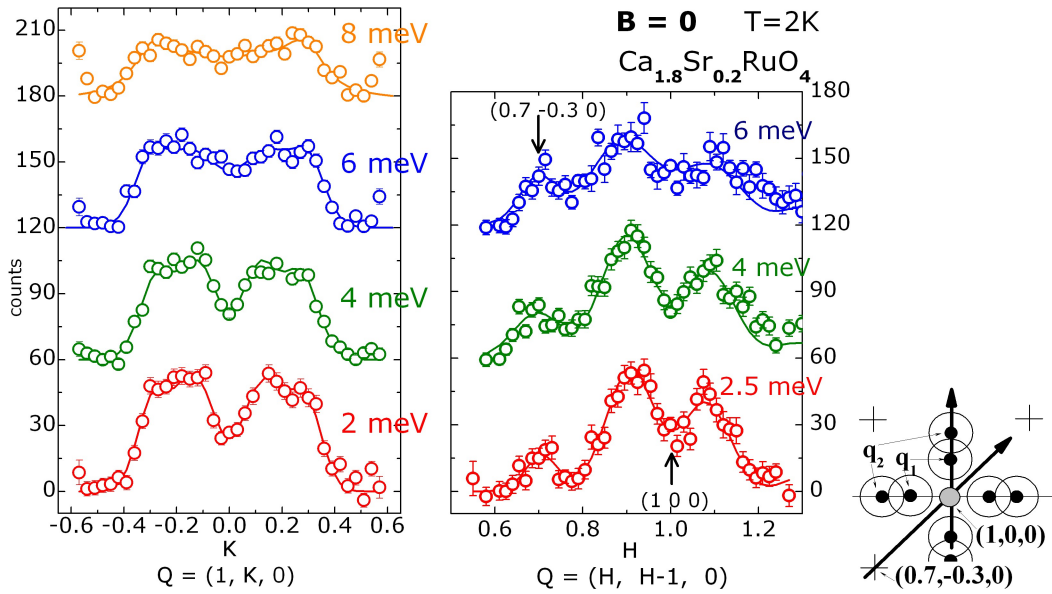
Figure 3.13: Transverse (left) and diagonal (right) scans across (1,0,0) at different energies. The sketch shows the scan paths and the position of the signals in reciprocal space.

zone centre in case of any long-range ferromagnetic (i. e. three-dimensional) order. Because the correlations in the paramagnetic state are mainly two-dimensional and the L-component of Q is not significant, it *can* be regarded as a ferromagnetic zone centre, and the area in Figure 3.12 may be considered as a full Brillouin zone. For this reason, the map can be expected to contain any (sufficiently strong) magnetic scattering in reciprocal space[5].

The overall appearance of the intensity distribution is well described by four broad contributions separated by about 0.2 reciprocal lattice units from the zone centre. At the zone centre itself, there is a clear minimum. It is therefore obvious that the response at this energy consists of **broad peaks at incommensurate antiferromagnetic q-vectors**.

This is, however, not yet a satisfactory characterization of the magnetic response. Some of the questions that are of particular interest in this material are the following:

- Can the measured response be considered as one very broad signal or does it have additional structure?

- What is its energy dependence, and, more specifically:

---

[5]Because of lattice symmetry, actually one eighth of this map would already contain the full information.

- Do these excitations have a dispersion, and may it be related to a ferromagnetic interaction (a spin wave or paramagnon at finite energy producing a peak at finite Q)?

- What is the underlying origin of these excitations and can it be related to the electronic structure?

- Can the incommensurate peaks at (0.3,0.3,0) – the dominating response in Sr_2RuO_4 – still be observed here?

- Is the thus determined spectrum of spin fluctuations consistent with other experimental results?

These aspects will now be addressed in detail in this order.

Detailed structure of the signal.

Regarding the transverse scans in Figure 3.13, in particular the scans at 2, 4 and 6 meV energy transfer, one observes that the intensity increases very rapidly and sharply at about q=±0.35, and a flat plateau follows until q=±0.1. Because of this particular shape, it turned out impossible to describe the data by a single broad (Gaussian) peak on each side, as it cannot reproduce the plateau and the steep edge. In contrast, when using two peaks, it is easily possible to fit the data very well. These peaks are at the positions **q_1=0.12±0.01 and q_2=0.27±0.01**. The sketch in Figure 3.13 gives a schematic summary of the peak positions around (1,0,0).

A very remarkable aspect of this finding is the similarity to $Sr_3Ru_2O_7$. For this material, Capogna et al. [100] have published inelastic neutron scattering data and have found maxima at 0.09 and 0.25 in equivalent scans, i. e. at very similar positions. There, these two peaks are clearly separated (at least at 1 and 2 meV), while this is not possible in $Ca_{1.8}Sr_{0.2}RuO_4$ due to their larger width and strong overlap.

Energy dependence.

As function of energy, the overall shape of the signal does not change much. In the description of the data, the positions of the two peaks on either side can be held constant – there is no dispersion the signal. The most noteworthy change is the broadening which is observed at higher energy. It leads to smoother edges and a partial filling of the minimum in the centre.

Regarding the intensity at the incommensurate wave vectors, its maximum is between 2 and 4 meV.[6] Taking the average of the intensity over the q-range of the incom-

---

[6] The energy range of the thermal neutron experiments starts at 2 meV, and no data has been collected in this sample orientation on the cold neutron spectrometers. Therefore no energy scan is available which could really show the maximum at the characteristic energy.

mensurate maxima from the constant energy scans and then fitting a single relaxor function (2.32) to these points, one obtains a characteristic energy of 2.7±0.1 meV.

In Chapter 2.2.3, a model for the description of magnetic scattering in a metal near an antiferromagnetic instability has been discussed. Besides its amplitude χ', equation (2.29) describes the response in terms of two parameters: a characteristic energy and a correlation length, ε and ξ. Remember that the actual width in a constant energy scan depends on the energy and increases significantly at energy transfers higher than ε (see equation 2.30). Accordingly, the energy maximum in a constant-q scan depends on $|q - q_0|$. In general, one cannot expect that (2.29), which is derived for an idealized model and with its few adjustable parameters, yields a full description of the response in this complicated system, but if the observed scattering can really be understood in terms of a near antiferromagnetic instability, it should capture some important aspects.

In the present situation with two peaks on each side, it has been tried to use a function consisting of the sum of twice (2.29) with different q_0 (according to the two positions 0.12 and 0.27 as found above), taking properly into account the magnetic form factor and the resolution function of the spectrometer[7]. To reduce the set of parameters, equal correlation lengths and characteristic energies have been assumed. With such a procedure, it is indeed possible to fit the scans in Figure 3.13a very well, as show the lines, which have been obtained within such a model. It is, however, not well possible to simultaneously fit the whole dataset (i. e. the scans at all energies) with a single parameter set, because the calculated intensity at high energies is too large. This is probably a consequence of the heavy overlap of the intensities stemming from different q_0 which has simply been summed – neglecting the coupling of the excitations is probably an unphysical oversimplification. In addition, it might be too simple to neglect the possibility that in-plane and out-of plane components of χ'' (which are simultaneously measured) behave in a different way. The intensity prefactors have therefore been determined separately, leaving the shape and the varying widths as the essential content of the model.

The shape thus obtained is very similar to that when simply taking the sum of four Gaussians (with the respective symmetry constraints), but this more sophisticated antiferromagnetic fluctuation model is superior to fitting independent Gaussians in that the broadening towards higher energies is implicitly contained and does not require the q-widths to be fitted separately. In other words, the ξ parameter can be held *constant* at the different energy transfers, and the broadening is described correctly by (2.29). The restriction here is that under the given circumstances[8] ε and ξ are correlated – with ε fixed to 2.7 meV, one obtains for ξ a value of 9.7±0.4 relative

---

[7]For a correct integration, the response throughout the whole Brillouin zone was modelled, i. e. a total of eight peaks (four equivalent by symmetry for each q_0).

[8]The features are not well resolved neither on the q- nor on the energy axes: on the q-axis due to the large width and the overlap of several contributions, and on the energy axis because the lower effective boundary (significantly below 2 meV) is not measured.
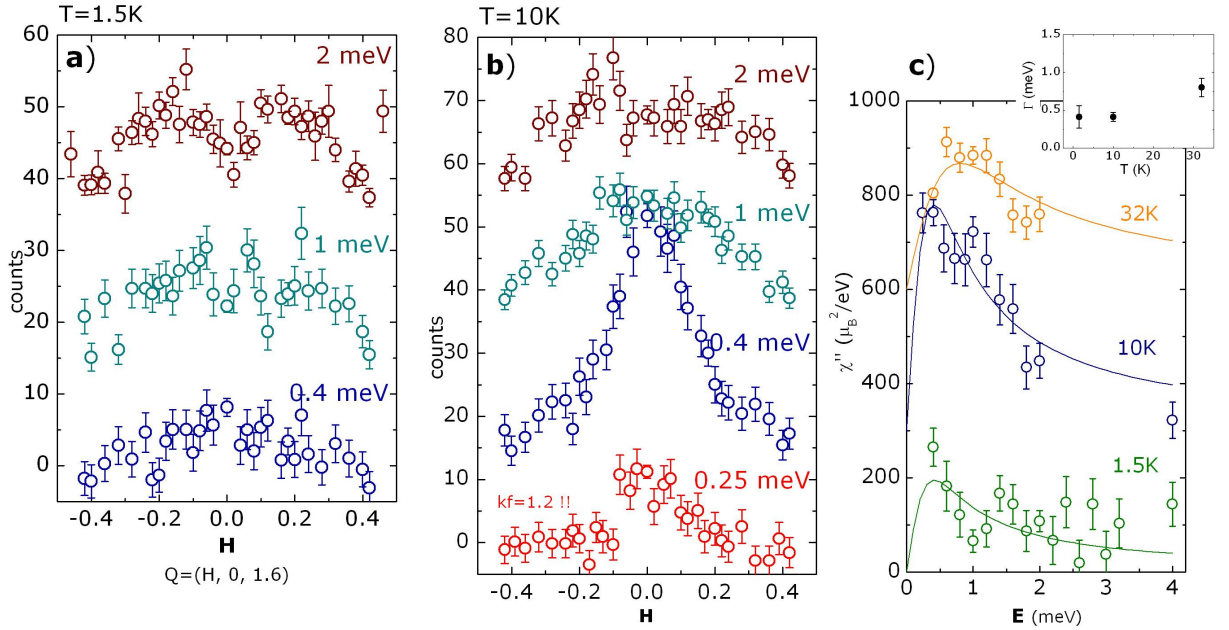
Figure 3.14: Low energy part of the magnetic response in $Ca_{1.8}Sr_{0.2}RuO_4$ without magnetic field. (a) and (b): constant energy scans at low temperature (a) and at 10 K (b). Data are taken as rocking scans (i. e. L is not constant) across (0,0,1.6). The 0.25 meV scan at 10 K has been measured with different k_f (k_f=1.2Å^{-1}), so its intensity is not directly comparable to the other scans. Background has been subtracted. Energy scans on Q=(0,0,1.6) are shown in (c). The intensity has been corrected for the Bose factor in order to obtain, together with the calibration factor, the imaginary part of the susceptibility. Lines are fits to a single relaxor function. The obtained Γ's are shown in the inset.

length units, which on an absolute length scale is about 6 Å. For comparison, this is even shorter than the value for the incommensurate signals in Sr_2RuO_4, which is about 10 Å [111,112]. A value of 6 Å corresponds to less than twice the lattice spacing and means that the correlations still have a very short length scale.

Antiferromagnetic nature of the signal and possible ferromagnetic contribution.

That it is possible to describe the data using the equations for a nearly antiferromagnetic metal, does of course support the truly antiferromagnetic character of the magnetic correlation. If there was still doubt against this, the most serious objection could be that in fact a ferromagnetic signal is superimposed on one or several incommensurate contributions. There are several reasons against this scenario:

- An excitation of ferromagnetic character (paramagnon, magnon) would be expected to disperse outwards from (1,0,0). In a constant energy cut like the map in Figure 3.12, a dispersive excitation would yield a ring of intensity around (1,0,0). Regarding the intensity map, the outer contributions are clearly not ring-like and centred on the axes. The inner ones could be circular, and the diagonal scans in Figure 3.13 seem indeed to support such a scenario, as there are strong maxima on the diagonals which have about the same intensity as the inner contributions in the transverse scans[9]. However, the intensity is also easily explained by an overlap of two broad contributions centred on the axes. Similarly, the geometric argument is not very helpful: if it was a ring with radius r in reciprocal space, the maximum on the diagonal would be expected at the k-coordinate $r/\sqrt{2}$, while in the case of overlap at $r/2$. This difference is hard to resolve for a small radius, and in general the anisotropies of the system can cause the dispersion to be not circular or an incommensurate peak to have different widths in different directions. Thus, concerning the shape of the signal, the intensity map probably remains the best information: regarding carefully its various presentations in Figure 3.12, there is some indication that the intensity is *not* spread ring-like.

- In the diagonal scans, it is again the missing shift of the peaks with increasing energy, which points to an overlap of axis-centred peaks which give rise to the observed intensity. If the peaks were due to a ferromagnetic dispersive mode, the shift would be seen clearer on the diagonals, because there is not such an overlap of different contributions like on the axes.

- Following the discussion of the q-ω-shape of a paramagnon in Section 2.2.3 (Equation (2.26) and Figure 2.3), it is obvious that high spectral weight is concentrated in the region at low energy and low q. Regarding the scans at 0.4 and 1 meV taken on the cold spectrometers (Figure 3.14a), there would have to be a strong enhancement of intensity which is clearly not observed. Also in $Ca_{1.38}Sr_{0.62}RuO_4$ (discussed later in this chapter) the low energy response is clearly different from these data. This is probably the strongest argument against a significant ferromagnetic contribution to the fluctuation spectrum.

This does, of course, not rule out that there is a small ferromagnetic contribution to the spectra – some indication does still exist, and in the next section it will be shown that at higher temperature such a contribution becomes very important. The main statement is that at low temperature it is small and that it is not the origin of the incommensurate response, which is thus of truly (incommensurate) antiferromagnetic character.

Concerning the detailed structure of this incommensurate antiferromagnetic response, it is more difficult to give a final answer. As discussed above, it can be

---

[9]In the diagonal scans, the form factor effect is strong. Averaging the right and the left side, one can reasonably compare to the transverse scan.

well described by the sum of two contributions at different q-vectors on the *a*/b** axes which behave like (2.29). This is however no proof that this is really a physically correct description. In particular, it is not possible to clearly separate these two contributions. The widths of the broad antiferromagnetic response perpendicular to the *a*/b** axes (see also Figure 3.18) is slightly smaller than the total width along the axis, but larger than the width of a single peak at q_1 or q_2, which means that one has at least to assume an anisotropy in the correlation lengths. In conclusion, it has to be clearly pointed out that despite the good description of the data within this rather simple model the underlying structure of the signal might in reality be more complicated.

Relation to the band structure

As discussed earlier, the magnetic response $\chi''(\mathbf{Q}, \omega)$ is related to the band structure – essentially the Fermi surface geometry – of the material. In Sr_2RuO_4, this concept has been nicely demonstrated and proven very successful thanks to the very detailed theoretical and experimental results which are available. A long-standing problem is that for the Ca-doped compounds much less information is available. This may be partly because compared to Sr_2RuO_4 these compounds have attracted somewhat less interest, and on the other hand due to the fact that they are more complicated: experimentally, techniques like quantum oscillations are not applicable due to the inherent disorder caused by the Ca/Sr mixture. Theoretically, the problem is more complex mainly due to the lower symmetry with a four times larger unit cell ($\sqrt{2}a \cdot \sqrt{2}a \cdot 2c$)[10] and, in consequence, the four times larger number of bands. Even if one had the band structure information, the calculation of χ_0 via the Lindhard function would still not be trivial because the matrix elements between different electronic states are not clear – while this is already not evident in Sr_2RuO_4, it is further complicated here by the presence of backfolded and hybridized bands.

The discussion mainly focuses on the γ-band: as argued earlier, these electronic states are probably the most relevant ones for the magnetic properties, and it seems to be this band which is most strongly affected by the structural changes induced by the Ca ions. A central issue is the question if the γ-sheet of the Fermi surface has, in $Ca_{2-x}Sr_xRuO_4$ around x=0.5, still its electronlike topology as in Sr_2RuO_4 or if it has changed to holelike. An ARPES measurement by Wang *et al.* [78] made a clear statement in favor of a holelike geometry in $Ca_{1.5}Sr_{0.5}RuO_4$ (but has also been criticized concerning the conclusion drawn from the data). Another argument in favor of a holelike topology is the rotated structure in general and the analogy to Sr_2RuO_4: there, early ARPES measurements reported erroneously a holelike γ-sheet, a fact that has been explained by surface effects [113]: on the surface of Sr_2RuO_4, the octahedra are rotated by approximately 9° [114] – similar to the Ca-doped compounds. Additionally, such a dependence between structure and Fermi

---

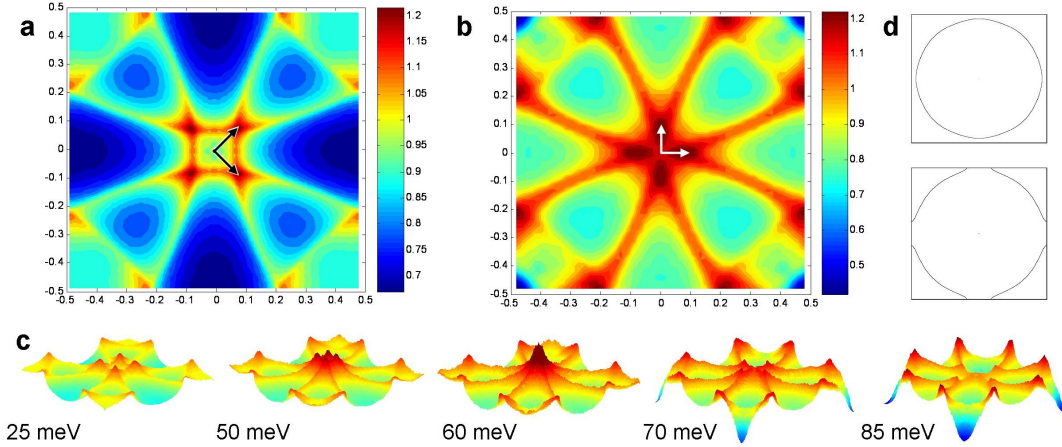[10]The body-centred cell in $I4_1/acd$ simplifies the problem, while in *Pbca* not even this applies

Figure 3.15: Lindhard function $\chi'_0(q,0)$ of the γ-band (parameters of Sr_2RuO_4) for different filling. In (a) and (b) the full q-dependence throughout the Brillouin zone is shown for the electronlike and holelike case (E_F shifted by 25 and 75 meV, respectively). In the bottom (c), the evolution is shown for a larger set of fillings; the γ-sheet for the two extreme cases is shown in (d). The energy values indicate the artificial shift of the Fermi level; with flatter bands as expected for $Ca_{1.8}Sr_{0.2}RuO_4$, the required values would be much lower.

surface topology may be connected to the discontinuous phase transition into the rotated phase in $Ca_{2-x}Sr_xRuO_4$ around x=1.5.[11]

To qualitatively understand how a Fermi surface topology change can eventually explain the observed magnetic scattering one may simply regard the effect of increasing the filling the γ-band in a rigid band structure above the van-Hove singularity. With the parameters for Sr_2RuO_4, one can then evaluate the Lindhard function for different filling of the γ-band. In order to demonstrate the influence of this effect, a calculation of the Lindhard function has been performed for different filling of the γ-band above and below the critical value. For this purpose, the parameters of Sr_2RuO_4 have been taken and the Fermi energy has been shifted by a variable amount. A representative summary of the results is shown in Figure 3.15. It is clearly seen that below the critical filling, there are nesting peaks on the diagonal of the Brillouin zone. When the filling increases, they move towards the centre, and at the critical value the system is close to a ferromagnetic (q=0) instability. Above, the central part (at small q) of

---

[11]Here one assumes that the system avoids an unfavorable state with the van-Hove singularity at the Fermi level by a phase separation into phases without and with finite rotation angle, i. e. with electron- and with holelike Fermi surface respectively. That would explain why the rotation angle does not continuously approach zero as well as the observed structural disorder effects. In this scenario, the holelike γ sheet would exist throughout the entire region of the rotated phases in the phase diagram.

Figure 3.16: Calculated Fermi surfaces of $Ca_{2-x}Sr_xRuO_4$. The picture is taken from Ko *et al.* [72] and corresponds to a structure with 12.8° rotation angle ($Ca_{1.5}Sr_{0.5}RuO_4$). Possible nesting vectors have been inserted as blue and orange dashed arrows. For detailed explanation of the figure, see text.
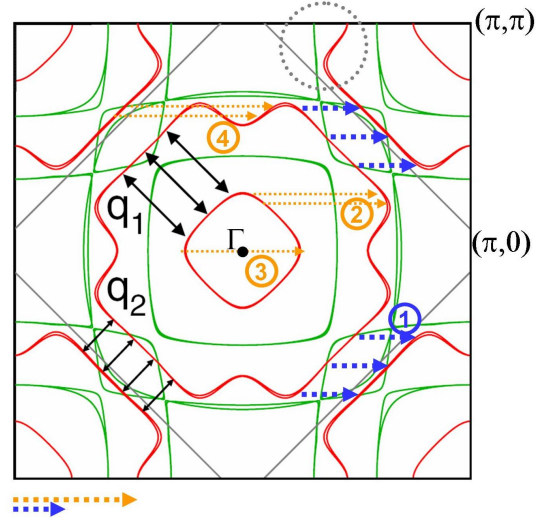
the response seems to be rotated by 45° with peaks on the *a*/b** axes. The spectral weight at these q's originates from scattering processes between regions of the Fermi surface in close vicinity to the point where it touches the zone boundary. Although there is no apparent long nested section of the Fermi surface, the very flat dispersion and the resulting high density of states at these points can account for the large contribution to $\chi(\mathbf{Q},\omega)$.

Such an effect may in principle explain the intensity which is observed at $q_1=(0.12, 0, 0)$ in $Ca_{1.8}Sr_{0.2}RuO_4$, and the same explanation has already been proposed qualitatively for $Ca_{1.38}Sr_{0.62}RuO_4$ [46], where the scans have a very similar shape. The results in Figure 3.15 also resemble those in Reference [115] for a general two-dimensional tight binding band, and the remarkable interplay of ferromagnetic and different types of incommensurate antiferromagnetic instabilities as illustrated in Figure 3.15 is obviously a rather general feature that one might expect to qualitatively persist even if some details of the band structure are different from this rather crude model. On the other hand, this part of the Fermi surface sheet is, due to the very flat dispersion of the band, very susceptible to changes of the band structure in general, and calculations of the Fermi surface, which will now be discussed, indicate that in this region the γ-sheet is so strongly altered that the nesting originates most likely from other regions of the Fermi surface.

The calculated Fermi surface. Figure 3.16 shows a calculation of the Fermi surfaces by E. Ko *et al.* It has been carried out for a structure similar to the one of $Ca_{1.5}Sr_{0.5}RuO_4$, i. e. does not explicitly contain the tilt distortion of the octahedra. Similar calculations for $Ca_{1.8}Sr_{0.2}RuO_4$ have not yet been published.

To understand the Figure, one first has to note that the Brillouin zone is set up like

in Sr_2RuO_4 and therefore contains redundant information – the actual zone here is a factor of two[12] smaller in the a/b-plane. The γ-sheet is drawn in red, and the others in green. It is remarkable that the α-sheet is essentially unchanged when compared to Sr_2RuO_4, except there is now an additional (holelike) sheet around the Γ-point which can be understood as the result of a simple backfolding. Secondly, there is now an additional small (electronlike) γ-sheet around the Γ-point.

Given the Fermi surfaces, one can attempt to identify the nested sections which may give rise to the observed magnetic scattering. Assuming the description found from the experimental data above, one has to look for the possible nesting vectors q_1=0.12 and q_2=0.27 (these two vectors are indicated in orange and blue below the figure of the Fermi surfaces). As argued in Chapter 2 (Figure 2.2), the nesting vectors should connect regions of the Fermi surface with a Fermi velocity of different sign. (The sign is not directly obvious from the figure of the Fermi surface, but for instance from the dispersion curves in the respective references; within one subset of sheets, for instance the red γ-sheets in (a), it is usually alternate, so an eventual nesting vector obviously must not cross an odd number of sheets.)

In their article [72], Ko *et al.* give two diagonal nesting vectors (q_1, q_2) within the γ-sheets which are included in their figure. This is at first sight in contrast to the experimental observation, but it appears likely that the sections connected by q_2 give in fact rise to a signal rather on the *a** axis than on the diagonal. This follows from the fact that for a vector $\sqrt{2}q_2$ along *a**, *two* nested sections contribute simultaneously and their total length is larger, as indicated by the blue dashed arrows labelled (1).

For the longer vector q_2=0.27, the identification of the nested sections is less obvious. Different possibilities (labelled (2), (3) and (4)) are indicated. Either of these, however, appears by far less favorable than the former ones, because the lengths of the nested sections are very small. Nevertheless, the sum of these individual contributions might yield a sizeable effect. In addition, the contribution may be enhanced because the dispersion of the γ band is extremely flat (as shows the LDA band structure which is not drawn here), so this region (especially for (3)) has a high weight in the Lindhard function.[13]

Corresponding calculations for $Ca_{1.8}Sr_{0.2}RuO_4$ are, as mentioned above, not yet published. Taking into account the more severe structural distortions and the lower symmetry does make them more complicated, but it is hard to estimate how large the effects on the results may be. One might expect that the main features should remain intact. This is indeed corroborated by preliminary unpublished results by D. J. Singh. The bands become hybridized, with mixed character, which leads to a reconnection of some Fermi surfaces that give the overall form a quite different appearance, but which does not significantly change the main conclusions, and some of the possible

---

[12]Only *nearly* two when correctly considering the 3D-structure of the reciprocal lattice

[13]How this large weight can compensate the absence of long nested parts of the Fermi surface, has been demonstrated above in connection with Figure 3.15, where a rather small part of the Fermi surface is responsible for the peaks in the susceptibility at q=(h,0,0), i. e. on the axes of the zone.

nesting vectors can still be identified.

Nesting of the α and β bands

The diagonal scans in Figure 3.13b prove the existence of a non-dispersive signal at q=(0.3, 0.3, 0), i. e. exactly at the same position as the prominent nesting peaks in Sr_2RuO_4. In Sr_2RuO_4 it is very well understood that these peaks originate from nesting of the α and β sheets of the Fermi surface. It therefore appears plausible that the situation in $Ca_{1.8}Sr_{0.2}RuO_4$ is essentially the same and that these peaks are still caused by the same nesting effect. Indeed the LDA Fermi surfaces in Figure 3.16 indicate that the α and β sheets are, apart doubling and backfolding, very little changed in comparison to Sr_2RuO_4.
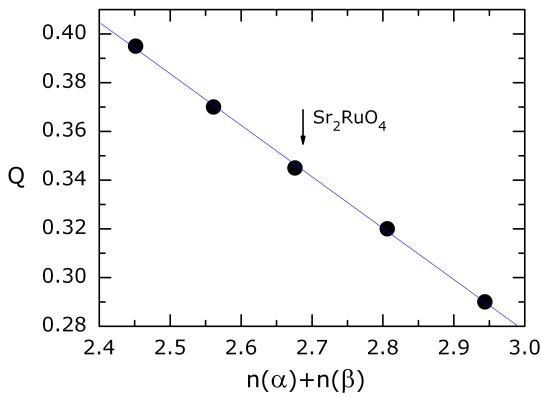
Figure 3.17: Position of the diagonal nesting peak (Q,Q,0) in units of $\frac{2\pi}{a}$ for different filling of the α and β bands (number of electrons), calculated for the band structure parameters of Sr_2RuO_4.

From the position of the nesting peak it is possible to estimate the filling of the band, because a larger number of electrons makes the β-sheet grow and the α-sheet shrink and thus the nesting vector shorter. Taking the band structure parameters of Sr_2RuO_4, this estimation is straightforward to perform by simply calculating $\chi''(\mathbf{Q}, \omega)$ along the diagonal for different band filling.

Within a significant range, the nesting condition remains intact and is simply shifted. The results of these calculations are summarized in Figure 3.17, which also proves that this relation is essentially linear in the regarded range. The absolute values have little significance and do not exactly match the experiments, but with the slope $\frac{dQ}{dn} = -0.211$ one obtains that a peak shift of 0.01 (in units of $\frac{2\pi}{a}$) corresponds to a shift in occupation number by 0.047 electrons.

In Sr_2RuO_4, the nesting peak is observed at Q=(0.3,0.3,0) [111]. The small peak on the left side of the scans in Figure 3.13b is at H=0.70, though with an uncertainty of about 0.015, i. e. exactly at an equivalent position. Assuming that the band structure of α and β has not significantly changed, one may conclude that in $Ca_{1.8}Sr_{0.2}RuO_4$ there is practically no shift of electrons (less than 0.1) between the α/β and the γ subsystem of bands in comparison with Sr_2RuO_4.

Relation to macroscopic measurement methods

Spin fluctuations manifest themselves in a number of properties that can be measured by other experimental methods. Apart the magnetic susceptibility, this is for instance the specific heat, on which there is detailed information for $Ca_{1.8}Sr_{0.2}RuO_4$.

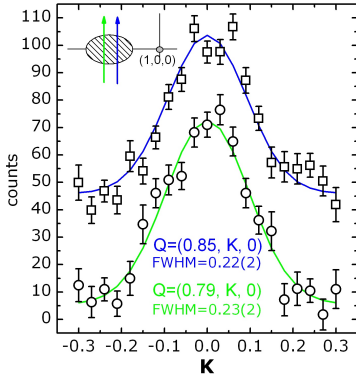**Figure 3.18:** Scans along b* across the broad maximum near (0.8,0,0) at E=2.5 meV and T=1.5 K.

Let us first make a rough estimate of the spin fluctuation contribution to the linear coefficient of the specific heat, as it has been discussed in Chapter 2.2.4. Using the expression (2.38), one needs the inverse spin fluctuation energy throughout the Brillouin zone, or for a simpler approximation the characteristic frequency Γ_0 at q=q_0 and the half widths in q-space. Here, for the simple estimate, only the broad incommensurate fluctuations are taken into account: according to the findings above, the ferromagnetic fluctuations are negligible, and the α/β nesting peak is relatively sharp and has a higher energy, and is therefore negligible, too.

From the mapping at 2.5 meV, which is approximately the characteristic energy $\hbar\Gamma_0$, one can easily extract the q-widths. For simplicity, the broad feature around $(1,0,0) \pm (0,.2,0)$ and equivalent positions is taken as elliptic – the longitudinal width being slightly larger than the transverse one which reflects the fact that the broad maximum seems to contain at least two contributions at q_1 and q_2 as discussed above. For the transverse width, one obtains 0.23 (in reciprocal lattice units), see Figure 3.18, and for the longitudinal one 0.27. The resolution of the spectrometer is approximately 0.03 (longitudinal) and 0.05 (transverse) and leads to a correction only within the error bars of the widths. When then taking Γ to be constant in an elliptic cylinder with these diameters and evaluate (2.38) in this way, one obtains

$$\gamma_{sf} \approx 160 \frac{mJ}{mol \cdot K^2} \tag{3.1}$$

This is in good agreement – better than can be expected from the accuracy of the method – with the real value of $175\frac{mJ}{mol \cdot K^2}$ from the direct measurement [37, 48].

The comparison with measurements of the macroscopic magnetic susceptibility will be given in detail in the following section.

3.4.2 Temperature dependence

A number of observations indicate that the low temperature state of $Ca_{1.8}Sr_{0.2}RuO_4$ behaves in a very unusual way and different from what an extrapolation from higher temperatures would lead to expect. Examples are a structural anomaly which sets in below about 30 K [53, 54], a suppression of the magnetic susceptibility [36], an anomalous T-dependence of the resistivity [44] and a suppressed specific heat coefficient [37, 48]. It is therefore an interesting question how the magnetic correlations change as function of temperature, because most of these properties are most likely

Figure 3.19: (a) Constant energy scans at different temperatures converted to absolute susceptibility units. (b) Imaginary part of the susceptibility χ'' at Q_{FM} for 0.4 and 1 meV energy transfer. The 0.4 meV curve is shifted by 400 $\frac{\mu_B^2}{eV}$. (c) Real part of the susceptibility obtained by Kramers-Kronig-like analysis together with the macroscopic susceptibility taken from reference [36].
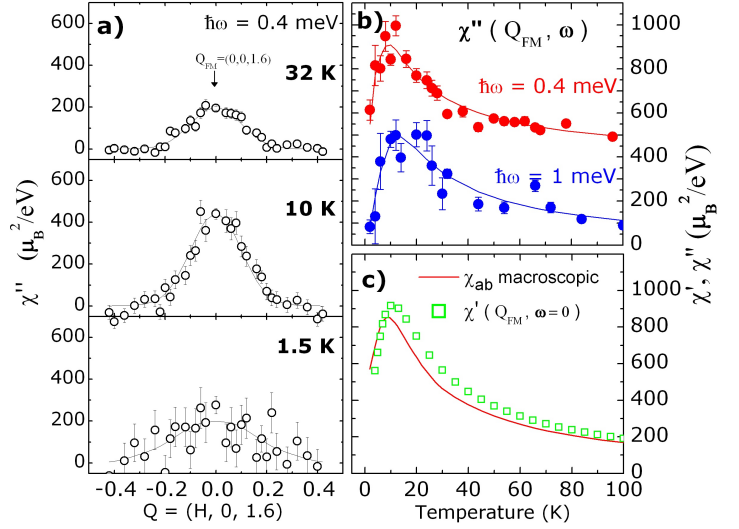
coupled to the magnetism. In particular, the behavior of the susceptibility must be reflected in the magnetic neutron scattering data.

From the scans at 1.5 and 10 K in Figure 3.14 it is already evident that the magnetic response changes significantly as function of temperature, both in intensity – by far more than the Bose factor could account for – and in shape. Two aspects of the temperature effect are interesting to be discussed in the following: firstly, the temperature dependence of the response around Q_{FM}, i. e. at (1,0,0) or (0,0,L). This can be related to the macroscopic magnetization (or susceptibility) of the crystal. Secondly, the distribution of spectral weight throughout Q,ω-space changes, as seen for instance in the shape of the constant energy scans.

Quasi-ferromagnetic signal as function of Temperature

In Figure 3.14 it has been shown clearly that the signal around the ferromagnetic position (centre of the scans) is strongly suppressed at 1.5 K. The incommensurate signal, which has a higher characteristic energy and is clearly visible only at 2 meV, does not significantly change between 1.5 and 10 K. At 10 K and above, there is a strong signal around Q_{FM}, which is attributed to a paramagnon. At 10 K, it has a high amplitude and the extremely low characteristic energy of about 0.4 meV. At 1.5 K, this paramagnon signal is strongly suppressed. There is weak indication in the energy scan (Fig. 3.14c) that it is shifted to even lower energies, but statistics is not very significant – the corresponding Q-scan does rather not support this.

The signal has been extensively studied as function of temperature. In Figure 3.19b the intensity as function of temperature is shown for the two energy transfers 0.4 and 1 meV after calibration of the intensity to absolute susceptibility units. Both data sets

exhibit a very pronounced maximum near 10 K. The decrease towards high temperatures can be regarded as a rather conventional behavior (like the Curie-Weiss law), but the steep decrease below 10 K is highly unusual. This suppression is obviously related to the other anomalies mentioned above, i. e. probably a consequence of the redistribution of the electronic occupation of the different orbitals [53] associated with the structural anomaly.

From the values of the imaginary part of χ at different energies, one can in principle determine the real part of χ. That is particularly interesting in this case, because the susceptibility at Q=0 (here Q_{FM} is identified with Q=0) is the quantity which is measured by macroscopic methods. From an energy scan, this information can simply be extracted – the maximum of the single relaxor fit (at $\omega = \Gamma$) is half the value of χ' at $\omega = 0$ (as can be simply proven by using the Kramers-Kronig relation). For the energy scans in Figure 3.14c this procedure yields $\chi = 534 \pm 18 \frac{\mu_B^2}{eV}$ at T=32 K and $960 \pm 40 \frac{\mu_B^2}{eV}$ at 10 K. Both values are in reasonable agreement with the macroscopic susceptibility ([36] and Fig. 3.19). At 1.5 K, statistics are low and the fit quite unstable, so the result (though only slightly too low) probably not very reliable.

For the other temperatures, no full energy scans are available, but only the data at 0.4 and 1 meV in Figure 3.19. As it has been discussed in Section 2.2.3 (Equations (2.33) and (2.34)), it is possible to extract the two parameters Γ and $\chi'(0)$ from the values of χ'' at two energies. In order to give stable and reasonable results, this procedure needs input values without too much statistical error, so a smooth line has been fitted to describe the temperature dependence in Figure 3.19b. With this line, the analysis can be well performed [14]. The so obtained Γ values are around 0.7 meV in the range above 20 K and lower for T<20 K, which appears reasonable with respect to the energy scans. More interesting are the results for $\chi(T)$: they are shown in Figure 3.19c together with the susceptibility obtained from the macroscopic measurement (taken from Ref. [36]; average of the in-plane directions).

This agreement is not perfect, but quite remarkable in view of the uncertainties arising from the different steps of the data treatment – the statistical error bars, the intricate calibration process into absolute units, and the quite rough averaging over the different anisotropies of the system would normally lead to expect larger deviations. The agreement demonstrates that (as it must be the case) the macroscopic magnetic properties are well understood in terms of the (microscopic) magnetic correlations, as observed in the measured fluctuation spectrum.

Moreover, the comparison to the susceptibility is one of the rare possibilities for a quantitative cross-check of the inelastic neutron scattering data. Therefore, as a sec-

---

[14]The fluctuations in the plane are expected to be anisotropic, so a *single "single relaxor"* may not be sufficient to describe their overlap. As argued in [116], the sum $\chi''(0.4\text{meV}) + \chi''(1\text{meV})$ may be a good approximation, tentatively accounting for two different characteristic energies. However, as the results at these two energies are very similar and as long as Γ lies between these values (i. e. the relaxor function is quite flat in this region) there is only a very little difference between the results of this method and the previous one.

Figure 3.20:
Constant en-
ergy scans in
$Ca_{1.8}Sr_{0.2}RuO_4$,
transverse through
(1,0,0) at different
energy transfers
and temperatures
(divided by the
Bose factor).
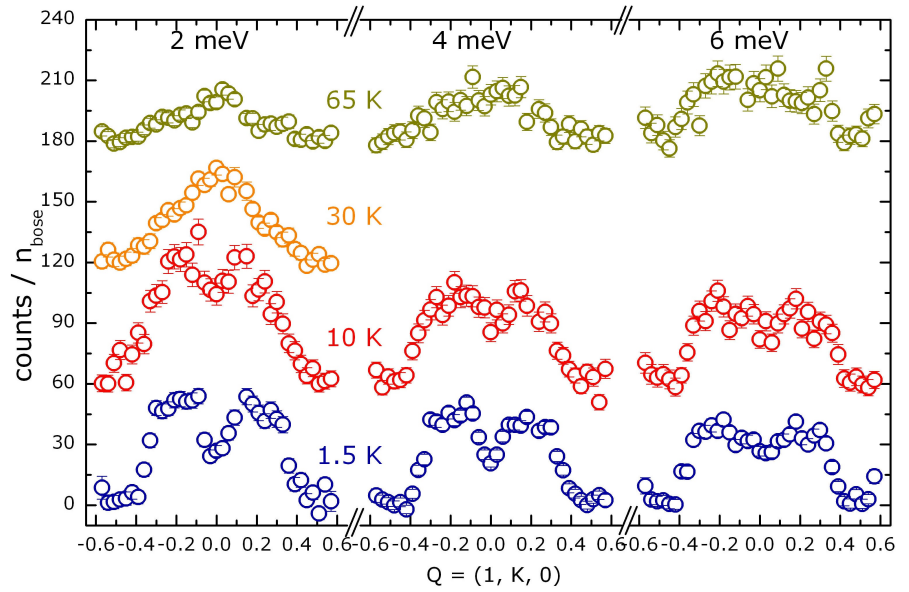
ond very noteworthy conclusion, the quantitative agreement proves that the signals have been correctly interpreted and that the experiments have captured all the relevant effects (and, for instance, not missed an important signal that might have been present only in a different region of q-ω-space).

Overall evolution of the signal at higher temperatures

The fluctuations at Q_{FM} have a low characteristic frequency, and after the analysis of the low-energy part of the spectrum that has just been given, let us now also briefly regard the temperature dependence of the higher energy part, which is more dominated by the incommensurate signals. Figure 3.20 summarizes the data that has been collected at higher temperatures (10, 30, 65 K) together with the corresponding low-temperature results which have already been discussed in the preceding sections. At the higher temperatures, the influence of the Bose factor gradually becomes important, and the data shown is therefore the original count rate divided by the Bose factor (a quantity essentially proportional to $\chi''(\mathbf{Q}, \omega)$, apart resolution effects).

In general, the signal has the tendency to decrease towards high temperature as is the usual case for magnetic signals; this confirms the frequently made observation in the Ruthenates that over a large temperature range this decrease approximately compensates the Bose factor, so that the measured count rate remains similar. There are, nevertheless, more changes than this trivial one. The maximum at 10 K is still visible in this energy range, though not so pronounced as at the lower energies. In general, one might expect the most perceptible effects in the range of the characteristic energy of the signal; indeed at 2 meV the changes as function of temperature seem to be most dramatic. To summarize the temperature effect one may state that
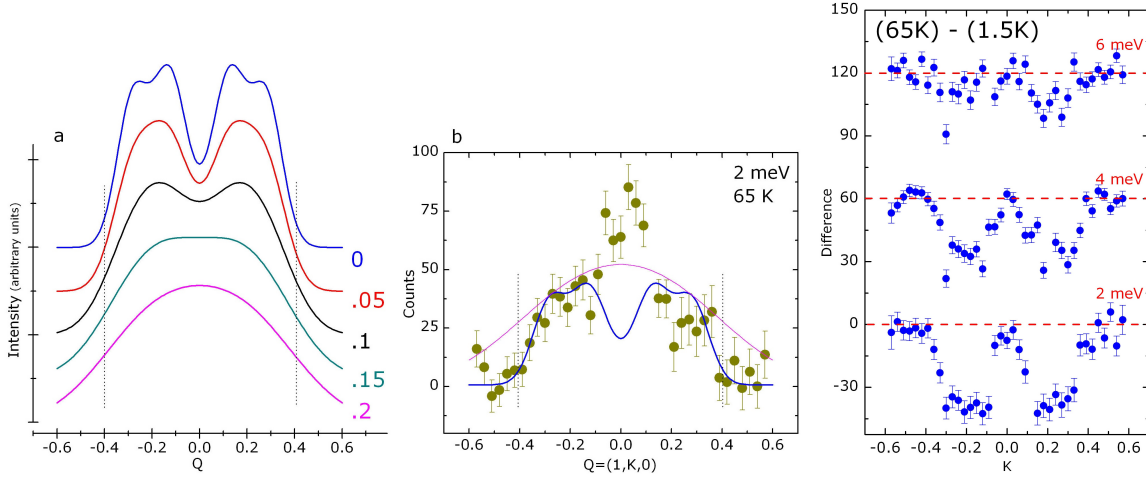
Figure 3.21: Considerations on the description of the high temperature data. Left: the effect of a q-broadening of the scan. Starting with the fit function used to describe the 2 meV data, a Gaussian broadening of varying strength has been applied. The numbers given are the full width of the Gaussian with which the original function has been convoluted. The vertical lines at ± 0.4 serve only as orientation. Middle: the 2 meV scan at T=65 K. The lines are the two extreme cases (0 and 0.2) from the left. Right: Differences $\chi''(T=65K) - \chi''(T=1.5K)$ for three different energy transfers (for original data, see Figure 3.20). The red lines are the respective zero lines.

the minimum in the centre is gradually filled and turns into a maximum at high temperature. This is most clearly seen at 2 meV, but is also the case at 4 and 6 meV. It should further be mentioned that even at the elevated temperatures acoustic phonon scattering can be excluded[15] to have a visible impact on the data shown.

As a rule of thumb deduced from the results on $Ca_{1.38}Sr_{0.62}RuO_4$ [110], the signals change their shape when $k_B T$ exceeds their energy. As far as one can decide on the basis of these data, this rule seems to apply also to $Ca_{1.8}Sr_{0.2}RuO_4$. Later in this chapter, in the context of the results on $Ca_{1.38}Sr_{0.62}RuO_4$ this effect is discussed in more detail and justified by a calculation that takes account of the temperature dependencies of the susceptibilities and characteristic energies.

Another statement arising from the data in $Ca_{1.38}Sr_{0.62}RuO_4$ has been that the influence of high temperature is essentially a broadening and that the constant energy scans can simply be described by broadening incommensurate Gaussian-like components. Bearing in mind that the system is governed by the competition of different (ferromagnetic and incommensurate) magnetic instabilities, another – conceptually different – approach is to take into account an additional component appearing at

---

[15]... by regarding the intensity of the acoustic phonon at (2,0,0) and using the ratio of the nuclear structure factors, Q^2 and the Bose factor.

high temperature. Then, the idea would be to use no significant broadening[16], but an additional ferromagnetic component to account for the temperature effect.

When comparing these to models, on has to bear in mind that this latter one introduces additional degrees of freedom, so makes it easier to produce convincing results. Nevertheless, the data support the second scenario. In Figure 3.21a, the effect of a broadening in Q is illustrated for different values of the gaussian broadening parameter and for a realistic function (the fit line used to describe the 2 meV data). The effect is as expected concerning the quite efficient filling of the central minimum. To produce a maximum, on the other hand, very extreme broadening is necessary.

For weak and intermediate broadening levels, the difference compared to adding a small ferromagnetic component of suitable width is rather small. A clear distinction is possible in the scan at 2 meV and 65 K, shown in Figure 3.21b. It is obvious that it cannot be described by the broadened version of the response at low temperature (pink line), but resembles rather the original 2 K-shape (blue line) with a strong additional contribution around K=0. This conclusion is corroborated by the differences of the high and low temperature signals, $\chi''(\text{T=65K}) - \chi''(\text{T=1.5K})$ (Figure 3.21). At 2 and 4 meV, where the error bars are small enough, one can state that even in shape the difference resembles much the low temperature signal. This results from a different temperature dependence of the incommensurate and the ferromagnetic part of the signal. $\chi'_{FM}(T)$ is known from the preceding section, but the shape of the scans is of course also determined by $\Gamma(T)$.

The conclusion from these rather qualitative considerations is that the ferromagnetic and incommensurate parts of the response vary independently and have to be treated separately. A more quantitative model is discussed later for Ca$_{1.38}$Sr$_{0.62}$RuO$_4$.

3.4.3 The dependence on the magnetic field

Response at different magnetic fields

The discussion in the preceding sections has provided a detailed characterization of the magnetic correlations in Ca$_{1.8}$Sr$_{0.2}$RuO$_4$ and demonstrated how the interplay of ferromagnetic and antiferromagnetic correlations is related to the temperature dependent behavior of the system, especially the anomalous state that it enters at low temperature when the susceptibility is strongly suppressed. The metamagnetic transition drives the system into a state with very high magnetization, so it is natural to expect that the magnetic field has a profound effect on the magnetic fluctuation spec-

---

[16]To a certain extent, high temperature will of course broaden the spectrum. Even in RPA – be it applicable here or not – the broadening is already included in the Lindhard function; this yields a q-broadening of the order $\frac{k_B T}{v_F}$ (where v_F is the Fermi velocity). For "typical" v_F's (like for instance in Sr$_2$RuO$_4$) this is only a tiny effect on the scales regarded here. In Ca$_{1.8}$Sr$_{0.2}$RuO$_4$, one can assume a (perhaps much) smaller v_F, but it is not known if it is small enough to have a sizeable effect.
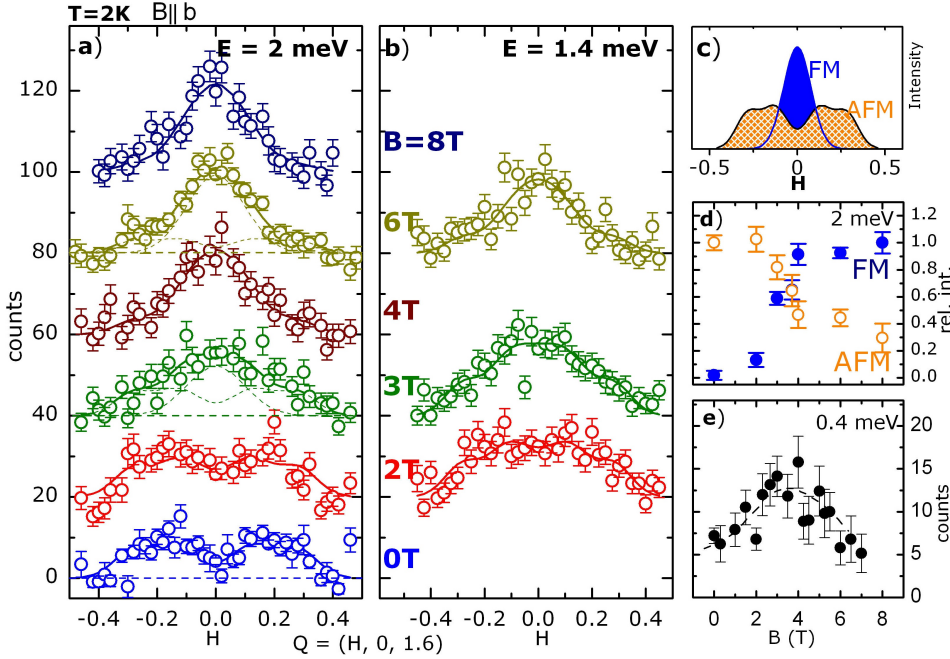
Figure 3.22: Magnetic scattering in $Ca_{1.8}Sr_{0.2}RuO_4$ at different magnetic fields. All data are collected with the field along the b-axis and at T≃2 K. (a) and (b): Constant energy scans at 2 and 1.4 meV as function of field. Lines are fits to a simple model sketched in (c) consisting of a Gaussian ferromagnetic component and an antiferromagnetic component with incommensurate peaks assumed to have the same shape as at B=0 (only scale factor fitted). At selected scans, these components are shown separately as dashed lines. The relative intensities (relative to their values at 0 resp. 8 T) are shown in (d). (e) contains the very low energy part (0.4 meV) as function of magnetic field.

trum. These effects are best observed at low temperature[17], and all data have been collected at 1.5 or 2 K.

The field effect on the magnetic fluctuations is best visible in the 2 meV constant energy scan which is presented in Figure 3.22a at a series of different magnetic fields. Starting with the already extensively discussed incommensurate signals without magnetic field, one observes the appearance of a central peak that entirely dominates the scan at the highest field, B=10 T. A very similar effect is observed in the scans with 1.4 meV energy transfer, although measured only at a smaller set of different fields. To describe the data, a simple phenomenological model has been assumed which consists of the incommensurate fluctuations and a ferromagnetic response, as sketched in Figure 3.22c. It can again, like in case of high temperature, be excluded that the observed effect is simply due to a broadening of the incommensurate response. How

---

[17]Only at very low temperature one might expect to cross the first order phase transition or, in the crossover case, to be sufficiently close to the critical or quantum critical end point.

Figure 3.23: Energy dependence of the magnetic scattering under field. In (a), a series of constant energy scans at B=6 T is shown. Energy scans at the central point Q=(0,0,1.6) are shown in (b) for different magnetic fields (lines are guide to the eye).
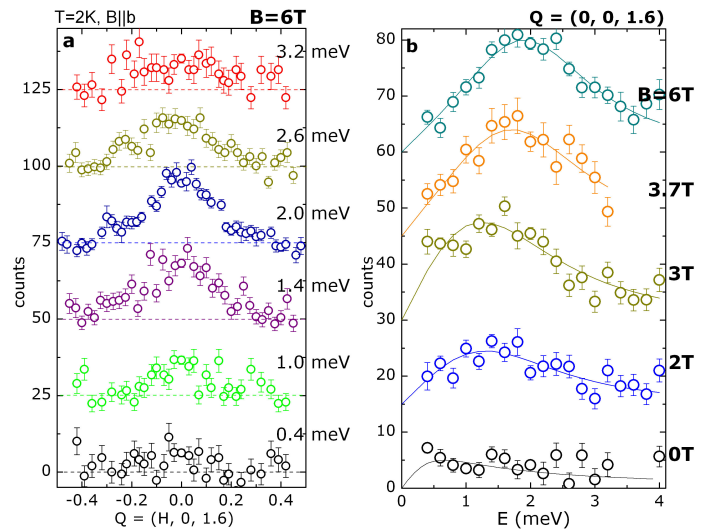
the incommensurate part changes at high fields, though, can not be resolved because of its decreasing intensity and the heavy overlap with the ferromagnetic peak. It has therefore been assumed that its shape does not change as function of magnetic field. In this model used to fit the data, it is essentially the intensity of these two contributions that changes as function of field. These intensities, as obtained by the fit and normalized to their values at 0 resp. 8 T, are displayed in Figure 3.22d. The important changes take place between 2 and 4 T. The metamagnetic transition for this field orientation is at approximately 3.5 T [52]. This strongly supports the conclusion that the observed changes in the fluctuation spectrum are indeed the manifestation of the metamagnetic transition.

The series of scans at different energy transfers in Figure 3.23 illustrates the energy dependence of this newly appeared ferromagnetic signal. Its maximum is obviously at about 2 meV, while there is only very little intensity at low energies, which may probably be interpreted as the indication of a gap in the excitation spectrum. Towards higher energy, the weak statistics and some ambiguity in the definition of the background make it difficult to decide, but there is certain indication that the decrease of intensity is accompanied by a spread over a larger Q-region (broadening of the signal). The energy dependence at Q$_{FM}$ is summarized in part (b) of the Figure, together with corresponding energy scans at other values of the magnetic field. In analogy to the treatment without magnetic field, it has again been tried to describe the energy dependence with a single relaxor function, but it turned out that such an attempt works reasonably well only until 2 T. At the higher fields, most clearly at 6 T, there is relatively little intensity at low energy, a well defined maximum and again a relatively rapid decrease.

For excitations that involve a spin flip, one expects an energy gap, that is determined by the effective field. For B=6 T, the energy $g\mu_B B$ is ∼0.7 meV. About the anisotropy fields which may cause the effective field to be not equal to the external field, however, there is not much known. The existence of a gap may partly explain the shift of the maxima in the energy scan towards higher energies and the reduction at low energies. It is not, on the other hand, clear that a true gap is expected, since non-spin-flip excitations ("longitudinal susceptibility") may significantly contribute to the observed signal. This aspect is discussed in more detail in the following section.

Enhancement of fluctuations at the transition

When the system passes, by variation of the magnetic field, through or close to a critical point in the phase diagram, it is expected that fluctuations are strongly enhanced. Regarding the energy scans (Figure 3.23b), it is indeed the case that at fields near 3 T, the intensity at small energy transfers is significantly higher than at lower magnetic fields. At higher fields, 3.7 T and 6 T, the amplitude remains similar, but spectral weight is shifted to higher energies. These observations point towards a critical enhancement of fluctuations at the transition. The maximum near 3 T in the field scan at the very lowest possible energy transfer of 0.4 meV (Figure 3.22e) supports this statement. However, this enhancement appears only weak, and is obviously far from a divergence as it would be expected at a truly critical point. One may therefore ask if the neutron experiment has really captured the full magnetic response, or if something has been missed – for instance a signal in the energy range below 0.4 meV, that could not be accessed in the experiment.

To address this issue, one has to quantitatively analyze the magnetic response in the inelastic neutron experiment. From the energy scans, one can extract the real part of the susceptibility by the Kramers-Kronig relation

$$\chi'(Q)|_{\omega=0} = \frac{1}{\pi} \int_{-\infty}^{\infty} \frac{\chi''(Q,\tilde{\omega})}{\tilde{\omega}} d\tilde{\omega} = \frac{2}{\pi} \int_0^{\infty} \frac{\chi''(Q,\tilde{\omega})}{\tilde{\omega}} d\tilde{\omega} \qquad (3.2)$$

To perform this analysis, a smooth line (see Figure 3.23b) has been fitted to describe the data, and with this line the integration (3.2) has been performed. With the scale factor discussed earlier, the result is available in absolute units.

A severe problem for the comparison is that the susceptibility or magnetization data is not available for this particular orientation of the magnetic field ([010] in the tetragonal notation), and the critical field depends strongly on the orientation. For B parallel to the orthorhombic a-axis, the transition is at approximately 2.5 T, but 6.5 T for the orthorhombic b-axis [52]. For the field along the orthorhombic [110] direction, which corresponds to [010] in the notation used here, the critical field is approximately 3.5 T. As a simple approximation for this case, the magnetization curve for the orthorhombic a-axis [37] is taken, but with the field axis scaled to account for
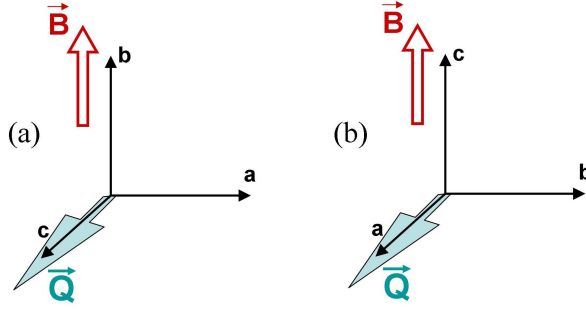
Figure 3.24: Sketch of the two different orientations of the crystal axes and the field used in the measurements. The measured signal contains only contributions from the components of $\chi''(\mathbf{Q}, \omega)$ perpendicular to Q. Among those, there are non-spin-flip (longitudinal component / parallel to the field direction) and spin-flip (perpendicular to the field direction) excitations. Due to twinning, the a- and b-axis cannot be distinguished experimentally.

the right critical field (multiplied by a factor 1.32). This procedure not only shifts the critical field, but also broadens the transition. In consequence, also the susceptibilities M/B and ∂M/∂B are reduced, which is an evident critical point for the quantitative comparison. This seems to be justified by the fact that the signature of the transition in the magnetoresistivity curves [52] is also broader and can be approximated by scaling the [100]-shape. Twinning should not have an effect along this direction, but sample inhomogeneities do, and may be worse in the very large crystal than in small single-domain pieces used for the magnetization measurements, leading to further broadening. For these reasons, both the slope of the magnetization curve and the value of the transition field should be reasonably well estimated and permit a rough quantitative analysis.

For the comparison with the neutron data, one has to take account of the different components of the susceptibility that are superimposed in the observed count rates (for a sketch, see Figure 3.24). Here, because the scattering vector is (0,0,L), the components χ''_{aa} and χ''_{bb} contribute to the cross section, and χ''_{aa} is transverse to the field and χ''_{bb} is longitudinal. They are therefore not equal, and since it is impossible to separate them, one only knows their sum. In the situation when the magnetization M is not proportional to the field H, the relations for the longitudinal and the transverse susceptibilities are:

$$\chi^{\parallel} = \frac{\partial M}{\partial H}$$
$$\chi^{\perp} = \frac{M}{H} \tag{3.3}$$

For a classical magnetic moment, this relation is directly evident. An intuitive justification, though not a strict proof, of this difference within the RPA framework and quantized spins (up/down) may be found in Figure 3.25.

An implication of (3.3) is that at a metamagnetic transition mainly $\chi^{\parallel}$ is expected to become large – the more, the sharper the transition is. On the other hand, $\frac{M}{H}$ is also

enhanced at the transition, but remains finite regardless how sharp the transition is.

In Figure 3.26, the two susceptibility components, which are derived from the magnetization curve, are shown, and their sum is compared with $\chi'(Q_{FM}, \omega = 0)$, which has been obtained by the Kramers-Kronig analysis of the energy scans (Figure 3.23b). The combination of higher intensity and shifted characteristic energy – both seemingly not a very large effect in the energy scans – accounts for the significant variation of the calculated $\chi'(Q_{FM}, \omega = 0)$ as function of the magnetic field and reflect the metamagnetic transition. The so obtained values follow the shape of the susceptibility curves. It is thus to be concluded that the ferromagnetic fluctuations are important in driving the metamagnetic transition. However, the conversion into absolute units with the scale factor used earlier yields a quantitative disagreement: they are approximately 30-40% below the susceptibility curve.

In view of the assumptions made before, it is not easy to estimate how accurate the quantitative comparison is. The rough qualitative agreement of the peak shape would support the argument that the scale of the magnetization or the neutron data is not exactly calibrated. On the other hand, regarding that the scaling of the field axis already tends to reduce the susceptibility values obtained from the magnetization curve and thus makes the disagreement smaller, it appears likely that the deviation is significant. This could mean that not all the magnetic fluctuations were captured by the neutron experiment. There is no indication in the data where additional spectral weight could originate from, but as any additional weight at low energy gives a very large contribution, it appears likely that the low-energy part of the spectrum has been (probably only slightly) underestimated.
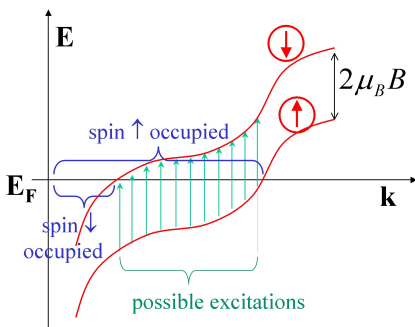

Figure 3.25: Possible spin-flip excitations within a single band. The magnetic field splits the energies ϵ_k for spin-up and spin-down electrons by $2\mu_B B$.

This has to be considered when calculating the transverse susceptibility $\chi^\perp$. Different parts of k-space are occupied for the two spin states. Spin-flip excitations with q=0 can take place only at those k for which one spin state is occupied and the other is empty. The number of such excitations is thus the difference of spin-up and spin-down electrons, or in other words, proportional to the magnetization M. These excitations have finite energy $\hbar\omega = 2\mu_B B$, and the Lindhard function therefore has the imaginary part of the form $M \cdot \delta(\hbar\omega - 2\mu_B B)$. The real part, by (3.2), then has the form $\frac{M}{H}$. The longitudinal susceptibility, in contrast, consists of the non-spin-flip excitations. The Lindhard function (2.13) for q=0 and ω=0 is real and reduces to the density of states at the Fermi level (sum of spin up and down, if the field is not zero), which is proportional to the number of electrons Δn that can be additionally polarized when the external field changes by a small amount ΔH. Therefore, $\chi^\parallel$ corresponds to the derivative of M.
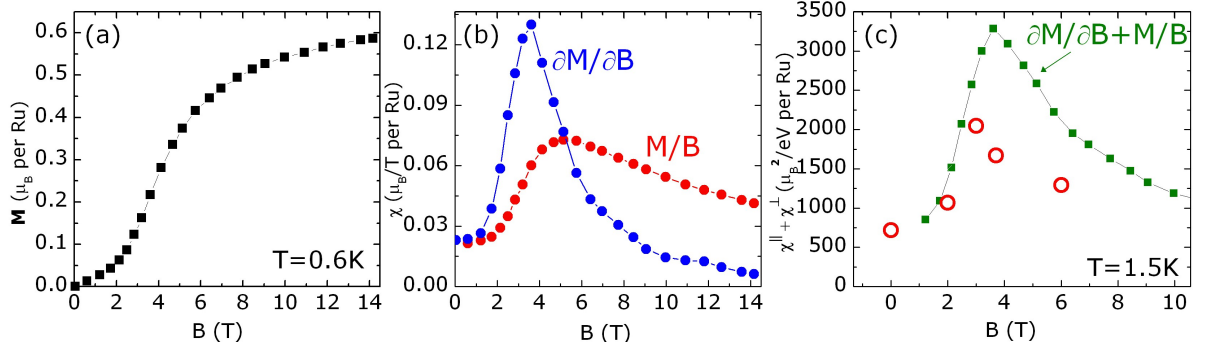
Figure 3.26: Field dependence of the susceptibilities in $Ca_{1.8}Sr_{0.2}RuO_4$. (a) Magnetization as function of field: data taken from [37] with the B-axis scaled by a factor 1.32 in order to approximate the [010] orientation used here (discussion see text). (b) Transverse and longitudinal susceptibilities derived from the magnetization curve. (c) Sum of the two susceptibility curves and $\chi'(Q_{FM}, \omega = 0)$ as derived from the Kramers-Kronig analysis of the energy scans.

3.4.4 Above the metamagnetic transition

Excitations in the high-field state

So far it has been been stated that the incommensurate antiferromagnetic fluctuations get replaced by a prominent signal of more ferromagnetic character upon application of a magnetic field. It is an interesting question, though, what is the character of this signal. In order to examine its q-dependence, two experiments have been performed in the high field state with the magnetic field aligned along the c-axis at B=10 T, first on the thermal neutron spectrometer IN22, and later, in order to access the lower energy region, on Panda. The field of the metamagnetic transition is about 6 T for B∥c. This configuration turned out less favorable in view of the intensity, but offers better resolution for studying the q-dependence; these measurements are difficult and time-demanding.

Figure 3.27 gives a summary of the data that has been collected at B=10 T in these two experiments – shown is always the same scan at different energy transfers which runs along the transverse direction across the 2D magnetic zone centre (1,0,0) and passes essentially through the whole Brillouin zone. In part (c) and (d), the field effect is once more summarized and proves, as already discussed for the other configuration, the disappearance of the antiferromagnetic and the simultaneous appearance of a ferromagnetic part as function of field. The most important conclusion from the data is that the central maximum at high field can impossibly be described by a broad and structureless peak, but requires a description with two maxima at symmetric positions on the positive and negative side of the centre. This splitting is resolvable at about
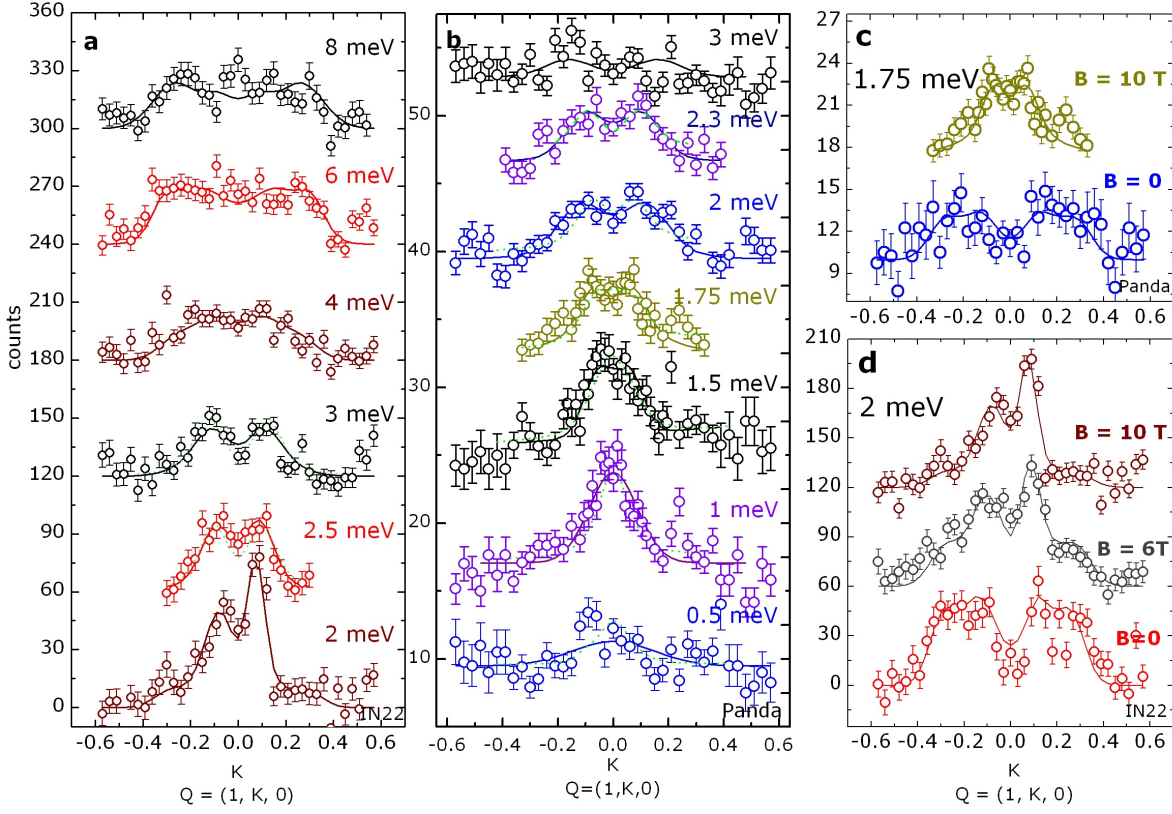
Figure 3.27: Constant energy scans at B=10 T on the thermal (a) and cold (b) spectrometer. The temperature is ~1.5 K and the field is along the c-axis. The count rates are normalized to monitor and correspond to approximately 4 minutes. The solid lines are fits with Gaussian functions at symmetric positions, and the green dotted lines using the global model for the magnon described in the text. In (c) and (d) the field effect on one of the scans is shown for each of the two setups.

1.75 meV and becomes larger at higher energies.[18] This led to the conclusion that the ferromagnetic excitation that appears above the metamagnetic transition has a dispersive character and strongly resembles a magnon in a conventional ferromagnet.

The properties of this excitation, as they can be deduced from the experimental data, are:

---

[18]At 2 meV, there is a discrepancy between the scans on IN22 and on Panda. The main reason is probably the focalization effect which is more pronounced on IN22 with k_f=2.662 Å and which is indeed expected on the right side. It is also known that there is a spurious contamination at K=0.12 which may deteriorate the scan (one point), but which can definitely be excluded to produce the observed peak (as is clear for instance from the comparison of the different field in Figure 3.27d). Note also that the focalization effect due to the slope of the resolution ellipsoid can further be enhanced by picking up part of the higher intensity at energies below 2 meV, see Figure 3.28c,d.

- It is gapped at low energies. At 0.5 meV, there is very little intensity remaining. The energy scan in Figure 3.28 clearly confirms the gap, although there is still nonzero intensity far below the maximum.

- The maxima in the constant energy scans disperse outwards. When fitting the position with a simple function consisting of two peaks at symmetric positions, one obtains Figure 3.28b. Using a quadratic function, one obtains a reasonable description of the dispersion.

- The peaks are relatively broad and in some cases not very well separated. The widths are larger than the intrinsic experimental resolution.

- The width increases with energy. At 4 meV, the two peaks are no more separable, and at 6 and 8 meV the shape of the scans closely resembles that at B=0 and can be described with the same function that has been used to fit the data without magnetic field.

- There is some weak indication that even at lower energies a small fraction of the incommensurate part seems to persist. There, it is not clearly separable, but rather some very weak intensity near K=0.2-0.3 before the central peaks reach the background level. Note that a similar conclusion had also been drawn from the data in Figure 3.22. This contribution is included in the fits as a small correction to the background and neglected when studying the dispersive mode.

For a magnon in a ferromagnet and with an external magnetic field, the general dispersion relation is, for small q:

$$\hbar\omega(q) = g\mu_B B + D \cdot q^2, \tag{3.4}$$

i. e. a quadratic dispersion with an energy gap at the zone centre. In view of the negligible c-axis correlation, (1,0,0) is again assumed as a magnetic zone centre. In the absence of broadening due to finite lifetime, the energy spectrum of the magnon is a delta function.

Modelling the spin wave

For a more quantitative description of this excitation, let us start with the quadratic dispersion relation (3.4). The approximate validity of this relation is already confirmed by the simple analysis of the peak positions. The first aspect one may discuss is the value of the gap. Since there may be anisotropy terms (arising from spin-orbit coupling etc.), the B in equation (3.4) is to be considered as an effective field containing the anisotropy and the external fields. With an external field of B_{ext}=10 T, the value of $g\mu_B B_{ext}$ is 1.15 meV, which is nearly exactly the maximum of the energy scan (Figure 3.28a). The energy scan shows a clear indication of the spin gap, but the decrease
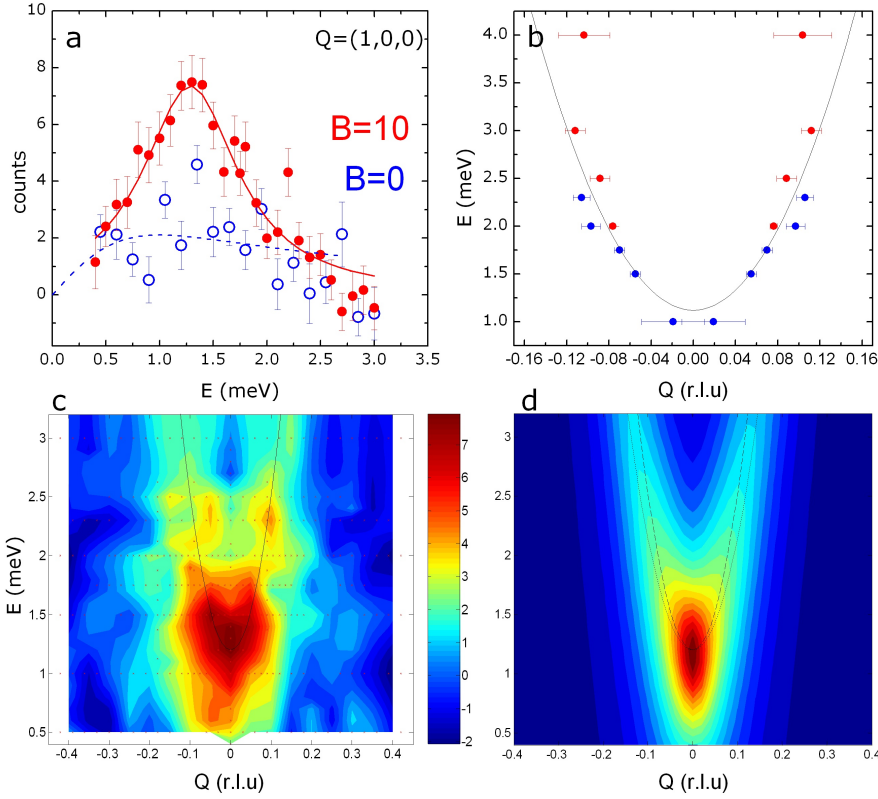
Figure 3.28: (a) Energy scan on (1,0,0) at B=0 and 10 T. Background has been subtracted. The line at 10 T is a fit to a lorentzian peak function. (b): The positions of the maxima in the constant energy scans (Figure 3.27) together with a fit to a quadratic dispersion gapped by 1.15 meV. Red points are from the IN22-measurement, blue points from Panda. (c): contour plot of the measured intensity in Q-ω-space; a smooth surface has been fitted to the data points the positions of which are indicated by the tiny red crosses. The line is the one obtained in (b). (d): Calculated intensity of the magnon cone, including the lorentzian energy broadening described in the text and convoluted with the resolution function.

towards low energy is by far not as sharp as expected for a well-defined gap, even taking into account the energy resolution of the spectrometer ($\sim$ 0.2 meV FWHM). Instead, the energy scan is very well fitted by a Lorentzian function. In general, this appears reasonable, as a lorentzian broadening is often used to describe the energy widths of excitation branches like phonons or magnons.

A further effect can be that part of the intensity stems from the longitudinal part of the magnetic fluctuations. They do not feel the spin gap and do not form magnons; the longitudinal susceptibility should qualitatively behave similar as at zero field. Concerning their amplitude, one might expect them to be even a bit smaller than at B=0, as the slope of the magnetization curve is a bit flatter above the transition. Although

they are superimposed to the (transverse) spin-wave excitations, they do therefore probably not influence the analysis much.

The width of the experimental resolution along the scan direction may be estimated to be about 0.03. This is by far less than the typical width of the peaks. To model the magnon scattering one may therefore not use a δ-function for the energy spectrum, but requires a significant broadening. The Lorentzian form, successfully used for the energy scan at Q=(1,0,0), turns out to work well for the entire magnon. That means, the spectrum is

$$\chi''(q,\omega) \propto \frac{1}{\omega_q} \cdot \left(\frac{\Gamma_q}{(\omega - \omega_q)^2 + \Gamma_q^2} - \frac{\Gamma_q}{(\omega + \omega_q)^2 + \Gamma_q^2} \right) \tag{3.5}$$

where ω_q is given by the dispersion relation (3.4), and the second summand plays practically no role in our case. The broadening introduced by the energy-width Γ also implies a significant broadening in Q-space, as required. There are different ways to account for the fading of the intensity towards higher energies. Using a factor $\frac{1}{\omega_q}$ describes the intensity decrease quite well, and it is possible to use a constant value for Γ then which is of the order of 1 meV. A conventional magnon (like in a Heisenberg ferromagnet), however, does not involve the $\frac{1}{\omega_q}$ prefactor. In the itinerant electron model, on the other hand, the intensity of a magnon branch is expected to vanish when approaching the Stoner continuum [12]. This might be the reason for the decreasing intensity of the excitation.

Another possibility allowing to do without this artificial factor is to use a Q-dependent Γ – this can be regarded as inspired loosely by the paramagnon formula (2.26). There, the corresponding prefactor is related to the spatial correlation length. The additional parameter c which is thereby introduced can thus be considered as effectively modelling an effect of finite spatial correlation and contains a length scale. Assuming a linear correction to $\Gamma(q)$,

$$\Gamma(q) = \Gamma_0 + c \cdot q, \tag{3.6}$$

one can also obtain an intensity distribution in Q-ω-space which is in practice very similar to the previous one, seemingly even a bit better.

With this model for the magnon it is possible to perform a global fit to the entire data set.[19] The model contains only four parameters: two related to the energy width (damping), Γ_0 and c, the value of the spin wave gap Δ, and the spin wave stiffness D. Using this model, the data can be consistently described – in some of the constant energy scans in Figure 3.27a,b the values of this fit function are included as the green dotted lines. The obtained parameters are summarized in Table 3.1.

After convolution with the resolution function, this model yields scattering as shown in Figure 3.28d. From the experimental data, by use of a suitable interpolation algorithm, a corresponding intensity map of Q-ω-space has been created (Figure 3.28c)

---

[19]All points from the Panda-experiment are included, and additionally the scans at 2.5 and 3 meV from IN22 in order to include better information at these higher energies.

Δ	1.16	$\pm$	0.03	meV
Γ_0	0.55	$\pm$	0.04	meV
c	5.6	$\pm$	0.5	meV Å
D	34	$\pm$	2	meV Å^2

Table 3.1: Parameters for the magnon with a lorentzian energy spectrum and Γ according to (3.6).

which looks similar to the calculated one. It is also very remarkable that the value obtained for the spin wave gap Δ, although an unconstrained parameter in the fit procedure, matches exactly the value expected by regarding only the external magnetic field, thus proving that further anisotropy terms are either unimportant or effectively average out.

An important remark concerns the obtained value of the spin wave stiffness D and the difference between this value and the one obtained from fitting the positions of the maxima in the constant energy scans (Fig. 3.28b),

$$D = 47 \pm 5 \text{ meV} \cdot \text{Å}^2.$$

In the presence of a broadened intensity distribution in Q-ω-space, the maxima obtained in Q- and in E-scans do not need to fall on the same curve – an effect that becomes directly evident when regarding the Figures 3.28d or 2.3 (in the context of which this is discussed in more detail). The lower value from the universal fit corresponds to the energy maxima, while the latter to the maxima in Q. The discrepancy is thus natural and no reason for concern, but just important to be aware of. Anyway, as Figure 3.28d demonstrates, the difference between the two so calculated curves is, in the relevant region, relatively small due to the large slope of the curves.

Is it a magnon?

When discussing magnons and paramagnons throughout this entire chapter, it is fundamental to ask what is the evidence that this excitation can really be called a magnon. The experimental observation is that this excitation looks qualitatively different from the quasi-ferromagnetic scattering at zero field that appears upon heating (which has been discussed above, and in more detail later for the case of $Ca_{1.38}Sr_{0.62}RuO_4$) in clearly showing a dispersive behavior. On the other hand, significant intrinsic broadening is necessary in the description of the scattering. Neither of these arguments, however, is very strong, because a paramagnon, i. e. scattering inside the Stoner continuum, can resemble a dispersion, as well as a true magnon can be, due to strong damping, heavily broadened.

From the experimental data, there is rather an indication in the dispersion (Fig. 3.28b), which is quite well described by a parabola. The "dispersion" of the paramagnon, in contrast, is according to Eq. (2.24,2.25) linear in q for small q [20], which is

---

[20]This applies also for the peak positions in the constant energy scans.

very hard to reconcile with the experimentally observed peak positions when requiring a gap at q=0 of the order of $2\mu_B \cdot 10T$. The formula (2.26), even when shifting the dispersion branch by the spin wave gap[21], is thus not appropriate to use here.

In terms of the itinerant electron model of magnetism, a magnon is a *collective* mode, in contrast to the particle-hole excitations that form the continuum in Q-ω-space. A magnon forms a sharp branch that resides outside this continuum, i. e. where $\text{Im}(\chi_0) = 0$ and will, in general, merge and fade away into the continuum at some wave vector q_c (see for instance Ref. [1, 12]). It is important to note that also inside the continuum there can be significant structure – structure that may for instance happen to resemble very much the dispersive behavior of a collective mode, as would be the case for a paramagnon (Eq. (2.26) / Fig. 2.3). In the terminology of this theory there is thus a well-defined difference between a magnon and a paramagnon. In practice, though, it may be that the two cases are similar and hardly distinguishable from each other.

At q=0, the continuum is gapped due to the magnetization of the sample and the exchange energy Δ. In the gap, i. e. near q=0, the excitation is thus a true magnon. Not known is the value of q_c, so eventually part of the branch of excitations may actually be a continuum mode. Regarding the data at 6 and 8 meV in Figure 3.27a, it closely resembles the zero field data, so this is either part of the longitudinal channel of the magnetic fluctuations, or the magnon branch has indeed disappeared into the continuum.

The conclusion from these arguments is that probably at least a part of the observed branch of excitations is a magnon in the strict sense, but with significant damping. How far this part extends, however, is hard to decide. The description as a magnon, though, works well until at least 3 meV (or q$\simeq$0.12 r.l.u.).

Independent of what is the correct name for the excitation, the important conclusion from the existence of this excitation is not so much the information about the band structure, but about the interaction between the electrons. This interaction is treated via the interaction parameter I. As pointed out in Section 2.2, the condition for the appearance of a spin wave outside the Stoner continuum is $\frac{1}{(g\mu_B)^2} \cdot I \cdot \chi_0^{\pm} = 1$, which will in general only be fulfilled for large enough I. If one knew χ_0, the observation of the magnon would thus allow a quantitative estimation of I. Also inside the continuum (where $\text{Im}(\chi_0)$ is usually very small on an absolute scale without exchange enhancement) a sizeable value of I is necessary to account for any sharp features strong enough to be observed in this kind of experiment. One can therefore conclude that in any case the existence of this excitation proves that a very strong ferromagnetic interaction between the spins is present in the system.

---

[21]To account for the magnetic field in a physically correct way would, however, be a non-trivial modification.

Why is the dispersion not seen in the data with B∥b? Despite the anisotropic behavior of the system and the different transition field, there is no reason to assume that the situation is fundamentally different when applying the magnetic field in another direction. The data collected with the c-axis perpendicular to field, though, have not revealed the dispersive behavior of the excitation around the ferromagnetic wave vectors, see Figure 3.23. The energy gap, on the other hand, is also visible, and a weak indication of broadening and the disappearance towards higher energy does at least resemble the findings for B∥c.

The most important reason for the different shape of the scans is certainly the experimental resolution. Along the vertical direction, the Q-resolution is very coarse. With *c* as the vertical axis, one integrates along the direction of practically no dispersion, so one effectively gains in intensity while keeping the relatively good resolution in the *ab*-plane. In the other case, when integrating over the *b*-direction, i. e. perpendicular to the spin wave cone, one may easily fill up the central minimum, which is anyway not very well pronounced and visible only at low energy transfers when the diameter of the spin wave cone is still quite small.

Another difference between the two setups is that different components of the susceptibility are measured. With the field along (010) and measuring at (0,0,L), one sees the components of χ in the *ab*-plane. Being equal along *a* and *b* without field, one of them has, with field, transverse character and becomes therefore gapped, while the other does not – in the measurement, they are always seen simultaneously. With the field along (001), χ_{ab} is only seen as a transverse component, while χ_c is the longitudinal one. Although it is not obvious what this overlap looks like in detail in either of these cases, it appears well possible that it gives rise to different shapes of the scans. More specifically, from the zero-field studies there is some evidence for χ_c being smaller than the in-plane components, meaning a (partial) polarization of the fluctuations in the *ab*-plane. The longitudinal component being smaller would also help to better resolve the transverse component which contains the magnon dispersion.

A short comment on specific heat. The discussion of the spin fluctuation contribution to the electronic specific heat coefficient under an applied magnetic field is more difficult than without field, as performed above. The fluctuation spectrum now has to be split into a transverse and a longitudinal part, and the spin waves, which exist in a region around q=ω=0 in q,ω-space have a distinct energy spectrum (normally δ-function like, or, like here, more Lorentz-like) and obey the dispersion relation (3.4). In the discussion of the specific heat in chapter 2.2.4, the energy spectrum has to replace the last term in equation (2.36) in order to get the spin-wave part of the free energy; when, for simplicity, approximating the spectrum by the δ-function, the calculation becomes much simpler because the integration does not have to be performed any more. As argued in Ref. [20], as a simple approximation one may exclude
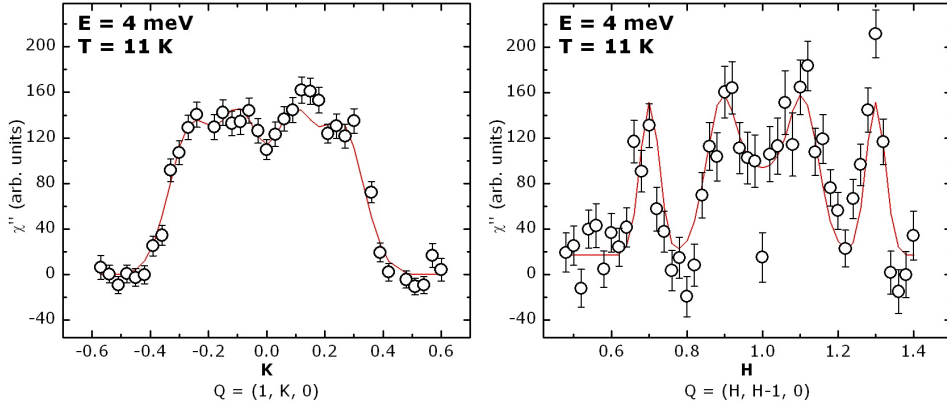
Figure 3.29: Magnetic scattering around $(1,0,0)$ in $Ca_{1.38}Sr_{0.62}RuO_4$. Left: Transverse scan; Right: diagonal scan (corrected for the magnetic form factor). The lines are symmetric sums of Gaussian fit functions.

the q's which belong to the spin-wave region from the sum over the transverse components in (2.2.4) and use the spin-wave free energy instead. For the quantitative evaluation, however, the necessary information is missing. Because the spin-wave spectrum has a gap proportional to B, the low temperature specific heat due to spin waves is expected to decrease with increasing magnetic field and to vanish for $T \to 0$. In particular, the specific heat is suppressed when $k_BT < \Delta(= 2\mu_BB)$ (1 Tesla corresponds to 1.3K). Qualitatively, both these effects can be found in the specific heat data, Figure 3.3: above the transition field (at which the specific heat is enhanced due to the enhanced longitudinal magnetic fluctuations) its rapid decrease towards higher magnetic fields is consistent with the opening of a gap and the spin-wave region becoming more extended in Q-space. Higher temperatures are then necessary to overcome the gap energy, in accordance with the shift of the upturn towards higher temperatures.

3.5 Magnetic correlations in $Ca_{1.38}Sr_{0.62}RuO_4$

The magnetic scattering in $Ca_{1.38}Sr_{0.62}RuO_4$ resembles that in $Ca_{1.8}Sr_{0.2}RuO_4$ in some important aspects. The overall appearance is qualitatively the same in that it is broadly distributed around $(1,0,0)$ and peaks at incommensurate wave vectors. In Figure 3.29 (left), a typical transverse scan with good statistics is shown. The shape of this signal has been discussed earlier [46]. With the better data available now, one can recognize that the scan cannot be described by a single Gaussian-like peak on each side, but that the structure of the scan requires at least two such contributions on each side, exactly like in the case of $Ca_{1.8}Sr_{0.2}RuO_4$. The positions of these are q_1=0.10 and q_2=0.26 ($\pm$0.01). Furthermore, the absolute intensity of the incom-

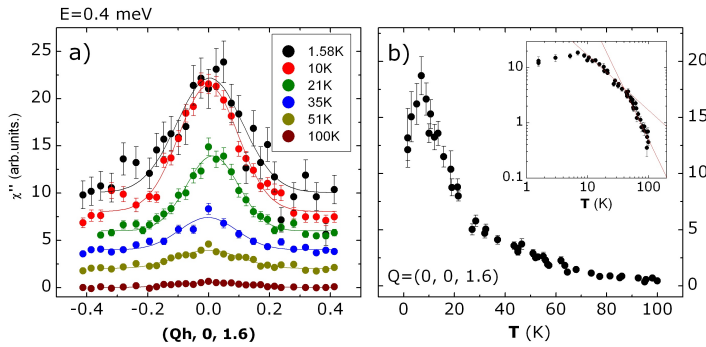Figure 3.30: Magnetic scattering in $Ca_{1.38}Sr_{0.62}RuO_4$ at low energy (0.4 meV). (a) Constant energy scans across $Q_{FM}=(0,0,1.6)$ at different temperatures (offsets: 100). (b) The signal at Q_{FM} as function of temperature (inset: double logarithmic plot of the same data).

mensurate scattering is identical to $Ca_{1.8}Sr_{0.2}RuO_4$ within the uncertainty due to the calibration procedure (estimated accuracy 10-20%). A difference to $Ca_{1.8}Sr_{0.2}RuO_4$ is that in the centre of the scan, i. e. at (1,0,0), the minimum seems to be less well pronounced. Finally, the diagonal scan (Figure 3.29 right) also exhibits maxima at wave vectors (0.3,0.3,0) separated from (1,0,0). Their experimentally determined position is 0.299±0.003, i. e. no shift compared to Sr_2RuO_4 is detectable. However, their intensity (though there is some uncertainty in the background subtraction) seems to be higher than in $Ca_{1.8}Sr_{0.2}RuO_4$.

So far, the conclusion would be that the observed magnetic correlations do not significantly differ for the two Sr-concentrations 0.2 and 0.62. In view of the quite different macroscopic behavior of these two systems – the latter having an extremely high macroscopic susceptibility at low temperature, apparently being near a ferromagnetic instability, and the former having a suppressed susceptibility and a metamagnetic transition instead – this might be a bit surprising. It is clear that there should be some important differences, and indeed the results which will now be discussed prove this. In fact, it is the region of low energy transfers which is particularly interesting.

3.5.1 Magnetic response close to the ferromagnetic instability

Figure 3.30 contains the magnetic scattering at 0.4 meV energy transfer. This is safely below the characteristic energy of the incommensurate response which is therefore not observed in these scans. The broad maximum around Q_{FM} is again similar to the one in $Ca_{1.8}Sr_{0.2}RuO_4$ (see for instance Figure 3.19) at higher temperature. Here this signal persists down to 1.5 K, in contrast to $Ca_{1.8}Sr_{0.2}RuO_4$, where it disappears almost completely. In order to further examine this signal, the energy dependence has been measured at different temperatures up to 35 K, see Figure 3.31. From these energy scans, one can extract the characteristic energy via the usual fit to a single relaxor function; the results are summarized in the inset. It turns out that the characteristic energy varies approximately linearly with temperature and reaches the very low value of 0.2 meV at 1.5 K.

When approaching a transition to a magnetically ordered state, it is expected that

Figure 3.31: Energy scans on $Q_{FM}=(0,0,2.4)$ in $Ca_{1.38}Sr_{0.62}RuO_4$ at different temperatures. The count rates have been converted to an approximate scale in absolute units. Lines are fits to a single relaxor function and the thus obtained parameters Γ and $\chi'(0)$ are summarized in the insets (lines are guide to the eye).
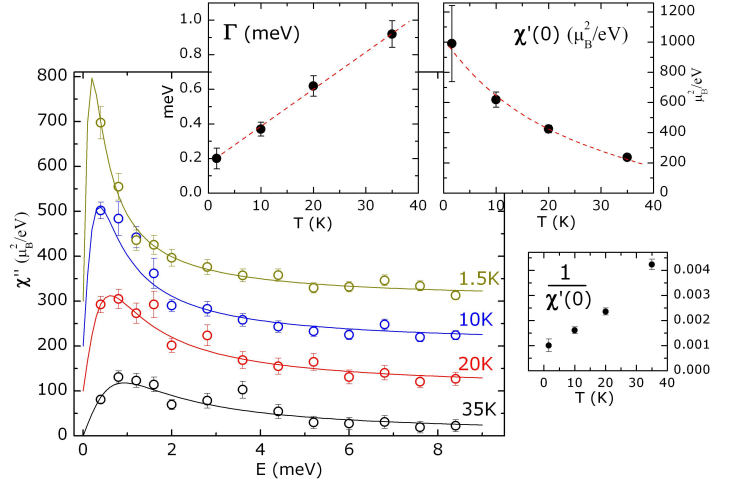
the frequency Γ of the spin fluctuations vanishes and that the susceptibility $\chi(0)$ diverges ($\frac{1}{\chi(0)}$ vanishes in the same way as Γ). Regarding $\Gamma(T)$ in Figure 3.31 one realizes that the system is obviously approaching the phase transition, but does not reach it, and the values remain finite. (The transition would, by extrapolation, seemingly be situated about 10 K below zero temperature, which might be taken as an approximate measure of the "distance" to the ferromagnetic instability.) It should be mentioned that Nakatsuji et al. [44] obtained a Weiss-temperature of about -5 to -10 K from fitting the susceptibility, which apparently resembles this finding, but is perhaps also a bit misleading because the material is not an antiferromagnet and shows more complicated behavior. The susceptibility extracted from the neutron data has a relatively steep increase in this temperature region, but is also not truly diverging towards low temperature. In addition, the imaginary part of the susceptibility in Figure 3.30 demonstrates the absence of such divergence[22][23]. The plot of $1/\chi$ contains a weak indication for a flatter slope at low temperatures than between 20 and 35 K. Another important observation is that the magnetic response in the inelastic neutron scattering experiment does not change significantly when further lowering the temperature from about 1.5 K (which is usually the lowest temperature in these experiments) to 50 mK, as it has been achieved once using the dilution cryostat on the

---

[22]Unfortunately, the full temperature dependence is only available for one energy transfer, so no Kramers-Kronig analysis is possible. The maximum slightly below 10 K is of course partly due to the temperature variation of the characteristic energy (Figure 3.31) which is about 0.4 meV at 10 K, so near this temperature $\chi''(0.4\,\text{meV})$ measures the maximum of the spectral function. Nevertheless, because the spectral function is quite broad near its maximum, a strong increase of χ' would easily compensate this effect, so the maximum in χ'' confirms the non-existence of any divergence.

[23]The double-logarithmic plot displays an interesting feature: at about 30 K, there is a crossover from a T^{-1} to a $T^{-2.3}$ temperature dependence. The reason for this is not clear. Interestingly, however, a similar, though weak feature is present between 20 and 30 K in a log-log-plot of the macroscopic susceptibility data.

IN14 spectrometer. There is no magnetic order observed, nor even a large enhancement, which supports the interpretation that the system is still a few Kelvin away from any ferromagnetic order. The low-temperature anomalies like the anomalous thermal expansion in $Ca_{1.8}Sr_{0.2}RuO_4$ [53,54] are weaker, but still present in $Ca_{1.38}Sr_{0.62}RuO_4$, and as they are related to the magnetic properties, they probably also play a role in $Ca_{1.38}Sr_{0.62}RuO_4$ and help to prevent it from reaching the ferromagnetic instability.

A comparison of the absolute value of χ with the value from the macroscopic measurement is not possible with high precision because the latter has not been measured on the same crystal used for the neutron experiment, and it varies steeply as function of Sr-concentration, see Figure 3.1 or Ref. [36]. From this plot, one may extract a value of about 1500 $\frac{\mu_B^2}{eV}$ for the Sr-concentration 0.62, which does not agree perfectly with the neutron result. In view of uncertainties due to concentration, different components (anisotropy) and calibration to absolute units, this may still be regarded as a reasonable agreement.

$Ca_{1.38}Sr_{0.62}RuO_4$ is apparently close to the transition to a ferromagnetic state, and the strong scattering around Q_{FM}, which has much lower frequency than the incommensurate one, is to be regarded as the paramagnon scattering related to this ferromagnetic instability.

3.5.2 A universal description of the magnetic response

So far, the analysis simply consisted of identifying a signal around Q_{FM} with a relatively low energy, and a broad signal around an incommensurate position which has a higher energy. These two parts have been looked at essentially independently from each other and have been described by appropriate Gaussian-like contributions (where the incommensurate one has additional structure which is accounted for by using two peaks).

Although it has been shown that it is justified to look at these different parts of the magnetic response separately, it is an obvious question if it is possible to describe the data in a way that is firstly more universal (i. e. uses common parameters at different energies and temperatures to describe the whole response), and secondly less phenomenological, but based on a deeper understanding of the underlying physics. Concerning the second point, the most desirable approach, which would be a band-structure based calculation of magnetic excitations including correlation effects etc., is again far beyond the present possibilities like in the case of $Ca_{1.8}Sr_{0.2}RuO_4$. However, following the idea that this system is a metal close to a magnetic instability, one may try to use the general expansions for $\chi''(\mathbf{Q}, \omega)$ as they have been discussed in Chapter 2.2.3 and which have been applied successfully to a number of other materials (for instance Refs. [117–122]). Though one may not expect a perfect description on this level, the circumstances from the experimental point of view are favorable in this case, because a large amount of data is available, and the fact that it has been
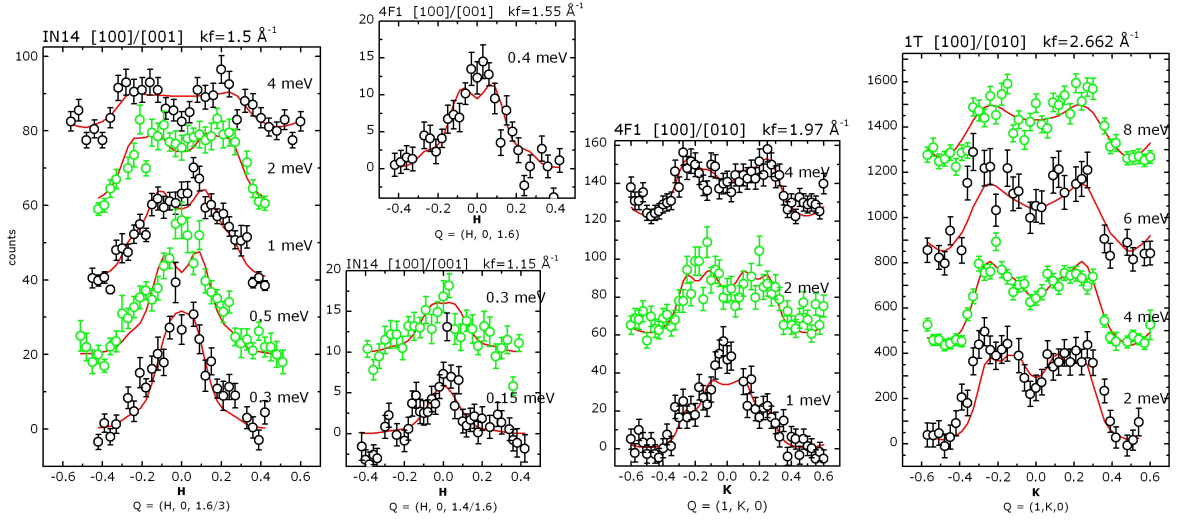
Figure 3.32: Magnetic scattering in $Ca_{1.38}Sr_{0.62}RuO_4$ at low temperature (0.05 K on IN14, 1.5 K else). The data (1T from [110]) have been taken in different configurations and on different spectrometers, as indicated. The line is a fit to a global model of a scattering function, as discussed in the text, with common parameters (Table 3.2) in all cases.

collected under a number of different conditions reduces the danger that experimental effects like resolution etc. influence the results.

Based upon the idea of different antiferromagnetic and ferromagnetic instabilities, one may try to use the formula

$$\chi''(\mathbf{Q}, \omega) = \sum_{\mathbf{Q_0} \,\epsilon\, \mathbf{IC_1}} \chi_1 \cdot \frac{\omega/\varepsilon_{ic}}{(\omega/\varepsilon_{ic})^2 + (1 + \Delta\tilde{\mathbf{Q}}_{ic}^2)^2} + \sum_{\mathbf{Q_0} \,\epsilon\, \mathbf{IC_2}} \chi_2 \cdot \frac{\omega/\varepsilon_{ic}}{(\omega/\varepsilon_{ic})^2 + (1 + \Delta\tilde{\mathbf{Q}}_{ic}^2)^2}$$
$$+ \chi_{fm} \cdot \frac{\omega/\varepsilon_{fm} \cdot \Delta\tilde{\mathbf{Q}}_{fm}}{(\omega/\varepsilon_{fm})^2 + (1 + \Delta\tilde{\mathbf{Q}}_{fm}^2)^2 \Delta\tilde{\mathbf{Q}}_{fm}^2} \qquad (3.7)$$

This formula for the imaginary part of the susceptibility, though lengthy, can easily be understood. The first two of the three summands describe the incommensurate antiferromagnetic part of the response. The expression is based directly on equation (2.29). Each of the two sums runs over the four incommensurate peak positions around (1,0,0):

$$\mathbf{IC_i} = \left\{ (1+q_i, 0, 0), \ (1-q_i, 0, 0), \ (1, q_i, 0), \ (1, -q_i, 0) \right\}, \qquad i = 1, 2 \qquad (3.8)$$

where q_1 and q_2 are the inner and the outer one of the two peaks used to describe the broad incommensurate response on each side of (1,0,0). This yields a total of eight

such incommensurate peaks situated on the four main symmetry directions around (1,0,0). When working near other points in reciprocal space, (1,0,0) would of course have to be substituted by the appropriate nearest point with integer H and K. The $\Delta\tilde{\mathbf{Q}}_{ic}$ that enters is the "distance" to the respective peak position Q_0, normalized by the correlation length ξ_{ic}, which determines the effective q-width of the signal:

$$\Delta\tilde{\mathbf{Q}}_{ic}^2 = \xi_{ic}^2 \cdot \left(\frac{2\pi}{a}\right)^2 \left((H_0 - H)^2 + (K_0 - K)^2\right) \tag{3.9}$$

Here and in the next equation, the notation $\mathbf{Q_0} = (H_0, K_0, L_0)$ and $\mathbf{Q} = (H, K, L)$ has been used for the components of the vectors. Note that L does not enter which means that these fluctuations are assumed to be strictly two-dimensional (i. e. L-independent).

The last term in the sum of (3.7) models the ferromagnetic component (paramagnon). It has the form of equation (2.26). In order to keep the treatment more general and to improve the fit, the possibility to account for a small three-dimensionality of the ferromagnetic response is included by allowing for a nonzero correlation length along *c*, as discussed later. For the paramagnon contribution, the equation corresponding to (3.9) is

$$\Delta\tilde{\mathbf{Q}}_{fm}^2 = (2\pi)^2 \left(\left(\xi_{fm}^{ab} \cdot \frac{H_0-H}{a}\right)^2 + \left(\xi_{fm}^{ab} \cdot \frac{K_0-K}{b}\right)^2 + \left(\xi_{fm}^{c} \cdot \frac{L_0-L}{c}\right)^2\right) \tag{3.10}$$

Here, $\mathbf{Q_0} = (H_0, K_0, L_0)$ is taken as the nearest true reciprocal lattice point, e. g. $\mathbf{Q_0}$=(1,0,1) for $\mathbf{Q}$=(1,0,0), or $\mathbf{Q_0}$=(0,0,2) for $\mathbf{Q}$=(0,0,1.6).

The procedure of simply summing up the different contributions is easy to justify when assuming that they originate from different regions/phases of the sample. Otherwise, treating the overlap of these contributions would in principle require a more sophisticated analysis taking into account their interaction with each other. Despite this limitation and the fact that there is large overlap, Equation (3.7) is able to describe the overall Q-ω-dependence of the magnetic scattering reasonably well, see Figure 3.32. The parameters are the following:

q_1	q_2	χ_1(=0.6χ_2)	ε_{ic} (meV)	ξ_{ic} (Å)
0.11	0.26	160 ± 10	2.5	9.5±0.5

χ_{fm}	ε_{fm} (meV)	ξ_{fm}^{ab} (Å)	ξ_{fm}^{c} (Å)
850±50	0.34±0.07	4.2±0.3	1.8±0.3

Table 3.2: Results of the fit to the model (3.7) at low temperature. q's are in relative lattice units, and χ's are in arbitrary units of the order of μ_B^2/eV.

Some of the parameters needed to be fixed, because there is strong correlation due to the broad signals which are overlapping in significant regions of Q-ω-space. This calculation nevertheless demonstrates that the magnetic scattering can be approximated using this model and a set of reasonable parameters.

The parameters for the incommensurate antiferromagnetic part are similar as in $Ca_{1.8}Sr_{0.2}RuO_4$. The relative strength of the ferromagnetic part is partly due to the fact that at higher energies it also contributes near the incommensurate wave vectors, thereby reducing the necessary value of $\chi_{1,2}$. A bit questionable are the values for ξ_{fm}^{ab} and ξ_{fm}^c: the out-of-plane correlation length is, as expected, very short; being shorter than the interlayer distance, it does not describe a correlation in the usual sense, but using it still improves the fit considerably. Also within the plane, the correlation is surprisingly short and does not yet seem to indicate the near ferromagnetic instability.

A severe problem in the comparison with the data is that the equation for the paramagnon (2.26) is strictly zero at the ferromagnetic Q-vectors. This is a consequence of the requirement that the total magnetization is conserved. Upon reduction to two dimensions this zero would extend to all L-values. A first obvious way to account for the observed nonzero intensity is the experimental resolution which yields a finite intensity at these points by averaging over Q and ω. As a second way to improve the description, the correlation length along the c-axis – formerly zero – has been allowed to take (very small) finite values ξ_{fm}^c. (With this, the magnetization is still conserved in the crystal, but not within a single plane.)

It is, however, questionable to what extent this reflects real physics or is just a means to account for effects that actually have another origin. A weak c-axis correlation is certainly possible[24], but the relevant underlying physics may be different. Spin-orbit coupling is expected to play a role, and it would lead to an energy splitting at Q=0. As it is not evident how to explicitly model it in this framework, the applied method, with the appropriate caution, may be a reasonable approximation. Nevertheless, a slightly different approach is given in the following.

A second version. Despite the already relatively good overall agreement of this model with the data, it would still be desirable to achieve a better description of the central peak in the low energy region (0.4, 0.5 and 1 meV). One might consider an additional artificial broadening by "smearing out" the calculated $\chi''(\mathbf{Q}, \omega)$ where necessary. However, this would have to be done in a very extreme way to turn the minimum into a maximum, but only in a very limited region of q-ω-space. Instead, it has been tried to use a modified formula by replacing the paramagnon term in (3.7) by a term like the two first ones, with $q = 0$. This is not justified theoretically (because it actually applies to antiferromagnetic fluctuations) but only as a phenomenological way to describe the data.

The agreement is in general better than before, especially the maxima at Q_{FM} are

---

[24]Consider that a really ferromagnetic state would have three-dimensional order. Then, for instance, (1,0,0) would have zero structure factor. Therefore, though weak, a c-axis correlation may in principle have an effect not only in the ordered state but also close to it. Quantitatively, it is probably not observable. Note also that in the case of Ti-doped Sr_2RuO_4 it is argued that it can be neglected.
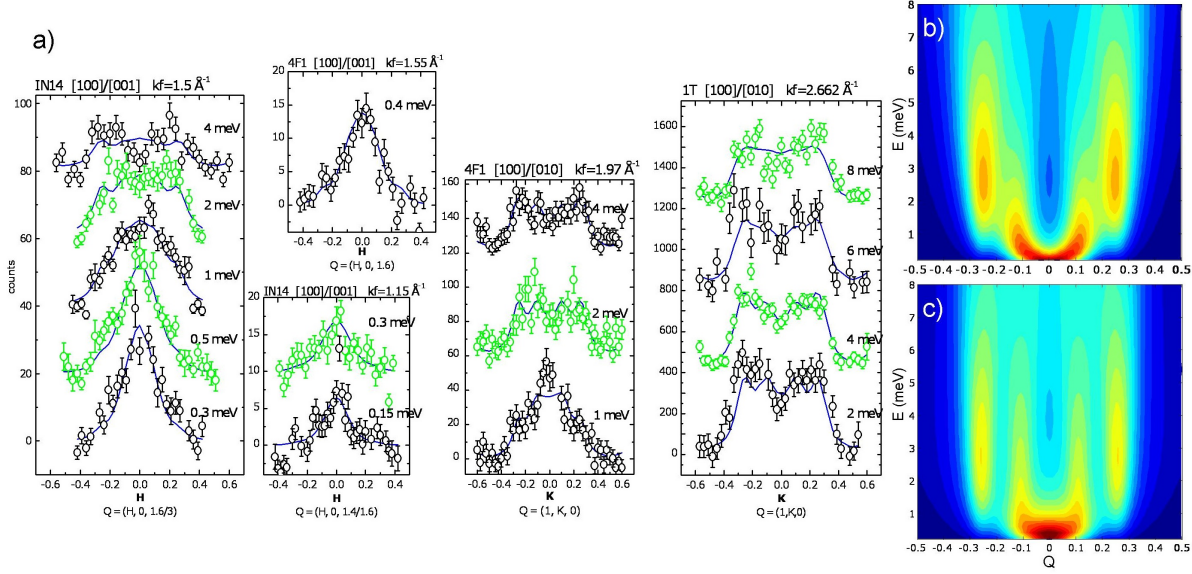
Figure 3.33: (a) Magnetic scattering in $Ca_{1.38}Sr_{0.62}RuO_4$ (same data as in Fig. 3.32) and fits within the modified model (see text). (b) and (c) are the values of $\chi''(\mathbf{Q},\omega)$ (Q=(H,0,1.6)) for the two versions of the fit function with the resulting parameters – in (b) for (3.7) with the paramagnon, and in (c) with the AFM-like fluctuation as used for the calculated lines in (a).

well reproduced[25]. The results are shown in Figure 3.33a, and the parameters that have been used are:

q_1	q_2	$\chi_1 (=0.66\chi_2)$	ε_{ic} (meV)	ξ_{ic} (Å)
0.11	0.26	220 ± 10	3.2 ± 0.3	9.6 ± 0.4
χ_{fm}	ε_{fm} (meV)	ξ_{fm} (Å)		
790 ± 30	0.29 ± 0.03 meV	4.8 ± 0.2		

Table 3.3:
Results of the low-temperature fit within the modified (AFM-like) model. Remarks as in Table 3.2.

The correlation length for the signal at Q_{FM} is still very short – as expected, this does not significantly depend on the model, but is the direct consequence of the very large width of the peak around Q=0 in the scans.

A few final comments about this description of the data should be given:
Firstly, the so obtained ε_{fm} of the (ferromagnetic) paramagnon can not directly be identified with the characteristic frequency Γ which is derived from the energy scans on Q_{FM} – both determine the energy scale of the (quasi-)ferromagnetic fluctuations,

---

[25]The disagreement in one of the 1 meV scans is most likely to an inexact modelling of the resolution function.

but ε_{fm} does so via the slope of the "dispersion" of the paramagnon. In this picture, Γ would be obtained as an effective average over Q and ω over the paramagnon. For the antiferromagnetic fluctuations, i. e. at Q=q_{ic} the values Γ and ε_{ic} are in principle identical, though a difference can arise in this specific case due to the overlap with intensity stemming from the paramagnon.

Secondly, a similar remark concerns the correlation lengths: due to their definition, they are (cf. (2.30)) not exactly the same as the correlation lengths that one would obtain from a lorentzian fit to a Q-scan, but about 14% smaller.

Thirdly, a potential anisotropy of the magnetic response is so far not considered. This would render the analysis more complicated and might readily solve some of the discrepancies within the current model. There is no reason to exclude that the susceptibility may have significant anisotropy, which may vary for its different components, but no further statement can be given at present.

Finally, it is very important to realize that the two approaches are in fact not so different as they may seem at first sight. Despite the conceptual difference that (3.7) introduces a dispersive behavior for the ferromagnetic component, the difference between the thus calculated $\chi''(\mathbf{Q}, \omega)$'s is in practice not so significant, as demonstrated in Figure 3.33(b,c). Due to the overlap of the various components it is possible, by slight variation of the parameters, to account for most features like for instance an effective dispersive behavior. The somewhat better agreement with the data tends to favor the more phenomenological approach. It is not to be interpreted as significantly physically different, and in particular not as evidence for an antiferromagnetic nature of this signal, but rather as a means to model the effects that are not captured by the standard formulae. Besides the spin-orbit-coupling induced anisotropies mentioned above, the disorder is probably important, furthermore the multi-band structure that allows for inter-band transitions, etc.

3.5.3 Temperature dependence

The studies presented so far predominantly focus on the range of low temperature and low energy transfers, because this is the most relevant one close to the magnetic instabilities. In $Ca_{1.38}Sr_{0.62}RuO_4$ there is the fortunate case that there is also extensive data available collected at higher temperatures and higher energy transfers – much more than for $Ca_{1.8}Sr_{0.2}RuO_4$ – because already earlier, i. e. before the identification and study of the ferromagnetic signal, much data has been collected, mostly by O. Friedt [110]. Being obtained on thermal neutron spectrometers with high flux these data have the advantage of relatively good statistics. Based on the new findings on the structure of the magnetic response, it appears very interesting to reexamine these data and to take them into account in the current analysis. For this purpose, all available (new and old) data have, in a careful treatment, been merged in order to make them comparable on the same scale. Figure 3.34 gives the summary of a
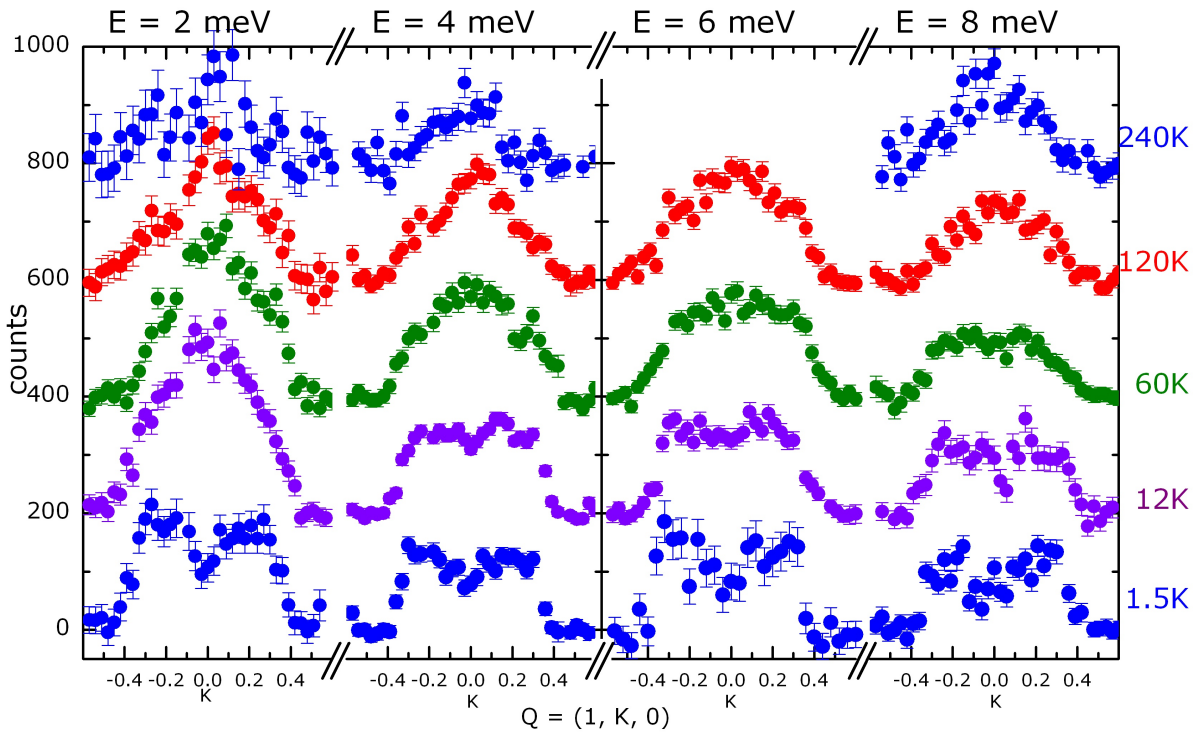
Figure 3.34: Magnetic scattering in $Ca_{1.38}Sr_{0.62}RuO_4$ in the range above 2 meV and at different temperatures. This is a summary of nearly all available data in this ω-T-range on this compound, from different measurements normalized to the same intensity scale and averaged (background subtracted, no Bose factor correction etc.). The majority of the raw data that has been included in this compilation has been measured by O. Friedt and is partly already published in his thesis [110].

large portion of these data, covering nearly the full range of temperatures and energy transfers possible on the thermal spectrometers[26].

Qualitative description

With this data set, it is possible to perform a similar analysis as in Section 3.4.2. Although this analysis gains more precision and significance thanks to the larger amount of available data, the conclusion is similar. Assuming just a broadening of the low temperature response, it is hardly possible to describe the shape of the scans at higher temperature. The reason is again that firstly the edges at ± 0.3 are very steep and stay it to some extent even at high temperature, and that secondly the peak at K=0 is quite sharp. The analysis for $Ca_{1.8}Sr_{0.2}RuO_4$ as shown in Figure 3.21

---

[26]limited below at about 2 meV by the energy resolution and above by the fact that at about 10 meV optical phonon scattering starts to severely contaminate the scans.

Figure 3.35: Describing the shape of the signal in a phenomenological way.

Taking the low-temperature signal as the "incommensurate" one, it is possible to identify the additional ferromagnetic component (Gaussian, as sketched on the right) as function of temperature.
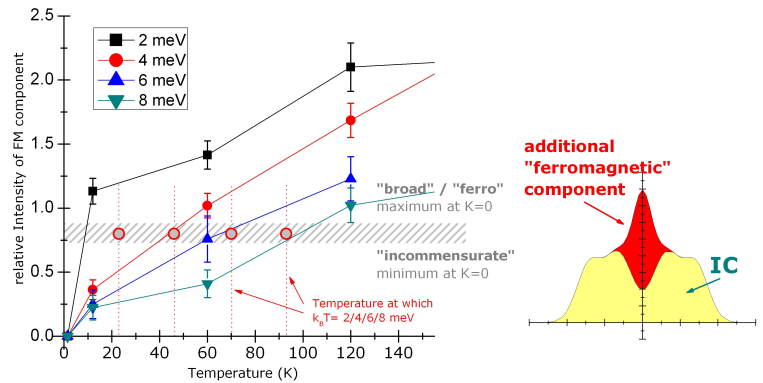
In the graph, the intensity (amplitude) of this component relative to the intensity of the incommensurate scattering is shown as function of energy transfer and temperature (i. e. for the scans in Figure 3.34). For a certain amplitude of the FM component, the overall shape of the scans changes and the minima in the centre turn into maxima. One has of course some freedom to define a "border" between these two cases – nevertheless a reasonable choice is about 3/4 (grey shaded line). Taking this value, one sees that, at least for 4, 6 and 8 meV, the lines cross this border – i. e. change their shape – when the thermal energy k_BT exceeds the excitation energy. By regarding the data in Figure 3.34, one can indeed convince oneself that *very* roughly, this applies to the scans in the upper left half of the figure (where T is large compared to E).

is nearly identical for $Ca_{1.38}Sr_{0.62}RuO_4$, and also the differences behave in qualitatively the same way as those in Figure 3.21.

This provides further support that even at high temperature there exists a ferromagnetic component that has to be regarded separately from the incommensurate one. In the energy and temperature range regarded here, the ferromagnetic part is, roughly speaking, dominant in those scans when the temperature is higher than the energy transfer, $k_BT > \hbar\omega$. This phenomenological rule is justified in Figure 3.35 on the basis of fits to the data. It seems to be quite well fulfilled, except at very low energy transfers. There, see for instance Figure 3.32 at 0.5 or 1 meV ($\hat{\approx}$ 6 or 12 K), the FM component dominates down to the very lowest temperatures, because at these energies there is never a significant amount of intensity from the antiferromagnetic part. Concerning the ferromagnetic component, it is to be expected that upon increasing the temperature and thereby growing distance from the ferromagnetic instability, the paramagnon scattering becomes less sharp in Q, i. e. broader. The second and, because it is already broad at low temperature, more important effect is that the characteristic frequency of the paramagnon scattering increases. This may qualitatively explain the above observation of how the energy where it appears correlates with the temperature.

A quantitative model

Because the temperature dependencies of the susceptibilities and the characteristic energies are known from the analysis of the neutron scattering data, one can give the reason for the scaling that has just been described in a phenomenological manner. Assume that the characteristic energies and the inverse susceptibilities depend linearly on the temperature:

$$\chi(T) = \frac{\tilde{\chi}}{T + \tilde{T}} \quad \text{and} \quad \Gamma(T) = \tilde{\Gamma}(T + \tilde{T}) \tag{3.11}$$

This form is suggested by the data in Figure 3.31 for the ferromagnetic position, and by the analysis in Reference [46] for the incommensurate signals, and it is assumed that these relations approximately hold over the entire temperature range that is regarded. Realistic parameters for such a model are given in Table 3.4.

With the usual single relaxor energy spectrum, the ratio of ferromagnetic to incommensurate intensity in a constant energy scan is

$$\frac{\chi''_{\text{FM}}(\omega, T)}{\chi''_{\text{IC}}(\omega, T)} = \frac{\tilde{\chi}_{\text{FM}}\tilde{\Gamma}_{\text{FM}}}{\tilde{\chi}_{\text{IC}}\tilde{\Gamma}_{\text{IC}}} \cdot \frac{\tilde{\Gamma}^2_{\text{IC}}(T + \tilde{T}_{\text{IC}})^2 + \omega^2}{\tilde{\Gamma}^2_{\text{FM}}(T + \tilde{T}_{\text{FM}})^2 + \omega^2} \tag{3.12}$$

The first factor has, for the parameters in Table 3.4, the value $\frac{1}{6}$. The condition for the second factor to be greater than a constant c is

$$T > \frac{A\tilde{T}_{\text{FM}} - \tilde{T}_{\text{IC}} + \sqrt{A(\tilde{T}_{\text{FM}} - \tilde{T}_{\text{IC}})^2 + (1 - A)\tilde{\Gamma}^{-2}_{\text{IC}}(c - 1) \cdot \omega^2}}{1 - A} \tag{3.13}$$

with $A = c \cdot \tilde{\Gamma}^2_{\text{FM}}/\tilde{\Gamma}^2_{\text{IC}}$. When putting in numbers, one realizes that the second summand under the square root dominates for most relevant values of c and ω, so the condition (3.13) describes approximately a straight line in the ω, T-plane with the slope $\sqrt{(c - 1)/(1 - A)}/\tilde{\Gamma}_{\text{IC}}$.

Figure 3.36 shows such lines for different values of the ratio (3.12) of ferromagnetic and incommensurate intensity and compares it to the line $\hbar\omega = k_B T$. By this comparison it becomes evident what is the origin of the scaling in the preceding section. There, a value of 0.75 had been arbitrarily chosen to define the dominance of the Q_{FM}-signal and thus the "broadening" of the scan. This line is close to $\hbar\omega = k_B T$ in Figure 3.36. On the other hand, these results also show that the real situation is a

	FM	IC
$\tilde{T}$	10	25
$\tilde{\Gamma}$	0.02	0.1
$\tilde{\chi}$	10000	12000

Table 3.4: Parameters used in the model 3.11. Units are K, meV/K and $\mu_B^2/$eV·K, respectively.

Figure 3.36: Ratio of ferromagnetic versus incommensurate intensity as function of temperature and energy transfer. The contour lines are calculated using (3.12) with the parameters in Table 3.4. The dashed red line represents $\hbar\omega = k_B T$.
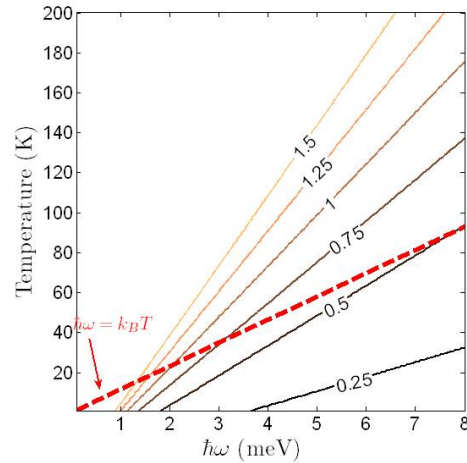
bit more complicated because the contour lines do not pass through the origin, and thereby explain the deviations in Figure 3.35. In particular, they demonstrate that at very low energy transfers the ferromagnetic signal is dominant at all temperatures.

3.6 Discussion and Conclusions

Two Sr-concentrations have been studied in great detail: x=0.2 and x=0.62[27]. Although these are only two samples, the results indicate how the magnetic correlations in the whole paramagnetic metallic and structurally distorted region of the $Ca_{2-x}Sr_xRuO_4$ phase diagram[28] can be consistently understood. The magnetic properties are obviously determined by magnetic instabilities of different character – on the one hand, a ferromagnetic one, and on the other hand, an incommensurate antiferromagnetic one.

Properties of the antiferromagnetic fluctuations The experiments on $Ca_{1.8}Sr_{0.2}RuO_4$ proved that the incommensurate response is a magnetic fluctuation of truly antiferromagnetic character. The properties of this antiferromagnetic signal one can be summarized as follows:

---

[27]Apart these, a sample with x=0.52 has been studied earlier in order to look for magnetic order at very low temperature (which was found to be absent). Secondly, an experiment was very recently performed on a sample with x=0.18 – this sample is in the *L-Pbca* region of the phase diagram (left to the first order phase transition near x=0.2). With a total mass of ∼0.4 g (13 small crystals coaligned) and not being able to cool below 50 K due to the danger of breaking the sample at the discontinuous structural phase transition, a signal was hardly detectable. Within a huge uncertainty, the scattering is consistent with that at x=0.2, but no further reasonable statement can be made at present about the quantitative or qualitative similarities and differences between these samples.

[28]This means the region x≥0.2 and, in principle x≤1.5, i. e. the whole $I4_1/acd$ region, although it is the less magnetic, the higher x.

- It is relatively independent of the Sr-concentration. This means that the shape of the signal, most precisely determined at low temperature, is essentially identical for x=0.2 and x=0.62. The characteristic energies lie at about 2.5 meV at low temperature. Also the amplitude of the signal is, within the accuracy of absolute calibration, equal for the two concentrations and amounts to approximately 200 $\frac{\mu_B^2}{eV}$ (one component of $\chi''(\mathbf{Q}, \omega)$).

- It is favorable to study the shape of the antiferromagnetic response in $Ca_{1.8}Sr_{0.2}RuO_4$ rather than in $Ca_{1.38}Sr_{0.62}RuO_4$ because the ferromagnetic component is nearly absent at low temperature. A very precise study on $Ca_{1.8}Sr_{0.2}RuO_4$ shows that it has a rather complicated structure. It forms wide regions of high intensity that are separated about 0.22 reciprocal lattice units from the 2D zone centre and covers a large part of the Brillouin zone. These broad spots have an internal structure, as it is most clearly seen from the constant energy scans. The intrinsic width of the single components is so large that they cannot be resolved, but with two contributions centred on the zone axes it is possible to achieve a good description of the observed signal.

- At high magnetic field, these fluctuations get strongly suppressed. As function of temperature, they change only very little in shape; their energy increases moderately, and their amplitude decreases.

These antiferromagnetic fluctuations point towards the general existence of an underlying antiferromagnetic instability in the system to which it is quite close. With more than 2 meV characteristic energy even at the lowest temperatures, however, the system is still clearly separated from the transition to any ordered state. Nevertheless, these fluctuations determine important properties of the system like the enormous electronic specific heat coefficient. For $Ca_{1.8}Sr_{0.2}RuO_4$ for instance, the quantitative analysis of the spin fluctuation contribution to the specific heat yields a very good agreement with the measured value.

It is very remarkable that the incommensurate response resembles that of $Sr_3Ru_2O_7$ [100] in that the latter is characterized by two peaks at 0.09 and 0.25. These are nearly the same positions as in $Ca_{2-x}Sr_xRuO_4$, a difference being only that in $Sr_3Ru_2O_7$ these maxima can be well separated from each other, indicating that probably disorder effects play an important role in $Ca_{1.8}Sr_{0.2}RuO_4$.

The origin of these fluctuations is most likely a band structure effect of Fermi surface sheets which have γ-character. The band structure in this system is, unfortunately, very complicated due to the structural distortions and the very large unit cell. The existing calculations of the band structure and the Fermi surfaces show a tendency in which one can identify possible nesting vectors within the γ-sheets that can explain the observed magnetic excitations. The fact that there is only little dependence on the Sr-concentration, and that also in $Sr_3Ru_2O_7$ the response is qualitatively similar indicates that this effect does not sensitively depend on a variation of the structural

distortions nor even the existence of double layers. It can therefore not be a coincidence or a result of very special details in the band structure, but is obviously a rather robust effect.

The existence of the rotational distortion of the structure (also present in $Sr_3Ru_2O_7$), though, is probably very important. LDA calculations [45,72] have proven that the rotation of the RuO_6-octahedra mainly influences the γ-band by reducing its bandwidth. The reason is that the octahedron rotation reduces the hopping between Ru d_{xy} states via the oxygen 2p orbitals, while the *xz* and *yz* states are less affected. In addition, a t_{2g}-e_g hybridization involving the $d_{x^2-y^2}$ orbital may play a role. The increase of the density of states and the effective mass and also the increased filling above the van Hove singularity can be explained by these effects.

Consistent with these considerations is the experimental observation that the α/β subsystem of bands has only little changed. This is concluded from the observation of the nesting peak at Q=(0.3,0.3,0) ($\triangle$h,k$\simeq$0.015) which is interpreted to have the same origin as in Sr_2RuO_4 [13, 111, 123], namely the nesting of the α and β sheets of the Fermi surface. There is no detectable shift of the position of this peak. In order to infer the occupation of these bands from the position of the nesting peak, one has to assume that the whole bands are essentially unchanged (rigid) – under this condition, the occupation number $n_\alpha + n_\beta$ can be deduced to have changed less than 0.1 in comparison to Sr_2RuO_4, where the occupation is $n_{xz}+n_{yz}=\frac{8}{3}$, $n_{xy}=\frac{4}{3}$ [57].

This allows a statement concerning the debate on the issue of orbital occupations and in particular the proposed orbital selective Mott transition scenario, as discussed in the introduction at the beginning of this chapter. The OSMT scenario [60] predicts an occupation $n_{xz}+n_{yz}=3$, $n_{xy}=1$ which is in clear contradiction to the observed position of the α/β-nesting peak and the mere existence of an α and β sheet of the Fermi surface proved by the observation of this peak. Instead, this result is in accordance with for instance the LDA calculations [61,72] and the ARPES experiment [78], which find only a minor increase of n_{xy} compared to Sr_2RuO_4, compatible with the accuracy of this analysis. Concerning the recent proposal by Liebsch et al. [74], there is no indication of the postulated shift towards $(n_{xy}, n_{xz}, n_{yz}) = (1, 0.5, 0.5)$, although this is not necessarily a contradiction because the significant changes may occur only later, i. e. even closer to the metal-insulator transition which is accompanied by the first-order structural transition.

Properties of the ferromagnetic fluctuations (without field) In addition to the incommensurate antiferromagnetic part of the magnetic response, a signal of rather ferromagnetic character plays an important role in both studied concentrations.

- It dominates the spectra at low energies (below typically 1 meV) and is broadly peaked at the 2D ferromagnetic zone centres Q_{FM}.

- No internal structure can be resolved. Any incommensurability with increasing

energy transfer can be caused by the antiferromagnetic part of the response and not necessarily by an intrinsic dispersion of the ferromagnetic part. The Q-width of the signal is significant, making the standard paramagnon formula not work very well and yielding very short correlation lengths in the range of few Angstroms, which is remarkable as the system seems to be very close to a ferromagnetic instability.

- This near ferromagnetic instability manifests itself in a very small characteristic energy of the signal. In the x=0.62 sample, it reaches the low value of about 0.2 meV at 1.5 K. That the system does not reach the ferromagnetic instability is apparently related to the structural anomalies; this is most evident in $Ca_{1.8}Sr_{0.2}RuO_4$, but likely still plays a role in $Ca_{1.38}Sr_{0.62}RuO_4$.

- Its temperature dependence can be exactly related to the temperature dependence of the macroscopic susceptibility, and even quantitatively there is a good agreement.

This ferromagnetic signal is, in principle, present at both the studied Sr-concentrations. The fundamental difference is that at x=0.2 it exists only at higher temperatures (greater than $\sim$10 K). Below, it gets strongly suppressed and is nearly (though perhaps not entirely) absent at 1.5 K. This reflects the sort of crossover into the more antiferromagnetic phase that is observed in the macroscopic susceptibility and other quantities and can be regarded as an indirect consequence of the meta-magnetic transition (which is situated at some distance in the (H,T)-phase diagram). More directly, it is related to the structural anomaly at which the RuO_6 octahedra are compressed, thereby also slightly changing the orbital occupancies.

Concerning the coupling between structure and magnetism, the ferromagnetic instability is obviously very sensitively related to this structural effect. The tilted structure in general, on the other hand, which is a much larger structural effect compared to x=0.62, seems to have not such a significant effect on its own, as the higher temperature response in $Ca_{1.8}Sr_{0.2}RuO_4$ (where there are still large tilt angles of about 6°) is qualitatively similar to the one in $Ca_{1.38}Sr_{0.62}RuO_4$ without the tilt distortion. (It may well be that the symmetry of the magnetic response is lowered, which could not be detected due to the twinning of the x=0.2 crystal.) The frequently made statement that the rotational distortion of the structure enhances the tendency towards ferro-magnetism and that the tilt favors antiferromagnetism is therefore, though not wrong, at least an oversimplification. The distortion of the octahedra themselves, at first view a tiny effect, seems to be very important, too. In this context it should be mentioned that even at x<0.2 one finds true ferromagnetism, for instance in Ca_2RuO_4 at high pressure [124], which is in the L-Pbca phase [125] – so there are reasons to assume that the L-Pbca phase has in general rather a tendency to ferro- than antiferromag-

netism[29] although the tilt angles are still very large in this structure.

The incommensurate response does not significantly change over wide regions in the x-T phase diagram, so it is mainly the ferromagnetic scattering which reflects the dramatic evolution of the magnetic properties in this part of the phase diagram. In this scenario it is expected that when further approaching to x=0.5 from above, this part of the spectrum should be strongly enhanced, as Ca$_{1.5}$Sr$_{0.5}$RuO$_4$ is yet considerably closer to ferromagnetism than Ca$_{1.38}$Sr$_{0.62}$RuO$_4$. (In this respect, the choice of x=0.5 as the Sr-concentration, although close to x=0.62, would probably have been a significant difference and even better for the study of the ferromagnetic instability.) Below x=0.5, the main changes, i. e. the suppression of the ferromagnetic fluctuations, appear only at low temperature.

One may think of these materials as being governed by two competing magnetic instabilities, the incommensurate antiferromagnetic and the ferromagnetic one, with an interplay between each other that depends on Sr-concentration and temperature (and magnetic field). The antiferromagnetic response does not change significantly when varying the Sr-content, and the finite characteristic energies ($\geq$2 meV) indicate that the system is never really very close to the corresponding phase transition. Nevertheless, the antiferromagnetic fluctuations are responsible for important physical properties like the huge specific heat coefficient. The ratio between the antiferromagnetic and ferromagnetic part is changed mainly by variation of the weight of the ferromagnetic component. When being very close to the instability, it is clear that a small variation of the parameters can cause large changes and make this part dominant. Interestingly, there are probably the same electrons, namely those of the γ-band, mainly responsible in either kind of magnetic behavior.

Even at high temperature of the order of 100 K and higher, that means far away from either magnetic instability, they both determine the magnetic response which is still best described in the model consisting of these two components. With the experimentally determined temperature dependencies of the relevant parameters, one can set up a model that accounts for the change in the shape of the scans and the dominance of the ferromagnetic signal as function of energy transfer and temperature.

The magnetic field effect The metamagnetic transition in Ca$_{1.8}$Sr$_{0.2}$RuO$_4$ manifests itself in the excitation spectrum by the appearance of a prominent ferromagnetic signal. In principle, this signal must be closely related to the one that is observed at higher Sr-content or when increasing the temperature. At 10 T, a structure in the signal and a dispersive behavior can clearly be observed, and the data well be described by a damped spin wave with quadratic dispersion and a gap corresponding exactly to the external magnetic field, like a conventional ferromagnetic magnon. As the main

---

[29]...and may perhaps even be superconducting like Ca$_2$RuO$_4$ (P. Alireza, private communication) – except that this phase is not stable down to low temperature at ambient pressure.

conclusion, it is evidence for a very strong ferromagnetic interaction which is induced at the metamagnetic transition.

This is the most remarkable result of this experiment. That the state with high magnetization above the transition resembles a ferromagnet is not so self-evident as it may intuitively appear at first sight. In principle, a high magnetization can be obtained in an ideal paramagnet just by polarizing spins by an external magnetic field, and in special cases, like when a peak in the density of states exists close to the Fermi level, one can also obtain a non-linear increase of the magnetization at a certain value of the magnetic field. When polarized only by the external field, such a sample would still have to be considered as a paramagnet, and a high magnetization alone would not be so remarkable. In a ferromagnet, on the other hand, it is the strong interaction of magnetic moments that makes it favorable for the system to be in a state with finite magnetization. The finding of the magnon-like mode proves the existence of a strong ferromagnetic interaction in $Ca_{1.8}Sr_{0.2}RuO_4$. Although a magnetic field is necessary to induce this interaction, the magnetization effect is much stronger than just that of the field, demonstrating that the system is essentially in a (though field-stabilized) ferromagnetic state above the metamagnetic transition. In particular, the metamagnetic transition is thus not just due to a spin-state transition, as one might assume in a picture of more localized magnetic moments.

To some extent, this may well be relevant for other metamagnetic transitions. There are, however, not many metamagnetic transitions in itinerant electron systems studied very well, and, more particularly, it seems that this is the first system for which such a strong statement can be made. Apart this Ruthenate, inelastic neutron scattering experiments have only been published for $CeRu_2Si_2$ [126]. In that experiment, a similar effect was found, i. e. a transfer of spectral weight from incommensurate towards ferromagnetic wave vectors, but has by far not been characterized in comparable detail, and there is not yet any statement on the nature of the ferromagnetic signal. Then, of course, studies have been performed on $Sr_3Ru_2O_7$ (S. Ramos et al., not yet published), which should on the one hand be more favorable due to the better-defined metamagnetic transition, but which may on the other hand probably also be more complicated. The appearance of a ferromagnetic signal near the transition field resembles these results. In contrast, they find very strong antiferromagnetic signals even above the metamagnetic transition which have surprisingly a lower energy scale than the ferromagnetic ones and which are very anisotropic (observed only in longitudinal scans), for which there has no indication been observed in $Ca_{1.8}Sr_{0.2}RuO_4$ so far. In general, one may expect that there are many similarities between the metamagnetism in $Sr_3Ru_2O_7$ and $Ca_{1.8}Sr_{0.2}RuO_4$, as is supported by the fact that below the transition the magnetic response looks very similar. If the mentioned differences point to some fundamentally different behavior, if they are rather to be considered as details, or if they can once be resolved by more accurate experimental data on both compounds, is a very interesting question that is worth further effort.

The difference of the observed ferromagnetic mode to the paramagnon-like scattering in $Ca_{1.38}Sr_{0.62}RuO_4$ or in $Ca_{1.8}Sr_{0.2}RuO_4$ at B=0 but higher temperature is, firstly, that of course the external field induces a spin gap and that the exchange field due to the sample magnetization gaps the continuum of transverse excitations by a value likely significantly larger. Even if the observed mode would lie predominantly inside the continuum and therefore be rather of "paramagnon-character", there would remain the quantitative difference that in $Ca_{1.8}Sr_{0.2}RuO_4$ at 10 T the ferromagnetic interaction is obviously stronger than in the other cases, thereby making the dispersive character more pronounced and visible in the measurement. Intuitively speaking, directly above the transition the behavior is more ferromagnetic than in the other cases which are rather in the crossover region of the phase diagram further away from the critical end point of the metamagnetic transition.

At the transition itself, an enhancement of the fluctuations is observed as a combination of increased amplitude and reduced energy of the fluctuations. Both are rather moderate effects, but this can be traced back to the broad signature of the metamagnetic transition in the magnetization curve. A rough quantitative estimation indicates that the measured magnetic fluctuation do mostly, but not entirely account for the differential magnetic susceptibility. The enhancement, but non-existing divergence of ferromagnetic fluctuations, which drive the metamagnetic transition, is consistent with passing close, but "not *very* close", by the (quantum) critical end point of the metamagnetic transition.

4 Strontium Ruthenate

4.1 Sr_2RuO_4 and spin-triplet superconductivity

Among the layered Ruthenates, Sr_2RuO_4 is certainly by far the most prominent member. Up to thousand published papers evidence its outstanding importance and the interest from the experimental and theoretical side. This interest is based upon the superconductivity which has been discovered by Yoshiteru Maeno et al. in 1994 [38].

This discovery has to be regarded in the context of high-temperature superconductivity in the Cuprates, which had been found by Bednorz and Müller in 1986 [127], the importance of which for the development of solid state physics can probably not be overestimated. In view of the enormous activities caused by this discovery and the huge progress that had very soon been achieved, it came – eight years later – as a breakthrough to find a superconductor that is very closely related to the Cuprates, but does not contain the Copper-oxide planes that seemed to be common to all the high temperature superconductors discovered so far. It has been the first material with the layered perovskite structure besides the Cuprates in which superconductivity has been found.

It became evident quite soon that, unlike the Cuprates, Sr_2RuO_4 is not interesting for practical applications because of the low transition temperature of at best 1.5 K in the purest samples, but all the more for fundamental research. This is not only due to the fact that Ruthenium in the place of Copper provides the possibility to study some interesting differences to the Cuprates. Much more importantly, strong evidence has soon been found that Sr_2RuO_4 is, in contrast to most other superconductors known to date, a spin-triplet superconductor. Spin-triplet pairing is a highly interesting concept, and while it is well established for superfluid ^{3}He [128, 129], it has been a long-standing question if it does in reality also apply to superconductivity. Among some other materials, like for instance UPt_3 [130], UGe_2 [131] and others, Sr_2RuO_4 is a very – perhaps the most – promising candidate, because by now there is very strong evidence for triplet pairing. Moreover, it is experimentally relatively well accessible because large and high-quality crystals are available and superconductivity appears at ambient pressure and still not *too* low temperature.

Despite the huge effort, the superconductivity in Sr_2RuO_4 is still being far from understood. This applies not only to the detailed nature of the superconducting state and the pairing mechanism, but even the triplet state at all is still disputed by some researchers.

Soon after the discovery of superconductivity, and before the first experimental evidence, the proposal of a triplet state by Rice and Sigrist in 1995 [132] has had a strong impact on the future work on Sr_2RuO_4.

While a number of results demonstrate the unconventional (non s-wave) nature of the superconducting state [133], the proof of triplet pairing is less simple. A strong experimental support of triplet superconductivity came from the measurement of the spin susceptibility by NMR Knight shift [134, 135] (and later by polarized neutron scattering [136]) which is unchanged upon cooling through T_C. This is expected for some of the possible triplet states and in clear contradiction to singlet superconductivity, so it is indeed a strong argument for the triplet state. Some difficulty, however, arises from the observation of the Knight shift for other field directions [137] which is not compatible with the explanation and could only be resolved by assuming that the d-vector of the superconducting gap changes its direction with the applied field. While these measurements probe the spin part of the wave function, a probe of the spatial part, i. e. a proof for odd parity, has been provided by a phase sensitive experiment using the Josephson effect in superconducting quantum interference devices [138, 139]. Again, it has been argued that a certain chiral d-wave (singlet) state might be consistent with these results [140]. Finally, the role of phonons is not entirely clear (note that also an isotope effect has been observed in Sr_2RuO_4 [141]); while phonons alone would favor an s-wave state, they might play a role in combination with a magnetic mechanism [142]. Despite all these considerations, however, the very most widely accepted picture by now is that Sr_2RuO_4 is a spin-triplet superconductor and that magnetic fluctuations provide the explanation for the pairing mechanism.

In order to stabilize a triplet state, magnetic fluctuations should have ferromagnetic character. An apparent problem is that the dominant magnetic fluctuations in Sr_2RuO_4 have more antiferromagnetic than ferromagnetic character [111] and would rather be expected to stabilize a d-wave singlet state. It is difficult to resolve this issue[1], and the existence of ferromagnetic fluctuations still appears as the most favorable explanation. If present, the crucial question is whether they are strong enough, so quantitative information is very important.

By regarding the magnetic fluctuations, this chapter contributes to the effort of identifying a mechanism for spin-triplet pairing, because the pairing is most likely related to magnetic fluctuations. Both their intensity and Q-dependence is important, and neutron scattering is in principle the best suited experimental tool to provide quantitative information about the magnetic fluctuations and thus for testing different proposals concerning the superconducting pairing mechanism. Some results on Sr_2RuO_4 doped with small amounts of Titanium are not directly relevant for superconductivity, but are a means to better study the magnetic excitations and add, in terms of a magnetically ordered state, further interesting aspects to the system.

---

[1]For instance, a large anisotropy of the fluctuations has been proposed as a way out [143]. This is, however, not quantitatively consistent with the experiment [144, 145].

4.2 Basic properties of Sr$_2$RuO$_4$ and magnetic fluctuations

As a result of the great interest that the discovery of superconductivity has attracted, Sr$_2$RuO$_4$ is by now very well studied by many different experimental techniques, most of which could be applied in the superconducting as well as in the normal state. As a material that can be prepared with extremely low disorder (residual resistivity below 1 $\mu\Omega$cm [146]) it is, in addition to many other techniques, accessible to quantum-oscillation measurements which have greatly contributed to the knowledge about its electronic structure. An extensive overview over all these measurements and a detailed summary of the properties of Sr$_2$RuO$_4$ is given in a review article by Mackenzie and Maeno [133], with special emphasis on the superconductivity.

Sr$_2$RuO$_4$ is a paramagnetic metal with pronounced two-dimensionality and Fermi-liquid properties at low temperature. Of particular importance – especially for the magnetic behavior – is the electronic structure and the Fermi surface. Fortunately, this is known for Sr$_2$RuO$_4$ to a great level of detail not only from a number of calculations [147–154], but also from complimentary experimental techniques like ARPES [113, 114, 155–157] and quantum oscillations [57, 158–160]. The agreement between the two latter techniques has, after some initial controversy due to surface effects, even become a prime example for the success of the ARPES technique. Also with the calculations, the agreement is in general very good.

The three partially occupied t$_{2g}$ states of the Ru^{4+} ion yield three sheets of the Fermi surface that are of essentially two-dimensional character (only weakly corrugated along the c-direction). A detailed summary of the Fermi surface properties is for instance given by Bergemann et al. in Reference [160]. The parameters given in this reference, which are based on a fit to the experimental results, have been used to calculate the band susceptibility via the Lindhard function according to the remarks in Chapter 2.2 (see Figure 4.1).

The susceptibility of Sr$_2$RuO$_4$ is nearly constant as function of temperature and amounts to about 28 $\frac{\mu_B^2}{eV}$ [161] and has a very small anisotropy between the a,b-plane and the c-axis, for which it is only a few percent higher. The density of states at the Fermi level is by different band structure calculations [147–149] given as approximately 4 states/eV·cell or slightly above. The enhancement of the susceptibility above its band structure value is thus about 6-7. Also the electronic specific heat coefficient of about 38 mJ/mol·K^2 is enhanced over its band structure value by a factor 3-4 (yielding a Wilson ratio of $\sim$2). These enhancements are to be regarded as an indication of strong electron correlation. From the Stoner enhancement factor $(1 - I \cdot \rho(E_F))^{-1}$ one can estimate the exchange interaction I.

Despite this enhancement, Sr$_2$RuO$_4$ is definitely not particularly close to a ferromagnetic instability (as for instance SrRuO$_3$ or Sr$_4$Ru$_3$O$_{10}$, which are ferromagnetic). In contrast, Sr$_2$RuO$_4$ is close to incommensurate antiferromagnetic order. The α and
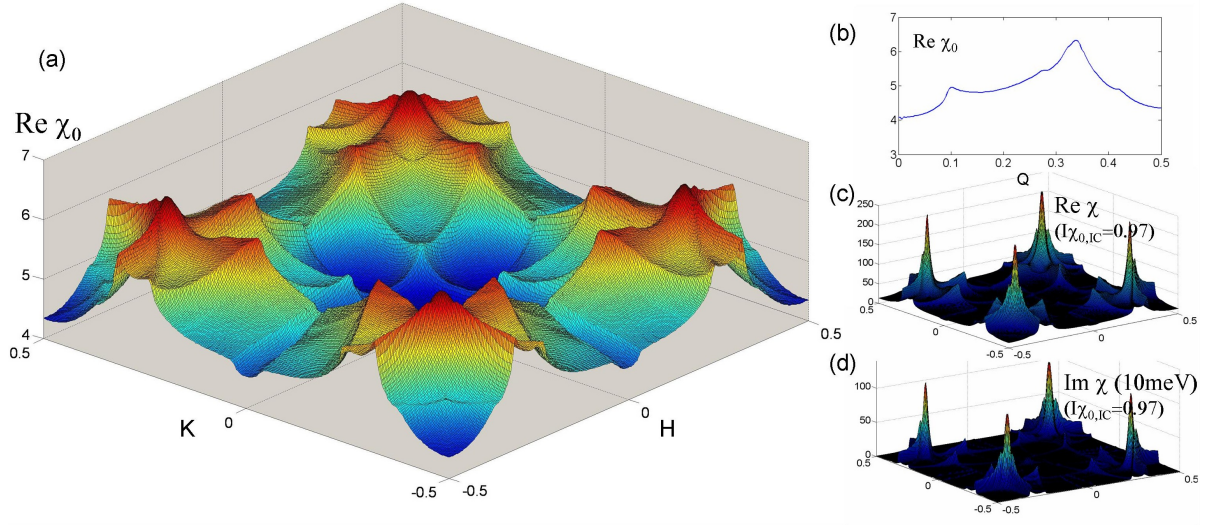
Figure 4.1: Susceptibility of Sr_2RuO_4 calculated from the band structure. (a) Real part of χ at zero frequency (Lindhard function) throughout the Brillouin zone and (b) for a diagonal scan from (0,0,0) to (0.5,0.5,0). (c) and (d) interacting susceptibility for $I \cdot \chi^0_{Q=Q_{IC}} = 0.97$ and constant I: real part ($\omega=0$) and imaginary part ($\omega=10$ meV). All units are μ_B^2/eV per Ru.

β sheet of the Fermi surface are nested at a wave vector $Q_{IC}=(0.3,0.3,0)$. In the Lindhard function, there is thus a large weight at this wave vector, and the corresponding maxima are the most prominent features in the plot of $\chi'_0(q)$ in Figure 4.1. This essential result has been found in calculations by a number of different authors[2]. The height of these maxima, though, appears rather modest in view of the absolute values of χ_0 throughout the Brillouin zone, but it has to be kept in mind that the effect of the denominator in the Stoner formula (2.17) can be dramatic even for small absolute variations if it is small, and secondly the imaginary part is more sensitive to the nesting condition and has much more pronounced maxima.

In Figure 4.2, the effect of how the fluctuations become critically enhanced by an increasing strength of the interaction parameter is illustrated in detail. It shows only that part of the susceptibility which originates from the α and β band, for different values of the Stoner enhancement factor, and demonstrates how the system becomes critical and approaches the magnetic instability. This is reflected as a drastic change in the imaginary part – sharp features with rapidly increasing intensity appear, and the energy spectra show the slowing down of these fluctuations. Although this illustration

---

[2]A brief discussion concerning the relevance of the complicated fine structure is given later in this chapter (Section 4.3.5). In part, they depend on details of the calculation and the assumed band structure parameters. Publications containing calculations of χ_0 include References [13,14,123,160, 162–167].
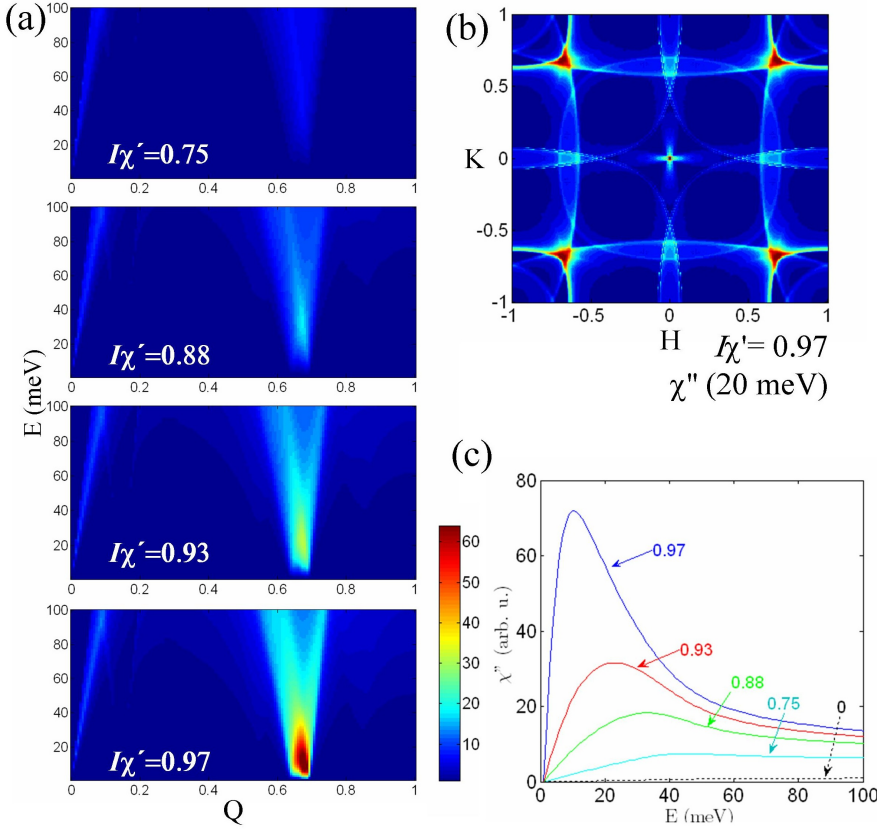
Figure 4.2: The imaginary part of the susceptibility of the α- and β-band calculated via the Lindhard function. (a): $\chi''(\mathbf{Q}, \omega)$ for different values of I. (b): χ'' as function of Q for constant energy (weak features enhanced). (c) Energy spectrum of χ'' at the nesting vector for the four cases in (a) and the bare susceptibility (dashed line). (Units are arbitrary.)

shows only the effect of α and β, the γ band does not significantly change the picture in the vicinity of Q_{IC}; on its own, it has no feature of comparable strength.

The fluctuations at Q_{IC} thus dominate the response in inelastic neutron scattering [111, 112, 123], and an estimate based on these neutron data yields $I\chi'_{ic} \sim 0.97$ [111]. By these measurements, the incommensurate signals are by now quite well characterized, but the question for the possible existence of magnetic response at other wave vectors has not been answered. If present, it is clear that such signals would be relatively weak. While some indication exists, it has not been possible to unambiguously resolve a signal at any other wave vector[3], in particular close to the zone centre. From the quantitative analysis of NMR data [134, 144, 168–171] it has been suggested that magnetic fluctuations of ferromagnetic character probably exist in addition to the incommensurate ones, but as this technique cannot directly probe the Q-dependence of χ'', the argumentation is quite involved and the conclusions have been partly contradictory.

---

[3]Except maybe an asymmetry / "shoulder" of the incommensurate peak [123].

Figure 4.3: Diagonal scan at 8 meV at 2 and 150 K. The open symbols have been measured with unpolarized neutrons on 2T; by use of polarized neutrons (IN20, H∥Q) it is possible to distinguish the magnetic or non-magnetic character of the various peaks.
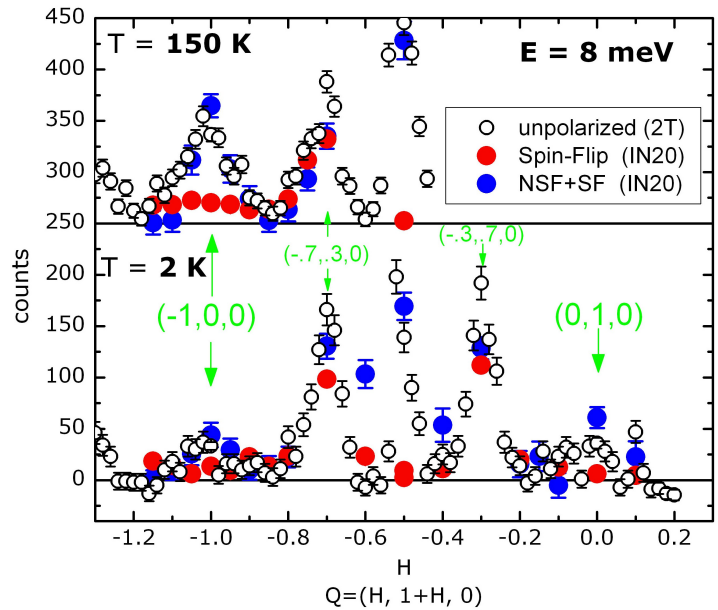
4.3 Measurement of magnetic excitations in Sr_2RuO_4 by inelastic neutron scattering

4.3.1 Neutron scattering experiments on Sr_2RuO_4

Although magnetic fluctuations in Sr_2RuO_4 are "strong" in the sense that the system is nearly critical and the excitations near the wave vector Q_{IC} clearly dominate the continuum, there are two major difficulties that need to be overcome in a neutron scattering experiment when trying to measure the magnetic fluctuations: firstly, their intensity is, on an absolute scale, still relatively weak (weaker than, for instance, the dominant signals in $Ca_{2-x}Sr_xRuO_4$ – on an absolute scale, roughly a factor 5), and secondly, the interesting energy ranges are such that there is a significant contribution from phonon scattering, which makes it nearly impossible to resolve the magnetic signal in an experiment with unpolarized neutrons. The use of polarized neutrons solves this second problem, but aggravates the first one, namely reduces the intensity by approximately another order of magnitude.

Unlike in some of the other cases, the availability of crystals has not been a problem here, so a large sample volume could be achieved by coaligning ten large single crystals of typically 3 cm length and 3-4 mm diameter each. This sample mount has been oriented in the a,b-plane and has been used in experiments on IN20 at the ILL and on 2T at the LLB. On IN20, the standard polarized neutron setup has been used with Heusler monochromator and analyzer and with Helmholtz coils at the sample position to allow the free choice of the neutron polarization direction. All measurements were performed with k_f=4.1 $Å^{-1}$ and with a PG filter. 2T was operated
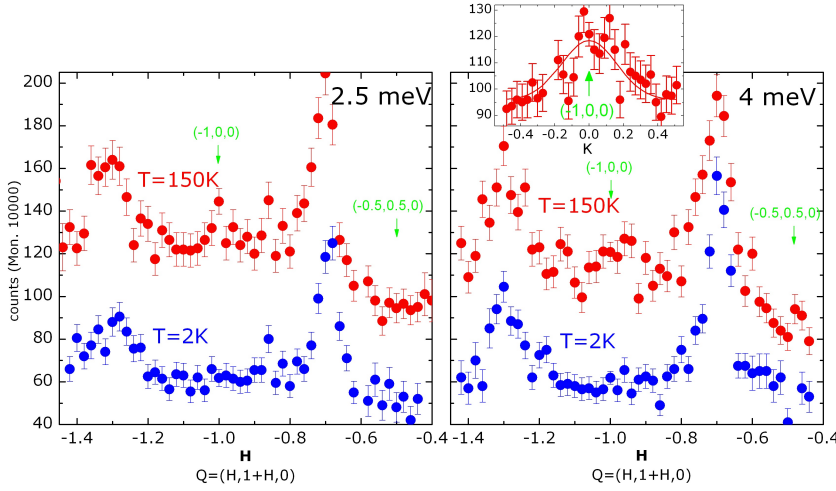
Figure 4.4: Diagonal scan with unpolarized neutrons at 2.5 and 4 meV (original count rate, no background correction, no offset). Inset: transverse scan across (-1,0,0) at T=150 K.

in its standard (unpolarized) setup with k_f=2.662 Å^{-1} (mostly) and k_f=4.1 Å^{-1} with two PG filters.

Thanks to the large sample, the intensity in the unpolarized experiment is relatively high, but as the accessible energy range is very limited by the need to avoid contamination from other signals, there is no significant gain in information compared to the previous experiment [111, 123], especially concerning the shape of the quasi-ferromagnetic scattering. Figure 4.3 shows a scan that runs along more than an entire diagonal of the Brillouin zone, thereby crossing the ferromagnetic wave vectors Q_{FM}, (-1,0,0) and (0,1,0), and the incommensurate peaks Q_{IC} at (-0.7,0.3,0) and at (-0.3,0.7,0). There are well pronounced maxima at any of these positions, and another one at (-0.5,0.5,0). By comparison with the data from the polarized experiment, one can decide which of these signals have magnetic origin. For this purpose, the data for the spin-flip channel and its sum with the non-spin-flip channel are, after multiplication with an appropriate scale factor, overlayed to the unpolarized data. As this data has been taken with the neutron spin polarization parallel to the scattering vector, any magnetic scattering is contained in the spin-flip channel, cf. Equation (2.3). It proves that the intensity at (-0.5,0.5,0) is entirely non-magnetic. Also, the largest part of the intensity near Q_{FM} is non-magnetic. What exactly is the origin of this intensity, is not entirely clear. Besides the general possibility of a spurious signal of unknown origin, phonon scattering is the most likely explanation, and the phonon dispersion [10] indeed contains branches with energies of this order at the zone boundaries. Its presence at other Bragg points like (2,1,0) and (3,0,0) further proves the non-magnetic character of this signal.

At even lower energy transfer one may exclude a phonon contribution (except acoustic phonons at the Γ-point). Figure 4.4 shows diagonal scans at two such energy transfers, 2.5 and 4 meV, at low and high temperature. The strong peak at (-0.5,0.5,0) has completely disappeared, and also the relatively sharp signal at Q_{FM}
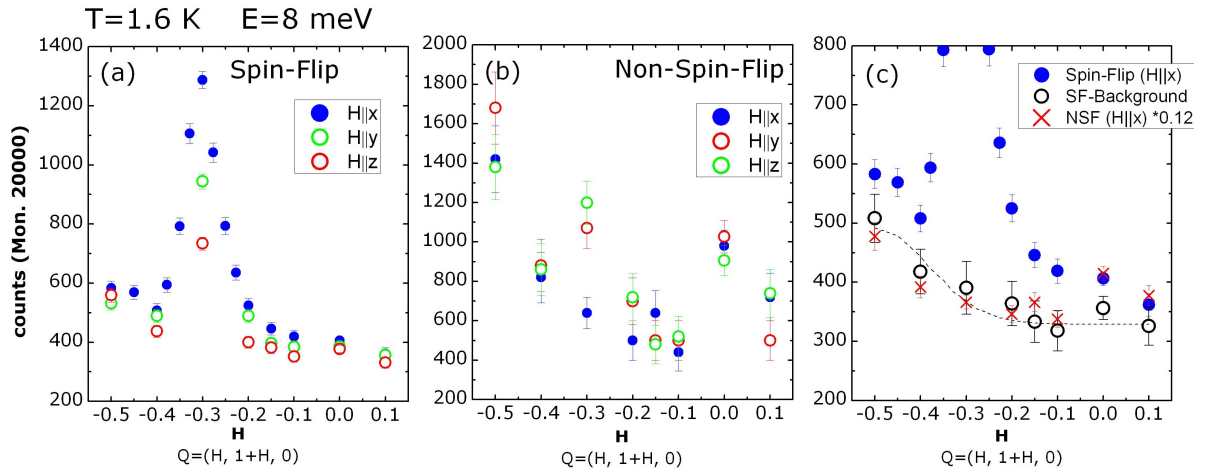
Figure 4.5: Diagonal scan at 8 meV on IN20 (scan runs across (-0.3,0.7,0) and (0,1,0)). (a) the three spin-flip count rates, (b) the three non-spin-flip count rates, and (c) a background analysis: The spin-flip background calculated from the spin-flip count rates, as function of scattering angle only (dashed line), and the non-spin-flip count rate (red crosses) divided by the flipping ratio and shifted by a constant offset.

is no longer present. The two incommensurate peaks are clearly visible, and the left one is weakened by a factor ∼2.5 compared to the right one due to the magnetic form factor. Around (-1,0,0), there is clearly higher intensity than at (-0.5,0.5,0), especially at T=150 K, and the transverse scan at 4 meV and 150 K (inset) supports this statement.

While this is an indication for the presence of a broad signal around Q_{FM} and somewhat confirms the intensity map in Ref. [123] which has been interpreted in a similar way there, it is not a proof of its magnetic character. In addition to the presence of definitely non-magnetic signals at higher energy (cf. Fig. 4.3 – only if purely phononic they could safely be excluded here), some doubt against it might arise from some poorly understood spurious signals at other places in reciprocal space[4] and from the difficulty to unambiguously define a background (which is strongly temperature dependent and increases with scattering angle). These data are thus not sufficient for a strong quantitative statement.

4.3.2 Polarization analysis

For a quantitative analysis, it is essential to regard the polarization analysis which supplies the desired information. A total of more than three weeks of beam-time has

---

[4]In this respect, the large sample volume is a disadvantage: by allowing to measure weak magnetic signals, also some "undesired" and usually negligible signals out of the vast number of possible spurious effects become visible.

been spent to study the magnetic excitations in Sr_2RuO_4 on IN20, the first of which was dedicated only to the study of the anisotropy of the incommensurate signals and is discussed already in the References [145] and [108]. Figure 4.5 shows a representative scan along the diagonal of the Brillouin zone, thereby running through both the incommensurate and the ferromagnetic Q-positions. The full polarization analysis is shown for the spin-flip (a) and the non-spin-flip (b) channels; the polarization directions x,y,z correspond to the scattering vector (x), the vertical direction (z) and the remaining in-plane direction (y), like in Eq. (2.3). (The spin-flip signals have been counted longer, so have shorter error bars.) As discussed in Chapter 2.1.2, the spin-flip count rates contain the magnetic signal that is both perpendicular to the scattering vector and to the neutron polarization, i. e. the x-signal contains the in-plane and out-of-plane component of χ'', while the others contain only one. In non-spin-flip, the x-signal contains none, and the others contain one component each. This is well comprehensible in the data in Figure 4.5, which also clearly shows the anisotropy of the incommensurate signal at (-0.3,0.7,0) in (a). The enhancement at (0,1,0) is present only in the non-spin-flip channel, which proves its non-magnetic character. The flipping ratio is not perfect, which may be a consequence of the large sample, the focusing conditions etc., and had values typically only in the range of 8-10 during the different experiments. Any non-spin-flip signal is therefore also present, reduced by this factor, in the spin-flip case, and vice versa. The finite flipping ratio, as determined on a phonon, has been considered in the treatment of the polarized data.

The final analysis has been performed on the spin-flip data only. It is better suited because it contains most of the magnetic scattering and has a lower background, and has therefore been measured with much better statistics. While the incommensurate peaks are well pronounced and can easily be measured with good statistics, a precise background determination is absolutely essential to resolve broad (weakly Q-dependent) and weak signals. The spin-flip background can be calculated by linear combination of the equations (2.3). As a result of taking the differences of count rates, the so obtained errors are relatively large (Fig. 4.5). The variation of the background as function of Q contains a part that depends on the scattering angle (which goes down to about 14° in the scan in Figure 4.5c) – by regarding many Q-scans, a function depending on the scattering angle could be fitted, which is shown in the figure as a dashed line. The variation of the background also reflects the variation of the non-spin-flip count rates; this is the part of the background that is due to the finite flipping efficiency. Although in the analysis of the magnetic signals, the magnitude of the magnetic part has, wherever possible, been obtained from the polarization analysis, these considerations show that the background, which is crucial for the results presented now, is relatively well understood and properly treated.

The results of the polarization analysis for scans parallel and diagonal to the zone axes are shown in Figures 4.6, 4.7 (for T=1.6 K) and 4.8 (T=150 K). In these figures, the sum of the two magnetic components (in-plane plus out-of-plane) is shown; this
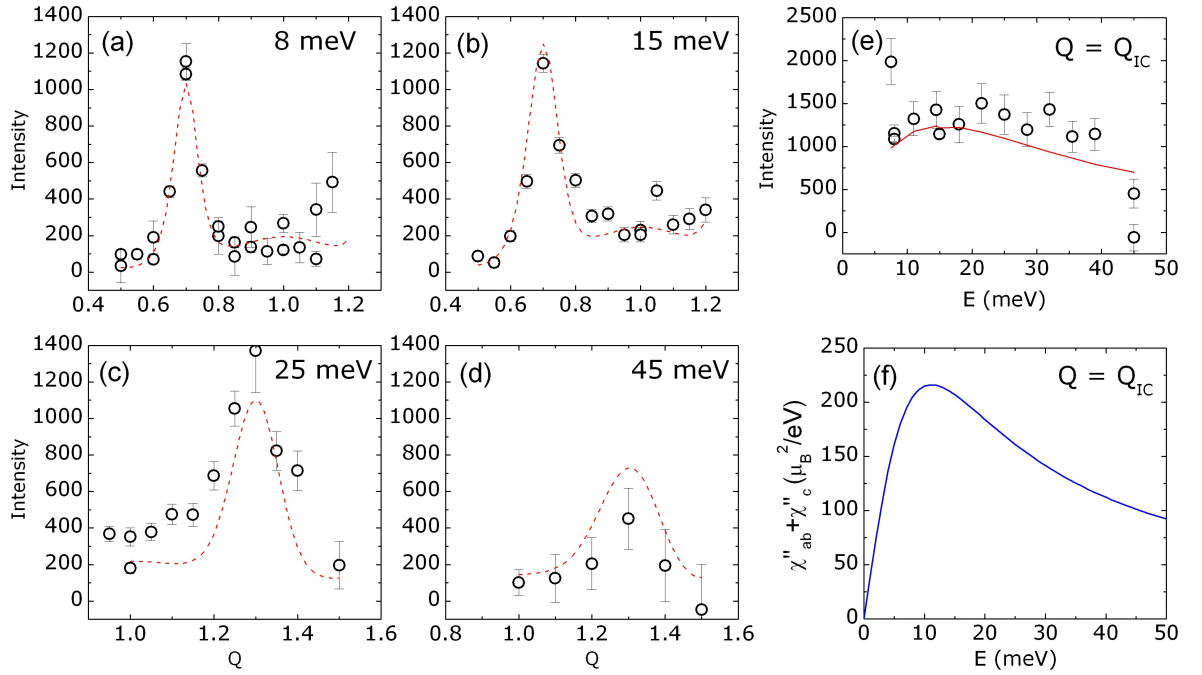
Figure 4.6: Magnetic signal (sum of in-plane and out-of-plane component) along diagonal scans at 1.6 K. Note that there is no background in this presentation (eliminated by polarization analysis). For kinematic reasons, the scan paths are not identical, but all run through one incommensurate peak towards (1,0,0). The signal has been corrected for the magnetic form factor and the Bose factor. Dashed lines are the values of the fit function (model convolved with the resolution function). In (e), an energy scan on the position of the incommensurate peaks is shown. The corresponding true susceptibility in absolute units is shown in (f).

is, apart flipping ratio corrections, basically the spin-flip signal for H‖x minus the spin-flip background. As the incident flux decreases significantly towards high energy, the data at high energy transfers tend to be less precise than at low energy transfers. Additionally, it is necessary for kinematic reasons (closing the scattering triangle, experimental limitations due to scattering angle, currents in the coils etc.) to work at different, though equivalent, Q-vectors (for instance (0.7,0.3,0) and (1.3,0.3,0)) at the different energy transfers. Therefore, the correction for the magnetic form factor has been applied in the figures in order to make the scans better comparable.

At first glance, these data may look neither very precise nor convincing, in particular in view of the fact that this is nearly all data that has been obtained during the measurements on IN20. The limited statistics confirm the statement that these measurements are extremely difficult even with the large sample and the high (probably the world's highest polarized) incident neutron flux. Thanks to the polarization analysis one can, however, draw much stronger conclusions than the first impres-
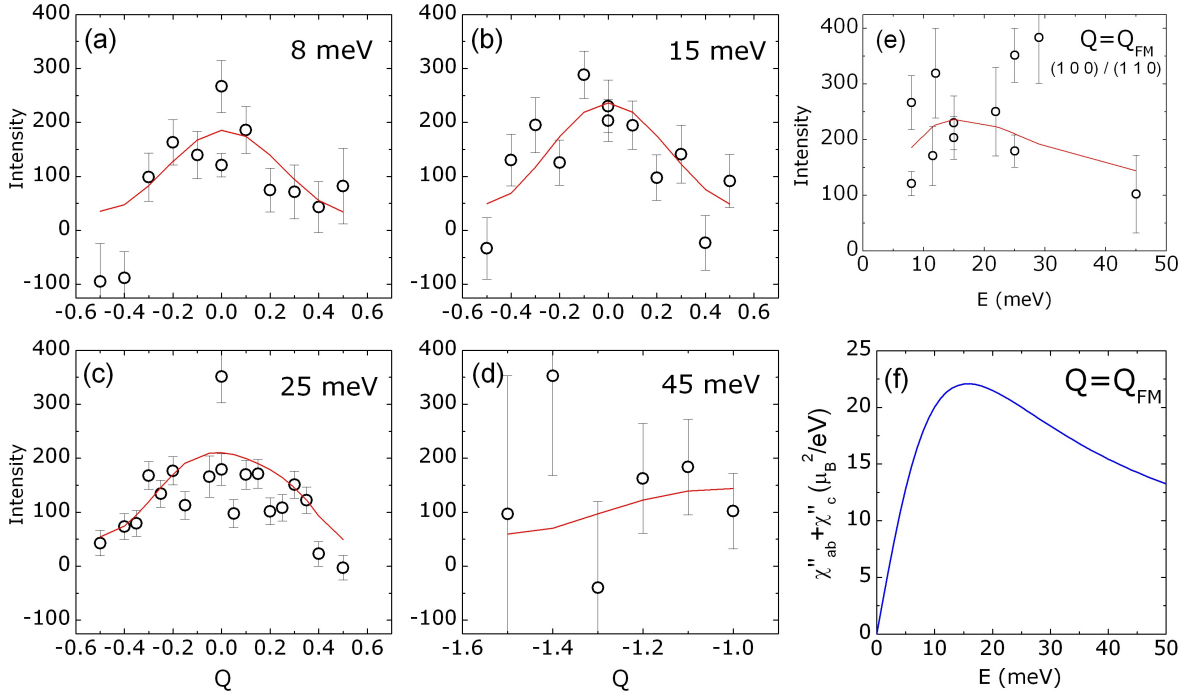
Figure 4.7: Magnetic signal (sum of in-plane and out-of-plane component) at 1.6 K along scans parallel to the a*/b* axes of the Brillouin zone. The same comments as in Figure 4.6 apply. The energy scan (e) shows the signal on the ferromagnetic wave vectors, and (f) is the corresponding susceptibility in real units.

sion might be. The first very important information is that in nearly all scans, there is nonzero intensity at the ferromagnetic wave vectors. Compared to the well-known incommensurate peaks, it is much weaker and broader in Q. In view of the statistics it has to be stressed that as a result of the polarization analysis, there is strictly no background underlying the data points; any positive intensity is thus truly magnetic. At some points, low statistics might cause some doubt at first sight, but the entirety of the measured points do, due to their great number, unambiguously prove the presence of a magnetic signal around the zone centre.

The second important information that is obtained from these data is the quantitative one. The calibration of the scattered intensity into absolute susceptibility units has been performed by using an acoustic phonon near (2,0,0) following the procedure described in Chapter 2.1.3 and the appendix A.1, and provides the value of the susceptibility at any Q-vector.

Thirdly, the polarization analysis gives no indication for an anisotropy of the magnetic response except at the incommensurate peak positions. Although where the signal is weak, the limitation in statistics is quite severe, in the average of the data at different energies the out-of-plane and in-plane components are identical.

4.3.3 Quantitative analysis of the susceptibility

For the description of the magnetic response, a simple phenomenological model is used. It consists of two parts: firstly, the incommensurate peaks centred at positions $(\pm 0.3, \pm 0.3, L)$ around any reciprocal lattice vector with integer H and K, and secondly the broad and weakly Q-dependent part. As it seems to be maximum at the (2D) zone centres, it will be called *ferromagnetic* for simplicity, although it is spread over a very large region of the Brillouin zone. The magnetic response is thus modelled as

$$\chi''(q,\omega) = \chi''_{IC}(q,\omega) + \chi''_{FM}(q,\omega) \tag{4.1}$$

As an expression for χ''_{IC}, Equation (2.29), which describes the magnetic response near an antiferromagnetic instability is well suited and physically well justified in this case. It depends on the parameters χ_{IC} (the real part of the susceptibility at $\omega=0$ and $Q=Q_{IC}$), the characteristic energy (ε or Γ) and a correlation length ξ (their anisotropy is neglected here).

For χ''_{FM} it is less obvious how it can appropriately be modelled, and the data do not reveal any special features or characteristics (like a dispersion or other particular Q-dependence) that indicate how to describe it. Therefore, its Q-dependence has been phenomenologically fitted by a broad Gaussian decay, characterized by its width (FWHM) W, and its energy dependence is incorporated as the usual single relaxor form with the characteristic energy Γ_{FM}:

$$\chi''_{FM}(q,\omega) = \chi'_{FM} \cdot \frac{\omega \Gamma_{FM}}{\omega^2 + \Gamma^2_{FM}} \cdot \exp\left(-\frac{\tilde{q}^2}{W^2} 4\ln(2)\right) \tag{4.2}$$

where $\tilde{Q}$ is the distance of Q to the nearest (2D-) Bragg point.

The results of a global fit to the whole data set are:

Table 4.1: Results of the fit to the model (4.1) with the polarized Sr$_2$RuO$_4$-data.

		T=1.6 K			T=150 K	
χ'_{FM}	=	22	± 1	$\frac{\mu_B^2}{eV}$ per Ru	22	± 2
W	=	0.53	± 0.04	r.l.u. ($\frac{2\pi}{a}$)	0.47	± 0.06
Γ_{FM}	=	15.5	± 1.4	meV	19.0	± 3.5
χ'_{IC}	=	213	± 10	$\frac{\mu_B^2}{eV}$ per Ru	89	± 7
ξ_{IC}	=	9.7	± 0.5	Å	6.1	± 0.5
Γ_{IC}	=	11.1	± 0.8	meV	17.8	± 2.9

The values given for the susceptibilities are the real parts (at zero frequency) for one component. For the ferromagnetic signal there is no detectable anisotropy and χ'_{FM} should correspond to the macroscopic susceptibility. On the incommensurate peak, this is only the average; in view of the anisotropy [145], χ'_c is larger and χ'_{ab} is smaller than this value. In general, the data at 150 K are less precise because less
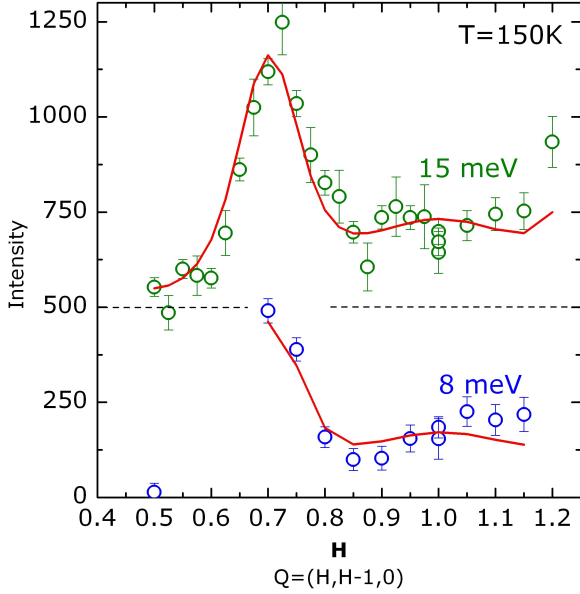
Figure 4.8: Magnetic signal (sum of in-plane and out-of-plane component) at 150 K along diagonal scans. Presentation corresponding to Figures 4.6 and 4.7. Data at 15 meV are shifted by 500 counts.

data has been collected at this temperature (120 independent data points at 1.6 K and 76 at 150 K).

The obtained values for χ'_{IC} and Γ_{IC} are at both temperatures of the same order as the ones given in References [111, 123], where this signal has been very thoroughly studied. The widths of the peak cannot be well determined here, because the density of data points is too low. The given values for ξ_{IC} may therefore be not very reliable, but the qualitative decrease to higher temperature is certainly correct. The obtained values of χ'_{IC} and Γ_{IC} at 1.6 K are slightly higher than in Ref. [111], like the one for Γ_{IC} of 11±1 meV. Here, the signal has been followed to much higher energy transfers, but with a smaller number of independent points; in Ref. [145], 8 and 13 meV are given for the out-of-plane and in-plane component, respectively, so this result is roughly consistent with the previous one. Even here, though, the agreement of the fitted spectrum with the energy scan is not perfect, and more correctly one should regard the two components (in-plane and out-of-plane) separately and then take their superposition.

More relevant in the current context is the ferromagnetic part. In contrast to the incommensurate signal, it is very little temperature dependent – there is no statistically significant change in any of the three parameters. In particular, the susceptibility remains constant, which is in very good agreement with the macroscopic measurement [161]. The value of the macroscopic susceptibility, however, is about 28 μ_B^2/eV. Normally, these values should be identical. The deviation of 20% is significant, but appears not very dramatic. If it was due to an inexact calibration, also the value of χ_{IC} would have to be corrected by the same ratio. As another possibility, it may also be related to the model itself – either the Q-dependence (some points seem to lie higher)
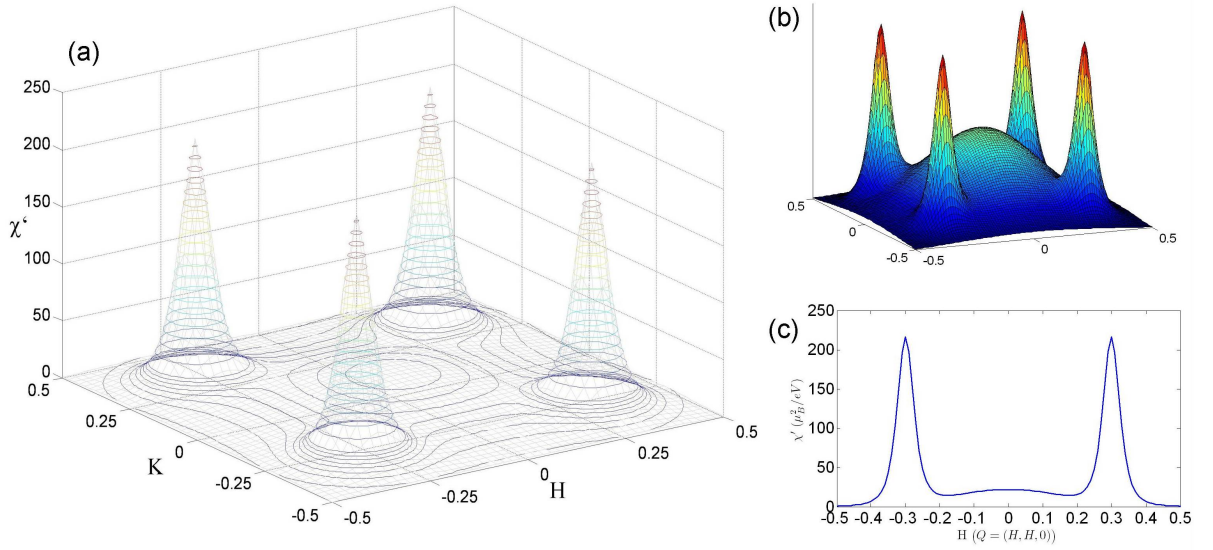
Figure 4.9: The real part of the susceptibility ($\omega = 0$) in Sr_2RuO_4 at 1.6 K throughout one Brillouin zone, modelled by (4.1) with the fitted parameters. (a) $\chi'(q)$ in $\frac{\mu_B^2}{eV}$ per Ru (contour lines: steps 2.5/10 below/above 20). (b) a sketch of the same model, but with the ferromagnetic part artificially enhanced by a factor 5. (c) a cut along the diagonal.

or the energy dependence may be not correctly captured. Especially the latter is not evident from the data; it is very important to note that the extracted value of χ'_{FM} relies on the assumption that the spectrum is relaxor-like. One might also speculate that there is another contribution to the spectrum, presumably at lower energies (see for instance Ref. [119] for a similar scenario in UPt$_3$), but it would have to be very small.

As this signal is independent of temperature while the incommensurate signal decreases, it becomes more dominant at high temperature, and while its relative strength is only about 10% at 1.6 K, it is a quarter at 150 K. The real part of the wave-vector dependent susceptibility within the model (4.1) at low temperature is shown in Figure 4.9.

The Q-extension of the signal is quite substantial. The slow variation with Q makes it indistinguishable from the background in a standard (unpolarized) neutron scattering experiment. With its width of about half the reciprocal lattice vector $2\pi/a$ it covers nearly the whole Brillouin zone; only at the truly antiferromagnetic vectors (0.5,0.5,0) its intensity is negligible. Although, as noted above, the term "ferromagnetic" does not apply in its strict sense to this signal, the approximation with a constant value throughout the Brillouin zone would also be a severe oversimplification.

Origin of the ferromagnetic signal In view of the description of the susceptibility which divides it into two parts – the incommensurate antiferromagnetic and the weakly q-dependent ferromagnetic one – these two parts are sometimes assigned to the α/β and to the γ band, respectively. Then, it is readily argued that the fluctuations in the γ band, which probably is the "active" one for superconductivity, are ferromagnetic, which is in agreement with spin triplet pairing. In other words, the broad ferromagnetic fluctuations would then drive the superconducting pairing, while the incommensurate peaks are considered as irrelevant.

However, while the assignment to the bands is absolutely reasonable for the incommensurate peaks, some caution is appropriate in simply assigning the ferromagnetic part to the γ band, although there is no doubt that it has a stronger tendency towards ferromagnetism than the others. For an electron in the γ band, the susceptibility around Q=0 is indeed higher, reflecting the enhanced density of states in the vicinity to the van Hove singularity, and $\chi(Q)$ even has some peaks on the diagonals (near Q=0.1) which arise from a weak nesting effect of the γ Fermi surfaces. (These peaks are, though, significantly weaker than the ones at Q_{IC}.) Nevertheless, also the α/β contribution to the susceptibility is significant and, because they contain twice as many electrons, larger over wide regions of the Brillouin zone, including at small Q's. It seems thus not justified to speak of a pure γ band signal.[5]

4.3.4 Comparison with NMR data

These results may be compared to measurements of nuclear magnetic resonance (NMR). This is interesting because the NMR technique also probes the magnetic fluctuations, but in a different way than inelastic neutron scattering. In NMR, one can measure the nuclear spin-lattice relaxation rate $\frac{1}{T_1}$, which is the relaxation rate of the nuclear magnetization to its thermal equilibrium. When divided by the temperature T, it can be expressed as [12]

$$\frac{1}{T_1 T} = \frac{k_B \gamma_N^2}{(g\mu_B)^2} \sum_q |A(q)|^2 \frac{\chi''(q,\omega)}{\omega} \tag{4.3}$$

Here, γ_N is the gyromagnetic ratio for the nucleus[6] $A(q)$ is the hyperfine coupling, which is an important and non-trivial ingredient that can in some cases, if it has a certain Q-dependence, allow for a distinction of contributions from different Q. Its correct determination, however, can also cause some complications[7]. Similar to neutron

---

[5]In this sense, also the incommensurate peak is not a pure α/β-signal, although here it is much clearer that they give by far the main contribution.

[6]Values of $\gamma_N/2\pi$ are 2.193 MHz/T for ^{101}Ru [137] and 5.772 MHz/T for ^{17}O [169].

[7]For 101Ru, $A(q) = -250$kOe/μ_B [135] (older value from Ref. [170] -300kOe/μ_B), independent of q. For ^{17}O, $A(q)$ is q-dependent and vanishes at q=(0.5,0.5,0) for geometric reasons on the (in-plane) O(1) site. The form $|A(q)|^2 = A^2[1+\frac{1}{2}(cos(q_h a)+cos(q_k b))]$ has been suggested [172] with $A = -18.5$

scattering, different components of χ'' have to be summed up (those perpendicular to the field). This allows a determination of anisotropies, as for instance in Reference [144]. In (4.3) this sum is not explicitly written; for an isotropic case, a factor 2 has to be inserted.

As the typical resonance frequencies are in the range of MHz and thus by far lower than the characteristic energy scales, NMR probes the slope of χ'' in the limit $\omega \to 0$ with respect to neutron scattering (ω's of the order THz). The obtained values for $\frac{1}{T_1 T}$ are thus simply the Brillouin zone average of the magnetic fluctuations in the zero frequency limit. They do, without further analysis, not provide any information about the Q-dependence and the antiferromagnetic or ferromagnetic nature of the signal, nor the characteristic energies.

A series of NMR measurements on both ^{17}O and ^{101}Ru have been carried out [134, 144, 168–170]. They find a temperature dependent signal which increases by a factor 2-3 between room temperature and low temperature. It has been shown [111, 144] that the absolute increase of the signal reflects the temperature dependence of the contribution from the incommensurate peaks. In addition, there seems to be a temperature-independent offset which has been ascribed to ferromagnetic fluctuations. Qualitatively, this is in obvious agreement with the new neutron results, because they prove that the broad ferromagnetic component does not change as function of temperature, in contrast to the incommensurate one. As it occupies a larger portion of the Brillouin zone, its contribution to the sum (4.3) is relatively large despite its small amplitude.

To make the analysis more quantitative, the averages over the Brillouin zone in the zero frequency limit, $\sum_q \chi''(q,\omega)/\omega$, can straightforwardly be evaluated. The results are (in $\frac{\mu_B^2}{\text{eV}}\text{meV}^{-1}$):

Table 4.2: Brillouin zone averages of the magnetic fluctuations in Sr$_2$RuO$_4$ (sum of in-plane and out-of-plane component); first value plain average, second value weighted with the $(1 + \frac{1}{2}(cos(q_h a) + cos(q_k b)))$ term. The two last columns are the resulting relaxation rates in s^{-1}K^{-1} under the assumption ^{101}A=250kOe/μ_B and ^{17}A$|_{q=0}$=33kOe/μ_B.

1.6 K				^{101}1/T$_1$T	^{17}1/T$_1$T
FM	840	1180		5.6	0.33
IC	1840	1350		12.2	0.38
Sum	2680	2530		17.8	0.71
Ref. [168]				15	0.8
150 K					
FM	730	1030		4.9	0.29
IC	1140	880		7.6	0.25
Sum	1870	1910		12.4	0.53
Ref. [168]				8.5	0.45

The values underline the importance of the ferromagnetic part. When comparing

or -28.8kOe/μ_B depending on the polarization [169]. For the sum of in-plane and out-of-plane, one may thus work with A$\simeq$33 like in [111].

the so obtained values for the NMR relaxation rates with the measured values that are also given in the table, one finds a reasonable agreement. The [101]Ru data tend to be overestimated, but have also significantly larger error bars in Ref. [168]. In particular, the contribution of the FM part to $1/T_1T$ is quantitatively in good agreement to the temperature-independent part (see corresponding figure in [168]).

Another quantitative comparison can be made with the specific heat coefficient γ. It has been determined by standard methods as 37.5 mJ/mol·K^2 [161, 173]. The spin-fluctuation contribution to the specific heat can be calculated using Equation (2.38). Using the parameters in Table 4.1, one can make a simple estimation by assuming Γ to be constant in cylinders that have the diameter of the Q-width of the fluctuation – this is the same method that has been successful in the case of $Ca_{1.8}Sr_{0.2}RuO_4$ in Chapter 3.

For the four incommensurate peaks ($\triangle q \simeq 0.08$ r.l.u.), the total contribution is only about 4 mJ/mol·K^2 (or slightly more when using Γ=8 meV). The broad ferromagnetic component contributes about 33 mJ/mol·K^2. Although this is a rather rough estimation, the sum is thus in excellent agreement with the macroscopic value. It is remarkable that the contribution of the broad ferromagnetic fluctuations is by far the dominant one, because they cover a much wider region in Q-space.

In conclusion, the relatively good overall quantitative agreement with the NMR and specific heat data strongly supports the correctness of the results and the conclusions inferred from the inelastic neutron scattering experiments, which go further than the conclusions from the other methods. From the NMR data, detailed information about the magnetic fluctuations could be extracted only under certain assumptions on their Q-dependence, anisotropies etc., so mostly requires an intricate reasoning. All this is information that the neutron data provides in a direct way, which is certainly more reliable. Their only weak point could be the high statistical uncertainties related to the low intensity. The comparison of the different methods, although it does not yield real new information, is thus important because the consistency proves that the analysis is correct and that the assumed phenomenological model for the susceptibility is, at least at the currently achievable level of accuracy, well suited.

4.3.5 Further possible implications of the results

It is obvious to ask whether the results from the experiments do contain new information that is relevant for superconductivity. The theory of superconducting pairing, in particular that of spin-triplet superconductivity, is quite complicated, and an in-depth analysis would be far beyond the scope and the intention of this thesis.

In general, when assuming a certain mechanism for the superconducting pairing, one has to regard the pairing interaction $V(\mathbf{k}, \mathbf{k}')$. With this, one has to solve the gap

equation [174]

$$\mathbf{d}_l(\mathbf{k}) = \sum_{\mathbf{k}',l'} \frac{V_{l,l'}(\mathbf{k}, \mathbf{k}') \cdot \mathbf{d}_{l'}(\mathbf{k}')}{2E_{l',\mathbf{k}'}} \tanh\left(\frac{E_{l',\mathbf{k}'}}{2k_B T}\right) \qquad (4.4)$$

where $E_{l,\mathbf{k}} = \sqrt{\varepsilon_{l,\mathbf{k}}^2 + |\mathbf{d}_l(\mathbf{k})|^2}$, and $\mathbf{d}_l(\mathbf{k})$ is the d-vector that contains the gap for the three spin states of the triplet on the Fermi surface sheet l and is replaced by a single complex scalar $\Delta_l(\mathbf{k})$ for singlet superconductivity.

A treatment in a relatively simple manner is presented for instance by Mazin and Singh [13, 175, 176], who linearize the gap equation to the form

$$\Delta_l(\mathbf{k}) = \sum_{\mathbf{k}',l'} V_{l,l'}(\mathbf{k}, \mathbf{k}') \cdot \Delta_{l'}(\mathbf{k}') \qquad (4.5)$$

(4.4) and (4.5) can be treated as an eigenvalue problem; the eigenvector specifies the gap function, and the eigenvalue T_C. In Sr_2RuO_4, however, it is a non-trivial question how to consider the interaction of the different bands[8]; this prohibits a straightforward calculation.

Very generally, for the pairing interaction (see for instance [13, 167, 177]) it is essential to know the susceptibility χ_0 and the interaction parameter $I(q)$. This is therefore the part of the argumentation where the experiment can provide information.

Firstly, for the susceptibility χ_0 there are, on one hand, the RPA expressions, as calculated for instance in Figure 4.1. On the other hand, there is the experimentally obtained model, Equation (4.1) with the parameters in Table 4.1. The latter is the interacting susceptibility, and the former is χ_0. There are nevertheless some evident discrepancies between these two in the way that the χ_0 calculated from the band dispersion contains a number of smaller features like ridges and secondary maxima which give it a rather complicated structure in detail that is not contained in (4.1). However, the fine structure in the calculated χ_0 is certainly not to be taken too seriously, as it depends sensitively on the band dispersion $\varepsilon_{l,\mathbf{k}}$, which is included only as a tight binding fit.[9]

More generally, although the RPA has been quite successful in the case of Sr_2RuO_4, it is nevertheless worth considering that its validity might still be limited (maybe in particular close to the magnetic transition). These arguments are intended

---

[8]According to M. Sigrist (private communication), this is entirely unclear.

[9]One probably gets a good impression of the accuracy of such calculations when regarding the χ_0's that have been published by a number of authors [13, 14, 123, 160, 162–167]. While there is relatively good agreement on the most relevant features, in particular the incommensurate peaks, it is quite instructive to regard the differences. They are mostly to be ascribed to different choices of the band structure parameters, different treatments of the matrix elements and partly some other assumptions and impressively demonstrate that these calculations are non-trivial and that small features in the calculated χ_0 are to be taken with some caution. The sensitivity of the RPA approach to small parameter changes is for instance discussed in Ref. [178].
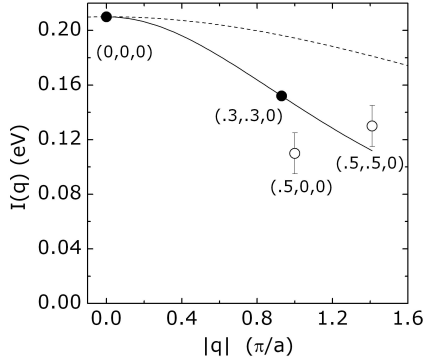
Figure 4.10: I(q) according to equation (4.6) for b=0.08 (dashed line) and b=0.44 (solid line).

to show that while the overall shape of the calculated χ_0, including the absolute values (which are important for the discussion at several points), are probably reliable, the fine structure is of less relevance for the discussion.

Another different issue is the possibility of interband transitions[10] which further questions the relevance of the calculated χ_0. Moreover, spin-orbit coupling is not included in the simple RPA approach. It might be an important ingredient and could account for the energy scale of the fluctuations and the fact that the calculations never give a contribution at finite ω at Q=0, which is seen in the experiment and included in the model (4.1).

These considerations put more weight on the experimentally determined Q-dependence of the susceptibility.

A very important point is the interaction parameter $I(q)$, because it is essential for the pairing potential which is mostly written in a form $V = I(q)^2 \cdot \chi(q)$ [167, 177].

$I(q)$ is frequently – often due to the lack of better knowledge – approximated as a constant, but this can be a *very* crude approximation[11]. It is, though, not evident how to appropriately model the Q-dependence in order to describe it in a better way. Mazin and Singh give for the Ruthenates

$$I(q) = \frac{I(0)}{1 + b \cdot (\frac{a}{\pi})^2 q^2} \tag{4.6}$$

with $b = 0.08$, based on an argument with the Oxygen contribution to the Stoner factor [13, 175].

This is a Q-dependence which is isotropic and decreases only by a very small amount of at most 13% at (0.5,0.5,0). With the absolute values of χ_0 and χ, one can straightforwardly determine $I(q) = \chi_0(q)^{-1} - \chi(q)^{-1}$. For q=0 and q=$Q_{IC}$, this can quite precisely be calculated. For q=(0.5,0,0) and (0.5,0.5,0) the observed χ is within error

---

[10]pointed out by M. Sigrist (private communication)

[11]Already for the simpler case of Nickel, Lowde and Windsor [11] conclude a quite strong variation as function of Q.

bar not different from zero, so one may tentatively assume it to be not larger than $\sim 10 \mu_B^2/eV$. To account for this, one has to assume $b = 0.44$, i. e. a much steeper Q-dependence. The comparison is illustrated in Figure 4.10 [12].

In view of the few available data points for such a fit, some caution should apply to the quantitative statement. Qualitatively, this new form of $I(q)$ makes the pairing potential V larger at small Q=k'-k. In the model as in Ref. [13], which compares singlet and triplet states, this tends to favor the triplet solution over the singlet solution. The stronger Q-dependence of I could thus open a way to better understand the formation of triplet pairs in Sr_2RuO_4.

4.3.6 Magnetic fluctuations in the superconducting state

The experiments that have been discussed so far have all been carried out in the normal state of Sr_2RuO_4 (owing to the considerable effort needed to achieve temperatures below 1.5 K in a neutron experiment). Although there is by now not yet enough information to give a conclusive picture of the behavior of the spin fluctuations in the superconducting state, a few comments should be made about it. As the spin fluctuations most likely play a role for the pairing mechanism, it would of course be extremely interesting to precisely probe the spectrum of magnetic excitations in the superconducting state and its differences to the normal state. In the high-T_C Cuprates for instance, this has been studied in a vast number of experiments, and the most prominent feature is the so-called resonance peak (for a brief review see for instance [179] and references therein).

In Sr_2RuO_4, this possibility has been studied in a number of theoretical works [14, 180–182], which show that a resonance peak might also exist in Sr_2RuO_4 and tentatively suggest an energy scale of about 1 meV. In general, such a feature is neither restricted to a certain type of superconductivity nor intrinsic to singlet or triplet pairing, but a consequence of the modification of the RPA susceptibility by a coherence factor which contains the superconducting gap function. It is thus determined in a complicated way by the interplay of the superconducting gap and the Fermi surface topology. In a neutron scattering experiment, although one would not directly measure the gap function, one might gain very valuable information to determine the superconducting gap.

Up to now, such experiments have not been successful. Two attempts have been made earlier to observe an effect on the incommensurate peaks when cooling below T_C [112, 123]. No difference between the scans above and below T_C could be observed down to about 0.5 meV. A new similar experiment has been performed in a dilution cryostat on 4F2 with a larger sample and in a (110)-(001) orientation, which

---

[12]The used values (in μ_B^2/eV) for χ_0 are 4.0 for q=0, 6.4 at q=(.3,.3,0), 4.8 at (.5,0,0) and 4.4 at (.5,.5,0). Due to different conventions, a factor two is between these χ_0's and I's compared to those in Ref. [13].
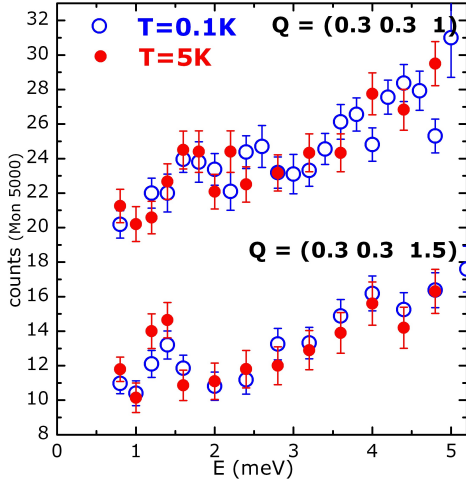
Figure 4.11: Energy scans on the incommensurate peak (with different L-component; shifted by 10 counts) at 5 K and 0.1 K. (Experimental background is approximately 10 counts.)

allows for different L-components (the L-component might be important, as argued for instance in Ref. [180]). Some results of energy scans on the incommensurate peaks are shown in Figure 4.11. Again there is no significant difference between the data from above and below T_C. An indication of a maximum or a shoulder near 1.5 meV is currently not understood; the absence of a temperature dependence however excludes its interpretation as a resonance peak or a similar phenomenon.

In general, experiments of this type are very difficult: firstly due to the technical effort related to the low temperature and secondly due to the very low intensity. The low intensity is a consequence of the low energy transfers far below the characteristic energy (and thus the maximum amplitude) of the fluctuation, the requirement of a good energy resolution with low k_f on a cold neutron triple-axis spectrometer (which generally has less flux than thermal spectrometers) and the more severe restrictions concerning the sample volume and mounting in the dilution cryostat. Nevertheless, if a large effect existed in the regarded energy range, it would have been visible.

A difficulty in the interpretation is that the absence of this observation may have a variety of reasons, including rather simple ones like that the effect occurs outside the regarded energy range or is weaker than the sensitivity of the measurement. A complication in the understanding of superconductivity in Sr_2RuO_4 comes from the existence of three different bands which probably play different roles. It appears by now likely that the "active" band for superconductivity is the γ band, i. e. this band drives the superconducting transition and then induces a gap also in the "passive" α and β bands [174, 183]. The gaps on different Fermi surface sheets may thus have different amplitudes, likely smaller on α and β.

The γ band is not related to the incommensurate signals, so an effect is rather expected on the more ferromagnetic-like fluctuations closer to the zone centre. In the recent experiment, energy scans have also been performed at momentum transfers (0,0,L). Due to the much lower amplitude of these fluctuation (made even worse by its

higher characteristic energy) no signal has been distinguishable from the background.

Coming back to the incommensurate peak, the absence of a change below T_C could also be easily explained if the gap function on the α and β bands has minima or nodes (zeros) on the diagonals of the Brillouin zone, as deduced for instance from field-orientation dependent specific heat measurements [184, 185].

At the current level, the measurements of $\chi''(\mathbf{Q}, \omega)$ in the superconducting state do not yield substantial new information about the nature of the superconducting state. As they could in principle provide strong arguments concerning the gap structure, it would be highly desirable to continue them under more favorable experimental conditions.

4.4 Sr_2RuO_4 and Ti-doping

As clearly proved by the study of magnetic fluctuations, Sr_2RuO_4 is close to magnetic order. One may therefore expect that a small variation of a suitable parameter can induce large changes in the magnetic properties. Besides pressure [186, 187], doping offers interesting opportunities. In Chapter 3 the effect of Calcium doping is extensively discussed. Very large changes in the physical properties occur, however at rather high Ca-contents and not directly related to the dominant incommensurate antiferromagnetic instability.

A different and very interesting effect is also achieved by doping Sr_2RuO_4 with Titanium, which acts on the Ruthenium site instead replacing Strontium. Already at the low Ti-content of nearly 3% magnetic order is induced [188], which is characterized by a propagation vector (0.307, 0.307, 1) and an ordered moment of approximately 0.3 μ_B that is oriented along the c-direction [189]. This can obviously be straightforwardly understood as a freezing of the incommensurate magnetic fluctuations in Sr_2RuO_4 into a static spin density wave – the anisotropy of the incommensurate fluctuations in Sr_2RuO_4 [145] corresponds to the direction of the ordered moment, and the nesting vector Q_{IC} to the propagation vector of the spin density wave. The finite L-component L=1 is a subtlety[13] that obviously arises from the weak but existing three dimensionality of the electronic properties and which is of little importance in practice as the inter-plane coupling is very weak (the correlation lengths along c are short and the dispersion of excitations expected to be negligible). The magnetic state is obviously characterized by a high degree of disorder and some glassy behavior with a slow decay of the remnant magnetization. Magnetization measurements [188, 190] have established a phase diagram, and ordering temperatures reach 15-20 K for x$\geq$10%.

Titanium can be relatively easily incorporated in the structure of Sr_2RuO_4 as a replacement of Ruthenium as it has the same oxidation number (Ti^{4+}; electronic config-

---

[13]Note the difference to the bilayer Ruthenate, see Chapter 5.
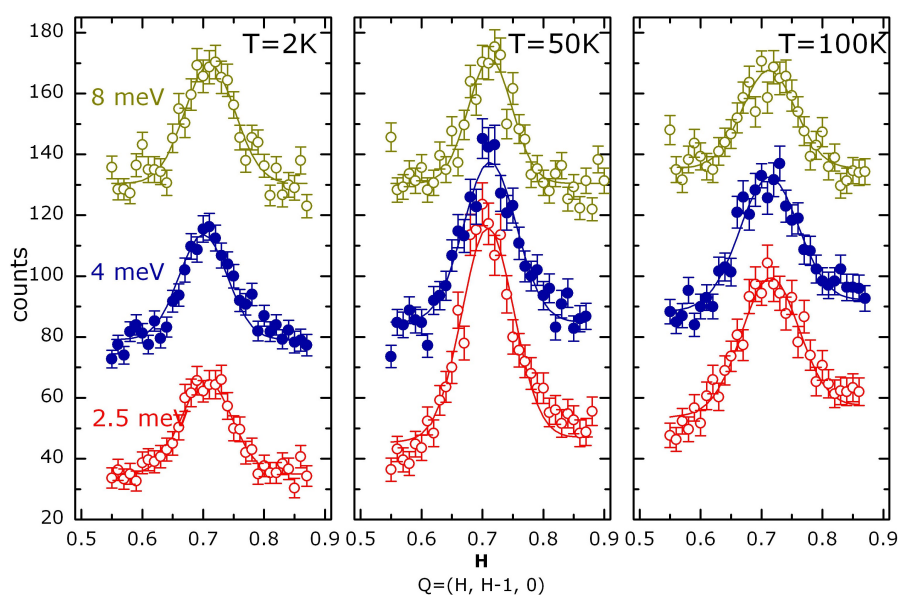
Figure 4.12:
Inelastic neutron
scattering data on
$Sr_2Ru_{0.91}Ti_{0.09}O_4$:
scans on 2T (raw
data) along the
zone diagonal for
various tempera-
tures and energy
transfers.

uration $3d^0$ and thus nonmagnetic) and a similar ionic radius. The structure is there-
fore not significantly influenced, and no superstructure reflections corresponding to
any structural distortions are observed. In principle, the chemical composition can be
arbitrarily varied until Sr_2TiO_4 [191, 192]. This is an insulator, and a metal-insulator
transition has been observed near the Ti-concentration x=0.2 [193].

The Ti^{4+} ion has the same charge, but not the same number of electrons as Ru^{4+}. If
the Titanium and Ruthenium d-states formed a common band, this would change the
effective valence and band filling and thus have strong effects on the whole electronic
structure. It is thus important to note that this is not the case and that Titanium is re-
ally in its 4+ state. This is for instance supported by the consideration that Ti^{3+} would
have a larger ionic radius which is in contradiction to the reduced lattice volume [188].
Furthermore, an x-ray spectral analysis (for $SrRu_{1-x}Ti_xO_3$) [194] proves a large energy
splitting between Ru 4d and Ti 3d that is thought to decouple these bands and has
found no indication of Ti^{3+}, which has recently been confirmed also for $Sr_2Ru_{1-x}Ti_xO_4$
experimentally [193] and theoretically [195]. The electronic structure as in Sr_2RuO_4
can thus be assumed to remain essentially intact for small amounts of Titanium. The
initial effect of the doping is therefore rather to introduce some disorder and to de-
crease the average number of Ru neighbors, i. e. the effective Ru coordination, and
thereby likely reducing the Ru 4d bandwidths.

4.4.1 In the ordered state: 9% Ti

In $Sr_2Ru_{0.91}Ti_{0.09}O_4$, i. e. at a Titanium concentration of 9%, magnetic superstructure
reflections at (0.7,0.3,0) and equivalent positions appear below a quite broad transi-
tion near 25 K. Inelastic neutron scattering experiments have been performed on a

sample consisting of five coaligned large crystals on the spectrometers 2T and 4F1 at Saclay. As it turned out during this project, the sample contained an impurity phase of bilayer Ruthenate. As shown in detail in Chapter 5, the bilayer Ruthenate also develops magnetic order with a propagation vector (0.25,0.25,0), and with a slightly higher T_C. Due to the larger ordered moment and because the elastic magnetic amplitude depends on the square of the moment, the corresponding magnetic Bragg reflection of the impurity phase was of similar intensity as the reflection of the majority $Sr_2Ru_{0.91}Ti_{0.09}O_4$ phase.

The imperfect sample quality limits the accuracy in the treatment of the data. In Chapter 5 the presence of magnetic excitations in $Sr_3(Ru_{0.9}Ti_{0.1})_2O_7$ is shown and discussed, and due to their width and the proximity in Q-space one expects some overlap of the excitations of the two phases. In the inelastic experiments, this problem has been thoroughly addressed in a number of scans at different energies, wave vectors and running in different directions. From these studies it became obvious that the measured response is clearly centred at wave vectors (0.3,0.3,0) and its equivalents in two dimensions. At (0.25,0.25,0) and equivalents, there is nonzero intensity which seems mainly to arise from the width of the former signal, and hardly any additional weight is visible at these positions[14]. This proves that by far the main contribution to the measured response stems from $Sr_2Ru_{0.91}Ti_{0.09}O_4$ and that despite the impurity the results are reasonably reliable.

In contrast to, for instance, the well-known case of a Heisenberg antiferromagnet with local moments whose excitation spectrum is characterized by spin waves that exist over the whole Brillouin zone and which applies to many real materials of interest, the characterization of the excitation spectrum in the present situation is less simple. A correct description of the excitations in an itinerant electron incommensurate antiferromagnet can be a formidable task, as is impressively demonstrated by Chromium, the textbook example of an incommensurate spin density wave ordered state. Although only an element and with a simple crystal structure, its magnetism is an extremely intriguing problem that is still under debate[15]. It is known that different types of excitations can exist – besides conventional spin waves, amplitude and phason modes are in principle possible [197]. Both dispersive and non-dispersive modes have been found in chromium [198–202]. In principle, band theoretic calculations in RPA similar to the ferromagnetic or paramagnetic cases discussed in Chapter 2 are also possible (see for instance [203,204]), but very complicated. In addition to collective modes, there is a continuum of excitations which is gapped by an energy related to T_N (roughly $\Delta \simeq 1.76 k_B T_N$ [205]).

There may still be significant differences between the case of Chromium and $Sr_2Ru_{0.91}Ti_{0.09}O_4$, due to the more complicated (crystal and electronic) structure in-

---

[14]See Figure 4.12; the impurity phase would be expected to contribute at H=0.75.

[15]For a (not very recent) review see Ref. [196]. The number of publications is vast, including inelastic neutron scattering, and ranging from the late 1970's to today.
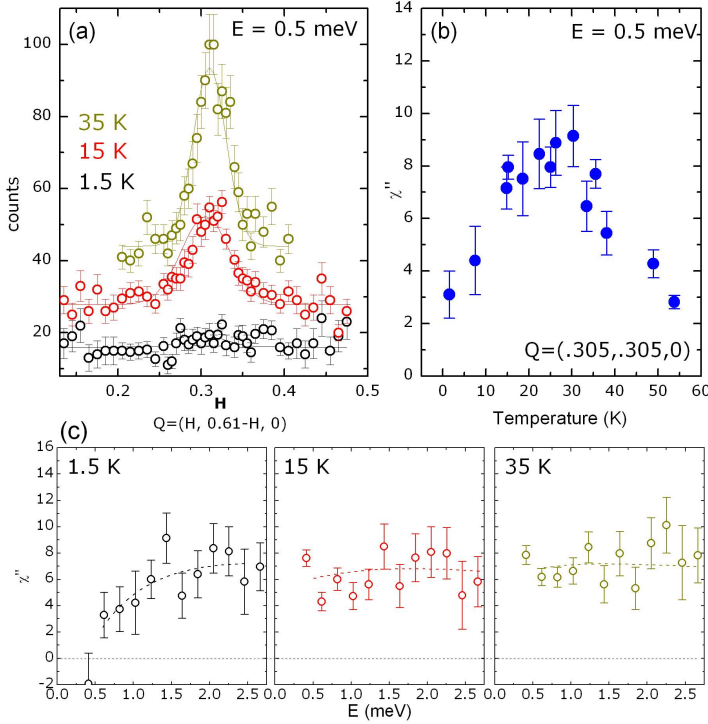
Figure 4.13: Magnetic excitations in Sr$_2$Ru$_{0.91}$Ti$_{0.09}$O$_4$. (a) Constant energy scans at different temperatures (raw data; offset 15 counts). (b) Temperature dependence of the peak intensity. (c) Energy scans on Q=(0.3,0.3,0) at different temperatures; lines are guide to the eye only. Data in (b) and (c) are corrected for the Bose factor after subtraction of the background.

cluding disorder and the significantly lower T$_N$. Other examples for systems with similar ground states are rare, an exception being metallic V$_2$O$_3$, for which inelastic neutron scattering experiments have been carried out [206, 207]. There, the excitations were found to have the character of broad magnetic fluctuations.

Figure 4.12 shows some inelastic neutron scattering data from the thermal spectrometers. The shape of the signal does not depend on the energy transfer nor on the temperature and can be described by a single Gaussian peak with constant position and energy-independent width (only a few percent broader at 100 K). There is obviously no dispersion or any other remarkable feature in this signal. It is thus most likely to be interpreted as a spin fluctuation inside the Stoner continuum. Note that 2.5 meV would approximately correspond to the estimated gap below the continuum.

Data at lower energy transfers (collected on the cold neutron spectrometer) are shown in Figure 4.13. The amplitude of the signal at 0.5 meV energy transfer is apparently strongly temperature dependent and nearly completely suppressed at 1.5 K. The energy scans have, due to their weak statistics, limited significance, but indicate that the signal is only weakly energy dependent except at low temperature, where it is suppressed at low energies.

From this temperature effect one thus has to conclude that the excitation spectrum changes below the ordering temperature. According to the expectations, one should observe the opening of a gap in the continuum and the formation of spin wave modes in it. The gap seems to be indeed present, but it is hardly possible to see any spin
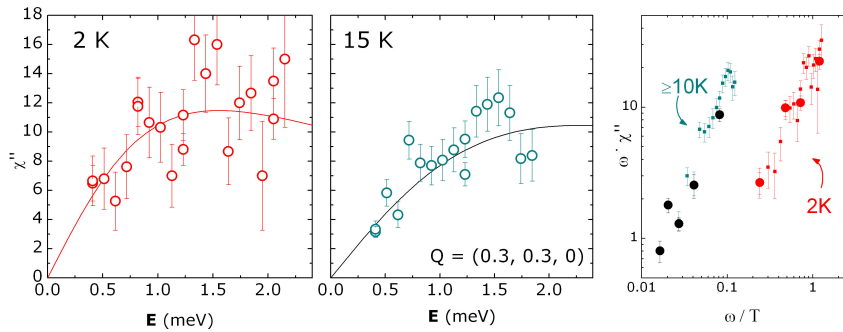
Figure 4.14: Magnetic scattering in $Sr_2Ru_{0.975}Ti_{0.025}O_4$: energy scans on Q=(0.3,0.3,0) at 2 and 15 K and plot of the same data versus ω/T (black points include T=10, 20 and 25 K). Lines are fits to a single relaxor.

waves, neither could the continuum boundary be well resolved. The strongest indication for the formation of a gap comes from the temperature dependence in Figure 4.13(b): it would explain the remarkable reduction of the intensity at low energies below the temperature of the maximum close to T_N. About spin waves, there is currently no reliable information – it is for instance not known how steep their dispersion could be and if they were observable in this q,ω-range at all. Furthermore, in the spin-wave scattering cross section [2], the size of the ordered moment explicitly enters (linearly); as the ordered moment is small, there might be only a small amount of spectral weight shifted from the continuum to the spin-wave modes.

4.4.2 Near the critical concentration: 2.5% Ti

An NMR experiment [47] indicates that below the critical concentration for the onset of magnetic order, the incommensurate fluctuations become strongly enhanced – in particular their out-of-plane component, as it is consistent with the anisotropy in Sr_2RuO_4 and the direction of the ordered moment.

As an additional remark, this enhancement of magnetic fluctuations provides an argument against their constructive role in the mechanism of superconductivity: if they were responsible for the pairing, a positive effect on the transition temperature would be expected, but T_C is suppressed in exactly the same manner as for other impurity elements, and superconductivity completely disappears at 0.25% Ti-content [208–210].

Near the concentration of about 2.5% Ti, non-Fermi-liquid behavior is observed in the temperature dependence of the resistivity and the specific heat [208]. As 2.5% is the critical concentration at which magnetic order appears at very low temperatures,

one may expect quantum critical behavior that manifests itself in certain scaling laws for various physical quantities, like resistivity, specific heat etc. [18, 211, 212]. In the context of inelastic neutron scattering, it is interesting to regard the behavior of the magnetic susceptibility and to test whether it obeys a scaling law like [213]

$$\chi''(q_{ic}, \omega, T) = T^{-\alpha} \cdot g\left(\frac{\omega}{T}\right) \tag{4.7}$$

or, equivalently, $\omega^\alpha \cdot \chi''(q_{ic}, \omega, T) = \tilde{g}(\frac{\omega}{T})$ (with $\tilde{g}(\frac{\omega}{T}) = (\frac{\omega}{T})^\alpha g(\frac{\omega}{T})$) where g is a function that depends only on the ratio ω/T.

Such ω/T-scaling has been found to be valid in a number of different materials, in particular – but not only – heavy fermion compounds[16]. Also for Sr_2RuO_4, the concept of ω/T-scaling has already been tested [123], and it has turned out to be well fulfilled for both α=1 and 0.75 in the temperature range 60-300 K, but not at 10 K. This is understood in the way that Sr_2RuO_4 is not at a quantum critical point, and is consistent with the crossover to Fermi-liquid behavior at low temperature, as observed for instance in the T^2-like resistivity below 20-30 K [146].

Following these considerations, the region in which the scaling law can be applied should extend to much lower temperature in $Sr_2Ru_{0.975}Ti_{0.025}O_4$ than in Sr_2RuO_4. Some data on $Sr_2Ru_{0.975}Ti_{0.025}O_4$ had already been obtained earlier in the thermal neutron energy range (unpublished). At low temperature, the characteristic energies of the fluctuation and thus the significant enhancements of intensity are expected in the range of low energy, so the cold neutron data are very interesting in this context. Figure 4.14 shows the data that has been obtained on 4F at temperatures of 2, 10, 15, 20 and 25 K, in particular full energy scans at 2 and 15 K.

There is an increase of intensity at low energies in the 2 K-scan, but the evident result is that this enhancement is rather modest and far below the expectation of diverging fluctuations. The attempt of a scaling plot (with α=1) in the right part of the figure thus clearly shows that the fluctuations at low temperature are not consistent with a scaling behavior. The data at the higher temperatures, in contrast, fall on a single curve. To unambiguously establish the validity of the scaling law, and in particular for a precise determination of α, one would of course need data over a much wider energy and temperature range. Given the validity for Sr_2RuO_4 [123], there is however little doubt about its validity, likely even to much lower temperature ($\leq$10 K) than in Sr_2RuO_4, so the most remarkable result is rather the deviation at low temperatures.

This may have different reasons. For example, one might suspect that the Ti concentration of the used sample is still not exactly at the critical concentration. As quantum critical behavior down to very low temperature would be observed only at exactly the critical concentration, this could be a reason for any deviation. As there is little

---

[16]For instance in $CeCu_{6-x}Au_x$ [214, 215], $UCu_{5-x}Pd_x$ [216], $Ce(Rh,Pd)Sb$ [217, 218], $La_{2-x}Sr_xCuO_{4+y}$ [219], $La_2Cu_{1-x}Li_xO_4$ [220], $Ce(Ru_{1-x}Fe_x)_2Ge_2$ [221] and $Ce_{1-x}La_xRu_2Si_2$ [222] (in a slightly modified form ω/T^β with $\beta < 1$).

doubt about the concentrations[17], and the deviations are rather large, another conclusion appears more probable, namely that the system does not show the expected scaling behavior down to very low temperatures. This conclusion has also been drawn for other materials, like $Ce_{1-x}La_xRu_2Si_2$ (x=7.5%) [222] for which extensive and precise data exists that obeys well the scaling law, but which shows a saturation below about 3 K that seems not yet well understood. The absence of truly divergent fluctuations at low temperature may thus be not unique to $Sr_2Ru_{0.975}Ti_{0.025}O_4$ and may have a more universal origin, most likely related to disorder.

In the case of $Sr_2Ru_{1-x}Ti_xO_4$ it appears clear that disorder plays a very important role. This is not only generally expected due to the doping, but is also observed in the physical behavior: the studies of the magnetic properties by macroscopic susceptibility/magnetization, neutron scattering, etc. [188, 189] yield a picture of relatively poorly defined states with broad transitions, glassy behavior and very short correlation lengths. Disorder in general is expected to wash out the original quantum critical point, similar to the argument at the metamagnetic transition in $Ca_{1.8}Sr_{0.2}RuO_4$. As from the theoretical side, disorder effects are more difficult to consider and therefore not contained in many models, it is not surprising that magnetic fluctuations in $Sr_2Ru_{0.975}Ti_{0.025}O_4$, although it is very close or at a quantum critical point, deviate from simple scaling behavior. The effects of disorder and short correlations most likely make the Ti-doped Ruthenates in general a system in which the observation of quantum critical physics is difficult.

4.5 Summary

The detailed study of Sr_2RuO_4 by inelastic neutron scattering has provided a complete quantitative picture of the magnetic fluctuations throughout the whole Brillouin zone. These measurements are technically difficult, and it has been demonstrated that the use of polarized neutrons is crucial to obtain the desired information. As the main new result, the existence of "ferromagnetic" fluctuations has been shown, which are isotropic, only weakly Q-dependent with a half-width of about $\frac{\pi}{a}$ and have a characteristic energy of 15-20 meV.

In combination with the incommensurate signals, the thus obtained model for $\chi(q)$ is consistent with the results of other measurement methods: macroscopic susceptibility, specific heat and the Nuclear Magnetic Resonance relaxation rates.

In the superconducting state, only few data have been collected and show no effect on the incommensurate wave vectors for different L-values when cooling through T_C. The main effect may probably be seen on the just mentioned ferromagnetic fluctuations, but could not yet be measured. As a quantitative ingredient for the discussion of

---

[17]In particular, there is, unlike in $Sr_2Ru_{0.91}Ti_{0.09}O_4$, no indication of any problem with the sample quality.

the pairing mechanism, the Q-dependent interaction parameter $I(q)$ can be estimated from the experimental $\chi(q)$ and the band structure. It turns out that its Q-dependence has to be significantly stronger than assumed so far [13, 175] in order to account for the observations.

Ti-doping enhances the incommensurate fluctuations. In the ordered state (9% Ti) there is, apart the opening of a gap at low energies (of the order 0.5 meV), no qualitative change of these fluctuations. Near the critical concentration of 2.5%, where magnetic order sets in at low temperatures, the ω/T scaling as it would be expected at a quantum critical point, is not observed down to 1.5 K, which is probably related to disorder or related effects that make this system more complicated and prevent a divergence of magnetic fluctuations.

5 Bilayer Ruthenates

5.1 Spin density in $Ca_3Ru_2O_7$

5.1.1 The bilayer Ruthenate $Ca_3Ru_2O_7$ and its metamagnetic transition

In contrast to the single-layer Ca/Sr-Ruthenates, which are by now studied in great detail and yield lots of interesting phenomena when varying the chemical composition, the knowledge about the phase diagram of $Sr_{3-x}Ca_xRu_2O_7$ is still very poor[1]. The work that has been published so far dates from about ten years ago and contains susceptibility, resistivity, x-ray powder diffraction and specific heat measurements [223, 224] (and, for a few x, some ARPES data [225]). There are some disagreements and apparent problems with sample quality (for instance when erroneously reporting a ferromagnetic state for $Sr_3Ru_2O_7$), so up to now no conclusive phase diagram of $Sr_{3-x}Ca_xRu_2O_7$ exists. It seems clear that very similar to the case of $Ca_{2-x}Sr_xRuO_4$, the structural effect of the smaller Ca ions determines the relatively drastic changes in the physical behavior between $Sr_3Ru_2O_7$ and $Ca_3Ru_2O_7$, and at least one true structural phase transition must exist between these two extremes. Also here, the structural distortions are stronger on the Ca-side, and on this side there is again antiferromagnetic order. Furthermore, in the intermediate region, the antiferromagnetism is suppressed and an either weakly ferromagnetic or at least nearly ferromagnetic state observed, accompanied by a significant increase in the electronic specific heat coefficient – the vague similarity to $Ca_{2-x}Sr_xRuO_4$ immediately comes to one's mind. Finally, $Sr_3Ru_2O_7$, as discussed in the context of the metamagnetic transition, bears resemblance to $Ca_{1.8}Sr_{0.2}RuO_4$. One may therefore say that the bilayer Ca/Sr-Ruthenates probably behave in a qualitative way similar to the single-layer system, as one would also naively expect. An interesting aspect is added to the problem by the existence of bilayers, which reduces the two-dimensionality and opens possibilities for (possibly even more complicated) new behavior.

While a more detailed study of the phase diagram of $Sr_{3-x}Ca_xRu_2O_7$ would certainly be worthwhile and reveal interesting results, the two end members $Ca_3Ru_2O_7$ and $Sr_3Ru_2O_7$ have been studied in great detail during the recent years. In $Sr_3Ru_2O_7$, this

---

[1] Note that in the commonly used notation, x=0 corresponds to the Sr-side of the phase diagram, unlike in $Ca_{2-x}Sr_xRuO_4$.

(a)

(b)
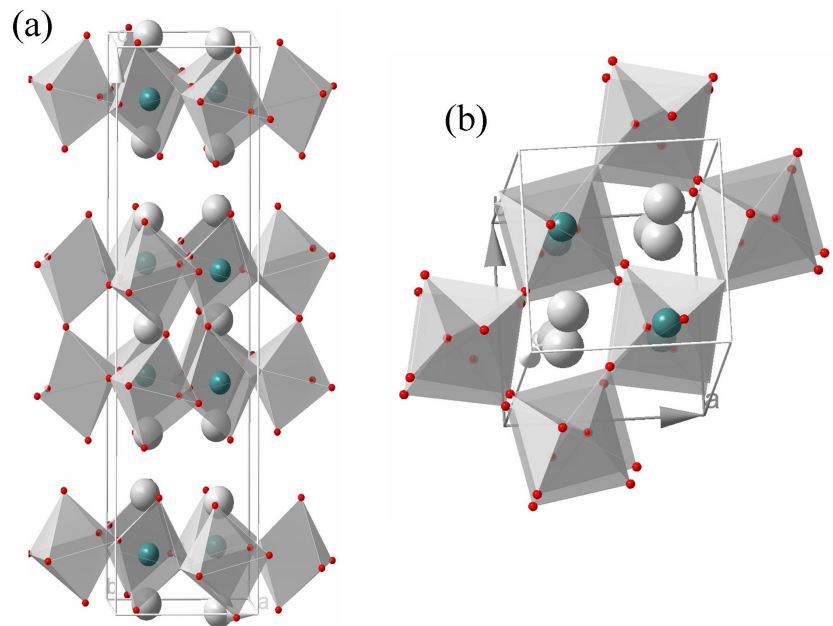
Figure 5.1: Structure of $Ca_3Ru_2O_7$. (a) view onto the a,c-plane (b) the central bilayer unit viewed from above.

is mainly due to its metamagnetic transition and quantum critical behavior (see Chapter 3). In addition, doping influences the magnetic properties, as will be discussed below.

$Ca_3Ru_2O_7$ has at first sight similar properties as Ca_2RuO_4: upon cooling it displays a structural phase transition with a simultaneous increase in resistivity, and a transition from paramagnetism to antiferromagnetic order. The structure of $Ca_3Ru_2O_7$ is, like that of Ca_2RuO_4, orthorhombic and characterized by a substantial rotation and tilt of the RuO_6-octahedra in the range of 14-15° [226, 227]. The tilt axis is the b-axis, and the space group is *Bb2₁m* [2]. In contrast to $Sr_3Ru_2O_7$ which has only the rotational distortion [90], the rotations of the octahedra within the bilayers are coupled via the bridging interlayer oxygen atom, which enforces the same rotation sense of the so coupled octahedra in the adjacent layers. (In $Sr_3Ru_2O_7$, their rotation is opposite.) In the same way, the tilt has to be opposite. This combination makes it impossible to find an inversion centre, which makes the structure acentric. This lack of centrosymmetry is thus directly related to the rotation and tilt of the octahedra, and because both are large effects, it cannot be neglected, nor reasonably be approximated in a centrosymmetric way.

At T=48 K there is a first order discontinuous structural phase transition below which the lattice is elongated along the *a* and *b*-direction and compressed along

---

[2]In the literature, there is major confusion about the correct assignment of the orthorhombic axes *a* and *b*, which is quite important in view of the very anisotropic behavior of the material. All authors give $a < b$, but identify different directions as the easy and hard axis etc. The correct notation is that in Refs. [226, 228] and some subsequent papers, while the publications from the group of G. Cao, which present the majority in this field, are wrong. The easy axis is *b* (i. e. the longer axis).
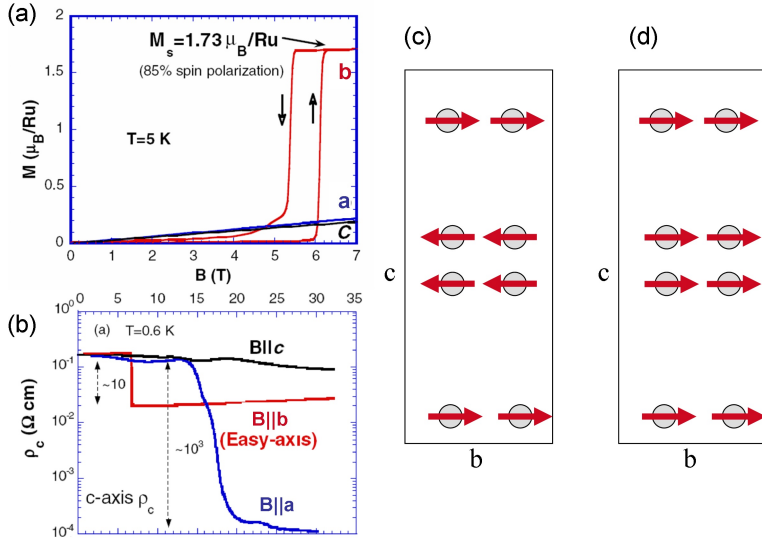
Figure 5.2: Metamagnetic transition in $Ca_3Ru_2O_7$. (a) Magnetization curve, (b) resistivity as function of field (both figures from Cao et al. [233]; assignment of a and b directions has been corrected). (c) and (d) are a sketch of the magnetic structure (projection on b,c-plane) below (left) and above (right) the metamagnetic transition, which may naturally account for the drop in ρ_c at the transition.

c [226, 229] (without significant changes in tilt, unlike in Ca_2RuO_4, where the effect is much larger [43]). Below this phase transition, the in-plane and out-of-plane resistivity are both slightly enhanced, but one cannot speak of a true metal-insulator transition. The c-axis resistivity ρ_c is nonmetallic over the entire temperature range except at very low temperature, while the in-plane resistivity is mostly metallic. Therefore it seems now clear (after some contradictory reports in the literature) that at low temperature the system is in a metallic state, though with a relatively high resistivity [228, 230]. Quantum oscillations [228, 231] and ARPES measurements [232] indicate an extremely small Fermi surface of about 0.3% the area of the Brillouin zone.

Below T_N=56 K, $Ca_3Ru_2O_7$ is in an antiferromagnetically ordered state. Like in Ca_2RuO_4, this seems to happen independently of the structural transition, but, in contrast, at a *higher* temperature. The magnetic structure at low temperature as known so far consists of ferromagnetically coupled bilayers with the spin direction parallel to the *b*-axis. That means there is obviously a relatively strong ferromagnetic coupling within a single plane as well as to the adjacent plane within one bilayer unit. Only between different bilayers, where the magnetic coupling is expected to be relatively weak, the coupling is antiferromagnetic yielding the overall antiferromagnetic state ("A-type antiferromagnet") of $Ca_3Ru_2O_7$. Within this scenario, the observed properties (easy and hard axis etc.) are readily explained.

This type of antiferromagnetic order also explains another remarkable feature of $Ca_3Ru_2O_7$: the metamagnetic transition, which is observed at about 6 T for fields along the b-axis [234], see Figure 5.2. As the coupling between different bilayer units is weak, this magnetic field is sufficient to flip the entire polarization of each second bilayer unit at a relatively low energy cost, thus turning the antiferromagnetic state into a fully ferromagnetic one, as indicated in parts (c) and (d) of the Figure. This may also

intuitively explain the resistivity drop in ρ_c at the transition as a spin-valve effect [235].

In general, the very anisotropic behavior of all properties that depend on the direction (resistivity, magnetic field, etc.) produces a great amount of interesting effects that is hard to overview as a whole. For instance, other field directions yield a metamagnetic behavior only weaker and at much higher fields. Moreover, the phase between 48 and 56 K appears interesting (with a proposed reorientation of the magnetic moments within the antiferromagnetic state) and seems to add further interesting aspects to the system. The summary of such observations led to the proposals of complex H,T-phase diagrams for the different field directions, including spin-flop, spin-flip and rotated spin phases with various proposals for orbital order [236–238]. In the context of this chapter, especially the low temperature properties are of interest. Here, the situation appears relatively simple, as only the two phases below and above the metamagnetic transition play a role.

At this metamagnetic transition (B=6 T, B‖b), also the structural effect has been investigated [230,239]. A strong magnetostriction is indeed observed, but these studies mainly focused on relatively high temperatures. There, the magnetic field induces a transition which has the character of the 48 K structural transition, and the high-field phase is different from the high-field phase that arises at low temperature from just flipping the spin direction of one bilayer at B=6 T, B‖b. (For some phase diagrams illustrating this difference, see for instance Ref. [238].) At the 6 T metamagnetic transition at low temperature, no significant structural effect as function of field has been observed – this is insofar well understandable as the magnetic configuration of the whole bilayer does, except the reversal of the spin direction, not change at this transition, so even in the case of strong magnetoelastic coupling no sizeable effects are expected.

In general, the metamagnetic transition in $Ca_3Ru_2O_7$ does therefore not have much in common with the metamagnetic transition in $Ca_{1.8}Sr_{0.2}RuO_4$. In $Ca_3Ru_2O_7$, although weakly metallic, the magnetic properties and in particular the metamagnetic transition are well understood in a picture of localized magnetic moments. Both sides of the transition are magnetically ordered states, and this magnetic order differs in nothing else than the bilayer relation, so the electronic configuration and other properties may also expected to be identical. Furthermore, in contrast to $Ca_{1.8}Sr_{0.2}RuO_4$, the metamagnetic transition has well-defined first order character with a pronounced hysteresis etc.

5.1.2 Measurement of the spin density in $Ca_3Ru_2O_7$

Experimental

For the determination of the spin density, a single crystal (irregular plate-like shape, estimated 20 mm^3) has been used on the diffractometer 5C1. It was untwinned with

experimental lattice constants of 5.37, 5.66 and 19.52 Å and oriented with the b-axis parallel to the magnetic field (within about 1°). The standard configuration of 5C1 has been used. Due to their relatively weak intensity, it was not possible to measure the antiferromagnetic reflections reasonably well ((0,0,3) and (1,1,0) have been identified). The zero-field phase has been studied later for its nuclear and magnetic structure on the four-circle diffractometer 5C2, which is much better suited for this type of measurement [240]. On 5C1, the focus has been entirely on the measurement of flipping ratios at **B=7 T** and **T=1.5 K**.

A total of about 600 flipping ratios has been measured, with typical measuring times of about 10 minutes for strong and 30 minutes for weak reflections. After averaging of identical (h,k,l) and Friedel pairs, 320 reflections are included in the refinement. Out of these, 148 are really symmetrically independent, and about the half of these has a flipping ratio which deviates from 1 by more than twice the error bar σ. In view of the restrictions imposed by the experimental geometry this is a relatively large number and constitutes already a good data set – the large ordered moment of about 1.7 μ_B per Ru is very helpful in measuring significant flipping ratios on many Bragg reflections. A very special technical problem occurred during the measurement: the cooling of the cryoflipper stopped working for several days. It was carefully checked that the data were still reproducible, but with different (surprisingly not too much different) flipping ratios than with the flipper fully operational; the data set has therefore been divided into two subsets. Later these conditions were carefully investigated with a FeCo test sample yielding a value of 40.3% for the beam polarization p^-. This value was appropriately taken into account during the refinement. Normally, the efficiency of the flipper is practically 100%, and the normal beam polarization on 5C1 is 92%.

Thanks to the large magnetic moment, also the observed effects are very large, and it is well possible to observe the metamagnetic transition at the expected field in the neutron diffraction data. The perhaps most striking example for the size of these effects is the (0,0,6) Bragg reflection. It has a not very large nuclear structure factor, which is of the same order as the magnetic structure factor, so that the flipping ratio becomes *very* different from 1. The effect of the metamagnetic transition on the count rates, when the overall magnetization suddenly changes, is therefore extreme, see Figure 5.3.

For the refinement of the spin density, the accurate knowledge of the nuclear structure factors is important. As mentioned, a detailed structural analysis on the same single crystal has been carried out recently by Olaf Schumann [240], but the results are not yet available. These new data are of course expected to yield the most precise structural information on $Ca_3Ru_2O_7$, but the preliminary impression is that in the relevant aspects it confirms the results of the
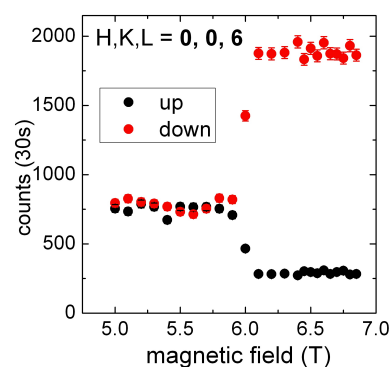
Figure 5.3: Intensity of the (0,0,6) Bragg reflection in $Ca_3Ru_2O_7$ for the two spin directions as function of the magnetic field, showing the drastic effect at the metamagnetic transition.
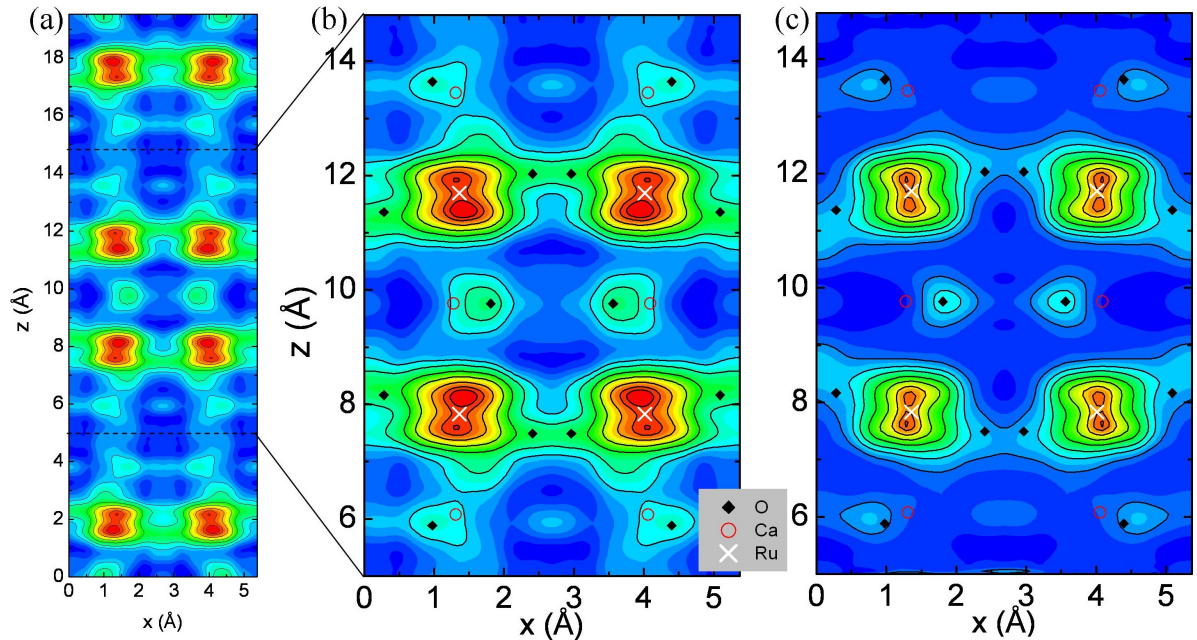
Figure 5.4: Projections of the spin density in $Ca_3Ru_2O_7$ onto the a,c-plane. (a) shows the full unit cell and corresponds to the view in Figure 5.1b, and (b) is a zoomed view of the central bilayer. While (a) and (b) have been obtained by Fourier inversion using only the (h,0,l) reflections, map (c) shows the same area as obtained by the maximum entropy treatment of the full data set.

powder diffraction experiment published by Y. Yoshida [226]. The structural data from this reference have therefore been used in the current spin density refinement.

Results

As discussed in Chapter 2, an important issue in the data treatment is the lack of centrosymmetry, which required the re-implementation of the maximum entropy algorithm. Nevertheless, it is possible to obtain, as a first step, already some very meaningful information with little effort and by use of only very basic mathematical tools.

This is based upon the consideration that the phase of reflections of the form (h,0,l), i. e. with k=0, is zero, so these are real numbers. In the calculation of the form factors (nuclear and magnetic), the scattering density enters only as the integral over the b-direction. In other words, they depend only on the projection (which has the desired centrosymmetry) of the scattering density onto the a,c-plane. Therefore, from these reflections the projection can be reconstructed. For this purpose, it is favorable that the a,c-plane corresponds to the scattering plane in this experimental setup, so that a relatively large number of reflections (h=0..10, l=0..36) could be accessed.
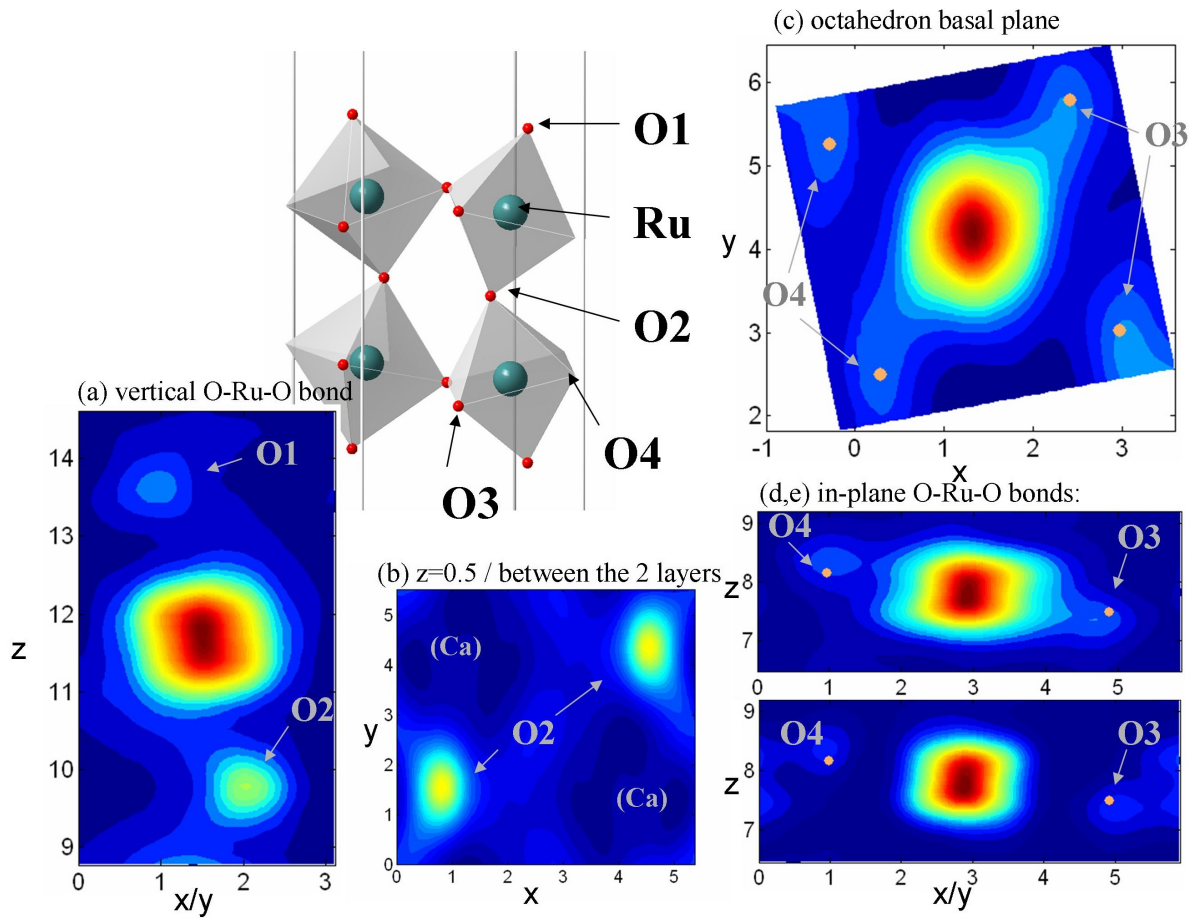
Figure 5.5: Various slices through the spin density in $Ca_3Ru_2O_7$. The x,y,z coordinates correspond to directions parallel to the axes of the unit cell, and all scales are in Angstrom (measured from the corners of the orthorhombic unit cell). "x/y" denotes a direction in the x,y-plane not parallel to one of the axes (zero point of these scales arbitrary). The high intensity always corresponds exactly to the Ru sites. Further remarks: In (b) – the plane in the middle of the bilayer – the Calcium sites are indicated, at which there is no magnetization. In (c) the slice has been performed in the plane defined by the four oxygen atoms (the "basal plane" of the RuO$_6$-octahedron), i. e. a tilted plane with respect to the unit cell and with non-constant z.

This procedure has been performed for 59 symmetrically inequivalent reflections with k=0. The result is presented in Figure 5.4. There is a direct relation between this figure and the nuclear structure in Figure 5.1a which allows to attribute the features in the density map to the crystal structure. The eight most prominent regions of high density are directly recognized as the places where the Ru sites project to. Also, the tilt is well recognized in the density map. An enlarged version of the central bilayer

is displayed in part (b) of the Figure, together with the projected atomic positions. In the projection there is of course some uncertainty from where (which atomic sites) the density actually comes from; in particular, the Calcium and apical oxygen atoms contribute to nearly the same points. There is nevertheless hardly any doubt that the maxima stem from the Ruthenium sites and the other contributions mainly from the oxygen sites.

In order to obtain the amount of the magnetic moment belonging to the individual atoms more quantitatively, not only the projection, but also the true three-dimensional map is not well suited, as it is not evident to which atom the magnetization at an arbitrary point (x,y,z) should be counted[3]. Therefore, a simple refinement has been carried out assuming localized magnetic moments on the Ruthenium and oxygen atomic sites and spherical form factors using the `maglsq` subroutine of the Cambridge crystallographic library. The results for the magnetic moments (in μ_B) are:

Ru 1.38 (3)
O1 0.19 (4)
O2 0.23 (4)
O3 0.11 (3)
O4 0.04 (2)

The meaning of the different oxygen sites is given in the drawing in Figure 5.5. The given errors for the magnetic moments are probably underestimated, as this refinement did not account for the non-spherical density especially on the Ruthenium ion, which clearly plays a role as is evident from the spin density maps. Nevertheless, not only the sum of the moments comes out correctly as 1.8 μ_B per Ru (consistent within error bar with the 1.73 μ_B from Ref. [233]), but also the relative distribution among the different atomic sites should roughly reflect the true distribution – insofar as localized moments on the atomic sites are a good model at all. The most important information is that 75% of the total magnetization is carried by the Ruthenium ions, and the remaining quarter has rather oxygen-character.

These findings are qualitatively confirmed by the spin density map as it has been obtained from the maximum entropy treatment. In Figure 5.5, a number of slices through the three-dimensional density map is shown, in order to get an as good as possible impression of the spatial distribution. The relevant features are the following:

- The spin density is, as expected, mainly situated on the atomic sites. On some of the bonds (Ru-O), there is also some small, but significant density.

- Not only on the Ruthenium sites, but also on the oxygen sites there is a significant amount of magnetization. This applies especially to the O2 atom (the

---

[3]For instance, when simply counting to the nearest atomic position, the oxygens would get much of the density which should (see the various Figures) actually be attributed to Ruthenium, as the Ru wave function is more extended in space.
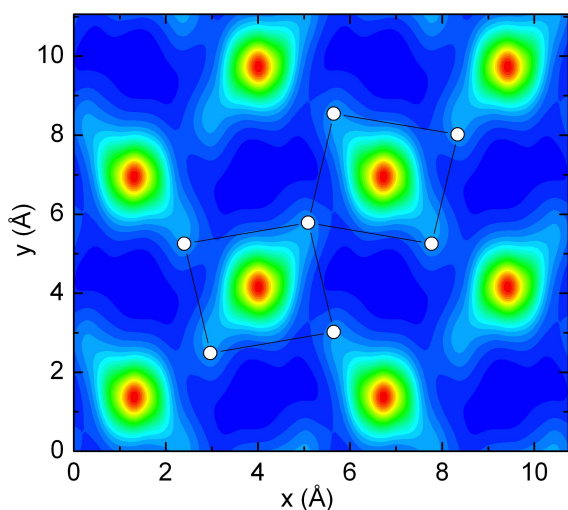
Figure 5.6: One of the RuO_2-layers (± 1.2Å integrated along c). The oxygen positions of two RuO_6 octahedra are indicated.

atom connecting the two layers) and O1, the apical oxygen atom. The two in-plane oxygen atoms have only a small magnetization. This is consistent with the magnetic moments given in the table above.

- The Calcium atoms have no significant magnetization. The map (b) shows no intensity on the Ca-sites.

- The spin density on Ruthenium is clearly not spherical, but more extended along the vertical direction. In the plane, it is much more isotropic, but still seems to possess a minor twofold anisotropy (c).

There is thus a quite strong contrast to the single-layer Ruthenate, in which the spin density has predominantly in-plane character: the Ruthenium spin density is more extended in the a,b-plane, the in-plane oxygen atoms have much, and the apical oxygen atoms nearly no magnetization. In $Ca_3Ru_2O_7$, this is opposite.

The magnetic polarizations of the atoms may be compared to the results of density functional calculations by Singh and Auluck [235]. They find 1.23 μ_B on Ru and 0.21 μ_B on the interlayer bridging oxygen (O2), which is relatively well consistent with the results obtained here. The other oxygen atoms are calculated to have lower polarization, and among these the O1 was predicted to have the lowest (0.08 μ_B) – although the absolute deviations are only small, this contradicts the current finding that also O1 has a higher magnetization than the in-plane oxygens.

Concerning the electronic configuration, it has been suggested on the basis of Raman spectroscopic studies [237] that $Ca_3Ru_2O_7$ is in a ferro-orbitally ordered state. With this term it is meant that the Ru 4d states are occupied like $n_{xy}=2$ and $n_{xz}+n_{yz}=2$, i. e. the d_{xy} would generally be fully occupied (this description implicitly assumes a rather localized picture.) This proposal seems at least partly motivated by the studies on Ca_2RuO_4; however, in contrast to Ca_2RuO_4, the compression of the RuO_6 octahedra is negligible in $Ca_3Ru_2O_7$ [226]. Nevertheless, this scenario is consistent with the

spin density data: if the d_{xy} states are fully or nearly fully occupied, the spins of these two electrons cancel out, so that these states do not contribute to the spin density. The magnetic moment is then carried by the d_{xz} and d_{yz} states. This can explain the fact that the spin density extends more along the vertical axis than along the in-plane directions. The d_{xz} and d_{yz} orbitals do also hybridize with the O1 and O2 atoms, so if they can accommodate part of the charge of the oxygen 2p-shell, also these oxygen atoms can become magnetic. Finally, the predominant occupation of the d_{xy} orbitals is consistent with the LSDA calculation [235], although it also shows that an occupation (2,1,1) for d_{xy}, d_{xz} and d_{yz} is certainly not exact (this is already clear from the fact that in this high-spin configuration the expected moment would be 2 μ_B).

One may therefore assume that the proposed d_{xy} orbital ordered state is at least qualitatively correct. More quantitatively, from the measured polarization of the Oxygen atoms one can estimate that there are about 4.4 electrons in the Ruthenium t_{2g} states, out of which, in view of the Ru polarization, 2.9 should be in the majority and 1.5 in the minority spin bands. The majority spin bands are therefore nearly completely filled, making $Ca_3Ru_2O_7$ almost half-metallic. Among the minority spin bands, the shape of the spin density suggests that d_{xy} is occupied more than the others (thereby reducing the d_{xy} total spin moment).

Less clear is the question for eventual further orbital ordering effects (like, for instance some of the more complicated ordering patterns that have been proposed for Ca_2RuO_4). This question is hard to answer on the base of the present data because the symmetry constraints exclude most antiferro-orbital patterns, as they would require a larger unit cell[4]. Nevertheless, when regarding the spin density in the layers, there is a deviation from the four-fold symmetry. This is seen for instance in Figure 5.5c-e, where the octahedron's basal plane and the O-Ru-O bonds are shown. On one of the diagonals (O-Ru-O) of the basal plane, there seems to be higher density than on the other. This leads to a pattern as shown in Figure 5.6, which one would probably call an antiferro-orbital order. This order is, though, very weak. For a rough estimation of its amplitude, one may take the projected density in the basal plane of the octahedron and determine the integrated difference (absolute value) to the density which is rotated by 90° around the central Ru site, i. e. $\frac{1}{2}\sum|\rho_{xy} - \rho_{yx}|$. In a case of fourfold symmetry, this would be zero. Here, it is near 0.1, so this number could be given as an upper limit for the additional moment on one of the diagonals compared to the other.

Such an additional antiferro-orbital order would be a very interesting result. In resonant x-ray scattering experiments, it has been searched, but not found[5]. On the one hand, the effect is quite weak, so one may suspect an artefact for whatever reason; on the other hand, showing up in the maximum entropy solution makes it quite credible

---

[4] And, of course, it would require the measurement of additional reflections that do not belong to the space group. There is so far no indication of such superstructure reflections.

[5] I. Zegkinoglou and B. Bohnenbuck, private communication

– it is thus at present hard to estimate how reliable this result really is. This is some work that is still in progress. Here, the measurement of flipping ratios in the antiferromagnetic phase and the more precise structural information[6] from the four-circle diffractometer are expected to soon put this statement on a more reliable foundation.

5.2 Magnetism in Ti-doped $Sr_3Ru_2O_7$

5.2.1 Ti-doping and magnetic order in $Sr_3Ru_2O_7$

Among the bilayer Ruthenates, $Sr_3Ru_2O_7$ has, during the recent years, attracted very much attention since the discovery of quantum-critical effects at its metamagnetic transition (see Chapter 3). For this reason it is by now very well studied experimentally and on very high quality samples. Nevertheless, the current level of knowledge is still not such that the complicated behavior, especially the magnetic properties, are fully understood.

When aiming to understand the magnetic properties, it can be interesting to study the effect of doping on the system. This idea has, for instance, been part of the motivation to study the series $Ca_{2-x}Sr_xRuO_4$ or Ti- and other doping in the case of the spin-triplet superconductor Sr_2RuO_4. Doping may enhance or weaken the phenomena, and thus help to better reveal and understand them. Especially when there is competition of different magnetic instabilities, it can be very useful to selectively enhance one of them. In $Sr_3Ru_2O_7$, there seems to be a competition between (incommensurate) antiferromagnetic and ferromagnetic correlations — not only generally expected from the presence of the metamagnetic transition, but also more directly proved by the neutron scattering experiments ([100] and unpublished results by S. Ramos et al.) or ^{17}O-NMR [102]. It is thus very interesting to observe how a slight variation of the chemical composition affects the properties of the system.

In the case of the bilayer Ruthenate, this is a very new research field, in contrast to the single-layer Ruthenates, for which a lot is known about doping with different elements – in particular Ti – as discussed in Chapter 4. Also, the perovskite (113-) Ruthenate has already been quite thoroughly studied concerning doping with Titanium [194, 241–243]. For the double-layer Ruthenates, in contrast, there is up to now nearly no information – as mentioned, only the pure substances $Ca_3Ru_2O_7$ and $Sr_3Ru_2O_7$ have been intensively investigated. One may of course argue that the bilayer Ruthenate should have some properties similar to $SrRuO_3$ and Sr_2RuO_4 (because in the Ruddelsden-Popper series it is located between these), and to some extent it certainly has.

---

[6]Note that the structure in Ref. [226] appears a bit doubtful, because the four in-plane Ru-O bond lengths are quite asymmetric, with the Ru ion not being situated in the centre of the basal plane. One could suspect that this might eventually introduce artificial asymmetries in the spin density.

The first of the two existing reports on doped $Sr_3Ru_2O_7$ [244] does not regard Ti, but Mn doping and states that the paramagnetic metal $Sr_3Ru_2O_7$ is turned into an antiferromagnetic Mott insulator at about 2.5% Mn-doping. The metal-insulator transition is insofar different from perovskite $SrRu_{1-x}Ti_xO_3$ as there it occurs only for much higher Ti-content, $x\sim0.5$ (and its mechanism and the role of percolation is being discussed [194, 241]). By neutron powder diffraction, peaks corresponding to antiferromagnetic order have been identified at $(\frac{1}{4},\frac{1}{4},0)$ and $(\frac{1}{4},\frac{3}{4},0)$, which appear simultaneously to the Metal-Insulator transition [244]. Finally, at this transition, a change in the lattice constants is seen – c shortens and a elongates by about 10^{-3} upon cooling. The structural effect is thus much smaller than in Ca_2RuO_4, but rather comparable to $Ca_3Ru_2O_7$ or the structural anomaly in $Ca_{1.8}Sr_{0.2}RuO_4$. The appearance of incommensurate antiferromagnetic order at a wave vector on the diagonal of the Brillouin zone at a few percent doping strongly resembles the case of $Sr_2Ru_{1-x}Ti_xO_4$, despite the "minor" differences that the latter has lower ordering temperatures, a different propagation vector and no clear metal-insulator transition associated with the magnetic order.

In addition to this study of Mn substitution, one very recent publication addresses Ti-doped $Sr_3Ru_2O_7$ [245] and reports susceptibility, specific heat and resistivity data. The observation is a disappearance of the 16 K-peak in the magnetic susceptibility and a transition to an insulating state above 5% Ti-content. The authors do, surprisingly, not address the issue of possible antiferromagnetic order, but rather do the opposite, namely conclude the enhancement of ferromagnetic fluctuations. (This is mainly inferred from the disappearance of the susceptibility peak, an increasing Weiss temperature obtained from a high-temperature fit to the susceptibility, and a comparison to the metamagnet $Y(Co_{1-x}Al_x)_2$.) This conclusion appears a bit doubtful in view of the effect of Mn-doping, the analogy to $Sr_2Ru_{1-x}Ti_xO_4$ and that the possibility of antiferromagnetic order seems not to be taken into account (for instance, the increase in specific heat C/T could as well arise from antiferromagnetic fluctuations).

First results of J. Farrell from St. Andrews confirm the insulating behavior for Ti-concentrations higher than 5% and the disappearance of the susceptibility peak. There is again no direct evidence for magnetic order – while ferromagnetism can be excluded, the susceptibility does not clearly reveal an antiferromagnetic transition, which may be due to the contamination by small amounts of a ferromagnetic $Sr_4Ru_3O_{10}$ impurity phase.

In this situation, there is an obvious need for neutron scattering experiments in order to clarify the conjecture of magnetic order and what is the nature of magnetic correlations. The following section addresses the diffraction experiments on single crystals with two different Ti-concentrations and unambiguously states the existence of magnetic order. While this basically confirms the expectations, the question of magnetic correlations in view of the relation to $Sr_3Ru_2O_7$ is very interesting and so far very puzzling and will be addressed afterwards in the subsequent section, which reports some preliminary inelastic neutron scattering experiments.

A reason for the interest in the investigation of magnetic correlations by inelastic neutron scattering are the still not very well understood magnetic properties of $Sr_3Ru_2O_7$, especially what magnetic correlations are involved in the metamagnetic transition and the formation of the strange phase around the quantum critical point. The attractive feature of Ti-doping is that it proves the existence of a magnetic instability not considered so far: a propagation vector along the diagonal of the Brillouin zone for which there had no indication been seen in the data on pure $Sr_3Ru_2O_7$. Characterizing this new type of magnetic instability and addressing the question how such different behavior can evolve from each other by small variation of the Ti-content, are interesting reasons for a detailed study of Ti-doped $Sr_3Ru_2O_7$.

5.2.2 Magnetic order probed by elastic neutron scattering

Elastic neutron scattering measurements were performed on crystals with 7.5% and 10% Ti-concentration on 4F1 and on IN12. These crystals had been grown in St. Andrews by J. Farrell and have been mounted in two different orientations: either with *a* and *b* in the scattering plane, or with *a* and *c*. Here and in the following, always the tetragonal notation of the Brillouin zone is used, with a=b≈3.9 Å and c≈20.6 Å. On 4F1, the polarized neutron setup has been used, allowing for full linear polarization analysis in order to probe the magnetic nature of the signal. On IN12, the standard setup was used with a Be-Filter and the sample in a vacuum box which significantly reduced the background at low scattering angles and thus permitted easy measurement of $(\frac{1}{4},\frac{1}{4},0)$.

The history of experiments on Ti-doped Ruthenates is full of impurity phases. As a matter of fact, the presence of elastic magnetic signals in $Sr_3(Ru_{1-x}Ti_x)_2O_7$ has already been relatively clear before the first measurement on these samples, because a corresponding signal in the single-layer $Sr_2Ru_{1-x}Ti_xO_4$ had been identified as the contribution from a 327-impurity phase. Unfortunately, the new samples of bilayer Ruthenates also contained impurity phases: the triple layer and, in some of them, the single-layer phase, each of them in the sizeable amount of several percent. It appears relatively safe to assume that they do not influence the magnetic order itself seriously, so the results are meaningful despite some impurity (also in the single-layer Ruthenates, the impurity phase simply showed up as an additional peak not changing the original one). The stoichiometry concerning the Ti-content may eventually slightly change, but is a negligible effect for the current purpose. It is a more severe problem that $Sr_4Ru_3O_{10}$ has ferromagnetic order below about 105 K with a moment of 1 μ_B per Ru [82]. Though not a problem for diffraction itself, this is, despite the relatively small impurity amount, extremely harmful in the polarized neutron experiment as it very efficiently depolarizes the neutron beam. As well for the inelastic data, see below, this is harmful.

The polarized neutron experiment confirms the magnetic nature of the incommensurate peaks near $(\frac{1}{4},\frac{1}{4},0)$, although with the ferromagnetic impurity the flipping ratios are significantly reduced from their usually very high values on 4F1: as determined on nuclear Bragg reflections, they are between 3 and 9, depending on the spin direction. Thus, the signal is also present in the non-spin-flip channel with H∥Q, but reduced by the factor R – this is strong evidence for the magnetic origin of this peak. Normally, the bad flipping ratios preclude a reasonable polarization analysis. One may add, in the cross sections (2.3), the non-spin-flip term to the spin-flip one with a prefactor $^1/_{R+1}$ (the spin-flip term gets $^R/_{R+1}$), and vice versa, in order to account for this. In view of the statistics, which is also relatively weak on the incommensurate peak, the conclusion still can have only partially quantitative character. The intensities of the incommensurate peak in the spin-flip channel are, for the neutron spin parallel to x=(1,1,0), y=(0,0,1) and z=(1,-1,0):

$\mathsf{I}_x = \quad 37 \pm 6$
$\mathsf{I}_y = \quad 15 \pm 4$
$\mathsf{I}_z = \quad 27.5 \pm 3$

This is consistent with a ratio 12:1 of out-of-plane versus in-plane magnetic moment, each with an error ± 1. It can thus be concluded that the magnetic moment has a large out-of-plane component – most probably, it is indeed oriented parallel to the c-axis. This appears plausible in view of the fact that also in the single-layer Ti-doped Ruthenate the magnetic moment was found to point along the c-direction [189]. The anisotropy of the magnetic fluctuations in Sr_2RuO_4 [144,145] which leads to the magnetic moment direction along the c-axis in the Ti-doped samples is a consequence of the spin-orbit coupling. This anisotropy which favors the c-direction should in principle not be very different in the bilayer Ruthenate. There, the electronic structure has less but still pronounced two-dimensional character. (The role of the rotational distortion of the structure is not evident – the result indicates that it seems not to be important in this context.) In particular, the elongation of the RuO_6 octahedra along the c-axis, the main local distortion at the Ru-site, is still present in $Sr_3Ru_2O_7$ [90].

For the more detailed analysis of the magnetic reflections, the use of unpolarized neutrons is thus favorable, and it turned out that the conditions on IN12 were very well suited to perform these measurements. A representative part of the data set is summarized in Figure 5.7. At low temperature, signals were found at all positions $Q+q_i$, where Q is a vector (h,k,0) with integer h and k, and q_i is a vector with h,k near (but not exactly) $\pm\frac{1}{4}$. The intensity of these peaks decreases, the larger the scattering vector, and they completely disappear when raising the temperature to 30 K. Even without the polarized neutron result, this would be strong evidence for the magnetic origin of these signals.

The magnetic peaks appear relatively sharp in Q. With an approximate model for the resolution function of the spectrometer, one can analyze their width. The (1,-1,0) Bragg reflection appears resolution limited, while the magnetic reflections are slightly broadened, see Figure 5.7. A convolution of a Lorentzian peak function with the
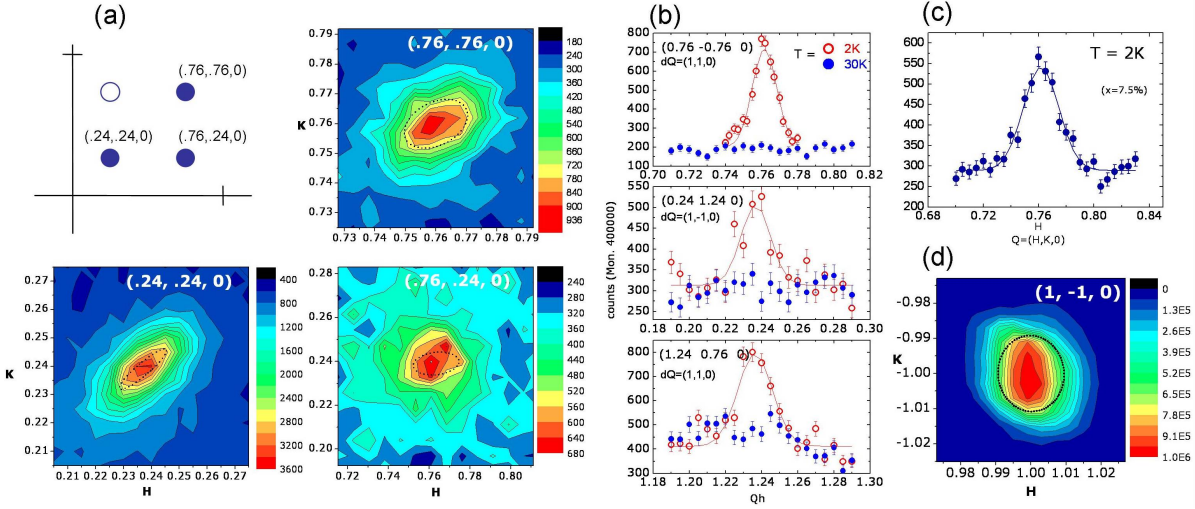
Figure 5.7: Elastic magnetic scattering in $Sr_3(Ru_{1-x}Ti_x)_2O_7$. Figure (a) shows maps of the magnetic scattering near the quarter-positions for $Sr_3(Ru_{0.9}Ti_{0.1})_2O_7$. The calculated resolution ellipsoid at the respective scattering vectors is indicated as the dotted line. Diagonal scans at 2 and 30 K are shown in (b). In (c), a longitudinal scan is shown for the sample with 7.5% Ti. For comparison with the magnetic peaks, the fundamental structural Bragg reflection (1,-1,0) is shown in (d). In all cases, the count rates are normalized to a monitor corresponding to approximately one minute counting time.

experimental resolution yields, by fitting to the data of the intensity maps, a correlation length of 168±5 Å in the a,b-plane (assuming that the intensity is extended along L, see below). Though perhaps still a simplistic description, this demonstrates that the magnetic correlation within the layers extends over quite a large distance.

Along the vertical direction, in contrast, there is only very little correlation. A limited region of finite L-components of the scattering vector could be measured by tilting the cryostat. Magnetic intensity is found at all values of L, but the various peaks at different (H,K,0) have different L-dependence, see Figure 5.8. Those around (0,0,0) and (1,1,0) have their maxima at L=0, while the ones around (1,0,0) at L=1. This means the maxima are always found at positions separated by (±0.24,±0.24,0) from the true Bragg points of the body-centred lattice (h+k+l even), and the intensity at positions like (0.76,0.24,0) is not a real magnetic Bragg peak but rather originates from the wide extension of the (0.76,0.24,±1) reflections. One can thus draw the following conclusions: the magnetic order is three-dimensional and reflects the layered structure, which is body-centred in the tetragonal unit cell (neglecting the structural distortions). On the other hand, the intensity distribution as function of L is very broad – this indicates a very short correlation length (the quantitative analysis cannot be performed due to unfavorable resolution conditions along this direction). Perhaps there may even be an L-independent part, suggesting a disordered component, but proba-

Figure 5.8: Magnetic intensity as function of L, measured by tilting the cryostat. Closed symbols are intensities obtained from full rocking scans. The background has been subtracted, i. e. any intensity is truly *magnetic*. An attempt to visualize this result is given in the two sketches: the intensity forms streaks along the L-direction with maxima (thick regions) either at odd or even L-values (b). In the L=0 plane (a), closed circles indicate true maxima and open circles those positions where the peaks arise only from the large L-extension.
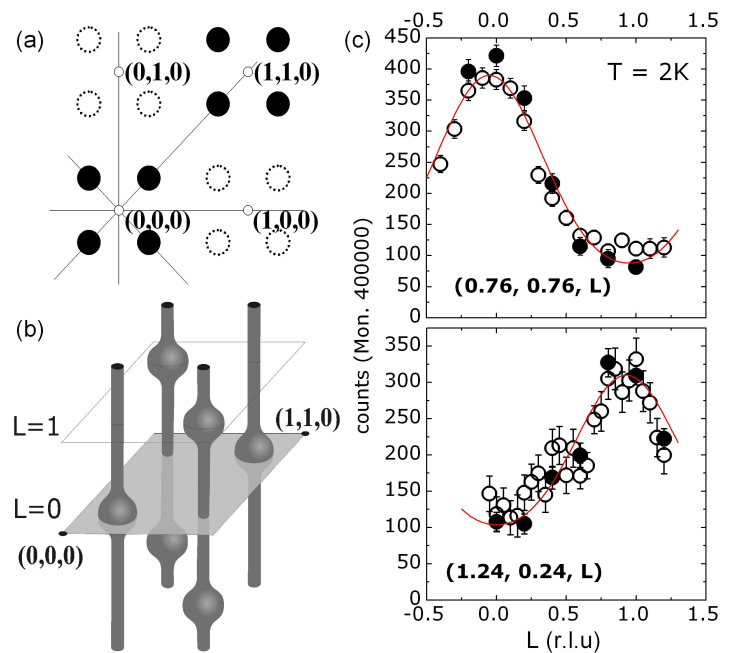
bly the finite intensity at some distance from the maximum in Figure 5.8 simply arises from the large width alone when considering the overlap with the intensity stemming from the next maximum (not in the measured range) at $L_{max}\pm2$.

This type of magnetic order represents a noteworthy difference to the magnetic order in the Ti-doped single-layer Ruthenate: there, the propagation vector has a finite L-component, (0.307, 0.307, 1) [189].

The coupling *within the two layers that form the bilayer* is ferromagnetic. Due to the very limited accessible L-range, it is not possible to observe the modulation arising from the bilayer structure factor, $\cos^2(2\pi Lz/c)$ (where z is the distance between the layers); in the case of antiferromagnetic coupling, in contrast, the intensity at L=0 should be zero. A ferromagnetic coupling would correspond to $Ca_3Ru_2O_7$, where the two layers are also coupled ferromagnetically. In general, *any* magnetic coupling within the bilayer is probably strong, and although (unlike in $Ca_3Ru_2O_7$) of antiferromagnetic character in the a,b-directions in $Sr_3(Ru_{1-x}Ti_x)_2O_7$, this is reflected by the long in-plane correlation length. The relative weakness of the inter-bilayer coupling leads to only weakly correlated order along the vertical direction.

To give further details about the magnetic structure is difficult because the current measurement contains only very few inequivalent reflections, and the evaluation of the intensities is further complicated by the disorder effects. Not excluding other possibilities, one may state that the "simplest" model, a sinusoidal spin-density wave with propagation vector (0.24, 0.24, 0) is consistent with the observations, if its amplitude is between 0.5 and 1 μ_B. This size of the ordered moment is significantly larger than
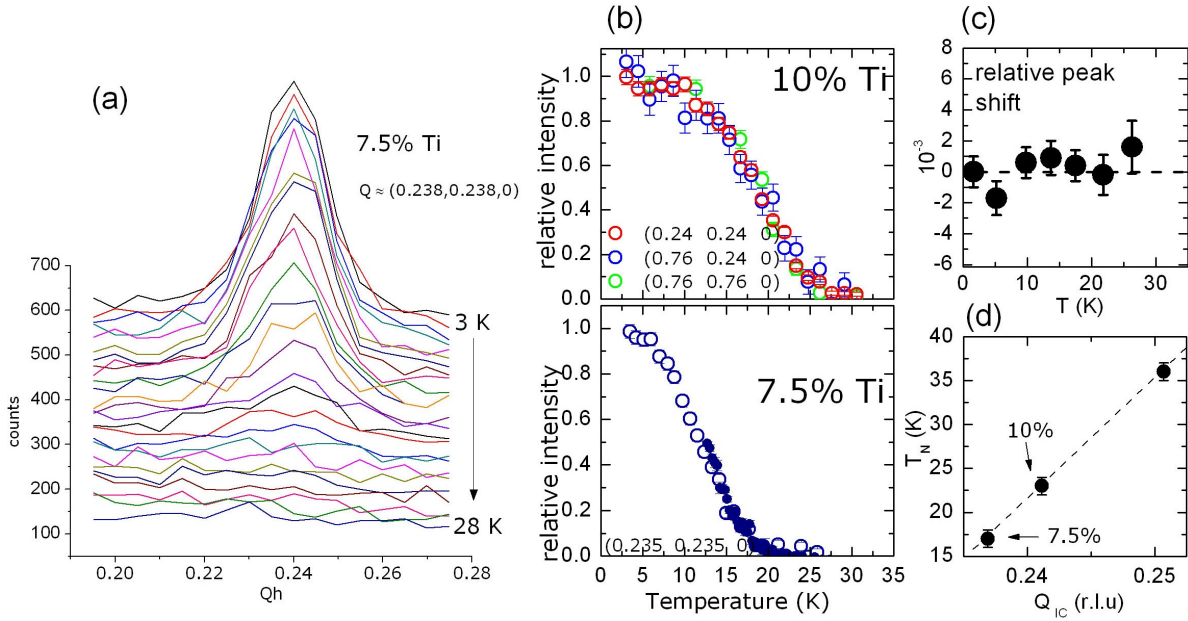
Figure 5.9: Temperature dependence of elastic magnetic scattering in $Sr_3(Ru_{1-x}Ti_x)_2O_7$. (a) The variation of the magnetic reflection with temperature in $Sr_3(Ru_{0.925}Ti_{0.075})_2O_7$ (transverse scans). (b) The intensity of several magnetic reflections (fit to scans, background subtracted) as function of temperature for the two Ti-concentrations. The position of the peaks is constant (c), but depends on the Ti-concentration and T_N (d).

in $Sr_2Ru_{1-x}Ti_xO_4$ ($\sim 0.3\ \mu_B$). The elastic intensity depends on the square of the magnetic moment. The relatively large value of the magnetic moment is the reason for the high measured intensities and can explain why the 327-impurities in the single-layer Ruthenates could give rise to scattering of nearly the same strength as the majority phase.

The temperature dependence of the magnetic signals is summarized in Figure 5.9. The various magnetic peaks have the same temperature dependence and disappear simultaneously, as expected. For 10% Ti, the ordering temperature is about 5 K higher than for 7.5% Ti. As $T_N(x)$ does most probably not vary linearly with the Ti-content x, one cannot extrapolate the critical value of x where the order appears. It may be a similar value like in the case of Mn-doping [244]. There is, though, a remarkable difference in the ordering temperatures, which are much higher for the Mn-doped crystals.

As stated above, the propagation vector is not exactly at quarter-values, i. e. not commensurate with the lattice. On the cold triple-axis spectrometer, the position of the peaks can be quite precisely determined, and the positions of equivalent peaks around several different reciprocal lattice points are well consistent. As function of temperature, no shift can be resolved, but it turns out that the position is not equal

for the two concentrations: q=0.2369(2) for x=7.5% and q=0.2411(2) for x=10%. With only two concentrations studied, one cannot specify in more detail the doping dependencies of T_N and q. There is, however, a noticeable implicit relation between T_N and q (Figure 5.9d): when including a third point, which is obtained from the study of the impurity signal in a 214-crystal, there is some evidence for a linear relation between these two quantities. One might speculate that order could perhaps become more stable if it is commensurate with the lattice (q=1/4), but at present the data is definitely not sufficient for a strong statement.[7] In addition, sample quality might be important for such rather small effects (possible deviations in stoichiometry, though, are obviously irrelevant for this type of plot). One would clearly need a greater number of points to clarify this issue.

Structural effect at the magnetic transition   At the magnetic ordering temperature, there is also a structural effect. Normally, a diffraction experiment like in the setup with a multi-crystal on a thermal triple-axis spectrometer with coarse resolution cannot measure relative changes of lattice constants very precisely. However, on the edge of a strong Bragg reflection, where the slope $|dI/dq|$ is large and the count rate very high (but safely below saturation), the measured intensity is extremely sensitive to a change of the lattice constant – provided that no part of the spectrometer is moved during the procedure. This "trick" has been applied to the (2,0,0) Bragg reflection of $Sr_3(Ru_{0.9}Ti_{0.1})_2O_7$ on IN22. It yields a relative elongation of the lattice constant *a* by $1.15 \cdot 10^{-4}$ when cooling through T_N. The c-axis was not in the scattering plane, so it is not sure if it simultaneously shortens, as might be suspected. The elongation of the in-plane lattice constant resembles the structural effect that is observed in an astonishingly large number of similar compounds, like for instance the single-layer $Ca_{2-x}Sr_xRuO_4$, in $Ca_3Ru_2O_7$, in Ca_2RuO_4 (there, it is more than an order of magnitude larger) or in the closely related Mn-doped $Sr_3Ru_2O_7$. Although these materials differ in the detailed nature of their low temperature phases (different type of magnetic order or magnetic correlations), it is very interesting and remarkable that this is obviously a quite universal effect.

5.2.3 Magnetic excitations in $Sr_3(Ru_{0.9}Ti_{0.1})_2O_7$

Inelastic neutron scattering experiments have been performed on the cold neutron triple-axis spectrometer IN12 and on the thermal neutron triple-axis spectrometer IN22. For this measurement, five newly grown single crystals between 1 and 2 cm length have been coaligned with the *a* and *b*-axes in the scattering plane (Figure 5.10). This setup turned out to be in principle well suited for measuring the magnetic

---

[7]In such a case, it would be interesting to see if also the correlation length is longer. The peak width seems indeed to be smaller, but due to the quite different experimental conditions, a precise comparison is very difficult.
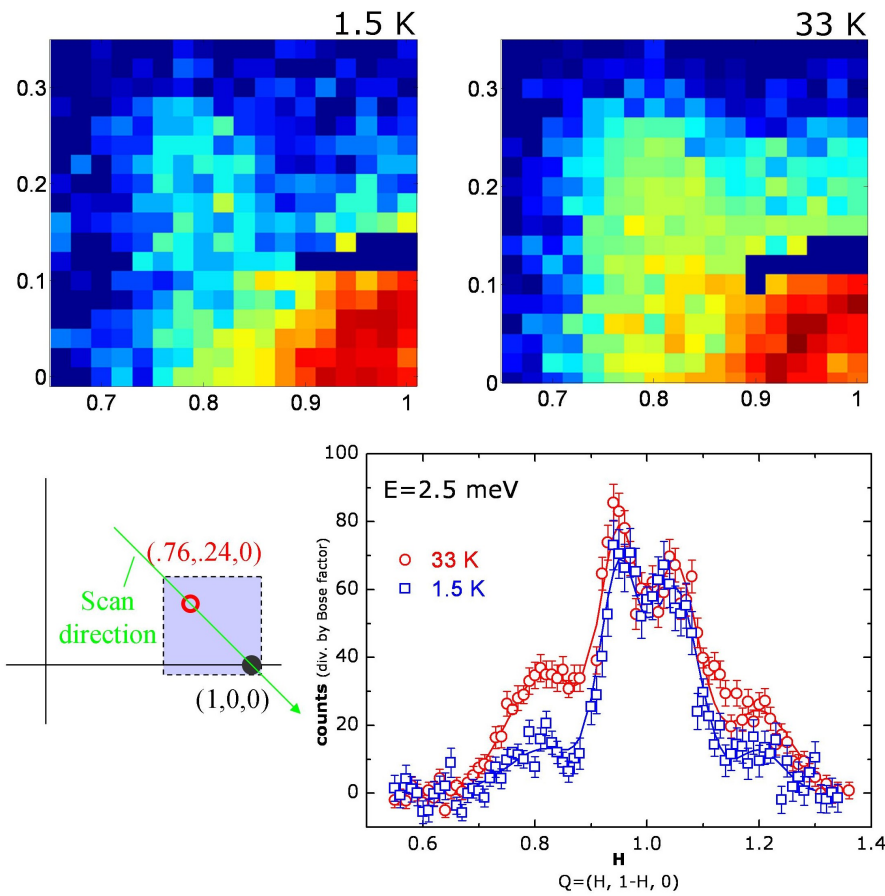
Figure 5.11: Inelastic scattering at 2.5 meV in $Sr_3(Ru_{0.9}Ti_{0.1})_2O_7$. The maps show the distribution of intensity near (1,0,0) and (0.76,0.24,0) at 1.5 and 33 K. Below: two diagonal scans (corrected for the Bose factor). The enhancement at H=0.8 and 1.2 is clearly more than the Bose factor.

excitations; in particular, the intensity of the signals was, compared to some other Ruthenates, in an at least reasonable range. A serious problem was caused only by the presence of the $Sr_4Ru_3O_{10}$ impurity phase. Its ferromagnetic order causes the presence of magnons which significantly contribute to the inelastic neutron scattering cross section and in some Q-regions overlay the signals to be studied.

The overall distribution of intensity in the Brillouin zone is probably best visualized in the intensity maps at E=2.5 meV in Figure 5.11. There are several important contributions:

- The highest intensity is found near Q=(1,0,0). As in the single-layer Ruthenate, this is not a Bragg point of the reciprocal lattice, but as the magnetic correlations have strongly two-dimensional character, it can be regarded as a ferromagnetic zone centre.

- Another maximum, though much smaller, is also observed near the Q-vector of the incommensurate magnetic order, Q=(0.76,0.24,0). Its maximum seems slightly shifted towards (1,0,0), which is probably mainly due to the beginning overlap with the intensity around (1,0,0).
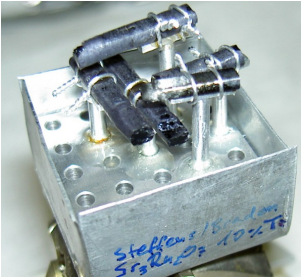
Figure 5.10: Sample used for inelastic measurements on $Sr_3(Ru_{0.9}Ti_{0.1})_2O_7$: five crystals coaligned with the c-axis vertical

The signal near (1,0,0) is symmetric around (1,0,0) and has dispersive character. In the intensity maps, one can clearly identify the quarter-circle centred at (1,0,0) which arises from the constant-energy cut through the dispersion cone. It is most probably due to a ferromagnetic magnon and seems to have its origin in the ferromagnetic $Sr_4Ru_3O_{10}$ impurity phase. This is supported by its temperature dependence: there is no perceptible change at T_N, and it can be followed up to 150 K, the highest measured temperature. Near 90 K, which is about the ferromagnetic ordering temperature in pure $Sr_4Ru_3O_{10}$, it becomes significantly broadened. A quite peculiar feature in its temperature dependence is the quickly increasing separation of the peaks towards higher temperature, which indicates a softening of the dispersion. As an impurity phase, the $Sr_4Ru_3O_{10}$ components are probably quite diluted in the crystal, so its properties may differ from that of pure $Sr_4Ru_3O_{10}$. There is nevertheless good reason to believe that the dispersive signal around (1,0,0) is related to $Sr_4Ru_3O_{10}$. Of course this does not mean that this scattering does entirely originate from $Sr_4Ru_3O_{10}$ – also the 327-phase may well contribute, but it is impossible to separate these contributions.

The overwhelming strength of this signal compared to all other features is (even in view of the fact that $Sr_4Ru_3O_{10}$ has a large ordered moment) quite astonishing and might be taken as a reason for deep pessimism regarding the significance of the collected data for the $Sr_3(Ru_{0.9}Ti_{0.1})_2O_7$ studies at all. There are nevertheless some features that can well be separated and provide interesting information about $Sr_3(Ru_{0.9}Ti_{0.1})_2O_7$.

Regarding the diagonal scans in Figure 5.11, there is a remarkable temperature effect. After correction for the Bose factor, the inner (magnon) signal is temperature-independent, while the outer component at H=0.8 and the symmetric one at H=1.2 are strongly enhanced at 33 K. This unambiguously proves that this signal is independent from the strong ferromagnetic one. As it is found at the wave vector of the incommensurate antiferromagnetic order, it is interpreted as the excitations of the spin density wave.

It can be reasonably separated from the ferromagnetic component up to about 6 meV energy transfer; above, the dispersion of the magnon causes significant overlap with it. Up to 6 meV, though, this signal can be well studied, and constant energy scans in (1,1,0)-direction are not contaminated by the magnon scattering. Figure 5.12 contains a detailed characterization of these excitations. The constant energy scans across this signal have the same shape in the entire range of temperatures and energy transfers that has been studied. (22 K is below, and 33 K above the ordering temperature of the sample.) In particular, in the ordered state at 1.5 K there is no dispersive feature; the peak width does not depend on the energy transfer and is larger than the resolution. The width and the absence of dispersion speak against the in-
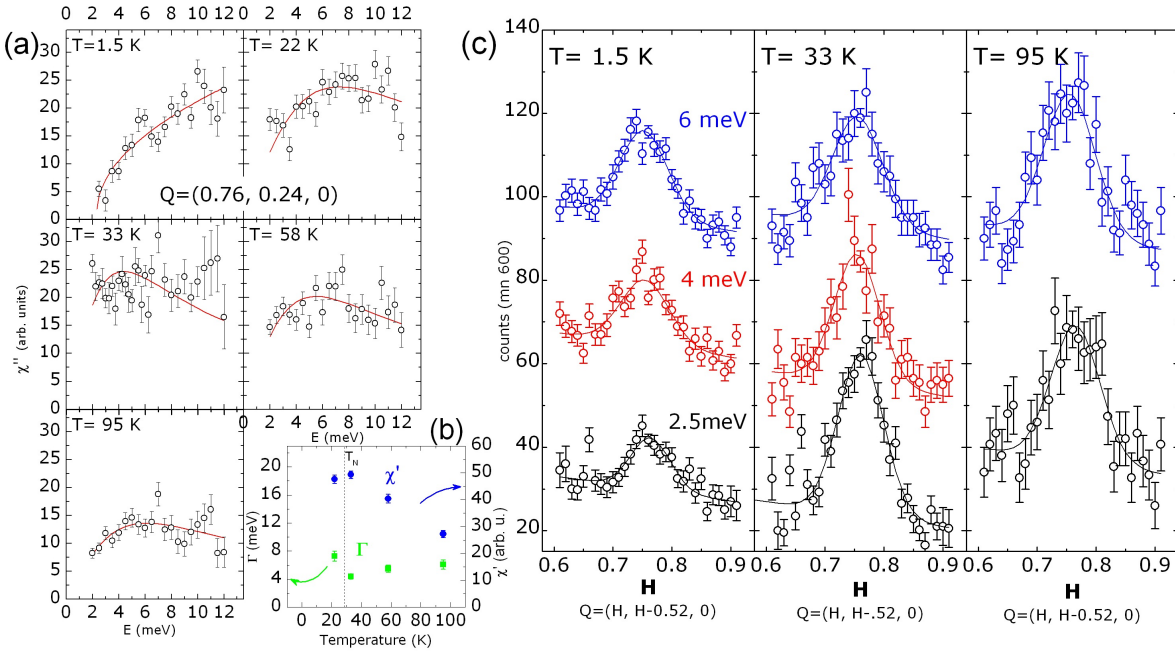
Figure 5.12: Magnetic excitations at the incommensurate wave vector (0.76, 0.24, 0). (a): Energy scans at five temperatures, (b) summarized the fits of single relaxor functions (T≥22 K). In (c), a series of constant energy scans across this signal is shown.

terpretation as a collective mode but rather as excitations within the continuum. It is, however, not possible to entirely rule out the relevance of one or several modes with a very steep dispersion. Further support for this statement comes from the shape (the width) of the constant energy scans, which is essentially unchanged when heating to temperatures above T_N.

While the width remains the same, there is nevertheless a significant temperature dependence in the intensities and spectral functions, which manifests itself in the energy scans (Fig. 5.12a). Above T_N, the energy scans can be approximately fitted with a single relaxor function – the better, the higher the temperature. The maximum of spectral weight (Γ) shifts to lower energies, as expected when approaching the transition. It can, however, not be seen in the data that it approaches zero, as normally expected. It has to be kept in mind, though, that close to the transition this spectral form may be inadequate as only one component (χ_{zz}, as M‖z) is expected to diverge, while the others remain finite. At 22 K, the reduced intensity at low energies indicates the beginning of opening a gap. At 1.5 K, there is clear indication for the formation of a gap below about 2 meV.

It is in general a very interesting question what is the relation between the magnetic correlations in $Sr_3(Ru_{0.9}Ti_{0.1})_2O_7$ to those in $Sr_3Ru_2O_7$. It is highly astonishing that the wave vector at which magnetic order appears in Ti-doped $Sr_3Ru_2O_7$ seems to have
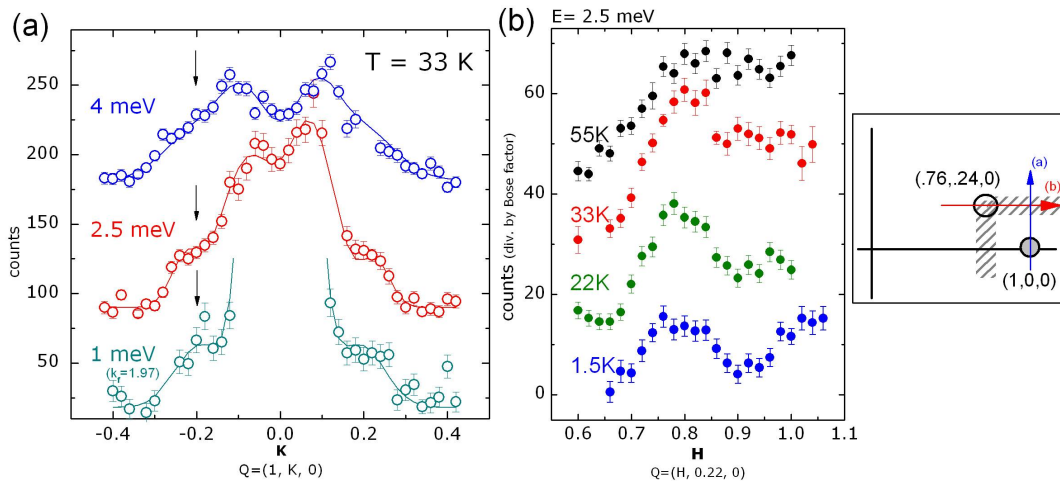
Figure 5.13: (a) Transverse scans across (1,0,0), showing a pronounced shoulder at K=±0.2 (1 meV data not directly comparable due to a different k_f). (b) Scans ∥H across the incommensurate peak towards the shoulders in (a), as indicated in the sketch.

no relation to the magnetic correlations in pure $Sr_3Ru_2O_7$. This is in sharp contrast to the single-layer Ruthenates. There, the magnetic instability at which magnetic order appears under Ti-doping is already observed in Sr_2RuO_4 in the form of strong magnetic fluctuations. In $Sr_3Ru_2O_7$, inelastic magnetic signals have been identified on the a/b-axes rather than on the diagonal, at q=0.09 and 0.25 [100]. In addition, ferromagnetic fluctuations have been found at higher temperatures, but no indication for anything related to the diagonal propagation vector of magnetic order in the Ti-doped samples[8].

Concerning ferromagnetic fluctuations, as they have also been suggested by Hooper et al. [245], one cannot make any clear statement, because the measured intensity around any ferromagnetic wave vectors is overlayed by the signal from the impurity phase. It is well possible that a ferromagnetic contribution from $Sr_3(Ru_{0.9}Ti_{0.1})_2O_7$ also exists, but it cannot be separated. Even if present, their existence would probably not answer the question about the relation between the incommensurate wave vectors on the axes and the diagonals.

Regarding the transverse scans across (1,0,0) at T=33 K in Figure 5.13, there is a distinct shoulder on both sides near ±0.2. Its position thus resembles the outer incommensurate peak in $Sr_3Ru_2O_7$ (q≈0.25). The inner one, if present, suffers from the overlap with the ferromagnetic signal and can definitely not be observed. It is tempting to identify this shoulder with the incommensurate peak in $Sr_3Ru_2O_7$. This signal, while well observable at 33 K at different energy transfers, seems to be not present or at least much weaker at 1.5 K (not shown). In view of a signal at this position,

---

[8]Although not identified as a peak, there seems to be some small intensity also on the diagonals of the published data in Ref. [100]. It is, however, extremely weak.

one might speculate about its connection to the one on the diagonal, as the value of H is nearly identical[9], or in other words, it is in the middle between two of the four incommensurate magnetic peaks that form the corners of a square around (1,0,0). To clarify this, a scan has been performed at various temperatures along the line which connects the incommensurate magnetic peak on the diagonal of the Brillouin zone with the shoulder in the scan through (1,0,0), see Figure 5.13. It gives the impression that at low temperature (1.5 and 22 K) the fluctuations at (0.76,0.24,0) form a rather well separated peak, while at higher temperature there is a more continuous flatter connection. This impression is supported by the two intensity maps in Figure 5.11 in which the incommensurate peak on the diagonal seems to be somewhat more isolated at 1.5 K. One might thus speculate that the (1,0.25,0)-signals as they exist in $Sr_3Ru_2O_7$ and seem to be present also in this case, become somewhat elongated perpendicular to the axis; such symmetrically equivalent streaks would meat exactly at the magnetic peaks on the diagonals. This could then be an explanation why the vector of the dominant fluctuations respectively the magnetic order is on the diagonal of the Brillouin zone. However, the support for this scenario from the data is not yet very strong. In particular, the possible influence from the broad ferromagnetic scattering represents an uncertainty in this scenario. It is nevertheless a possibility how one might be able to reconcile the different wave vectors of magnetic signals as soon as this can be verified on samples of higher purity and eventually different Ti-concentrations.

5.3 Summary

The spin density study in $Ca_3Ru_2O_7$ has been experimentally well feasible due to the large induced magnetic moment above the metamagnetic transition. It provides a detailed mapping of the spin density distribution. Significant magnetization is found not only on the Ruthenium site, but also on the two Oxygen sites which do not belong to the layers. On Ruthenium itself, the spin density is very aspheric and elongated along the vertical O-Ru-O bonds. This distribution agrees with the proposals concerning the orbital occupation [235,237] which essentially correspond to a state of ferro-orbital order in which the d_{xy} states are fully or nearly fully occupied. In the layers, there is an additional, though quite weak indication for antiferro-orbital order.

In Ti-doped $Sr_3Ru_2O_7$, magnetic order with a propagation vector near $Q_{mag}^{327}=(\frac{1}{4},\frac{1}{4},0)$ has been found. The exact value of Q_{mag}^{327} depends on the Ti-concentration and seems to scale with the transition temperature. While the correlation length within the lay-

---

[9]The H-value of the shoulder, as well as the H,K-values of the incommensurate magnetic peak seem to be always somewhat lower than 0.24 (as expected from the propagation vector of magnetic order) or 0.25 (the value of the $Sr_3Ru_2O_7$-peak). This may be not very significant because all signals are very broad, and the overlap with the ferromagnetic signal generally tends to shift the maxima to lower values.

ers is long, there is only weak correlation between different bilayers. Furthermore, a structural effect similar to other Ruthenates has been observed at the magnetic transition.

The study of the excitation spectrum in $Sr_3(Ru_{0.9}Ti_{0.1})_2O_7$ has proven the existence of magnetic fluctuations at Q_{mag}^{327} both above and below T_N; below T_N, they are gapped below about 2 meV. Another broad signal is found on the axes of the Brillouin zone, separated about q=0.2 from (1,0,0). This is close to the position of the incommensurate magnetic response in pure $Sr_3Ru_2O_7$ [100] (peaked at q=0.09 and 0.25). The intriguing question how the spin dynamics of pure $Sr_3Ru_2O_7$ is related to the one of Ti-doped $Sr_3Ru_2O_7$ and its magnetic order, can not yet be finally answered because strong intensity centred at ferromagnetic wave vectors, which seems mainly to arise from an impurity phase, has rendered the study of these signals difficult. It turns out, though, that at both types of wave vectors – those on the axes like in $Sr_3Ru_2O_7$ and those on the diagonal – there is significant inelastic scattering.

6 Summary, conclusions and outlook

The largest part of the experimental work presented in this thesis has addressed the magnetic correlations in **$Ca_{2-x}Sr_xRuO_4$** and in particular the metamagnetic transition. In $Ca_{2-x}Sr_xRuO_4$ (here studied for x=0.2 and 0.62) there are strong magnetic correlations of both ferromagnetic and incommensurate antiferromagnetic character. The interplay of these magnetic instabilities governs the behavior of these materials.

In $Ca_{1.8}Sr_{0.2}RuO_4$, the ferromagnetic fluctuations are strongly suppressed at low temperature ($\sim$2 K). The antiferromagnetic response has been characterized in detail and was found to have a complicated structure consisting of at least two contributions on the axes of the Brillouin zone on each side of the 2D zone centre. These excitations can probably be ascribed to nesting vectors in the γ-sheet of the Fermi surface. In addition, nesting in the α and β-sheets gives rise to another, weaker signal closely related to the incommensurate signal in Sr_2RuO_4, thus proving that these two Fermi surfaces are still intact and that the filling of the bands has not significantly changed compared to Sr_2RuO_4.

Upon increase of the temperature, intense paramagnon scattering appears, which is in good agreement with the macroscopic magnetic susceptibility. These fluctuations of ferromagnetic character and low characteristic energy are significantly enhanced at the metamagnetic transition and seem to determine the thermodynamics of the metamagnetic transition. The antiferromagnetic fluctuations, in contrast, are entirely suppressed by the magnetic field. Above the metamagnetic transition, the excitations have a dispersive character and can be well described as a ferromagnetic magnon. This observation – to the best of our knowledge the first observation of this kind – proves the presence of a strong ferromagnetic interaction, and that $Ca_{1.8}Sr_{0.2}RuO_4$ above the metamagnetic transition is in an intrinsically ferromagnetic state.

$Ca_{1.38}Sr_{0.62}RuO_4$ is, without field, very close to the transition into a ferromagnetic state and shows, in addition to the incommensurate antiferromagnetic signals, strong ferromagnetic fluctuations. The superposition of ferro- and antiferromagnetic components fully describes the magnetic response, and its evolution up to temperatures above 100 K arises from the respective temperature dependencies of these components.

In **Sr_2RuO_4**, a thorough study of the magnetic fluctuation spectrum has been carried out using polarized neutrons in order to resolve weak magnetic signals. Thereby, the existence of magnetic fluctuations around the centre of the Brillouin zone, i. e. of ferromagnetic character, has been proved. These fluctuations are only weakly

Q-dependent and cover a large portion of the Brillouin zone; their momentum width (FWHM) is approximately π/a. These fluctuations do not significantly change between low temperature (1.6 K) and 150 K. Their amplitude is in accordance with the macroscopic magnetic susceptibility and amounts to only about 10% of the amplitude of the incommensurate fluctuations that have recently been well characterized. Furthermore, the characteristic energy of the ferromagnetic signal is higher and amounts to 15-20 meV. The derived model for $\chi(q)$ is in quantitative agreement with NMR and specific heat data from the literature. These comparisons underline the importance of the weakly Q-dependent part of the fluctuations.

These neutron scattering results present the first clear and direct observation of these fluctuations which have earlier been suggested for instance by NMR data. Moreover, their energy scale and Q-dependence is directly obtained. Although broad, they are peaked at the zone centre, and are below the limit of detection at the zone boundary, in contrast to the assumption of a Q-independent contribution that has so far sometimes been made. In the framework of an RPA analysis, this variation has to be attributed to a strong Q-dependence of the interaction parameter $I(q)$.

A detailed quantitative evaluation whether the effect of this ferromagnetic component is sufficient to account for the properties of the superconducting state in Sr_2RuO_4 within the framework of the various theoretical approaches would be highly desirable. In general, though, the existence of ferromagnetic fluctuations might resolve some of the problems associated with the previous models consisting of incommensurate and/or Q-independent magnetic fluctuations. In this sense, the results presented here support the hypothesis of magnetically mediated spin-triplet pairing in Sr_2RuO_4 and may be a basis for its quantitative explanation.

The measurements on **Ti-doped Sr_2RuO_4** have shown excitations that resemble the magnetic fluctuations in Sr_2RuO_4. In the ordered state (x=9% at low temperature) there is an indication of a gap in the excitation spectrum. Near the critical concentration x=2.5% the fluctuations at low temperature are enhanced, but do not obey an ω/T-scaling law down to T=2 K. This is probably to be regarded as an effect of disorder which inhibits the divergence of magnetic fluctuations and makes quantum critical behavior in $Sr_2Ru_{1-x}Ti_xO_4$ not observable like in a clean system.

On the bilayer Ruthenates, valuable information was obtained by elastic neutron scattering. In a study with polarized neutrons, the spin density of **$Ca_3Ru_2O_7$** has been determined. It shows a pronounced non-spherical distribution on the Ru sites, which is elongated along the vertical direction, and significant magnetization on the apical and the connecting interlayer oxygen atoms. These results qualitatively support the assumed occupation of the different Ru 4d states; in addition there is a weak indication of an antiferro-orbital pattern that needs further examination.

In **$Sr_3(Ru_{1-x}Ti_x)_2O_7$**, static spin-density wave order was found with a propagation vector $\sim(\frac{1}{4},\frac{1}{4},0)$ and characterized in detail for the Ti-concentrations 7.5 and 10%. A preliminary study of the magnetic excitation spectrum in $Sr_3(Ru_{0.9}Ti_{0.1})_2O_7$ shows

excitations at a Q-vector on the diagonal that corresponds to the propagation vector of the ordered state, which are gapped below about 2 meV at low temperature. Another incommensurate signal exists near q=0.2 on the axes; this probably corresponds to the signal in $Sr_3Ru_2O_7$. The relevance of ferromagnetic scattering can, due to an impurity signal, hardly be estimated.

At the end, one should try to give a realistic estimation of the current state of the investigations and point out possible future steps that appear worthwhile from today's point of view.

The bilayer Ruthenates are a relatively new field, and it appears almost certain that the continuation of these subjects will yield further interesting results.

Concerning the single-layer Ruthenates $Ca_{2-x}Sr_xRuO_4$ and Sr_2RuO_4 (in its normal state), substantial progress has been achieved in both cases, and the thus obtained picture appears consistent and complete. A significant improvement with reasonable effort seems impossible at the current state of sample growth, instrumental development and neutron flux. In Sr_2RuO_4, however, a more precise study of the magnetic fluctuations in the superconducting state would be – despite the great experimental difficulties – desirable because of the high potential of such measurements to provide further insight into the nature of superconductivity in Sr_2RuO_4.

In conclusion, the wide field of magnetism in the Ruthenates and the various fascinating phenomena associated with it can by far not yet be regarded as sufficiently studied and understood, and future theses will certainly be written about the Ruthenates. Nevertheless, a better and better overall understanding of the magnetism in the Ruthenates and related materials is emerging on the basis of these and other results and is a good reason to expect further interesting discoveries in the future.

A Appendix

A.1 The calibration of magnetic scattering intensity

This section describes the procedure of calibrating a magnetic intensity against an acoustic phonon, as briefly discussed in section 2.1.3, including the technical details. We first recall the formulas for the cross sections of phonon and magnetic scattering (2.1) and (2.4) and formulate them in terms of the functions `phonon` and `chi`. This is just an expansion of the cross-section formulas by a scale factor and two normalization constants Y (to be determined) and C (known) in order to split off these two functions in convenient units.

$$
\left(\frac{d^2\sigma}{d\Omega dE}\right)^{mag} = N\frac{k_f}{k_i}\frac{r_0^2}{4\pi\mu_B^2}\frac{Y}{\texttt{Scale}^{mag}}\cdot\texttt{chi} \tag{A.1}
$$

$$
\left(\frac{d^2\sigma}{d\Omega dE}\right)^{ph} = N\frac{k_f}{k_i}\frac{\hbar^2}{2}\frac{C}{\texttt{Scale}^{ph}}\cdot\texttt{phonon}
$$

where

$$
\texttt{chi} = \texttt{Scale}^{mag}\cdot\chi_{\mathsf{model}}\cdot F(\mathrm{Q})^2\cdot\frac{1}{1-e^{-\frac{E}{k_BT}}} \tag{A.2}
$$

$$
\texttt{phonon} = \texttt{Scale}^{ph}\cdot\frac{|F_{ac}(\mathrm{Q})|^2}{E_q\cdot C}\cdot\delta(E-E_q)\cdot\frac{1}{1-e^{-\frac{E}{k_BT}}}
$$

Here $F_{ac}(q)$ is the structure factor of the acoustic phonon (2.4), and $C = \lim_{q\to 0}|F_{ac}(\mathbf{Q})|^2$. This formulation represents the implementation of the dynamical structure factor, which is by F_{ac}^2/C normalized to 1 in its limit. Because in `phonon` E enters explicitly, meV has been assumed as the energy unit, i. e. one must use the (dimensionless) numbers $E = \frac{\hbar\omega}{1\,\mathrm{meV}}$ and $E_q = \frac{\hbar\omega_q}{1\,\mathrm{meV}}$. The Debye-Waller factor could be included, but is not important because in magnetic scattering one usually works at low temperature and small Q. The function `chi` contains a numerical model χ_{model} for the imaginary part of the susceptibility, which is the true one normalized by the factor to be determined:

$$
\chi_{\mathsf{model}} = \frac{\chi''(\mathrm{Q},\omega)}{Y} \tag{A.3}
$$

On a spectrometer, the intensity (in number of counts per monitor) is expected to be an unknown constant times the convolution of the cross section with the resolution
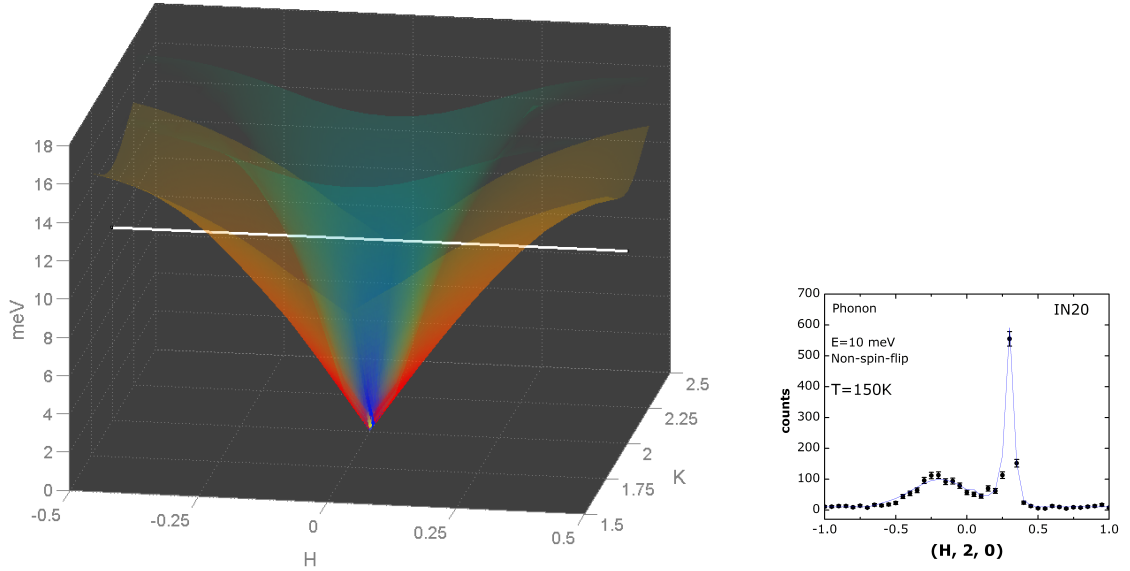
Figure A.1: **Left:** Acoustic phonons in Sr_2RuO_4 at $Q = (0, 2, 0)$. The red/orange surface is the dispersion of the transverse acoustic phonon; the z-value is the energy in meV, and the intensity of the color corresponds to the structure factor. One recognizes that its intensity is maximum along h^*, i.e. in a scan $(0, 2, 0) \pm x \cdot (1, 0, 0)$, and zero for $(0, K, 0)$, as expected for the transverse polarization. The white line corresponds to a constant energy scan at 10 meV. The blue surface is the longitudinal phonon; for a scan like the one shown it does not contribute significantly. (Accordingly, the intensity of the red surface fades away towards (0,K,0).) These surfaces are the function that has been used to fit the phonon scans.
Right: Constant energy scan at 10 meV measured on IN20 (counting time $\simeq$ 13s per point) and the fit to the function describing the phonon, taking account for the resolution of the spectrometer.

function. This convolution is performed numerically by the software (Matlab/ResLib) on the functions `phonon` and `chi` and, by adjusting the scale factors, fit to the experimentally measured count rates. This means in fact that $Scale^{ph}$ and $Scale^{mag}$ are fit in the way that the prefactors in the both equations (A.1) become equal. From this condition, Y is then easily determined:

$$Y = \frac{Scale^{mag}}{Scale^{ph}} C \frac{2\pi \hbar^2}{r_0^2} \mu_B^2 meV^{-2} = \frac{Scale^{mag}}{Scale^{ph}} C \cdot 1.489 \cdot 10^{-14} kg \cdot \frac{\mu_B^2}{eV} \qquad (A.4)$$

This is all the necessary information. One finally has to keep in mind that one usually measures a sum of different components of $\chi''(\mathbf{Q}, \omega)$, see (2.2). By explicit summation of the structure factor $F_N(\mathbf{G}) = \sum_j \bar{b}_j e^{i\mathbf{G} \cdot \mathbf{d}_j} e^{-W_j}$, one obtains $C \left(= \frac{\mathbf{G^2}}{M} |F_N(\mathbf{G})|^2 \right)$.

Some useful values are, for $Q = (2, 0, 0)$, and referring to one formula unit:

Sr_2RuO_4	$3.362 \cdot 10^{18} kg^{-1}$
$Ca_{1.38}Sr_{0.62}RuO_4$	$2.896 \cdot 10^{18} kg^{-1}$
$Ca_{1.8}Sr_{0.2}RuO_4$	$2.831 \cdot 10^{18} kg^{-1}$

For Sr-concentrations other than $x = 2$ there is no specific model of the lattice dynamics, so as an approximation the dispersion and the structure factors relative to C are taken to be the same as in Sr_2RuO_4.

As a final remark, one has of course to admit that some approximations could be made (linear dispersion, constant structure factor, resolution ellipsoid's volume, constant Bose factor, etc.) allowing to do the procedure with less computational effort, possibly even by hand. The described method is more general, does rely on fewer assumptions and can be expected to be more accurate. Although a powerful method, there remain uncertainties. Especially the effective resolution of the spectrometer can be very hard to accurately numerically model. As a pure estimation of the accuracy of the whole calibration procedure, 20 percent might be a realistic number.

A.2 Some remarks about the maximum entropy algorithm

The crystallographic unit cell is divided into a set of $N = n_x \cdot n_y \cdot n_z$ pixels ("volume elements") at which the magnetization is ρ_l. The magnetic form factor for a reflection $Q = (h, k, l)$ is calculated as

$$F_M(\mathbf{Q}) = \sum_{\mathbf{l}} \rho_{\mathbf{l}} e^{2\pi i \mathbf{Q} \cdot \mathbf{r_l}} \tag{A.5}$$

For symmetry reasons, one may oneself restrict to the asymmetric part of the unit cell. The sum can then be written as

$$F_M(\mathbf{Q}) = \sum_{\mathbf{j}} \rho_{\mathbf{j}} \left(\sum_{\mathbf{S}} e^{2\pi i \mathbf{Q} \cdot \mathbf{S}(\mathbf{r_j})} \right) \tag{A.6}$$

Where the S are the symmetry operations[1] of the space group and the index j runs only over the points in the asymmetric unit cell. The inner sum is split

$$\sum_{S} e^{2\pi i \mathbf{Q} \cdot S(\mathbf{r}_l)} = \sum_{S} \cos(2\pi \mathbf{Q} \cdot S(\mathbf{r}_l)) + i \cdot \sum_{S} \sin(2\pi \mathbf{Q} \cdot S(\mathbf{r}_l)) = c_j^{(Q)} + i s_j^{(Q)} \tag{A.7}$$

---

[1] for each point including only those that are not equivalent (give different $S(\mathbf{r_l})$), and including the identity, so that the site multiplicity is correctly considered.

The so defined $c_j^{(Q)}$ and $s_j^{(Q)}$ are calculated once and stored in memory ($N \cdot n(hkl)$ elements each, if $n(hkl)$ is the number of observed reflections). Thus no more evaluations of trigonometric functions are necessary, and the real and imaginary parts are split for the later calculations. $c_j^{(Q)}$ and $s_j^{(Q)}$ also contain the symmetry operations, which therefore do not have to be considered explicitly elsewhere. In the centrosymmetric case, only the $c_j^{(Q)}$ are needed.

With this, not only the $F_M^{(Q)}$ can be efficiently calculated, but also the derivatives

$$
\begin{aligned}
B_j^{(Q)} &= \frac{\partial}{\partial \rho_j} F_M F_M^* &= 2(F_M' \cdot c_j^{(Q)} + F_M'' \cdot s_j^{(Q)}) \\
A_j^{(Q)} &= \frac{\partial}{\partial \rho_j}(F_N F_M^* + F_N^* F_M) &= 2(F_N' \cdot c_j^{(Q)} + F_N'' \cdot s_j^{(Q)})
\end{aligned}
\tag{A.8}
$$

where the $A_j^{(Q)}$ are constant throughout the computation. With the further abbreviations

$$
\begin{aligned}
\mathtt{nn} &= F_N F_N^* \quad (= F_N'^2 + F_N''^2) & \tag{A.9} \\
\mathtt{mn} &= \frac{1}{2}(F_N F_M^* + F_N^* F_M) \quad (= F_N' F_M' + F_N'' F_M'') & \tag{A.10} \\
\mathtt{mm} &= F_M F_M^* & \tag{A.11} \\
\mathtt{a} &= \sin^2(\alpha_Q) & \tag{A.12}
\end{aligned}
$$

the desired derivative is

$$
\frac{\partial C(\rho^{(n)})}{\partial \rho_j} = 2\sum_Q \frac{R_{\mathrm{cal}}^{(Q)} - R_{\mathrm{obs}}^{(Q)}}{\sigma_{(Q)}^2} \cdot \frac{\partial R_{\mathrm{cal}}^{(Q)}}{\partial \rho_j}
\tag{A.13}
$$

$$
\frac{\partial R_{\mathrm{cal}}^{(Q)}}{\partial \rho_j} = \mathtt{a} \cdot \frac{(p^+ + p^-) \cdot A_j^{(Q)} \cdot (\mathtt{nn} + \mathtt{a} \cdot \mathtt{mm}) - 2\mathtt{a} \cdot (p^+ + p^-) \cdot \mathtt{nm} \cdot B_j^{(Q)}}{(\mathtt{nn} - 2p^- \cdot \mathtt{a} \cdot \mathtt{nm} + \mathtt{a} \cdot \mathtt{mm})^2}
\tag{A.14}
$$

Kurzfassung

In der vorliegenden Arbeit wurde der Magnetismus der geschichteten Ruthenate mittels verschiedener Methoden der Neutronenstreuung experimentell untersucht.

In der paramagnetisch metallischen Phase der einfach geschichteten Ruthenate der Serie $Ca_{2-x}Sr_xRuO_4$ wurden die magnetischen Korrelationen als Funktion des Sr-Gehalts (für x=0.2 und 0.62), der Temperatur und des magnetischen Feldes mit inelastischer Neutronenstreuung charakterisiert. Dabei zeigt sich, dass ferromagnetische Paramagnon-Streuung mit antiferromagnetischen Korrelationen bei inkommensurablen Wellenvektoren konkurriert. Beide weisen in der Temperaturabhängigkeit ihrer Amplituden und Energien Anzeichen naher magnetischer Instabilitäten auf, deren Wechselspiel das Verhalten dieser Materialien bestimmt. In $Ca_{1.8}Sr_{0.2}RuO_4$, das einen metamagnetischen Übergang zeigt, ist die Paramagnon-Streuung bei tiefer Temperatur stark unterdrückt, erscheint jedoch bei Erhöhung der Temperatur oder Anlegen eines magnetischen Feldes. Die Hochfeld-Phase von $Ca_{1.8}Sr_{0.2}RuO_4$ oberhalb des metamagnetischen Übergangs ist von starken ferromagnetischen Korrelationen geprägt und zeigt eine Anregung mit dem Charakter eines ferromagnetischen Magnons.

Im unkonventionellen Supraleiter Sr_2RuO_4 konnte mittels polarisierter Neutronenstreuung nachgewiesen werden, dass zusätzlich zu den bekannten magnetischen Fluktuationen bei Q=(0.3,0.3,0) ein Signal existiert, das um den Mittelpunkt der Brillouinzone zentriert ist und eine sehr große Q-Breite besitzt. Bei Berücksichtigung dieses Beitrags ergibt sich ein Modell für die Q-abhängige magnetische Suszeptibilität, das gut mit den Ergebnissen anderer, nicht Q-auflösender Messmethoden übereinstimmt. Durch Dotierung mit Titan werden die inkommensurablen Fluktuationen in der Nähe der kritischen Konzentration des Auftretens magnetischer Ordnung verstärkt, zeigen jedoch kein divergierendes Verhalten bis zu tiefen Temperaturen.

Für das doppelt geschichtete Titan-dotierte $Sr_3Ru_2O_7$ wurde nachgewiesen, dass ebenfalls magnetische Ordnung induziert wird, deren Propagationsvektor etwa $(\frac{1}{4},\frac{1}{4},0)$ ist; diese Ordnung wurde detailliert charakterisiert. Ober- und unterhalb der Ordnungstemperatur wurden Anregungen bei diesem Wellenvektor sowie einem weiteren, ähnlichen Vektor wie in reinem $Sr_3Ru_2O_7$, beobachtet.

Weiterhin wurde in einer Diffraktionsstudie mit polarisierten Neutronen die Spindichteverteilung in $Ca_3Ru_2O_7$ bestimmt.

Abstract

In this thesis, the magnetism of the layered Ruthenates has been studied by means of different neutron scattering techniques.

Magnetic correlations in the single-layer Ruthenates of the series $Ca_{2-x}Sr_xRuO_4$ have been investigated as function of Sr-concentration (x=0.2 and 0.62), temperature and magnetic field. These inelastic neutron scattering studies demonstrate the coexistence of ferromagnetic paramagnon scattering with antiferromagnetic fluctuations at incommensurate wave vectors. The temperature dependence of the amplitudes and energies of both types of excitations indicate the proximity to magnetic instabilities; their competition seems to determine the complex behavior of these materials. In $Ca_{1.8}Sr_{0.2}RuO_4$, which shows a metamagnetic transition, the ferromagnetic fluctuations are strongly suppressed at low temperature, but appear at higher temperature or application of a magnetic field. In the high-field phase of $Ca_{1.8}Sr_{0.2}RuO_4$ above the metamagnetic transition, a ferromagnetic magnon dominates the excitation spectrum.

Polarized neutron scattering revealed the existence of a very broad signal around the zone centre, in addition to the well-known incommensurate excitations at Q=(0.3,0.3,0) in the unconventional superconductor Sr_2RuO_4. With this additional contribution, it is possible to set up a general model for the Q-dependent magnetic susceptibility, which is well consistent with the results of other measurement methods that do not resolve the Q-dependence. Upon doping with Ti, the incommensurate fluctuations are enhanced, in particular near the critical concentration for the onset of magnetic order, but no divergence down to very low temperature is observed.

In the bilayer Ti-doped $Sr_3Ru_2O_7$, the existence of magnetic order with a propagation vector of about $(\frac{1}{4},\frac{1}{4},0)$ has been discovered and characterized in detail. Above and below T_N, excitations at this wave vector and another one, related to $Sr_3Ru_2O_7$, have been observed.

Furthermore, in a polarized neutron diffraction study, the spin density distribution of $Ca_3Ru_2O_7$ has been determined.

Kleine Danksagung

Nach so vielen Neutronen, nach all den Fluktuationen, Dispersionen und ihren Interpretationen, soll ein persönliches Wort des Dankes stehen für all die Dinge, ohne die diese Arbeit nicht möglich gewesen wäre.

Der große Dank dafür, diese Arbeit betreut und überhaupt ermöglicht zu haben, gebührt Herrn Professor Markus Braden. Über die unzähligen fachlichen Dinge hinaus, die ich in dieser Zeit bei ihm und von ihm gelernt habe – ich bin zuversichtlich, ich werde sie ausgiebig anwenden! – , danke ich ihm für so vieles, was über die eigentlichen Aufgaben eines "Doktorvaters" hinausgeht; kurz gesagt für all die verschiedensten Dinge, die dazu beigetragen haben, dass ich das Arbeiten in seiner Gruppe über die Jahre hinweg als so angenehm empfinden konnte und die Freude daran (und dabei) nicht zu kurz kam.

Sehr herzlich danke ich ihm für die vielfältige Förderung und das in mich gesetzte Vertrauen. Konkret diese Arbeit betreffend, danke ich für die wertvollen Verbesserungsvorschläge.

Herrn Professor Rosch danke ich sehr herzlich für die Bereitschaft, als Gutachter für diese Arbeit zu fungieren. Herrn Professor Bohatý danke ich für die Übernahme des Vorsitzes in der Prüfungskommission.

Gänzlich unmöglich gewesen wäre diese Arbeit ohne die entsprechenden Studienobjekte. Ein herzlicher Dank für die Proben und die Zusammenarbeit geht deshalb nach Schottland und Japan; dafür und für manches mehr in ganz besonderer Weise an Satoru Nakatsuji.

Dem französischen Staat danke ich für zahlreiche Neutronen, auch wenn die meisten von ihnen den Detektor leider nicht erreicht haben. Dabei denke ich vor allem an das LLB; die Aufenthalte dort und der intensive Kontakt zu vielen seiner Mitarbeiter sind ein integraler Bestandteil der letzten Jahre gewesen. Für mich nicht wegzudenken aus meiner persönlichen Neutronenstreuerfahrung ist Yvan Sidis. Ja, Yvan, du hattest es nicht immer leicht mit uns! Aber es hat Spaß gemacht, und ich glaube, wir waren auch recht erfolgreich.

Arsen Gukasov danke ich ebenfalls nicht nur für die Unterstützung bei den Experimenten, sondern in so mancher Hinsicht weit darüber hinaus. Ein großer Dank auch an Benoit Fauqué für die Gastfreundschaft in seinem Büro und die nette Gesellschaft!

Viele weitere Personen und Institutionen haben zum Gelingen der zahlreichen Experimente beigetragen. Dabei möchte ich besonders Peter Link vom FRM-2 sowie Jiri Kulda, Wolfgang Schmidt und Karin Schmalzl vom ILL hervorheben. Ich freue mich schon sehr auf die zukünftige engere Zusammenarbeit mit euch!

Allen Dienstreisen zum Trotz fand diese Arbeit doch überwiegend in Köln statt. Am II. Physikalischen Institut ist die Liste der Personen aus Wissenschaft, Verwaltung und Werkstätten lang, die ich hier gerne erwähnen würde – und doch würde das der Sache wohl nicht gerecht. Wenn ich an den Weg vom Eingang zu meinem Schreibtisch denke, so stelle ich fest, dass sich, ganz vorne angefangen, wohl hinter jeder Tür jemand verbirgt, dem oder der ich in irgendeiner Weise zu Dank für den Beitrag zum Gelingen dieser Arbeit verpflichtet bin.

Wenn ich dann auf einem der vielen möglichen Wege, von denen mich einige auch über die anderen Etagen führen mögen, in die Nähe meines Büros komme, häufen sich allmählich die Gesichter aus der Bradenschen Arbeitsgruppe, mit deren Mitgliedern mich eine besonders enge Beziehung verbindet. Ich habe das Zusammensein mit euch, nicht zuletzt auf vielen Reisen, aus vielen Gründen wirklich sehr genossen. Danke!

Buchstäblich in der hintersten Ecke des Instituts sitzt dann Daniel Senff und beschäftigt sich – meist – mit einem seiner Manganate. Vom Grundstudium an haben wir die vielen Abschnitte auf den verschlungenen Wegen zum Doktor gemeinsam zurückgelegt. Schade, dass sich zumindest die beruflichen Wege nun trennen. Dir herzlichen Dank für diese lange Zeit.

Mit dieser Arbeit endet auch – leider – eine noch viel längere Zeit in der schönen Stadt Köln. Dies ist nicht der Ort, auf das einzugehen, was mir hierzu in den Sinn kommt. Dennoch glaube ich, dass meine Familie, dass meine vielen Freunde und der Kölner Domchor in einer indirekten Weise zum Gelingen dieser Arbeit vielleicht mehr beigetragen haben als ihnen bewusst ist.

Guten Gewissens schließen kann ich hier nur, weil ich weiß, dass ich noch eine gewisse Weile da bin, und weil ich hoffe, mit manchen der hier genannten und gemeinten auch weiterhin in der einen oder anderen Form zu tun zu haben.

List of Publications

Field-induced paramagnons at the metamagnetic transition in $Ca_{1.8}Sr_{0.2}RuO_4$
P. Steffens, Y. Sidis, P. Link, K. Schmalzl, S. Nakatsuji, Y. Maeno, and M. Braden
cond-mat 0703806 (2007), submitted to Physical Review Letters.

Magnetoelastic coupling across the metamagnetic transition in $Ca_{2-x}Sr_xRuO_4$ ($0.2 \leq x \leq 0.5$)
J. Baier, P. Steffens, O. Schumann, M. Kriener, S. Stark, H. Hartmann, O. Friedt, A. Revcolevschi, P. G. Radaelli, S. Nakatsuji, Y. Maeno, J. A. Mydosh, T. Lorenz, and M. Braden
Journal of Low Temperature Physics **147***, 405 (2007).*

Structural Aspects of Metamagnetism in $Ca_{2-x}Sr_xRuO_4$: Evidence for Field Tuning of Orbital Occupation
M. Kriener, P. Steffens, J. Baier, O. Schumann, T. Zabel, T. Lorenz, O. Friedt, R. Müller, A. Gukasov, P. G. Radaelli, P. Reutler, A. Revcolevschi, S. Nakatsuji, Y. Maeno, and M. Braden
Physical Review Letters **95***, 267403 (2005).*

High-pressure diffraction studies on Ca_2RuO_4
P. Steffens, O. Friedt, P. Alireza, W. G. Marshall, W. Schmidt, F. Nakamura, S. Nakatsuji, Y. Maeno, R. Lengsdorf, M. M. Abd-Elmeguid, and M. Braden
Physical Review B **72***, 094104 (2005).*

Strongly Enhanced Magnetic Fluctuations in a Large-Mass Layered Ruthenate
O. Friedt, P. Steffens, M. Braden, Y. Sidis, S. Nakatsuji, and Y. Maeno
Physical Review Letters **93***, 147404 (2004).*

Anisotropy of the Incommensurate Fluctuations in Sr_2RuO_4: A Study with Polarized Neutrons
M. Braden, P. Steffens, Y. Sidis, J. Kulda, P. Bourges, S. Hayden, N. Kikugawa, and Y. Maeno
Physical Review Letters **92***, 097402 (2004).*

Oral presentations:

- SFB-Seminar SFB608, April 2007, Köln (Germany)

- Rencontres LLB-Soleil: Diffraction sur monocristal, March 2007, St. Aubin (France)

- DPG Frühjahrstagung, March 2007, Regensburg (Germany)

- Rencontres LLB-Soleil: Electrons fortement corrélés, June 2006, St. Aubin (France)

- Seminaire de la matière condensée, LLB, November 2005, Saclay (France)

- International Symposium on Spin-Triplet Superconductivity and Ruthenate Physics (STSR), October 2004, Kyoto (Japan)

- DPG Frühjahrstagung, Symposium "Orbital Physics", March 2004, Regensburg (Germany)

- Symposium Physics of Correlated Electron Systems, August 2003, St. Andrews (United Kingdom)

Bibliography

[1] S. L. W. Marshall, *Theory of thermal neutron scattering*, Oxford University Press, 1971.

[2] S. Lovesey, *Theory of neutron scattering from condensed matter, Vol. 2: Polarization effects and magnetic scattering*, Oxford University Press, 1984.

[3] G. Squires, *Introduction to the theory of thermal neutron scattering*, Cambridge University Press, 1978.

[4] T. Chatterji, *Neutron scattering from magnetic materials*, Elsevier, 2006.

[5] J. T. G. Shirane, S.M. Shapiro, *Neutron Scattering with a Triple-Axis Spectrometer*, Cambridge University Press, 2002.

[6] M. Cooper and R. Nathans, *The Resolution Function in Neutron Diffraetometry I. The Resolution Function of a Neutron Diffractometer and its Application to Phonon Measurements*, Acta. Cryst. **23**, 357 (1967).

[7] M. Popovici, *On the Resolution of Slow-Neutron Spectrometers. IV. The Triple-Axis Spectrometer Resolution Function, Spatial Effects Included*, Acta. Cryst. A **31**, 507 (1975).

[8] A. Zheludev, *3-axis RESolution LIBrary for MatLab*, Oak Ridge National Laboratory, http://neutron.ornl.gov/ zhelud/reslib.

[9] M. Braden, W. Reichardt, S. Nishizaki, Y. Mori, and Y. Maeno, *Structural stability of Sr_2RuO_4*, Phys. Rev. B **57**, 1236 (1998).

[10] M. Braden, W. Reichardt, Y. Sidis, Z. Mao, and Y. Maeno, *Lattice dynamics and electron-phonon coupling in Sr_2RuO_4: Inelastic neutron scattering and shell-model calculations*, Physical Review B **76**, 014505 (2007).

[11] R. D. Lowde and C. G. Windsor, *On the magnetic excitations in Nickel*, Advances in Physics **19**, 813 (1970).

[12] T. Moriya, *Spin Fluctuations in Itinerant Electron Magnetism*, Springer-Verlag Berlin Heidelberg, 1985.

[13] I. Mazin and D. Singh, *Competitions in Layered Ruthenates: Ferromagnetism versus Antiferromagnetism and Triplet versus Singlet Pairing*, Phys. Rev. Lett. **82**, 4324 (1999).

[14] D. Morr, P. Trautman, and M. Graf, *Resonance Peak in Sr_2RuO_4: Signature of Spin Triplet Pairing*, Phys. Rev. Lett. **86**, 5978 (2001).

[15] T. Izuyama, D.-J. Kim, and R. Kubo, *Band theoretical interpretation of neutron diffraction phenomena in ferromagnetic metals*, J. Phys. Soc. Japan **18**, 1025 (1963).

[16] G. G. Lonzarich and L. Taillefer, *Effect of spin fluctuations on the magnetic equation of state of ferromagnetic or nearly ferromagnetic metals*, J. Phys. C: Solid State Phys. **18**, 4339 (1985).

[17] W. F. Brinkman and S. Engelsberg, *Spin-Fluctuation Contributions to the Specific Heat*, Phys. Rev. **169**, 417 (1968).

[18] T. Moriya and T. Takimoto, *Anomalous properties around magnetic instability in heavy electron systems*, J. Phys. Soc. Japan **64**, 960 (1995).

[19] M. Hatatani and T. Moriya, *Ferromagnetic spin fluctuations in two-dimensional metals*, J. Phys. Soc. Japan **64**, 3434 (1995).

[20] G. G. Lonzarich, *The magnetic equation of state and heat capacity in weak itinerant ferromagnets*, J. Magn. Magn. Mat. **54-57**, 612 (1986).

[21] A. Ishigaki and T. Moriya, *Anomalous specific heat around ferromagnetic instability in metals*, J. Phys. Soc. Japan **65**, 376 (1996).

[22] R. Konno and T. Moriya, *Quantitative aspects of the theory of nearly ferromagnetic metals*, J. Phys. Soc. Japan **56**, 3270 (1987).

[23] D. M. Edwards and G. G. Lonzarich, *The entropy of fluctuating moments at low temperatures*, Philosophical Magazine B **65**, 1185 (1992).

[24] A. Ishigaki and T. Moriya, *On the spin fluctuation-enhanced specific heat around the magnetic instabilities*, J. Phys. Soc. Japan **68**, 3673 (1999).

[25] T. Moriya, *Spin fluctuations in nearly antiferromagnetic metals*, Phys. Rev. Lett. **24**, 1433 (1970).

[26] C. J. Gilmore, *Maximum Entropy and Bayesian Statistics in Crystallography: a Review of Practical Applications*, Acta Cryst. A **52**, 561 (1996).

[27] C. E. Shannon, *A mathematical theory of information*, Bell System Techn. J. **27**, 1948 (379-423, 623-656), Reprinted in C. E. Shannon and W. Weaver, The mathematical theory of communication (University of Illinois Press, Urbana, 1949).

[28] E. T. Jaynes, *Information Theory and Statistical Mechanics*, Phys. Rev. **106**, 620 (1957).

[29] R. J. Papoular and B. Gillon, *Maximum Entropy reconstruction of spin density maps in crystals from polarized neutron diffraction data*, Europhys. Lett. **13**, 429 (1990).

[30] D. M. Collins, *Electron density images from imperfect data by iterative entropy maximization*, Nature **298**, 49 (1982).

[31] S. F. Gull and G. J. Daniell, *Image reconstruction from incomplete and noisy data*, Nature **272**, 686 (1978).

[32] S. Kumazawa, Y. Kubota, M. Takata, and M. Sakata, *MEED: a program package for electron density distribution calculation by the maximum entropy method*, J. Appl. Cryst. **26**, 453 (1993).

[33] K. Burger, Enhanced versions of the maximum entropy program "meed" for x-ray and neutron diffraction, Universität Tübingen.

[34] J. Skilling and R. K. Bryan, *Maximum entropy image reconstruction: general algorithm*, Mon. Not. R. astr. Soc. **211**, 111 (1984).

[35] Maximum entropy data consultants, www.maxent.co.uk.

[36] S. Nakatsuji and Y. Maeno, *Quasi-Two-Dimensional Mott Transition System $Ca_{2-x}Sr_xRuO_4$*, Phys. Rev. Lett. **84**, 2666 (2000).

[37] S. Nakatsuji, D. Hall, L. Balicas, Z. Fisk, K. Sugahara, M. Yoshioka, and Y. Maeno, *Heavy-Mass Fermi Liquid near a Ferromagnetic Instability in Layered Ruthenates*, Phys. Rev. Lett. **90**, 137202 (2003).

[38] Y. Maeno, H. Hashimoto, K. Yoshida, S. Nishizaki, T. Fujita, J. Bednorz, and F. Lichtenberg, *Superconductivity in a layered perovskite without copper*, Nature **372**, 532 (1994).

[39] S. Nakatsuji, S. Ikeda, and Y. Maeno, *Ca_2RuO_4: New Mott Insulators of Layered Ruthenate*, J. Phys. Soc. Japan **66**, 1868 (1997).

[40] G. Cao, S. McCall, M. Shepard, J. E. Crow, and R. P. Guertin, *Magnetic and transport properties of single-crystal Ca_2RuO_4: Relationship to superconducting Sr_2RuO_4*, Phys. Rev. B **56**, R2916 (1997).

[41] M. Braden, G. André, S. Nakatsuji, and Y. Maeno, *Crystal and magnetic structure of Ca_2RuO_4: Magnetoelastic coupling and the metal-insulator transition*, Phys. Rev. B **58**, 847 (1998).

[42] C. Alexander, G. Cao, V. Dobrosavljevic, S. McCall, J. Crow, E. Lochner, and R. Guertin, *Destruction of the Mott insulating ground state of Ca_2RuO_4 by a structural transition*, Phys. Rev. B **60**, R8422 (1999).

[43] O. Friedt, M. Braden, G. André, P. Adelmann, S. Nakatsuji, and Y. Maeno, *Structural and magnetic aspects of the metal-insulator transition in $Ca_{2-x}Sr_xRuO_4$*, Phys. Rev. B **63**, 174432 (2001).

[44] S. Nakatsuji and Y. Maeno, *Switching of magnetic coupling by a structural symmetry change near the Mott transition in $Ca_{2-x}Sr_xRuO_4$*, Phys. Rev. B **62**, 6458 (2000).

[45] Z. Fang and K. Terakura, *Magnetic phase diagram of $Ca_{2-x}Sr_xRuO_4$ governed by structural distortions*, Phys. Rev. B **64**, 020509(R) (2001).

[46] O. Friedt, P. Steffens, M. Braden, Y. Sidis, S. Nakatsuji, and Y. Maeno, *Strongly Enhanced Magnetic Fluctuations in a Large-Mass Layered Ruthenate*, Phys. Rev. Lett. **93**, 147404 (2004).

[47] K. Ishida, Y. Minami, Y. Kitaoka, S. Nakatsuji, N. Kikugawa, and Y. Maeno, *Evolution of normal-state magnetic fluctuations by Ca and Ti substitutions in Sr_2RuO_4: ^{87}Sr-NMR study*, Phys. Rev. B **63**, 214412 (2003).

[48] T. Zabel, *Aufbau eines Tieftemperatur-Kalorimeters und kalorische Messungen an $TlCuCl_3$ und $Ca_{2-x}Sr_xRuO_4$*, PhD thesis, Universität zu Köln, 2004.

[49] S.-I. Ikeda, Y. Maeno, S. Nakatsuji, M. Kosaka, and Y. Uwatoko, *Ground state in $Sr_3Ru_2O_7$: Fermi liquid close to a ferromagnetic instability*, Phys. Rev. B **62**, R6089 (2000).

[50] B. Binz and M. Sigrist, *Metamagnetism of itinerant electrons in multi-layer ruthenates*, Europhys. Lett. **65**, 816 (2004).

[51] A. J. Millis, A. J. Schofield, G. G. Lonzarich, and S. A. Grigera, *Metamagnetic Quantum Criticality in Metals*, Phys. Rev. Lett. **88**, 217204 (2002).

[52] L. Balicas, S. Nakatsuji, D. Hall, T. Ohnishi, Z. Fisk, Y. Maeno, and D. J. Singh, *Severe Fermi Surface Reconstruction at a Metamagnetic Transition in $Ca_{2-x}Sr_xRuO_4$ (for $0.2 \leq x \leq 0.5$)*, Phys. Rev. Lett. **95**, 196407 (2005).

[53] M. Kriener, P. Steffens, J. Baier, O. Schumann, T. Zabel, T. Lorenz, O. Friedt, R. Müller, A. Gukasov, P. G. Radaelli, P. Reutler, A. Revcolevschi, S. Nakatsuji, Y. Maeno, and M. Braden, *Structural Aspects of Metamagnetism in $Ca_{2-x}Sr_xRuO_4$: Evidence for Field Tuning of Orbital Occupation*, Phys. Rev. Lett. **95**, 267403 (2005).

[54] J. Baier, P. Steffens, O. Schumann, M. Kriener, S. Stark, H. Hartmann, O. Friedt, A. Revcolevschi, P. G. Radaelli, S. Nakatsuji, Y. Maeno, J. A. Mydosh, T. Lorenz, and M. Braden, *Magnetoelastic Coupling Across the Metamagnetic Transition in $Ca_{2-x}Sr_xRuO_4$ ($0.2 \leq x \leq 0.5$)*, J. low Temp. Phys. **147**, 405 (2007).

[55] J. Baier, *Magnetoelastische Kopplung in multiferroischem $GdMnO_3$ und metamagnetischem $Ca_{2-x}Sr_xRuO_4$*, PhD thesis, Universität zu Köln, 2006.

[56] S. Nakatsuji and Y. Maeno, *Metamagnetic Transition in the Quasi-Two-Dimensional Mott Transition System $Ca_{2-x}Sr_xRuO_4$*, J. Low Temp. Phys. **117**, 1593 (1999).

[57] A. Mackenzie, S. Julian, A. Diver, G. McMullan, M. Ray, G. Lonzarich, Y. Maeno, S. Nishizaki, and T. Fujita, *Quantum Oscillations in the Layered Perovskite Superconductor Sr_2RuO_4*, Phys. Rev. Lett. **76**, 3786 (1996).

[58] T. Mizokawa, L. Tjeng, G. Sawatzky, G. Ghiringhelli, O. Tjernberg, N. Brookes, H. Fukazawa, S. Nakatsuji, and Y. Maeno, *Spin-Orbit Coupling in the Mott Insulator Ca_2RuO_4*, Phys. Rev. Lett. **87**, 077202 (2001).

[59] T. Mizokawa, L. Tjeng, H.-J. Lin, C. Chen, S. Schuppler, S. Nakatsuji, H. Fukazawa, and Y. Maeno, *Orbital state and metal-insulator transition in $Ca_{2-x}Sr_xRuO_4$ (x=0.0 and 0.09) studied by x-ray absorption spectroscopy*, Phys. Rev. B **69**, 132410 (2004).

[60] V. Anisimov, I. Nekrasov, D. Kondakov, T. Rice, and M. Sigrist, *Orbital-selective Mott-insulator transition in $Ca_{2-x}Sr_xRuO_4$*, The European Phys. J. B **25**, 191 (2002).

[61] Z. Fang, N. Nagaosa, and K. Terakura, *Orbital-dependent phase control in $Ca_{2-x}Sr_xRuO_4$ ($0 \leq x \leq 0.5$)*, Phys. Rev. B **69**, 045116 (2004).

[62] J. Jung, Z. Fang, J. He, Y. Kaneko, Y. Okimoto, and Y. Tokura, *Change of Electronic Structure in Ca_2RuO_4 Induced by Orbital Ordering*, Phys. Rev. Lett. **91**, 056403 (2003).

[63] T. Hotta and E. Dagotto, *Prediction of Orbital Ordering in Single-Layered Ruthenates*, Phys. Rev. Lett. **88**, 017201 (2001).

[64] M. Kubota, Y. Murakami, M. Mizumaki, H. Ohsumi, N. Ikeda, S. Nakatsuji, H. Fukazawa, and Y. Maeno, *Ferro-type orbital state in the Mott transition system $Ca_{2-x}Sr_xRuO_4$ studied by the resonant X-Ray scattering interference technique*, Phys. Rev. Lett. **95**, 026401 (2005).

[65] J. Lee, Y. Lee, T. Noh, S.-J. Oh, J. Yu, S. Nakatsuji, H. Fukazawa, and Y. Maeno, *Electron and Orbital Correlations in $Ca_{2-x}Sr_xRuO_4$ Probed by Optical Spectroscopy*, Phys. Rev. Lett. **89**, 257402 (2002).

[66] M. Sigrist and M. Troyer, *Orbital and spin correlations in $Ca_{2-x}Sr_xRuO_4$: A mean field study*, Eur. Phys. J. B **39**, 207 (2004).

[67] A. Koga, N. Kawakami, T. M. Rice, and M. Sigrist, *Orbital-Selective Mott Transitions in the Degenerate Hubbard Model*, Phys. Rev. Lett. **92**, 216402 (2004).

[68] P. van Dongen, C. Knecht, and N. Blümer, *Orbital-selective Mott transitions in the 2-band J_z-model: a high-precision quantum Monte Carlo study*, cond-mat , 0507682 (2005).

[69] C. Knecht, N. Blümer, and P. G. J. van Dongen, *Orbital-selective Mott transitions in the anisotropic two-band Hubbard model at finite temperatures*, Phys. Rev. B **72**, 081103 (2005).

[70] L. de'Medici, A. Georges, and S. Biermann, *Orbital-selective Mott transition in multiband systems: Slave-spin representation and dynamical mean-field theory*, Phys. Rev. B **72**, 205124 (2005).

[71] X. Dai, G. Kotliar, and Z. Fang, *The Orbital Selective Mott Transition in a Three Band Hubbard model: a Slave Boson Mean Field Study*, cond-mat , 0611075 (2006).

[72] E. Ko, B. J. Kim, C. Kim, and H. J. Choi, *Strong Orbital-Dependent d-Band Hybridization and Fermi-Surface Reconstruction in Metallic $Ca_{2-x}Sr_xRuO_4$*, Phys. Rev. Lett. **98**, 225401 (2007).

[73] A. Liebsch, *Mott Transitions in Multiorbital Systems*, Phys. Rev. Lett. **91**, 226401 (2003).

[74] A. Liebsch and H. Ishida, *Subband Filling and Mott Transition in $Ca_{2-x}Sr_xRuO_4$*, Phys. Rev. Lett. **98**, 216403 (2007).

[75] H.-J. Noh, S.-J. Oh, B.-G. Park, J.-H. Park, J.-Y. Kim, H.-D. Kim, T. Mizokawa, L. Tjeng, H.-J. Lin, C. Chen, S. Schuppler, S. Nakatsuji, H. Fukazawa, and Y. Maeno, *Electronic structure and evolution of the orbital state in metallic $Ca_{2-x}Sr_xRuO_4$*, Phys. Rev. B **72**, 052411 (2005).

[76] A. Gukasov, M. Braden, R. Papoular, S. Nakatsuji, and Y. Maeno, *Anomalous Spin-Density Distribution on Oxygen and Ru in $Ca_{1.5}Sr_{0.5}RuO_4$*, Phys. Rev. Lett. **89**, 087202 (2002).

[77] J. S. Lee, S. J. Moon, T. W. Noh, S. Nakatsuji, and Y. Maeno, *Orbital-Selective Mass Enhancements in Multiband $Ca_{2-x}Sr_xRuO_4$ Systems Analyzed by the Extended Drude Model*, Phys. Rev. Lett. **96**, 057401 (2006).

[78] S.-C. Wang, H.-B. Yang, A. K. P. Sekharan, S. Souma, H. Matsui, T. Sato, T. Takahashi, C. Lu, J. Zhang, R. Jin, D. Mandrus, E. W. Plummer, Z. Wang, and H. Ding, *Fermi Surface Topology of $Ca_{1.5}Sr_{0.5}RuO_4$ Determined by Angle-Resolved Photoelectron Spectroscopy*, Phys. Rev. Lett. **93**, 177007 (2004).

[79] D. Belitz, T. R. Kirkpatrick, and J. Rollbühler, *Tricritical Behavior in Itinerant Quantum Ferromagnets*, Phys. Rev. Lett. **94**, 247205 (2005).

[80] A. J. Schofield, *Oral presentation at SCES, Houston*, 2007.

[81] A. Kanbayasi, *Magnetic properties of $SrRuO_3$ Single Crystal*, J. Phys. Soc. Japan **41**, 1876 (1976).

[82] M. K. Crawford, R. L. Harlow, W. Marshall, Z. Li, G. Cao, R. L. Lindstrom, Q. Huang, and J. W. Lynn, *Structure and magnetism of single crystal $Sr_4Ru_3O_{10}$: A ferromagnetic triple-layer ruthenate*, Phys. Rev. B **65**, 214412 (2002).

[83] R. Gupta, M. Kim, H. Barath, S. L. Cooper, and G. Cao, *Field- and Pressure-Induced Phases in $Sr_4Ru_3O_{10}$: A Spectroscopic Investigation*, Phys. Rev. Lett. **96**, 067004 (2006).

[84] G. Cao, L. Balicas, W. H. Song, Y. P. Sun, Y. Xin, V. A. Bondarenko, J. W. Brill, S. Parkin, and X. N. Lin, *Competing ground states in triple-layered $Sr_4Ru_3O_{10}$: Verging on itinerant ferromagnetism with critical fluctuations*, Phys. Rev. B **68**, 174409 (2003).

[85] D. Fobes, M. H. Yu, M. Zhou, J. Hooper, C. J. O'Connor, M. Rosario, and Z. Q. Mao, *Phase diagram of the electronic states of trilayered ruthenate $Sr_4Ru_3O_{10}$*, Phys. Rev. B **75**, 094429 (2007).

[86] Z. Q. Mao, M. Zhou, J. Hooper, V. Golub, and C. J. O'Connor, *Phase Separation in the Itinerant Metamagnetic Transition of $Sr_4Ru_3O_{10}$*, Phys. Rev. Lett. **96**, 077205 (2006).

[87] Y. J. Jo, L. Balicas, N. Kikugawa, E. S. Choi, K. Storr, M. Zhou, and Z. Q. Mao, *Orbital-dependent metamagnetic response in $Sr_4Ru_3O_{10}$*, Phys. Rev. B **75**, 094413 (2007).

[88] G. Cao, S. Chikara, J. W. Brill, and P. Schlottmann, *Anomalous itinerant magnetism in single-crystal $Sr_4Ru_3O_{10}$: A thermodynamic and transport investigation*, Phys. Rev. B **75**, 024429 (2007).

[89] R. Perry, L. Galvin, S. Grigera, L. Capogna, A. Schofield, A. Mackenzie, M. Chiao, S. Julian, S. Ikeda, S. Nakatsuji, Y. Maeno, and C. Pfleiderer, *Metamagnetism and Critical Fluctuations in High Quality Single Crystals of the Bilayer Ruthenate $Sr_3Ru_2O_7$*, Phys. Rev. Lett. **86**, 2661 (2001).

[90] H. Shaked, J. D. Jorgensen, O. Chmaissem, S. Ikeda, and Y. Maeno, *Neutron Diffraction Study of the Structural Distortions in $Sr_3Ru_2O_7$*, J. Solid State Chem. **154**, 361 (2000).

[91] H. Shaked, J. D. Jorgensen, S. Short, O. Chmaissem, S.-I. Ikeda, and Y. Maeno, *Temperature and pressure effects on the crystal structure of $Sr_3Ru_2O_7$: Evidence for electronically driven structural responses*, Phys. Rev. B **62**, 8725 (2000).

[92] S.-I. Ikeda, N. Shirakawa, T. Yanagisawa, Y. Yoshida, S. Koikegami, S. Koike, M. Kosaka, and Y. Uwatoko, *Uniaxial-Pressure Induced Ferromagnetism of Enhanced Paramagnetic $Sr_3Ru_2O_7$*, J. Phys. Soc. Japan **73**, 1322 (2004).

[93] S. A. Grigera, R. A. Borzi, A. P. Mackenzie, S. R. Julian, R. S. Perry, and Y. Maeno, *Angular dependence of the magnetic susceptibility in the itinerant metamagnet $Sr_3Ru_2O_7$*, Phys. Rev. B **67**, 214427 (2003).

[94] S. Grigera, R. Perry, A. Schofield, M. Chiao, S. Julian, G. Lonzarich, S. Ikeda, Y. Maeno, A. Millis, and A. Mackenzie, *Magnetic Field-Tuned Quantum Criticality in the Metallic Ruthenate $Sr_3Ru_2O_7$*, Science **294**, 329 (2001).

[95] R. Perry, K. Kitagawa, S. Grigera, R. Borzi, A. Mackenzie, K. Ishida, and Y. Maeno, *Multiple First-Order Metamagnetic Transitions and Quantum Oscillations in Ultrapure $Sr_3Ru_2O_7$*, Phys. Rev. Lett. **92**, 166602 (2004).

[96] S. A. Grigera, P. Gegenwart, R. A. Borzi, F. Weickert, A. J. Schofield, R. S. Perry, T. Tayama, T. Sakakibara, Y. Maeno, A. G. Green, and A. P. Mackenzie, *Disorder-Sensitive Phase Formation Linked to Metamagnetic Quantum Criticality*, Science **306**, 1154 (2004).

[97] R. A. Borzi, S. A. Grigera, J. Farrell, R. S. Perry, S. J. S. Lister, S. L. Lee, D. A. Tennant, Y. Maeno, and A. P. Mackenzie, *Formation of a Nematic Fluid at High Fields in $Sr_3Ru_2O_7$*, Science **315**, 214 (2007).

[98] C. Honerkamp, *Charge instabilities at the metamagnetic transition of itinerant electron systems*, Phys. Rev. B **72**, 115103 (2005).

[99] B. Binz, H. B. Braun, T. M. Rice, and M. Sigrist, *Magnetic Domain Formation in Itinerant Metamagnets*, Phys. Rev. Lett. **96**, 196406 (2006).

[100] L. Capogna, E. M. Forgan, S. M. Hayden, A. Wildes, J. A. Duffy, A. P. Mackenzie, R. S. Perry, S. Ikeda, Y. Maeno, and S. P. Brown, *Observation of two-dimensional spin fluctuations in the bilayer ruthenate $Sr_3Ru_2O_7$ by inelastic neutron scattering*, Phys. Rev. B **67**, 012504 (2003).

[101] M. B. Stone, M. D. Lumsden, R. Jin, B. C. Sales, D. Mandrus, S. E. Nagler, and Y. Qiu, *Temperature-dependent bilayer ferromagnetism in $Sr_3Ru_2O_7$*, Phys. Rev. B **73**, 174426 (2006).

[102] K. Kitagawa, K. Ishida, R. Perry, T. Tayama, T. Sakakibara, and Y. Maeno, *Metamagnetic Quantum Criticality Revealed by ^{17}O-NMR in the Itinerant Metamagnet $Sr_3Ru_2O_7$*, Phys. Rev. Lett. **95**, 127001 (2005).

[103] J. Zhang, Ismail, R. G. Moore, S.-C. Wang, H. Ding, R. Jin, D. Mandrus, and E. W. Plummer, *Dopant-Induced Nanoscale Electronic Inhomogeneities in $Ca_{2-x}Sr_xRuO_4$*, Phys. Rev. Lett. **96**, 066401 (2006).

[104] J. H. Condon, *Nonlinear de Haas-van Alphen Effect and Magnetic Domains in Beryllium*, Phys. Rev. **145**, 526 (1966).

[105] P. Gegenwart, F. Weickert, M. Garst, R. S. Perry, and Y. Maeno, *Metamagnetic Quantum Criticality in $Sr_3Ru_2O_7$ Studied by Thermal Expansion*, Phys. Rev. Lett. **96**, 136402 (2006).

[106] M. Garst and A. Rosch, *Sign change of the Grüneisen parameter and magnetocaloric effect near quantum critical points*, Phys. Rev. B **72**, 205129 (2005).

[107] S. Nakatsuji and Y. Maeno, *Synthesis and Single-Crystal Growth of $Ca_{2-x}Sr_xRuO_4$*, Journal of Solid State Chemistry **156**, 26 (2001).

[108] P. Steffens, Struktur und Magnetismus in $Ca_{2-x}Sr_xRuO_4$, Master's thesis, Universität zu Köln, 2003, (unveröffentlicht).

[109] *International tables for Crystallography, Vol. C*, Kluwer, 2004.

[110] O. Friedt, *Interplay between electronic, magnetic and structural instabilities in $Ca_{2-x}Sr_xRuO_4$: A neutron scattering study*, PhD thesis, Université de Paris, 2003.

[111] Y. Sidis, M. Braden, P. Bourges, B. Hennion, S. NishiZaki, Y. Maeno, and Y. Mori, *Evidence for Incommensurate Spin Fluctuations in Sr_2RuO_4*, Phys. Rev. Lett. **83**, 3320 (1999).

[112] F. Servant, B. F. k, S. Raymond, J. Brison, P. Lejay, and J. Flouquet, *Magnetic excitations in the normal and superconducting states of Sr_2RuO_4*, Phys. Rev. B **65**, 184511 (2002).

[113] A. Damascelli, D. H. Lu, K. M. Shen, N. P. Armitage, F. Ronning, D. L. Feng, C. Kim, Z.-X. Shen, T. Kimura, Y. Tokura, Z. Q. Mao, and Y. Maeno, *Fermi Surface, Surface States, and Surface Reconstruction in Sr_2RuO_4*, Phys. Rev. Lett. **85**, 5194 (2000).

[114] R. Matzdorf, Z. Fang, Ismail, J. Zhang, T. Kimura, Y. Tokura, K. Terakura, and E. W. Plummer, *Ferromagnetism Stabilized by Lattice Distortion at the Surface of the p-Wave Superconductor Sr_2RuO_4*, Science **289**, 746 (2000).

[115] P. Monthoux and G. G. Lonzarich, *Magnetic interactions in a single-band model for the cuprates and ruthenates*, Phys. Rev. B **71**, 054504 (2005).

[116] P. Steffens, Y. Sidis, P. Link, K. Schmalzl, S. Nakatsuji, Y. Maeno, and M. Braden, *Field-induced paramagnons at the metamagnetic transition in $Ca_{1.8}Sr_{0.2}RuO_4$*, cond-mat , 0703806 (2007).

[117] N. R. Bernhoeft, S. M. Hayden, G. G. Lonzarich, D. M. Paul, and E. J. Lindley, *Dispersive Magnetic Density Fluctuations in Ni_3Ga*, Phys. Rev. Lett. **62**, 657 (1989).

[118] N. Bernhoeft, G. G. Lonzarich, D. M. Paul, and P. W. Mitchell, *Magnetic fluctuation spectra in weak itinerant ferromagnets*, Physica B **136**, 443 (1986).

[119] N. R. Bernhoeft and G. G. Lonzarich, *Scattering of slow neutrons from long-wavelength magnetic fluctuations in UPt_3*, J. Phys.: Condens. Matter **7**, 7325 (1995).

[120] G. G. Lonzarich, *Band structure and magnetic fluctuations in ferromagnetic or nearly ferromagnetic metals*, J. Magn. Magn. Mat. **45**, 43 (1984).

[121] G. G. Lonzarich, N. R. Bernhoeft, and D. M. Paul, *Spin density fluctuations in magnetic metals*, Physica B **156-157**, 699 (1989).

[122] G. Shirane, O. Steinsvoll, Y. J. Uemura, and J. Wicksted, *Dynamics of itinerant ferromagnets above T_C*, J. Appl. Phys. **55**, 1887 (1984).

[123] M. Braden, Y. Sidis, P. Bourges, P. Pfeuty, J. Kulda, Z. Mao, and Y. Maeno, *Inelastic neutron scattering study of magnetic excitations in Sr_2RuO_4*, Phys. Rev. B **66**, 064522 (2002).

[124] F. Nakamura, T. Goko, M. Ito, T. Fujita, S. Nakatsuji, H. Fukazawa, Y. Maeno, P. Alireza, D. Forsythe, and S. Julian, *From Mott insulator to ferromagnetic metal: A pressure study of Ca_2RuO_4*, Phys. Rev. B **65**, 220402(R) (2002).

[125] P. Steffens, O. Friedt, P. Alireza, W. Marshall, W. Schmidt, F. Nakamura, S. Nakatsuji, Y. Maeno, R. Lengsdorf, M. Abd-Elmeguid, and M. Braden, *High-pressure diffraction studies on Ca_2RuO_4*, Phys. Rev. B **72**, 094104 (2005).

[126] M. Sato, Y. Koike, S. Katano, N. Metoki, H. Kadowaki, and S. Kawarazaki, *Field-induced Ferromagnetic Correlation in the Metamagnetic Crossover in CeRu2Si2 as Studied by Neutron Scattering*, J. Phys. Soc. Japan **73**, 3418 (2004).

[127] J. G. Bednorz and K. A. Müller, Z. Phys. B: Condens. Matter **64**, 189 (1986).

[128] A. J. Leggett, *A theoretical description of the new phases of liquid ^3He*, Rev. Mod. Phys. **47**, 331 (1975).

[129] J. C. Wheatley, *Experimental properties of superfluid ^3He*, Rev. Mod. Phys. **47**, 415 (1975).

[130] R. Joynt and L. Taillefer, *The superconducting phases of UPt$_3$*, Rev. Mod. Phys. **74**, 235 (2002).

[131] S. S. Saxena, P. Agarwal, K. Ahilan, F. M. Grosche, R. K. W. Haselwimmer, M. J. Steiner, E. Pugh, I. R. Walker, S. R. Julian, P. Monthoux, G. G. Lonzarich, A. Huxley, I. Sheikin, D. Braithwaite, and J. Flouquet, *Superconductivity on the border of itinerant-electron ferromagnetism in UGe$_2$*, Nature **406**, 587 (2000).

[132] T. Rice and M. Sigrist, *Sr$_2$RuO$_4$: an electronic analogue of ^3He?*, J. Phys. – Condens. Matter **7**, L643 (1995).

[133] A. Mackenzie and Y. Maeno, *The superconductivity of Sr$_2$RuO$_4$ and the physics of spin-triplet pairing*, Rev. Mod. Phys. **75**, 657 (2003).

[134] K. Ishida, H. Mukuda, Y. Kitaoka, K. Asayama, Z. Mao, Y. Mori, and Y. Maeno, *Spin-triplet superconductivity in Sr$_2$RuO$_4$ identified by ^{17}O Knight shift*, Nature **396**, 658 (1998).

[135] K. Ishida, H. Mukuda, Y. Kitaoka, Z. Q. Mao, H. Fukazawa, and Y. Maeno, *Ru NMR probe of spin susceptibility in the superconducting state of Sr$_2$RuO$_4$*, Phys. Rev. B **63**, 060507 (2001).

[136] J. Duffy, S. Hayden, Y. Maeno, Z. Mao, J. Kulda, and G. McIntyre, *Polarized-Neutron Scattering Study of the Cooper-Pair Moment in Sr$_2$RuO$_4$*, Phys. Rev. Lett. **85**, 5412 (2000).

[137] H. Murakawa, K. Ishida, K. Kitagawa, Z. Q. Mao, and Y. Maeno, *Measurement of the Ru-Knight Shift of Superconducting Sr$_2$RuO$_4$ in a Parallel Magnetic Field*, Phys. Rev. Lett. **93**, 167004 (2004).

[138] K. Nelson, Z. Mao, Y. Maeno, and Y. Liu, *Odd-Parity Superconductivity in Sr$_2$RuO$_4$*, Science **306**, 1151 (2004).

[139] M. Rice, *Superfluid ^3He has a metallic partner*, Science **306**, 1142 (2004).

[140] I. Žutić and I. Mazin, *Phase-Sensitive Tests of the Pairing State Symmetry in Sr$_2$RuO$_4$*, Phys. Rev. Lett. **95**, 217004 (2005).

[141] Z. Mao, Y. Maeno, Y. Mori, S. Sakita, S. Nimori, and M. Udagawa, *Sign reversal of the oxygen isotope effect on T_c in Sr$_2$RuO$_4$*, Phys. Rev. B **63**, 144514 (2001).

[142] I. Schnell, I. I. Mazin, and A. Y. Liu, *Unconventional superconducting pairing symmetry induced by phonons*, Phys. Rev. B **74**, 184503 (2006).

[143] T. Kuwabara and M. Ogata, *Spin-Triplet Superconductivity due to Antiferromagnetic Spin-Fluctuation in Sr$_2$RuO$_4$*, Phys. Rev. Lett. **85**, 4586 (2000).

[144] K. Ishida, H. Mukuda, Y. Minami, Y. Kitaoka, Z. Mao, H. Fukazawa, and Y. Maeno, *Normal-state spin dynamics in the spin-triplet superconductor Sr$_2$RuO$_4$*, Phys. Rev. B **64**, 100501(R) (2001).

[145] M. Braden, P. Steffens, Y. Sidis, J. Kulda, P. Bourges, S. Hayden, N. Kikugawa, and Y. Maeno, *Anisotropy of the Incommensurate Fluctuations in Sr$_2$RuO$_4$: A Study with Polarized Neutrons*, Phys. Rev. Lett. **92**, 097402 (2004).

[146] N. E. Hussey, A. P. Mackenzie, J. R. Cooper, Y. Maeno, S. Nishizaki, and T. Fujita, *Normal-state magnetoresistance of Sr$_2$RuO$_4$*, Phys. Rev. B **57**, 5505 (1998).

[147] T. Oguchi, *Electronic band structure of the superconductor Sr$_2$RuO$_4$*, Phys. Rev. B **51**, 1385 (1995).

[148] D. Singh, *Relationship of Sr$_2$RuO$_4$ to the superconducting layered cuprates*, Phys. Rev. B **52**, 1358 (1995).

[149] I. Hase and Y. Nishihara, *Electronic Structures of Sr$_2$RuO$_4$ and Sr$_2$RhO$_4$*, J. Phys. Soc. Japan **65**, 3957 (1996).

[150] C. Noce and M. Cuoco, *Energy bands and Fermi surface of Sr$_2$RuO$_4$*, Phys. Rev. B **59**, 2659 (1999).

[151] P. K. de Boer and R. A. de Groot, *Electronic structure of magnetic Sr$_2$RuO$_4$*, Phys. Rev. B **59**, 9894 (1999).

[152] I. I. Mazin, D. A. Papaconstantopoulos, and D. J. Singh, *Tight-binding Hamiltonians for Sr-filled ruthenates: Application to the gap anisotropy and Hall coefficient in Sr_2RuO_4*, Phys. Rev. B **61**, 5223 (2000).

[153] T. Mishonov and E. Penev, *Tight-binding modelling of the electronic band structure of layered superconducting perovskites*, J. Phys.: Condens. Matter **12**, 143 (2000).

[154] A. Pérez-Navarro, J. Costa-Quintana, and F. López-Aguilar, *Electronic structure of Sr_2RuO_4 by means of local-density approximation plus strong correlation effects*, Phys. Rev. B **61**, 10125 (2000).

[155] H. Ding, S.-C. Wang, H.-B. Yang, T. Takahashi, J. C. Campuzano, and Y. Maeno, *Band reflection and surface reconstruction in Sr_2RuO_4*, Physica C **364-365**, 594 (2001).

[156] A. Puchkov, Z.-X. Shen, T. Kimura, and Y. Tokura, *ARPES results on Sr_2RuO_4: Fermi surface revisited*, Phys. Rev. B **58**, R13322 (1998).

[157] N. J. C. Ingle, K. M. Shen, F. Baumberger, W. Meevasana, D. H. Lu, Z.-X. Shen, A. Damascelli, S. Nakatsuji, Z. Q. Mao, Y. Maeno, T. Kimura, and Y. Tokura, *Quantitative analysis of Sr_2RuO_4 angle-resolved photoemission spectra: Many-body interactions in a model Fermi liquid*, Phys. Rev. B **72**, 205114 (2005).

[158] Y. Yoshida, R. Settai, Y. Onuki, H. Takei, K. Betsuyaku, and H. Harima, *Fermi Surface and Yamaji Effect in Sr_2RuO_4*, J. Phys. Soc. Japan **67**, 1677 (1998).

[159] C. Bergemann, S. Julian, A. Mackenzie, S. NishiZaki, and Y. Maeno, *Detailed Topography of the Fermi Surface of Sr_2RuO_4*, Phys. Rev. Lett. **84**, 2662 (2000).

[160] C. Bergemann, A. Mackenzie, S. Julian, D. Forsythe, and E. Ohmichi, *Quasi-two-dimensional Fermi liquid properties of the unconventional superconductor Sr_2RuO_4*, Adv. in Phys. **52**, 639 (2003).

[161] Y. Maeno, K. Yoshida, H. Hashimoto, S. Nishizaki, S. ichi Ikeda, M. Nohara, T. Fujita, A. P. Mackenzie, N. E. Hussey, J. G. Bednorz, and F. Lichtenberg, *Two-Dimensional Fermi Liquid Behavior of the Superconductor Sr_2RuO_4*, J. Phys. Soc. Japan **66**, 1405 (1997).

[162] K.-K. Ng and M. Sigrist, *Anisotropy of the Spin Susceptibility in the Normal State of Sr_2RuO_4*, J. Phys. Soc. Japan **69**, 3764 (2000).

[163] T. Takimoto, *Orbital fluctuation-induced triplet superconductivity: Mechanism of superconductivity in Sr_2RuO_4*, Phys. Rev. B **62**, R14641 (2000).

[164] T. Nomura and K. Yamada, *Perturbation Theory of Spin-Triplet Superconductivity for Sr_2RuO_4*, J. Phys. Soc. Japan **69**, 3678 (2000).

[165] I. Eremin, D. Manske, C. Joas, and K. H. Bennemann, *Electronic theory for superconductivity in Sr_2RuO_4: Triplet pairing due to spin-fluctuation exchange*, Europhys. Lett. **58**, 871 (2002).

[166] I. Eremin, D. Manske, and K. Bennemann, *Electronic theory for the normal-state spin dynamics in Sr_2RuO_4: Anisotropy due to spin-orbit coupling*, Phys. Rev. B **65**, 220502(R) (2002).

[167] I. Eremin, D. Manske, S. G. Ovchinnikov, and J. F. Annett, *Unconventional superconductivity and magnetism in Sr_2RuO_4 and related materials*, Ann. Phys. (Leipzig) **13**, 149 (2004).

[168] T. Imai, A. Hunt, K. Thurber, and F. Chou, *^{17}O NMR Evidence for Orbital Dependent Ferromagnetic Correlations in Sr_2RuO_4*, Phys. Rev. Lett. **81**, 3006 (1998).

[169] H. Mukuda, K. Ishida, Y. Kitaoka, K. Asayama, Z. Mao, Y. Mori, and Y. Maeno, *Novel Character of Spin Fluctuations in Spin-Triplet Superconductor Sr_2RuO_4: ^{17}O-NMR Study*, J. Phys. Soc. Japan **67**, 3945 (1998).

[170] K. Ishida, Y. Kitaoka, K. Asayama, S. Ikeda, S. Nishizaki, Y. Maeno, K. Yoshida, and T. Fujita, *Anisotropic pairing in superconducting Sr_2RuO_4: Ru NMR and NQR studies*, Phys. Rev. B **56**, R505 (1997).

[171] H. Mukuda, K. Ishida, Y. Kitaoka, K. Asayama, R. Kanno, and M. Takano, *Spin fluctuations in the ruthenium oxides RuO_2, $SrRuO_3$, $CaRuO_3$, and Sr_2RuO_4 probed by Ru NMR*, Phys. Rev. B **60**, 12279 (1999).

[172] C. Berthier, M. Julien, M. Horvatié, and Y. Berthier, *NMR Studies of the Normal State of High Temperature Superconductors*, J. Phys. I France **6**, 2205 (1996).

[173] A. P. Mackenzie, S. I. Ikeda, Y. Maeno, S. R. J. T. Fujita, and G. G. Lonzarich, *The Fermi Surface Topography of Sr_2RuO_4*, J. Phys. Soc. Japan **67**, 385 (1998).

[174] D. F. Agterberg, T. M. Rice, and M. Sigrist, *Orbital Dependent Superconductivity in Sr_2RuO_4*, Phys. Rev. Lett. **78**, 3374 (1997).

[175] I. Mazin and D. Singh, *Ferromagnetic Spin Fluctuation Induced Superconductivity in Sr_2RuO_4*, Phys. Rev. Lett. **79**, 733 (1997).

[176] I. Mazin and D. Singh, *Magnetism and spin-fluctuation induced superconductivity in Ruthenates*, J. Phys. Chem. Solids **59**, 2185 (1998).

[177] D. Fay and J. Appel, *Coexistence of p-state superconductivity and itinerant ferromagnetism*, Phys. Rev. B **22**, 3173 (1980).

[178] R. Werner and V. Emery, *Low-temperature electronic properties of Sr_2RuO_4. I. Microscopic model and normal-state properties*, Phys. Rev. B **67**, 014504 (2003).

[179] Y. Sidis, S. Pailhes, B. Keimer, P. Bourges, C. Ulrich, and L. Regnault, *Magnetic resonant excitations in High-Tc superconductors*, Phys. Stat. Sol. (b) **241**, 1204 (2004).

[180] M. Yakiyama and Y. Hasegawa, *Coherence peak in the spin susceptibility from nesting in spin-triplet superconductors: A probe for line nodes in Sr_2RuO_4*, Phys. Rev. B **67**, 014512 (2003).

[181] D. Fay and L. Tewordt, *Collective order-parameter modes for hypothetical p-wave superconducting states in Sr_2RuO_4*, Phys. Rev. B **62**, 4036 (2000).

[182] H.-Y. Kee, *Probing pairing symmetry in Sr_2RuO_4*, J. Phys.: Condens. Matter **12**, 2279 (2000).

[183] M. Zhitomirsky and T. Rice, *Interband Proximity Effect and Nodes of Superconducting Gap in Sr_2RuO_4*, Phys. Rev. Lett. **87**, 057001 (2001).

[184] K. Deguchi, Z. Q. Mao, H. Yaguchi, and Y. Maeno, *Gap Structure of the Spin-Triplet Superconductor Sr_2RuO_4 Determined from the Field-Orientation Dependence of the Specific Heat*, **92**, 047002 (2004).

[185] K. Deguchi, Z. Mao, and Y. Maeno, *Determination of the Superconducting Gap Structure in All Bands of the Spin-Triplet Superconductor Sr2RuO4*, J. Phys. Soc. Japan **73**, 1313 (2004).

[186] K. Yoshida, F. Nakamura, T. Goko, T. Fujita, Y. Maeno, Y. Mori, and S. NishiZaki, *Electronic crossover in the highly anisotropic normal state of Sr_2RuO_4 from pressure effects on electrical resistivity*, Phys. Rev. B **58**, 15062 (1998).

[187] D. Forsythe, S. Julian, C. Bergemann, E. Pugh, M. Steiner, P. Alireza, G. McMullan, F. Nakamura, R. Haselwimmer, I. Walker, S. Saxena, G. Lonzarich, A. Mackenzie, Z. Mao, and Y. Maeno, *Evolution of Fermi-Liquid Interactions in Sr_2RuO_4 under Pressure*, Phys. Rev. Lett. **89**, 166402 (2002).

[188] M. Minakata and Y. Maeno, *Magnetic ordering in Sr_2RuO_4 induced by nonmagnetic impurities*, Phys. Rev. B **63**, 180504 (2001).

[189] M. Braden, O. Friedt, Y. Sidis, P. Bourges, M. Minakata, and Y. Maeno, *Incommensurate Magnetic Ordering in $Sr_2Ru_{1-x}Ti_xO_4$*, Phys. Rev. Lett. **88**, 197002 (2002).

[190] K. Pucher, J. Hemberger, F. Mayr, V. Fritsch, A. Loidl, E.-W. Scheidt, S. Klimm, R. Horny, S. Horn, S. G. Ebbinghaus, A. Reller, and R. J. Cava, *Transport, magnetic, thermodynamic, and optical properties in Ti-doped Sr_2RuO_4*, Phys. Rev. B **65**, 104523 (2002).

[191] H. R. Oswald and S. Felder-Casagrande, *Structure and properties of perovskite-related Sr-Ru-Ti-O phases*, Solid State Ionics **63-65**, 565 (1993).

[192] K. Chandrasekaran, R. Vijayaraghavan, and U. V. Varadaraju, *Effects of oxygen non-stoichiometry and cationic substitutions on the properties of $Sr_2RuO_{4+\delta}$*, Mat. Chem. Phys. **56**, 63 (1998).

[193] S. Ray, D. D. Sarma, and R. Vijayaraghavan, *Electron-spectroscopic investigation of the metal-insulator transition in $Sr_2Ru_{1-x}Ti_xO_4$ (x = 0–0.6)*, Phys. Rev. B **73**, 165105 (2006).

[194] J. Kim, J.-Y. Kim, B.-G. Park, and S.-J. Oh, *Photoemission and x-ray absorption study of the electronic structure of $SrRu_{1-x}Ti_xO_3$*, Phys. Rev. B **73**, 235109 (2006).

[195] S. Halilov, D. Singh, J. Minár, A. Perlov, and H. Ebert, *Antiferromagnetic spin fluctuations and proximity to a quantum critical point in Sr_2RuO_4*, Phys. Rev. B **71**, 100503(R) (2005).

[196] E. Fawcett, *Spin-density-wave antiferromagnetism in chromium*, Rev. Mod. Phys. **60**, 209 (1988).

[197] B. H. Grier, G. Shirane, and S. A. Werner, *Magnetic excitations in chromium. II*, Phys. Rev. B **31**, 2892 (1985).

[198] C. R. Fincher, G. Shirane, and S. A. Werner, *Magnetic excitations in chromium*, Phys. Rev. B **24**, 1312 (1981).

[199] P. Böni, B. J. Sternlieb, G. Shirane, B. Roessli, J. E. Lorenzo, and S. A. Werner, *Polarization dependence of the magnetic fluctuations in Cr below T_N*, Phys. Rev. B **57**, 1057 (1998).

[200] C. R. Fincher, G. Shirane, and S. A. Werner, *Magnetic Excitations of the Incommensurate Spin-Density Wave in Chromium Metal*, Phys. Rev. Lett. **43**, 1441 (1979).

[201] S. K. Burke, W. G. Stirling, K. R. A. Ziebeck, and J. G. Booth, *Magnetic Excitations in the Incommensurate Phases of Chromium Metal*, Phys. Rev. Lett. **51**, 494 (1983).

[202] B. J. Sternlieb, G. Shirane, S. A. Werner, and E. Fawcett, *Fincher-Burke excitations in the transverse spin-density-wave phase of chromium*, Phys. Rev. B **48**, 10217 (1993).

[203] R. S. Fishman and S. H. Liu, *Spin dynamics of chromium. I. Formalism and commensurate alloys*, Phys. Rev. B **54**, 7233 (1996).

[204] R. S. Fishman and S. H. Liu, *Spin dynamics of chromium. II. Incommensurate alloys*, Phys. Rev. B **54**, 7252 (1996).

[205] P. A. Fedders and P. C. Martin, *Itinerant Antiferromagnetism*, Phys. Rev. **143**, 245 (1966).

[206] W. Bao, C. Broholm, S. A. Carter, T. F. Rosenbaum, G. Aeppli, S. F. Trevino, P. Metcalf, J. M. Honig, and J. Spalek, *Incommensurate spin density wave in metallic $V_{2-y}O_3$*, Phys. Rev. Lett. **71**, 766 (1993).

[207] W. Bao, C. Broholm, G. Aeppli, S. A. Carter, P. Dai, T. F. Rosenbaum, J. M. Honig, P. Metcalf, and S. F. Trevino, *Magnetic correlations and quantum criticality in the insulating antiferromagnetic, insulating spin liquid, renormalized Fermi liquid, and metallic antiferromagnetic phases of the Mott system V_2O_3*, Phys. Rev. B **58**, 12727 (1998).

[208] N. Kikugawa and Y. Maeno, *Non-Fermi-Liquid Behavior in Sr_2RuO_4 with Nonmagnetic Impurities*, Phys. Rev. Lett. **89**, 117001 (2002).

[209] A. Mackenzie, R. Haselwimmer, A. Tyler, G. Lonzarich, Y. Mori, S. Nishizaki, and Y. Maeno, *Extremely Strong Dependence of Superconductivity on Disorder in Sr_2RuO_4*, Phys. Rev. Lett. **80**, 161 (1998).

[210] Z. Mao, Y. Mori, and Y. Maeno, *Suppression of superconductivity in Sr_2RuO_4 caused by defects*, Phys. Rev. B **60**, 610 (1999).

[211] J. A. Hertz, *Quantum critical phenomena*, Phys. Rev. B **14**, 1165 (1976).

[212] A. J. Millis, *Effect of a nonzero temperature on quantum critical points in itinerant fermion systems*, Phys. Rev. B **48**, 7183 (1993).

[213] S. Sachdev and J. Ye, *Universal quantum-critical dynamics of two-dimensional antiferromagnets*, Phys. Rev. Lett. **69**, 2411 (1992).

[214] A. Schröder, G. Aeppli, E. Bucher, R. Ramazashvili, and P. Coleman, *Scaling of Magnetic Fluctuations near a Quantum Phase Transition*, Phys. Rev. Lett. **80**, 5623 (1998).

[215] A. Schröder, G. Aeppli, R. Coldea, M. Adams, O. Stockert, H. Löhneysen, E. Bucher, R. Ramazashvili, and P. Coleman, *Onset of antiferromagnetism in heavy-fermion metals*, Nature **407**, 351 (2000).

[216] M. C. Aronson, R. Osborn, R. A. Robinson, J. W. Lynn, R. Chau, C. L. Seaman, and M. B. Maple, *Non-Fermi-Liquid Scaling of the Magnetic Response in $UCu_{5-x}Pd_x$ (x=1,1.5)*, Phys. Rev. Lett. **75**, 725 (1995).

[217] J.-G. Park, D. T. Adroja, K. A. McEwen, and A. P. Murani, *Non-Fermi liquid behaviour in the dynamic susceptibility of $Ce(Rh_{0.8}Pd_{0.2})Sb$*, J. Phys.: Condens. Matter **14**, 3865 (2002).

[218] J.-Y. So, J.-G. Park, D. T. Adroja, K. A. McEwen, A. P. Murani, and S.-J. Oh, *Understanding the origin of non-Fermi liquid behaviour in doped Kondo insulators*, J. Phys.: Condens. Matter **15**, S2153 (2003).

[219] B. Keimer, R. J. Birgeneau, A. Cassanho, Y. Endoh, R. W. Erwin, M. A. Kastner, and G. Shirane, *Scaling Behavior of the Generalized Susceptibility in $La_{2-x}Sr_xCuO_{4+y}$*, Phys. Rev. Lett. **67**, 1930 (1991).

[220] W. Bao, Y. Chen, Y. Qiu, and J. L. Sarrao, *Novel Dynamic Scaling Regime in Hole-Doped La_2CuO_4*, Phys. Rev. Lett. **91**, 127005 (2003).

[221] W. Montfrooij, M. C. Aronson, B. D. Rainford, J. A. Mydosh, A. P. Murani, P. Haen, and T. Fukuhara, *Extended versus Local Fluctuations in Quantum Critical $Ce(Ru_{1-x}Fe_x)_2Ge_2$ (x=x_c=0.76)*, Phys. Rev. Lett. **91**, 087202 (2003).

[222] W. Knafo, S. Raymond, J. Flouquet, B. F. k, M. A. Adams, P. Haen, F. Lapierre, S. Yates, and P. Lejay, *Anomalous scaling behavior of the dynamical spin susceptibility of $Ce_{0.925}La_{0.075}Ru_2Si_2$*, Phys. Rev. B **70**, 174401 (2004).

[223] G. Cao, S. C. McCall, J. E. Crow, and R. P. Guertin, *Multiple magnetic phase transitions in single-crystal $(Sr_{1-x}Ca_x)_3Ru_2O_7$ for 0<x<1.0*, Phys. Rev. B **56**, 5387 (1997).

[224] S. Ikeda, Y. Maeno, and T. Fujita, *Weak ferromagnetism in two-dimensional bilayered $Sr_{3-x}Ca_xRu_2O_7$*, Phys. Rev. B **57**, 978 (1998).

[225] A. Puchkov, M. Schabel, D. Basov, T. Startseva, G. Cao, T. Timusk, and Z.-X. Shen, *Layered Ruthenium Oxides: From Band Metal to Mott Insulator*, Phys. Rev. Lett. **81**, 2747 (1998).

[226] Y. Yoshida, S.-I. Ikeda, H. Matsuhata, N. Shirakawa, C. H. Lee, and S. Katano, *Crystal and magnetic structure of $Ca_3Ru_2O_7$*, Phys. Rev. B **72**, 054412 (2005).

[227] G. Cao, K. Abboud, S. McCall, J. E. Crow, and R. P. Guertin, *Spin-charge coupling for dilute La-doped $Ca_3Ru_2O_7$*, Phys. Rev. B **62**, 998 (2000).

[228] Y. Yoshida, I. Nagai, S.-I. Ikeda, N. Shirakawa, M. Kosaka, and N. Mori, *Quasi-two-dimensional metallic ground state of $Ca_3Ru_2O_7$*, Phys. Rev. B **69**, 220411(R) (2004).

[229] G. Cao, L. Balicas, Y. Xin, L. E. Crow, and C. S. Nelson, *Quantum oscillations, colossal magnetoresistance, and the magnetoelastic interaction in bilayered $Ca_3Ru_2O_7$*, Phys. Rev. B **67**, 184405 (2003).

[230] E. Ohmichi, Y. Yoshida, S. I. Ikeda, N. Shirakawa, and T. Osada, *Colossal magnetoresistance accompanying a structural transition in a highly two-dimensional metallic state of $Ca_3Ru_2O_7$*, Phys. Rev. B **70**, 104414 (2004).

[231] G. Cao, L. Balicas, Y. Xin, E. Dagotto, J. E. Crow, C. S. Nelson, and D. F. Agterberg, *Tunneling magnetoresistance and quantum oscillations in bilayered $Ca_3Ru_2O_7$*, Phys. Rev. B **67**, 060406 (2003).

[232] F. Baumberger, N. J. C. Ingle, N. Kikugawa, M. A. Hossain, W. Meevasana, R. S. Perry, K. M. Shen, D. H. Lu, A. Damascelli, A. Rost, A. P. Mackenzie, Z. Hussain, and Z.-X. Shen, *Nested Fermi Surface and Electronic Instability in $Ca_3Ru_2O_7$*, Phys. Rev. Lett. **96**, 107601 (2006).

[233] G. Cao, X. N. Lin, L. Balicas, S. Chikara, J. E. Crow, and P. Schlottmann, *Orbitally driven behaviour: Mott transition, quantum oscillations and colossal magnetoresistance in bilayered $Ca_3Ru_2O_7$*, New J. Phys. **6**, 159 (2004).

[234] G. Cao, S. McCall, J. E. Crow, and R. P. Guertin, *Observation of a Metallic Antiferromagnetic Phase and Metal to Nonmetal Transition in $Ca_3Ru_2O_7$*, Phys. Rev. Lett. **78**, 1751 (1997).

[235] D. J. Singh and S. Auluck, *Electronic Structure and Bulk Spin-Valve Behavior in $Ca_3Ru_2O_7$*, Phys. Rev. Lett. **96**, 097203 (2006).

[236] S. McCall, G. Cao, and J. E. Crow, *Impact of magnetic fields on anisotropy in $Ca_3Ru_2O_7$*, Phys. Rev. B **67**, 094427 (2003).

[237] J. F. Karpus, R. Gupta, H. Barath, and S. L. Cooper, *Field-induced Orbital and Magnetic Phases in $Ca_3Ru_2O_7$*, Phys. Rev. Lett. **93**, 167205 (2004).

[238] J. F. Karpus, C. S. Snow, R. Gupta, H. Barath, and S. L. Cooper, *Spectroscopic study of the field- and pressure-induced phases of the bilayered ruthenate $Ca_3Ru_2O_7$*, Phys. Rev. B **73**, 134407 (2006).

[239] C. S. Nelson, H. Mo, B. Bohnenbuck, J. Strempfer, N. Kikugawa, S. I. Ikeda, and Y. Yoshida, *Spin-charge-lattice coupling near the metal-insulator transition in $Ca_3Ru_2O_7$*, Phys. Rev. B **75**, 212403 (2007).

[240] O. Schumann, Phd thesis, to be written (university of cologne).

[241] K. W. Kim, J. S. Lee, T. W. Noh, S. R. Lee, and K. Char, *Metal-insulator transition in a disordered and correlated $SrTi_{1-x}Ru_xO_3$ system: Changes in transport properties, optical spectra, and electronic structure*, Phys. Rev. B **71**, 125104 (2005).

[242] L. Mieville, T. H. Geballe, L. Antognazza, and K. Char, *Ti and Ca substitution in $SrRuO_3$ thin films by sequential deposition process*, Appl. Phys. Lett. **70**, 126 (1997).

[243] M. Abbate, J. A. Guevara, S. Cuffini, Y. Mascarenhas, and E. Morikawa, *Electronic structure and metal-insulator transition in $SrTi_{1-x}Ru_xO_3$*, Eur. Phys. J. B **25**, 203 (2002).

[244] R. Mathieu, A. Asamitsu, Y. Kaneko, J. P. He, X. Z. Yu, R. Kumai, Y. Onose, N. Takeshita, T. Arima, H. Takagi, and Y. Tokura, *Impurity-induced transition to a Mott insulator in $Sr_3Ru_2O_7$*, Phys. Rev. B **72**, 092404 (2005).

[245] J. Hooper, M. H. Fang, M. Zhou, D. Fobes, N. Dang, Z. Q. Mao, C. M. Feng, Z. A. Xu, M. H. Yu, C. J. O'Connor, G. J. Xu, N. Andersen, and M. Salamon, *Competing magnetic fluctuations in $Sr_3Ru_2O_7$ probed by Ti doping*, Phys. Rev. B **75**, 060403 (2007).

Index

Offizielle Erklärung

Ich versichere, dass ich die von mir vorgelegte Dissertation selbstständig angefertigt, die benutzten Quellen und Hilfsmittel vollständig angegeben und die Stellen der Arbeit – einschließlich Tabellen, Karten und Abbildungen –, die anderen Werken im Wortlaut oder dem Sinn nach entnommen sind, in jedem Einzelfall als Entlehnung kenntlich gemacht habe; dass diese Dissertation noch keiner anderen Fakultät oder Universität zur Prüfung vorgelegen hat; dass sie – abgesehen von unten angegebenen Teilpublikationen – noch nicht veröffentlicht worden ist sowie, dass ich eine solche Veröffentlichung vor Abschluss des Promotionsverfahrens nicht vornehmen werde. Die Bestimmungen der Promotionsordnung sind mir bekannt. Die von mir vorgelegte Dissertation ist von Prof. Dr. M. Braden betreut worden.

Köln, den 13. September 2007

Paul Steffens